

Porous Monolithic Polymeric Supports with Uniform Diameter and Tailored Functional Groups

Von der Fakultät Chemie der Universität Stuttgart
zur Erlangung der Würde eines
Doktors der Naturwissenschaften (Dr. rer. nat.) genehmigte Abhandlung

vorgelegt von

Hande Acikalin

aus der Türkei

Hauptberichter: Prof. Dr. Michael R. Buchmeiser

1. Mitberichter: Prof. Dr. Thomas Sottmann

2. Mitberichter: Prof. Dr. Johannes Kaestner

Tag der mündlichen Prüfung: 10.11.2023

Institut für Polymerchemie
der Universität Stuttgart

2023

This work was carried out from December 2018 to June 2022 at the Institute of Polymer Chemistry, University of Stuttgart, under the supervision of Prof. Dr. Michael R. Buchmeiser.

Erklärung über die Eigenständigkeit der Dissertation

Ich versichere, dass ich die vorliegende Arbeit mit dem Titel:

„Porous Monolithic Polymeric Supports with Uniform Diameter and Tailored Functional Groups“

selbstständig verfasst und keine anderen als die angegebenen Quellen und Hilfsmittel benutzt habe; aus fremden Quellen entnommene Passagen und Gedanken sind als solche kenntlich gemacht.

Declaration of Authorship

I hereby certify that the dissertation entitled:

„Porous Monolithic Polymeric Supports with Uniform Diameter and Tailored Functional Groups“

is entirely my own work except where otherwise indicated. Passages and ideas from other sources have been clearly indicated.

Name/Name: Hande Acikalin

Unterschrift/Signed: _____

Datum/Date: _____

Acknowledgements

I would like to take this opportunity to thank all my colleagues at the Institute of Polymer Chemistry at the University of Stuttgart and the CRC 1333 project for the very good cooperation and the wonderful time we spent together.

My special thanks go to Prof. Dr. Michael R. Buchmeiser for the opportunity to do a Ph.D. in his research group, the extremely interesting task, the very good supervision, and the provision of excellently equipped laboratories.

Many thanks to Dr. Dongren Wang. Without his constant, self-sacrificing commitment, the operation of the institute would hardly be possible. Special thanks to Dr. Yavuz Caydamli for his immense support and care that made my academic life at ease. I would like to thank my friends Alina Fox, Dr. Philipp Hauser, Dr. Mohasin Momin, Jonas Gross, Ayla Sirin, Boshra Atwi and Koushani Kundu for their great friendship during Ph.D.

Many thanks to Dr. Elisabeth Ruethlein for her important contributions to the CRC project. Special thanks to Felix Ziegler and Dr. Pradeep Panyam for their immense support and experimental contribution on my project.

I am grateful to Prof. Dr. Thomas Sottmann and Prof. Dr. Johannes Kaestner for their willingness to be my examiners and for the interesting collaboration projects.

I would like to thank all those who provided the technical and analytical support to complete this thesis work. Ulrich Hageroth for SEM/EDX measurements, Kuan Meng for TEM measurement. Shravan R. Kousik, Dr. Petia Atanasova and Dr. Kaloian Koynov for CLSM measurement. Many thanks to Kamila Parastatidou for assisting me in ordering the chemicals and other required things.

Thanks a ton, to all my colleagues in Stuttgart for their support and intimacy on and off the academia. My very special thanks to my family members Aydin A., Gülseren A., and Derya A. for their life-long love, support, and intimacy. Many thanks to Ayşe Firat and Muge Colakoglu for their immense support during Ph.D.

Contents

Abbreviations and Symbols	viii
Motivation.....	x
Zusammenfassung	xii
Abstract	xvii
1. BRIEF THEORETICAL SURVEY.....	1
1.1 Polymeric Monolithic Support Materials.....	2
1.2 Characterization Techniques.....	6
1.2.1 Inverse size-exclusion chromatography (ISEC).....	6
1.2.2 Brunauer-Emmett-Teller (BET)	9
1.3 Ordered Mesoporous Materials (OMMs): Historical Perspective and Recent Developments	13
1.3.1 Hard Templating.....	15
1.3.2 Soft Templating	17
1.3.3 Ordered Mesoporous Materials (OMMs): Prospects and Applications	19
1.4 Polyurethanes: Prospects and Applications	23
1.5 Olefin Metathesis-Derived Polymers and Monoliths	24
1.5.1 Ring-Opening Metathesis Polymerization (ROMP)	26
1.5.2 Living Ring-Opening Metathesis Polymerization (ROMP)	28
1.6 Supported Catalysts for Continuous Flow Synthesis	31
1.6.1 Packed Reactors.....	32
1.6.1.1 Monolithic Flow-Through Reactors	34
1.6.1.2 Silica-Based Monolith Reactors	35
1.6.1.3 Polymer-Based Monolith Reactors.....	37
1.7 Hydrosilylation of Alkynes.....	39
1.8 Ionic Liquids	42
1.9 Supported Ionic Liquid Phase (SILP) Catalysis	43
2. RESULT AND DISCUSSION	47
2.1 Tailoring Mesoporosity in Poly(norborn-2-ene)-Based Monolithic Supports	48
2.1.1 Working hypothesis.....	48
2.1.2 ROMP-derived monoliths based on the reaction parameters.....	51

2.1.3 ROMP-derived monoliths using Pluronic F-127 as an additive	58
2.1.4 Summary and Outlook.....	60
2.2 A Hard-Templating Approach to Functional Mesoporous Poly (Norborn-2-ene)-Derived Monolithic Supports.....	61
2.2.1 Introduction	61
2.2.2 Results and Discussion	63
2.2.3 Summary and Outlook.....	82
2.3 Tailoring Mesoporosity in Poly(urethane)-Derived Monolithic Supports	83
2.3.1 Introduction	83
2.3.2 Result and Discussion.....	84
2.3.3 Tailoring Mesoporosity in Polyurea-Derived Monolithic Supports.....	89
2.3.4 Summary and Outlook.....	91
2.4 Hydrosilylation of Alkynes Using Surface-Functionalized Monolithic Supports with Tailored Mesoporosity.....	92
2.4.1 Introduction	92
2.4.2 Result and Discussion.....	94
2.4.2.1 Preparation and Characterization of Surface-Functionalized Poly(urethane) -Derived Monolithic Supports	94
2.4.2.2 Preparation and Characterization of Surface-Functionalized ROMP-Derived Monolithic Supports	101
2.4.3 Summary and Outlook.....	105
3. EXPERIMENTAL AND SPECTROSCOPIC DATA.....	107
3.1 General	108
3.2 Spectroscopic Data	116
4. REFERENCES	118
5. APPENDIX	130
6. CURRICULUM VITAE.....	182

Abbreviations and Symbols

FT-IR	Fourier-transform infrared spectroscopy
[BMIM ⁺][BF ₄ ⁻]	1-Butyl-3-methylimidazolium tetrafluoroborate
Å	Angstrom
ISEC	Inverse-size exclusion chromatography
ϵ_p	Volume fraction of pores
ϵ_t	Total porosity
ϵ_z	Volume fraction of the inter-microglobules void volume
<i>g</i>	Gram
IL	Ionic liquid
mL	Milliliter
min	Minute
NBE	Norborn-2-ene
NHC	<i>N</i> -Heterocyclic carbene
PrOH	Propanol
ROMP	Ring-opening metathesis polymerization
SILP	Supported ionic-liquid phase
THF	Tetrahydrofuran
wt.-%	Weight percentage
DMNH6	1,4,4a,5,8,8a-hexahydro-1,4,5,8- <i>exo-endo</i> -dimethanonaphthalene
mmol	Millimol
BET	Brunauer–Emmett–Teller
OMM	Ordered mesoporous material

IUPAC	International Union of Pure and Applied Chemistry
SNW	Silica nanowire
SIPS	Solvent-induced phase separation
TMPTNC	Trimethylolpropane-tris-(5-norbornene-2-yl-carboxylate)
OMC	Ordered mesoporous carbon
PS	Polystyrene
Ar	Argon
DFT	Density functional theory
FH	Flory-Huggins
PUR	Poly(urethane)
DBTDL	Dibutyltin dilaurate
HMDI	Hexamethylene diisocyanate trimer
HF	Hydrogen fluoride
OA	Oleic acid
THP	1,1,1-Tris(hydroxymethyl)propane
PDI	Polydispersity Index
MMC	Macro(mono)cyclization
O	Oligomerization products
MDI	4,4-Methylenebis(phenyl isocyanate)
OMO	Ordered mesoporous organosilica
MTBE	Methyl <i>tert</i> -butyl ether
N ₂	Nitrogen
RCM	Ring-closing metathesis
HMS	Hollow mesoporous silica
PEG	Polyethylene glycol

Motivation

Catalysis plays a crucial role in 80 % of all chemical processes in the pharmaceutical, agrochemical, and chemical industries. Catalysis can be classified as heterogeneous if the catalyst is in a different phase than the substrates or as homogeneous if both the catalyst and the substrates are in the same phase [1]. One notable advantage of homogeneous catalysis over heterogeneous catalysis is high selectivity for the desired products. In the last decades, three Nobel prizes in chemistry have been awarded to scientists for their contributions to transition-metal/organometallic catalysis, an important class of homogeneous catalysis in which a metal atom surrounded by ligands acts as a catalytic active center [2]. The advancement of organometallic catalysis allows for the comprehension of molecular-scale information as well as further enhancements of catalytic selectivity and activities by tuning the electronic properties of the ligands. However, although the activity of homogeneous organometallic catalysts is exceptionally high compared with that of heterogeneous ones, their economical, toxicological, and environmental impacts remain an issue [3].

Recent developments in the field of organometallic catalysis were inspired by biocatalytic systems, i.e., enzymes [4]. In such systems, the catalytic cavity keeps the catalytic center in one place. This increases the affinity between the substrate and the catalyst, which accelerates the reaction. Another crucial point regarding biocatalysts is the pre-orientation of the substrates in a high-energy conformation, which results in increased reactivities and/or selectivities.

Based on the benefits of biocatalytic systems, several studies have been reported in the field of heterogeneous catalysis in confined spaces [5,6]. Recent research has focused on the combination of heterogeneous and homogeneous organometallic catalysis. This strategy, known as “molecular heterogeneous catalysis”, aims to combine the high activity and selectivity of molecular homogeneous catalysis with the advantages of heterogeneous catalysis, i.e., simplicity of removing and reusing a catalyst. The pore-containing support materials (i.e., porous polymers, porous carbon materials, porous inorganic materials, and porous organic/inorganic hybrid materials) enable an efficient impact on the reactivity and selectivity due to confinement effects. In order to observe these effects, the size of the pores (d_{pore}) is required to be only slightly larger than the dimensions of organometallic catalysts (~ 1 nm), therefore

mesoporous materials ($2 < d_{\text{pore}}/\text{nm} < 50$) are more suitable supports. Macroporous materials ($d_{\text{pore}} > 50 \text{ nm}$), on the other hand, have too large of cavities to induce confinement effects, while microporous materials have too small cavities to accommodate the catalyst and enable efficient mass transport. Thus, the unique mesoporosity, high surface area, and mesoporous channels of ordered mesoporous materials thus offer advantages in a wide range of applications that require efficient surface access and diffusion.

Inspired by the whole concept, the collaborative research center (CRC 1333) Molecular Heterogeneous Catalysis in Confined Geometries has investigated the influence of confinement on selected organometallic-catalysed transformations in organic chemistry (i.e., transfer hydrogenation, olefin metathesis, and asymmetric addition). Within the CRC, various porous materials, such as mesoporous silica, polymers, carbons, and organic/inorganic materials are being investigated for the immobilization of an organometallic catalyst. Here, the diffusion process of the reactants and products throughout the mesoporous materials is crucial for the catalytic reactions in the functionalized porous materials. The diffusion process depends on the size and shape of the pores and diffusing molecules as well as the repulsive and attractive interactions between the diffusing molecules and pore walls [7,8].

Polymeric, monolithic materials have the major advantage of fast mass transport between the monolithic support (stationary phase, catalyst bed) and the surrounding liquid (mobile phase, reaction mixture). For us in chromatography or heterogeneous catalysis, as well as for CRC1333, controlling the pore diameter of the materials is key. However, despite extensive research, producing uniform porous materials remains a significant challenge. Reaction parameters that determine the pore size of the materials often also affect other properties. With different ratios of precursor, for example, not only the pore size, but also the symmetry of the pore system can change, leading to different monolithic materials. In this work, we employ new methods to produce uniform polymeric, monolithic materials for the immobilization of catalysts. As part of CRC 1333, projects on catalysis, materials, and analytics involved close collaboration.

Zusammenfassung

Poröse Materialien spielen im Alltag eine entscheidende Rolle. Aufgrund ihrer geringen Dichte und hohen Stabilität werden sie in der Natur häufig als stabilisierendes Gerüst, z. B. in Knochen oder Holz, eingesetzt. Die Grundstruktur dieser Materialien besteht aus einem festen Hohlraum (Poren), der mit einem flüssigen oder gasförmigen Medium (Adsorbens) gefüllt ist. Das Volumen dieser Poren im Verhältnis zum Volumen des Feststoffs bestimmt die Porosität des Materials und die spezifische Oberfläche, die die für ein Adsorptionsmittel zugängliche Fläche beschreibt und sowohl die äußere und innere Oberfläche des Materials als auch die innere umfasste Oberfläche der Poren. Die vielfältigen Anwendungsmöglichkeiten basieren auf bemerkenswerten Eigenschaften wie großem Porenvolumen und Oberfläche, einer hydrophoben bzw. hydrophilen Oberfläche, hoher chemischer und thermischer Stabilität, elektrischer Leitfähigkeit, einfacher Handhabung und geringen Herstellungskosten.

Bezeichnenderweise haben mesoporöse strukturierte Materialien, die nach Definition der International Union of Pure and Applied Chemistry (IUPAC) Poren mit einem Durchmesser zwischen 2 nm und 50 nm aufweisen, aufgrund ihrer großen Oberflächen und Volumina große Aufmerksamkeit erhalten [9]. Dazu gehören bekannte Materialien wie die M41-Gruppe (MCM-41, MCM-48, MCM-50) und die SBA-Serie [10] sowie mesoporöse Materialien aus anorganischen, organischen oder hybriden Gerüsten [12] und kovalente organische Gerüste (COFs) [13]. Mesoporöse Materialien können geordnet oder ungeordnet sein und sind durch die Porengrößenverteilung gekennzeichnet. Die einzigartigen Eigenschaften geordneter mesoporöser Materialien (OMMs), einschließlich hoher spezifischer Oberflächen (bis zu $1.000 \text{ m}^2 \text{ g}^{-1}$) und wohldefinierter, einheitlicher Porengrößen, machen sie für spezifische praktische Anwendungen wie Katalyse, Energiespeichersysteme und Photokatalyse geeignet, Photoelektrokatalyse, Lithium-Ionen-Batterien, heterogene Katalyse, Extraktion von Metallen, Extraktion von Lanthaniden- und Aktinidenspezies, chirale Trennungen, Einfangen und die Art der Bindung von Kohlendioxid (CO_2), optische Geräte und magnetooptische Geräte. Von diesen Anwendungen ist die heterogene Katalyse vorherrschend [11,14]. Bei heterogenen katalytischen Prozessen ermöglicht die Immobilisierung der Katalysatoren auf festen Trägern eine einfache Abtrennung und Wiederverwendung des Katalysators und verhindert die Kontamination des Produkts mit Katalysatorspuren. Da die Aufarbeitung und

Reinigung sowie die Synthese des Katalysators selbst oft aufwendig und teuer sind, sind immobilisierte Katalysatoren sowohl aus ökologischer als auch ökonomischer Sicht ein wünschenswertes Ziel.

Mesoporöse Materialien verfügen über mehrere Eigenschaften, die sie zu hervorragenden Trägermaterialien für immobilisierte Katalysatoren machen. Diese Materialien sind mechanisch stabil und kostengünstig, quellen in organischen Lösungsmitteln nicht und ermöglichen aufgrund ihrer großen Oberfläche hohe Katalysatorbeladungen. Für ein gutes Trägermaterial ist nicht nur die Fläche der Oberfläche wichtig, auch die Poren müssen gut zugänglich sein. Die Struktur mesoporöser Materialien kombiniert eine große Oberfläche mit optimaler Zugänglichkeit immobilisierter Katalysatormoleküle durch Substrate und Regenerationsreagenzien. Im Vergleich zur heterogenen Batch-Katalyse bieten Reaktionen im kontinuierlichen Fluss zusätzliche Vorteile. Ein großer Vorteil besteht darin, dass Katalysatorabtrennung und -recycling durch einen kontinuierlichen Prozess ersetzt werden, was die Aufarbeitung vereinfacht. Eine Reaktion im kontinuierlichen Fluss ist skalierbar und ermöglicht die Erweiterung einer kontinuierlichen mehrstufigen Synthese durch die Hinzufügung verschiedener Reaktorsäulen in einem Aufbau. Gleichzeitig benötigen immobilisierte Katalysatoren in Hochdurchsatzreaktoren ein Trägermaterial, das für hohe Flussraten geeignet ist und keine hohen Drücke innerhalb der Kolonne verursacht.

Auf dieser Grundlage ergeben sich die folgenden wissenschaftlichen Fragestellungen/Probleme als Hauptziele dieser Dissertation. Das erste Kapitel enthält einen kurzen theoretischen Überblick über den historischen Hintergrund und die jüngsten Entwicklungen polymerer monolithischer Träger. Der Text beschreibt außerdem kurz die Grundlagen, Klassifizierung und Synthese von OMMs. Darüber hinaus ist die Technologie der unterstützten ionischen Flüssigkeitsphase (SILP) auf Basis ionischer Flüssigkeiten (IL) ein Thema im theoretischen Teil dieser Studie [15,16]. Der strukturelle Entwurf und die Charakterisierung von mesoporösen polymeren, monolithischen Trägermaterialien, die aus Poly(urethan) (PUR) und Poly(norborn-2-en) abgeleitet sind, werden im folgenden Abschnitt dieser Arbeit behandelt. Ein kompletter Prozess wurde entwickelt, um polymere monolithische Träger mit definierter Mesoporosität und Durchflussporosität zu synthetisieren, was einen schnellen Stofftransfer ermöglicht. Die Synthese des monolithischen Trägers erfolgte durch lösungsmittelinduzierte Phasentrennung (SIPS), die auf der Flory-

Huggin-Theorie basiert [17]. Durch Variation des Verhältnisses und der Art der Chemikalien für die Monolithsynthese, wie Monomer, Vernetzer, Initiator und porogene Lösungsmittel, konnte die Porosität präzise gesteuert werden. Ein derart konzipiertes System ermöglicht die Herstellung polymerer monolithischer Träger mit der gewünschten Mesoposität. Das monolithische Trägermaterial ermöglicht hohe Durchsätze, ohne dass es zu übermäßigen Gegendrücken (<10 bar) kommt, was für bestimmte Anwendungen kritisch ist. Darüber hinaus wurde die Herstellung mesoporöser Kanäle mithilfe des Harttemplat-gestützten Ansatzes erreicht. Bei der Herstellung von OMMs spielen die Vorläufer und synthetischen Versuchsbedingungen eine wichtige Rolle für die Eigenschaften des Endprodukts.

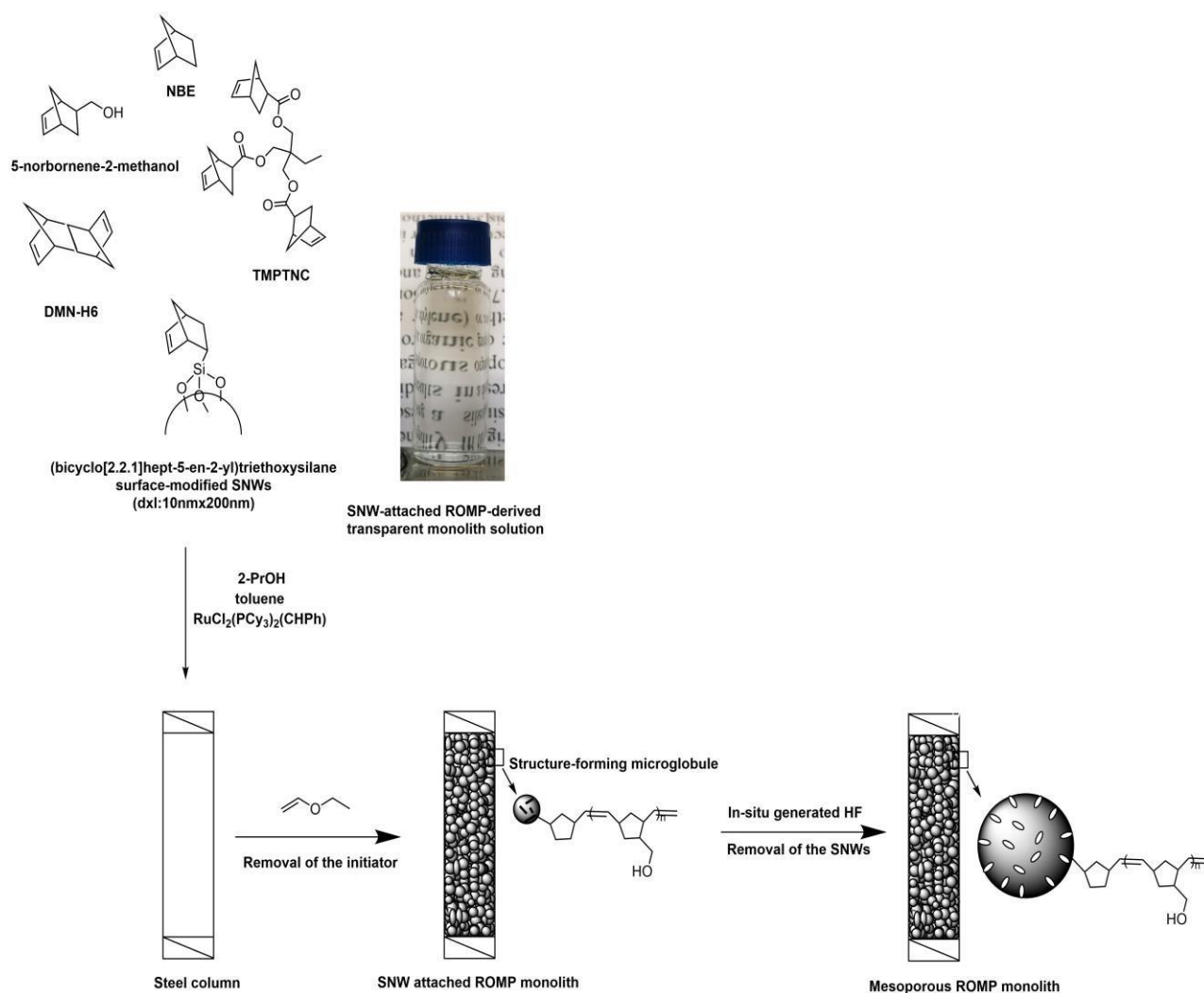


Abbildung 1: Monolithsynthese unter Verwendung einer transparenten Polymerisationsmischung mit vollständig dispergierten SNWs.

Hier berichten wir über die ersten durch Ringöffnungsmetathese-Polymerisation (ROMP) abgeleiteten monolithischen Träger auf Poly(norborn-2-en)-Basis mit maßgeschneiderter Mesoporesizität unter Verwendung eines auf SiO₂-Nanodrähten (SNW) basierenden Harttemplat-Ansatzes, der sich stark von anderen unterscheidet Hard-Templating-Ansätze, da sie den Zugang zu definierten Mesoporen ermöglichen. Wir befassen uns daher mit zwei Hauptparametern: Erstens müssen die SNWs mit der Polymerisationsmischung kompatibel sein, sodass die Agglomeration vollständig unterdrückt wird und die einzelnen SNWs vollständig in der Polymerisationsmischung dispergiert sind. Dies könnte durch eine Behandlung wie (Bicyclo[2.2.1]hept-5-en-2-yl)triethoxysilan erreicht werden. Zweitens ist eine geeignete chemische Ätzmethode erforderlich, um die SNWs ohne mechanische Verformung von der Oberfläche des Monolithen zu entfernen. Die Entfernung der SNWs erfolgte mit in situ erzeugter Flußsäure (HF) unter kontinuierlichem Fluß bei Raumtemperatur, was hohe lineare Flußraten ($>2 \text{ mms}^{-1}$) bei niedrigem Gegendruck ($< 6 \text{ bar}$) ermöglichte.

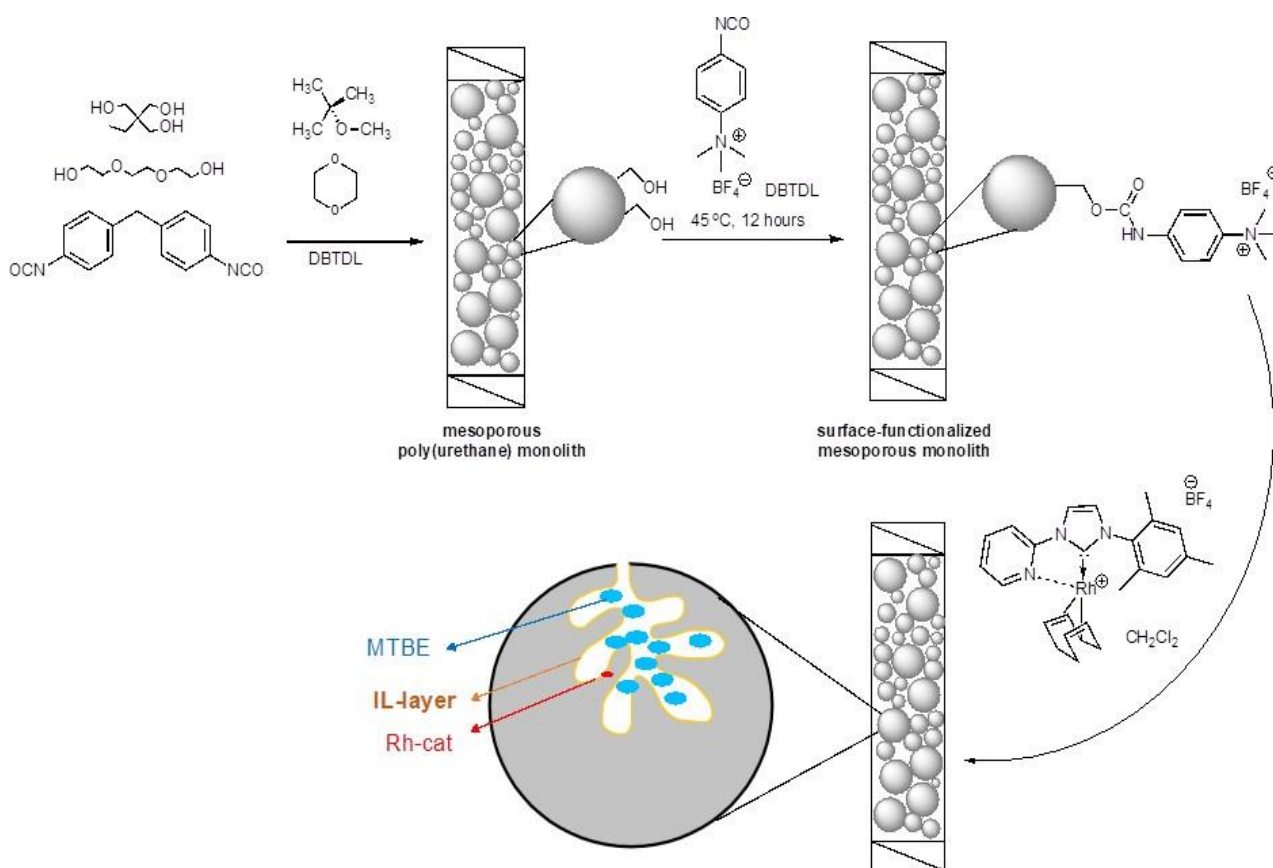


Abbildung 2: Oberflächenfunktionalisierung und Immobilisierung von [BMIM⁺][BF₄⁻], das einen kationischen Rh(I)-NHC-Komplex enthält, auf der Oberfläche eines hydroxylhaltigen Monolithen auf Polyurethanbasis.

Diese Studie konzentrierte sich auch auf Einschlusseffekte mithilfe eines zweiphasigen Flüssigkeit-Flüssigkeit-Systems. Auf diese Weise wurden von PUR und ROMP abgeleitete monolithische Träger unter SIPS-Bedingungen hergestellt. Anschließend wurden die mit Hydroxyl (OH)-Oberfläche funktionalisierten monolithischen Träger mit $[\text{NCO-C}_6\text{H}_4\text{-NMe}_3^+][\text{BF}_4^-]$ oberflächengepfropft, um anschließend die IL, 1-Butyl-3-methylimidazoliumtetrafluorborat $[\text{BMIM}^+][\text{BF}_4^-]$, zu immobilisieren. , enthält einen neuen kationischen Rh-NHC-Katalysator. Durch anschließende Immobilisierung der IL, $[\text{BMIM}^+][\text{BF}_4^-]$, die einen neuen kationischen Rh-NHC-Katalysator enthält, entstand der trägergestützte SILP-Katalysator in der ionischen Flüssigphase. Die Hydrosilylierung terminaler Alkine wurde unter diskontinuierlichen und kontinuierlichen Bedingungen unter Verwendung eines Rh-NHC-Komplexes auf von PUR und ROMP abgeleiteten monolithischen Trägern durchgeführt.

Abstract

Porous materials play a crucial role in everyday life. Due to their low density and high stability, they are often applied in nature as a stabilizing framework, e.g., in bones or wood. The basic structure of these materials consists of a solid cavity (pores), which is filled with a liquid or gaseous medium (adsorbent). The volume of these pores in relation to the volume of the solid determines the porosity of the material and the specific surface area, which describes the area accessible to an adsorbent and includes both the outer and inner surface of the material, as well as the inner surface of the pores. The multitude of possible applications are based on noteworthy properties such as large pore volume and surface area, a hydrophobic or hydrophobic surfaces, high chemical and thermal stability, electrical conductivity, ease of handling, and low manufacturing costs.

Significantly, mesoporous structured materials, which the International Union of Pure and Applied Chemistry (IUPAC) defines as having pores with a diameter between 2 nm and 50 nm, have received much attention because of their high surface areas and volumes [9]. They include well-known materials such as the M41 group (MCM-41, MCM-48, MCM-50) and the SBA series [10], as well as mesoporous materials composed of inorganic, organic, or hybrid frameworks [12] and covalent organic frameworks (COFs) [13]. Mesoporous materials can be ordered or disordered, characterized by pore size distribution. The unique features of ordered mesoporous materials (OMMs), including high specific surface areas (up to $1,000 \text{ m}^2 \text{ g}^{-1}$) and well-defined, uniform pore sizes, make them suitable for specific practical applications such as catalysis, energy storage systems, photocatalysis, photo electrocatalysis, lithium-ion batteries, heterogeneous catalysis, the extraction of metals, the extraction of lanthanide and actinide species, chiral separations, capturing, and the mode of binding of carbon dioxide (CO_2), optical devices, and magneto-optical devices. Of these applications, heterogeneous catalysis is predominant [11,14]. In heterogeneous catalytic processes, the immobilization of the catalysts on solid supports allows for easy separation and reuse of the catalyst and prevents the contamination of the product with catalyst traces. Since work-up and purification, as well as the synthesis of the catalyst itself, are often laborious and expensive, immobilized catalysts are a desirable goal, both ecologically and economically.

Mesoporous materials have several properties that make them excellent carrier material for immobilized catalysts. These materials are mechanically stable and inexpensive, do not swell in organic solvents, and allow for high catalyst loadings due to its large surface area. For a good carrier material, not only the area of the surface is important, but the pores must also be easily accessible. The structure of mesoporous materials combines high surface area with optimal accessibility of immobilized catalyst molecules by substrates and regeneration reagents. Compared with heterogeneous batch catalysis, reactions in continuous flow have additional advantages. As major benefits, catalyst separation and recycling are replaced by a continuous process, which simplifies work-up. A reaction in continuous flow is scalable and allows for the extension of a continuous multistep synthesis through the addition of different reactor columns in one setup. At the same time, immobilized catalysts in high-throughput reactors need a carrier material that is suitable for high flow rates and does not cause high pressures inside the column.

Based on the above, the following scientific questions/problems emerge as the main objectives of this dissertation. The first chapter includes a brief theoretical survey of the historical background and the recent developments of polymeric monolithic supports. The text also briefly describes the fundamentals, classification, and synthesis of OMMs. In addition, ionic liquid (*IL*)-based supported ionic-liquid phase (*SILP*) technology is a topic in the theoretical part of this study [15,16]. The structural design and characterization of mesoporous polymeric, monolithic support materials derived from poly(urethane) (PUR) and poly(norborn-2-ene) are addressed in the following section of this thesis. An entire process was designed to synthesize polymeric monolithic supports with defined mesoporosity and flow-through porosity, which allows for fast mass transfer. The synthesis of the monolithic support was accomplished by solvent-induced phase separation (*SIPS*), which derives from the Flory–Huggin’s theory [17]. By varying the ratio and nature of chemicals for the monolith synthesis, such as monomer, crosslinker, initiator, and porogenic solvents, the porosity could be precisely controlled. Such a designed system allows for the preparation of polymeric monolithic supports with the desired mesoporosity. The monolithic support material allows high throughputs without causing excessive back pressures (<10 bar), which is critical for specific applications. In addition, the fabrication of mesoporous channels was accomplished by utilizing the hard template-assisted approach. In regard to the

preparation of OMMs, the precursors and synthetic experimental conditions play a major role in the properties of the final product.

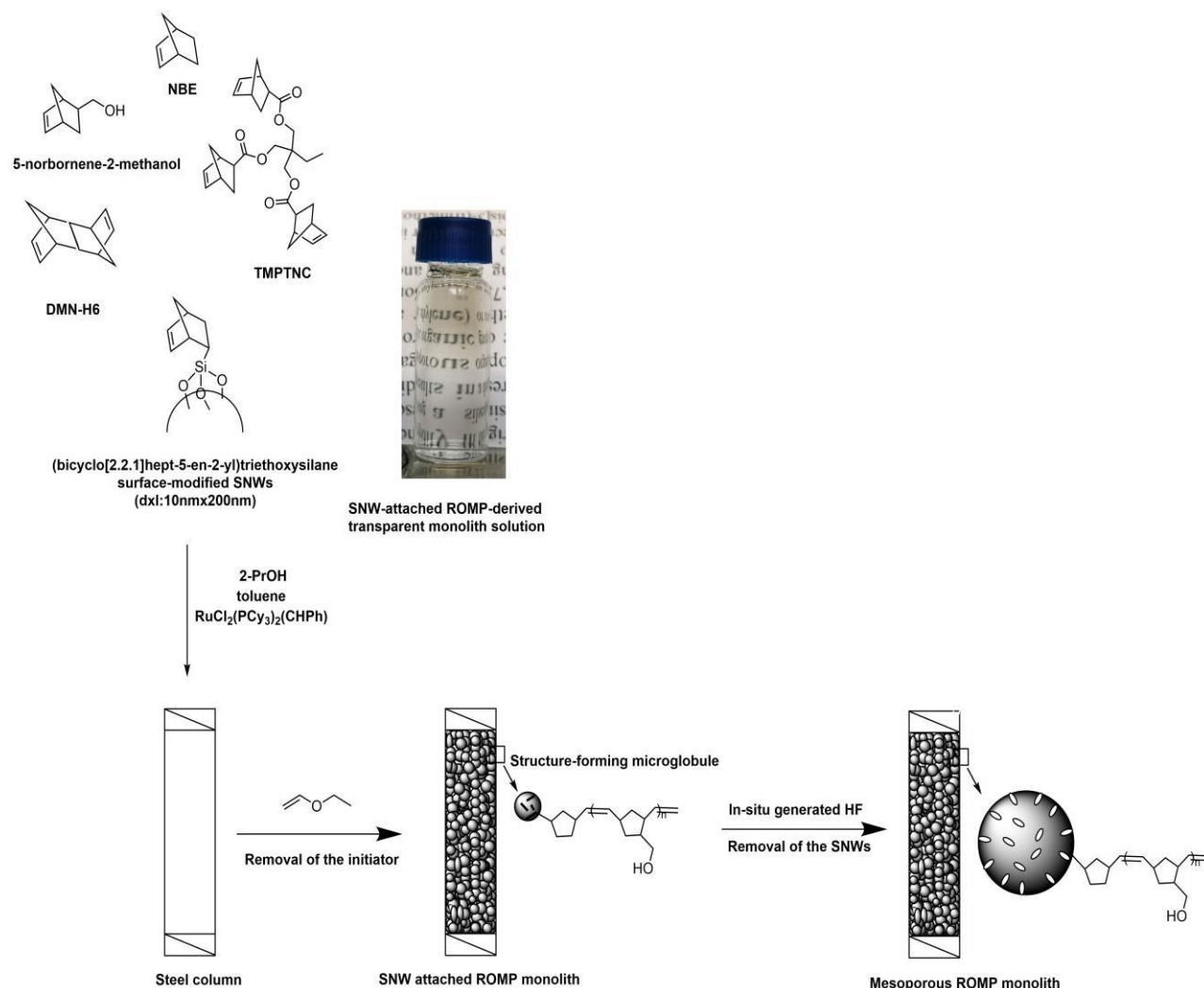


Figure 1: Monolith synthesis using a transparent polymerization mixture with fully dispersed SNWs.

Here, we report on the first ring opening metathesis polymerization (ROMP)-derived, poly(norborn-2-ene)-based monolithic supports with tailored mesoporosity using a SiO_2 nanowire (SNW)-based hard templating approach, which strongly differs from other hard templating approaches in that it provides access to defined mesopores. We hence address two main parameters: First, the SNWs must be compatible with the polymerization mixture such that agglomeration is fully suppressed, and the individual SNWs are fully dispersed within the polymerization mixture. This could be accomplished using a treatment such as (bicyclo[2.2.1]hept-5-en-2-yl)triethoxysilane. Second, a suitable chemical etching method is required to remove the SNWs from the monolith's surface without mechanical deformation. Removal of the SNWs was

accomplished with *in-situ* generated hydrofluoric (HF) acid under continuous flow at room temperature, allowing for high linear flow rates ($>2\text{mms}^{-1}$) at low backpressure ($< 6\text{bar}$).

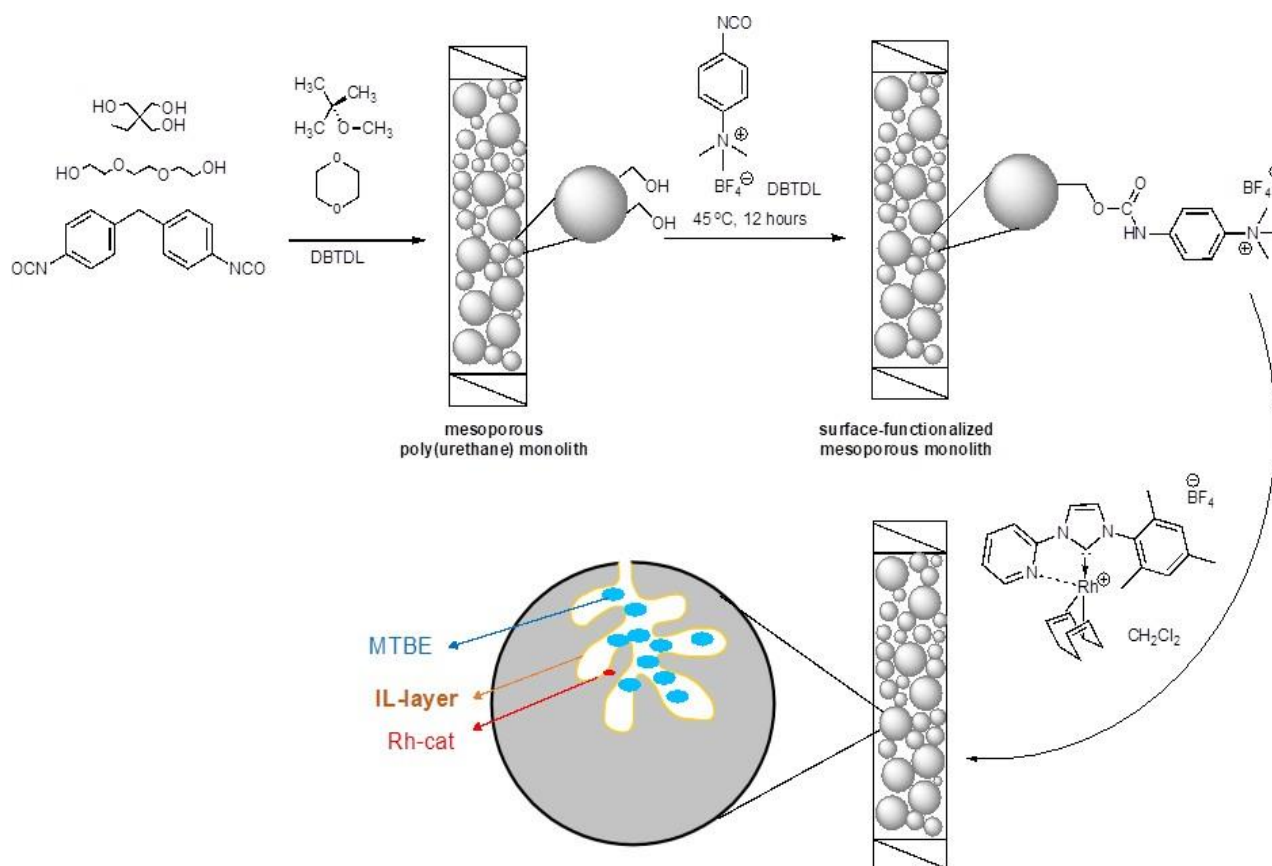


Figure 2: Surface functionalization and immobilization of [BMIM⁺][BF₄⁻], containing a cationic Rh(I)-NHC complex onto the surface of a hydroxyl-containing polyurethane-based monolith.

This study also focused on confinement effects using a biphasic liquid-liquid system. In this manner, PUR- and ROMP-derived monolithic supports were prepared under *SIPS* conditions. Then the hydroxyl (OH)-surface-functionalized monolithic supports were surface grafted with [NCO-C₆H₄-NMe₃⁺][BF₄⁻] for the subsequent immobilization of the IL, 1-butyl-3-methylimidazolium tetrafluorborate [BMIM⁺][BF₄⁻], containing a new cationic Rh-NHC catalyst. Subsequent immobilization of the IL, [BMIM⁺][BF₄⁻], containing a new cationic Rh-NHC catalyst, created the supported ionic liquid phase *SILP* catalyst. Hydrosilylation of terminal alkynes were carried out under batch and continuous conditions using a Rh-NHC complex on PUR- and ROMP-derived monolithic supports.

Chapter 1

1. BRIEF THEORETICAL SURVEY

1.1 Polymeric Monolithic Support Materials

In the 1950s, the term "monolith" was first introduced by *Robert Synge* [18]. However, the porous hydrogel structures collapsed under hydrostatic pressure. *Mould et al.* [19] described the chromatographic separation of high molecular weight polysaccharides using co-polymers of 2-hydroxyethyl methacrylate and ethylene dimethacrylate. Continuous research studies in the 1970s resulted in the development of various types of organic monoliths from polymers, such as styrene derivatives [20], poly(vinyl chloride) [21], and polyurethane [22]. In terms of the most appealing properties of organic monoliths, such as mechanical stability and permeability, attempts were made to prepare monolithic materials but initially were unsuccessful. Then, the chromatographic separation of proteins by using different column types was studied by *Belenki et al.* in the 1980s. Using well-packed, continuous monolithic supports was found to allow good chromatographic separation [23]. In the 1990s, monolithic poly(glycidyl methacrylate-co-ethylenedimethacrylate) disks were commonly applied to chromatographic separation [24]. Afterward, different monolithic formats were developed. Cross-linked structures were created in chromatographic tubes. Silica-based columns were introduced by *Tanaka et al.* in 1996. These chromatographic columns are characterized by special features, such as high flow rates and low back pressures [25]. Over the years, new surface chemistries have been developed to extend the applicability of monolithic columns [26].

Polymeric monoliths are defined as continuous skeletons prepared from an interpenetrating network of cross-linked organic or inorganic porous material. Monolithic structures are predominantly useful in separation science and heterogeneous, continuous catalysis [27,28]. Monolithic polymeric supports can be synthesized by using different synthesis techniques. Thus far, *SIPS* has been used in the *Buchmeiser* research group [29] to synthesize monolithic support materials. This method allows the preparation of monolithic materials with the desired porosity by choosing phase separation conditions. Separating growing polymer chains from the solution starts during the phase separation process and forms a cross-linked, interconnected microglobule. The onset of phase separation can be determined by the synthesis parameters and conditions, such as the reaction temperature, the solvent mixtures, and the cross-linking degree. The phase separation is governed by FH interaction parameter (χ_{FH}). According to FH theory [17], the *SIPS* process can be

controlled by temperature and the differences between the Hildebrand solubility parameters of the polymer and solvent mixture.

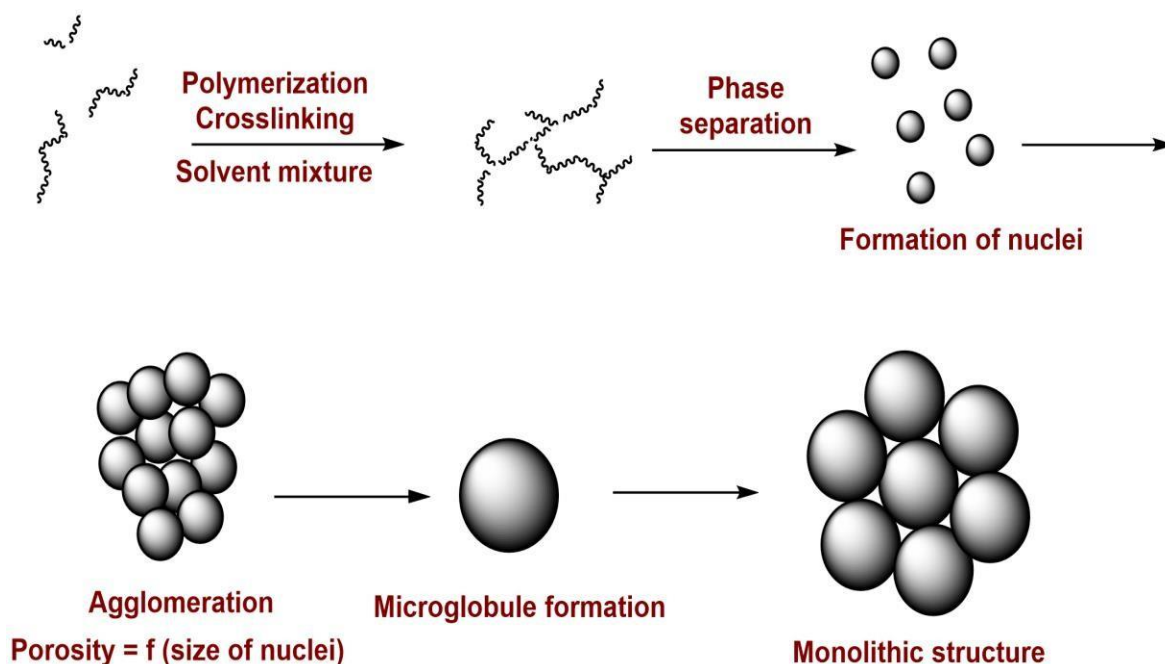


Figure 3: Solvent Induced Phase Separation (SIPS).

The rate of phase separation in the polymerization process is the main factor that affects the porous properties of polymer monoliths, such as the average pore size, the number of pores, and the specific surface area. Phase separation is controlled by (i) the compatibility of the porogens and emerging polymer, (ii) the volume of porogenic solvents, (iii) the rate of the polymerization, and (iv) the amount of cross-linking monomer. Phase separation begins when the growing polymer chain becomes insoluble in the solvent mixture and first leads to the formation of nanoglobules, then microglobules via agglomeration. The solvent mixture composition, cross-linking degree, reaction temperature, and polymerization time are the most effective parameters for tailoring the pore size distribution of a monolith.

Preparing polymer monoliths is simple and easy. However, preparing monolithic stationary phases yielding very good separation performance necessitates a precisely tuned pore structure and chemistry because of the many experimental variables controlling the properties of the polymer (reaction time, temperature, and polymerization mixture composition). A polymerization mixture is placed in a stainless-steel column, fused-silica capillary, or microfluidic channel. In this mixture, functional and cross-linking monomers are dissolved in porogenic solvents in the presence of a

suitable polymerization reaction initiator. The reaction is then initiated by elevated temperatures or UV irradiation. Finally, the column is flushed to remove the unreacted components of the polymerization mixture.

Porogenic solvents are a crucial component of a polymerization mixture, defining the porous properties of monolithic stationary phases such as monolith morphology, surface area, pore volume, and permeability. A porogenic solvent is generally chosen for its solvation properties for the monomers. The solvent is considered a microporogen or a macroporogen if it has thermodynamically good or bad solvation properties, respectively. Porogenic solvents control the porous properties of the monolith by solvating polymer chains during the initial phases of the polymerization reaction and by the phase separation of the polymers formed within the polymerization mixture. During the process of making monolithic supports, solvents such as methanol, 1-propanol, 1,4-butanediol, hexane, cyclohexanol, decanol, dodecanol, and toluene have been extensively used. In general, monolithic supports are synthesized by mixing monomer initiators in the presence of one or even two porogenic solvents. The good solubility of a free monomer in the presence of microporogens lowers the local monomer concentration and results in smaller pores. In contrast, using macroporogens often obtains larger pores because of earlier phase separation [30]. The choice of porogens for preparing porous polymer monoliths highly depends on the monomer used for the polymerization mixture. *Sinityna et al.* published a series of porogens for preparing poly(glycidyl methacrylate-co-ethylene dimethacrylate) monolithic layers, including solutions of polystyrene in a toluene–dodecanol mixture and poly(dimethylsiloxane) in a hexane–dodecanol mixture. Using polystyrene (PS) to make a monolith was found to be the best way to obtain antibody–monolith adhesion [31]. *P. Holdšvendová et al.* described the use of high molecular mass polystyrene and chlorobenzene to create poly(glycerol dimethacrylate) monoliths. This mesoporous monolith was used to separate small molecules with up to 34 000 plates/m [32]. *Buchmeiser et al.* published ROMP-derived norborn-2-ene (NBE)- and cis-cyclooctene (COE)-based monoliths in the presence of 2-propanol as a macroporogen and toluene as a microporogen [33].

Other ways to control the porosity include changing the type and amount of cross-linking reagent. Increasing the cross-link density leads to smaller pore sizes. In contrast to the temperature and porogen's parameters, changing the cross-link density also

causes substantial changes in the final monolith compositions [34]. *Xu et al.* combined several dimethacrylates with stearyl methacrylate in capillaries. The connecting hydrocarbon chain differed in length and the number of branches, but the ratio of monomer to cross-linker was constant. Because the size of the small pores changed, seeing how the chemistry of the cross-linker affected the separation of small molecules was possible by chromatography [35]. *F. Svec et al.* found that polymerization time had a considerable effect on the porous properties of poly(glycidyl methacrylate-co-ethylene dimethacrylate) monoliths [36]. These monoliths exhibited a surface area of 500 m²/g and a pore volume of 3.8 mL/g after 1 h at 55 °C. However, after 10 h, the surface area and pore volume were substantially lower, reaching 120 m²/g and 1.1 mL/g, respectively. Another study on the control of the porous structure via reaction time was published by *G.K. Bonn's group* [37]. They created monolithic poly(4-methylstyrene-co-1,2-(4-vinylphenyl) ethane capillary columns using polymerization times ranging from 30 min to 24 h. The surface area dropped from 76 to 23 m²/g and the pore volume from 70 to 40%. Interestingly, using a column polymerized for only 45 min, a high column efficiency of 65 000 plates/m was observed in the isocratic separation of small aromatic molecules, in which monomer conversion was 39%.

The specific surface area of a monolithic structure strongly depends on its isothermal adsorption behavior. The adsorption mechanism is formulated by using suitable equations [38]. The monolithic material porosity is classified as 1) micropores (< 2 nm) 2) mesopores (2–50 nm), or 3) macropores (> 50 nm) [39]. Notably, while the micrometer-sized macropores in monolithic materials serve as transport pores, the micropores serve adsorption purposes. Pore volumes and high surface areas in a material result from the micropores and mesopores, while the macropores help overcome diffusion difficulties by improving mass transfer. In the relative pressure range of approximately 0.05–0.35, the BET and Langmuir equations are the most useful for describing the adsorption process. Additionally, thermodynamic parameters, such as the changes in free energy (ΔG), entropy (ΔS), and enthalpy (ΔH), can determine the adsorption behavior. Desorption behavior results from the equal energy release supplied during the adsorption process [38]. The kinetic adsorption behavior is also referred to as a change in substance concentration at the interface. Kinetic studies provide useful information about the mechanism involved in the adsorbent–adsorbent reaction and time, which is required for determining the solid adsorbents for specific applications [40]. Applying porous materials in many fields depends on direct contact

with a support surface that promotes the interacting sites. For large surface areas, many micropores should be introduced into the polymer. The largest surface area comes from micropores, followed by the mesopores. Therefore, the pore size distribution of the monolith should be adapted to the desired application during its production. Key parameters such as temperature, pore-forming solvent mixture composition, and cross-linking monomer content allow the pore size to be set within a wide range, from tens to thousands of nanometers. The polymerization temperature is a particularly effective control tool because of its effect on polymerization kinetics, allowing the production of macroporous polymers with different pore size distributions from a single polymerization mixture. The effect of temperature can be explained by the difference in the number of nuclei resulting from changes in the polymerization temperature. Since the monomers are thermodynamically better solvents for the polymer than the porogen, the temperature mainly affects reaction kinetics, which is typically related to the specific surface areas. The half-lives of typical initiators in free-radical polymerization, such as AIBN, are lower at higher temperatures, so a more substantial number of growing polymer nuclei are present at higher temperatures, and smaller pore sizes are formed [34].

1.2 Characterization Techniques

1.2.1 Inverse size-exclusion chromatography (ISEC)

The primary factor in defining the functional characteristics of polymer monoliths is the pore space structure. Most natural and synthetic porous media contain pores with irregular geometry and heterogeneous sizes. Several structural parameters are relevant in describing the complicated pore structure, including the pore size distribution (PSD), which represents the distribution density of pores within a certain range of dimensions and serves as a statistical descriptor of the diverse size features.

The commonly used techniques can be categorized into four classes: gas sorption, mercury intrusion, microscopy, and solute exclusion. Of these, solute exclusion is the most suitable for investigating structures under similar conditions to those in chromatographic applications. Solute exclusion is used to figure out the size of a solute based on the known pore sizes of the adsorbents or empirical retention data compared

to that of standards. The inverse application of the size-exclusion chromatography (SEC) concept, ISEC [41], utilizes a set of molecular probes with defined sizes to determine pore dimensions and is also referred to as chromatographic/macromolecular porosimetry.

The ISEC principle, first applied in determining pore distributions in cellulose fibers, was introduced by *Halász* and *Martin* for the characterization of chromatographic stationary phases and has been further refined and extended [17, 41].

ISEC has many advantages over alternative methods. Column experiments with intact samples packed in a bed, as opposed to the special sample preparation procedures used in electron microscopy, can preserve sample integrity and are simple to perform. ISEC does not require any equipment other than a chromatography system, which is cheap and easy to develop. Operating conditions such as high pressure, low temperature, and drying conditions, which are involved in gas sorption or mercury intrusion, are not imposed in ISEC. Experimental conditions similar to those in normal operations result in less significant morphological changes, thus assuring structural information that is relevant to properties of functional interest. ISEC characterization of pore statistics covers a range of chromatographic stationary phases, including silica, modified silica, carbohydrate gels, and synthetic polymer-based adsorbents. Further, the non-destructive nature of ISEC is an advantage in the structural characterization of monolithic columns.

According to the ISEC principle, the defined hydrodynamic volumes of narrow polymer standards in a solvent are used to determine pore size distribution. The chemical compatibility between the solute and molecular probes is crucial for specific applications. Commonly, a set of PS standards ($D \leq 1.02$, $162 \leq M_n \leq 2,000,000$ g/mol) in CHCl_3 is used to determine the pore dimensions of monolithic materials. Retention times and volumes corresponding to each PS standard are determined from the peak maximum. Each retention volume is then corrected for the extra-column volume of the equipment.

The equation:

$$(\Phi = 0.62 \times M_w^{0.59}, \text{CH}_2\text{Cl}_2)$$

is used to relate the hydrodynamic volume of a PS sample to the pore diameter [41]. Φ [\AA], a microglobule, can be characterized by a certain diameter (d_p) and porosity ($\epsilon_p = V_p / V_t$). V_p is the retention volume of the lowest molecular mass, which is an unretained tracer through the column (toluene, $M_w = 92$ g/mol). The volume fraction between the interconnected microglobules is defined as interstitial porosity ($\epsilon_z = V_z / V_t$). V_z is defined as the retention volume of the excluded molecular mass, and V_t is the geometrical column volume ($V_t = \pi r^2 h$). Since the column structure is considered as a long, cylindrical tube, where r is the column radius and h is the column length, the total relative porosity (ϵ_t) can be calculated using the sum of the pore porosity (ϵ_p) and intermicroglobular porosity (ϵ_z), as follows:

$$(\epsilon_t) = (\epsilon_z) + (\epsilon_p)$$

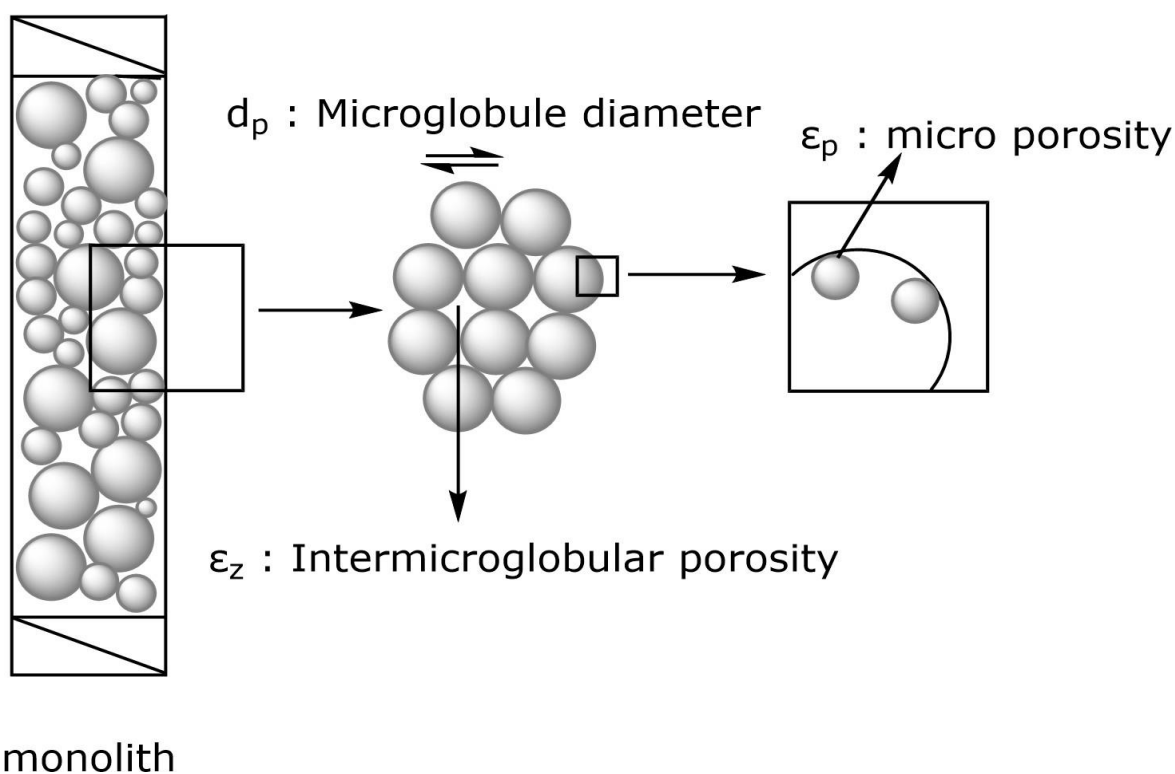


Figure 4: Characterization of the porosity of a monolithic support.

The plot of the relative abundance (ΔR ; %) of the pores vs. the pore sizes in the material gives information related to the relative pore size distribution of a characterized material. Since the evaluation of the material is in its solvated state, ISEC is the most qualified method for determining the pore size distribution of a material, which is used in catalysis applications using liquid transport phases. Because ISEC is based on a simplified pore model, it can provide comparative descriptions of pore

statistics, which can be used for understanding macromolecular retention and transport behavior in chromatographic processes. However, no information on the pore geometry can be deduced from ISEC, as ISEC is insensitive to the assumed pore model. Similarly, ISEC cannot directly test how connected the pores are in the adsorbent, which is an important structural parameter that affects how solutes move. In these cases, it might be helpful to combine ISEC with other methods of PSD characterization, like microscopy, to obtain more knowledge about the pore structure.

1.2.2 Brunauer-Emmett-Teller (BET)

Surface area is one of the most important physical properties of a porous material and the accurate determination of the surface area in a porous material is important for applications in many fields, such as gas storage, separation processes, catalysis, etc. There are two common approaches for computing the surface areas of porous materials: first, the isotherm-based approach, which relies on computing the monolayer coverage based on the BET theory [42]; and second, the geometry-based approach, which uses a probe molecule to roll over individual atoms to compute the available surface area. The former method is commonly used in the experimental characterization of surfaces because it requires knowledge of only the adsorption isotherm, which can be relatively easy to measure.

The BET theory, which was initially developed to describe the multi-layer adsorption of gas molecules on a solid surface, is typically used for this purpose. The BET analysis is performed based on the adsorption isotherms of non-reactive gas molecules (such as nitrogen at 77 K or argon at 87 K) at a range of pressures that covers the monolayer coverage of molecules. The obtained isotherms are transformed into the linearized BET plot, where the monolayer loading can be determined. One of the issues with the BET method, however, is the choice of the linear region in the linearized BET plot; conventionally, the linear region in the BET analysis is chosen from a relative pressure range (P / P_0) between 0.05 and 0.30, known as the BET standard pressure range with the assumption that the monolayer formation will occur in this pressure range.

Surface adsorption can occur via two mechanisms: physisorption and chemisorption. These mechanisms are distinguished by the nature of the intermolecular attractions

between the molecule and the surface, with the former being a physical interaction and the latter interacting via chemical bonding. Chemisorption is associated with chemical valence forces, or the stronger chemical interactions (10–100 kcal/mol) that form between the adsorbate and substrate. Hence, it requires a lot of energy, comparable to that associated with chemical bond formation, to remove the adsorbed species. Chemisorbed molecules are linked to reactive parts of the surface and the adsorption process. There is a substantial rearrangement of electron density, and thus it is often a dissociative and possibly irreversible phenomenon. Chemisorption is necessarily confined to a single monolayer; therefore, it is useful for the characterization of catalyst surfaces and is also the key mechanism of heterogeneous catalysis of chemical reactions.

According to the IUPAC technical report (2015), physisorption is a general phenomenon in which an adsorbable gas (adsorbent) interacts with the solid surface (adsorbent) via Van der Waals forces, causing the density of the gas molecules to increase on the solid surface [43]. The area where the increased density is located is called the adsorption space, and the gas molecules in this area are called the adsorbate. This type of adsorption exhibits relatively fast kinetics in the gas phase, and all surfaces in high vacuum ($\sim 10^{-8}$ Pa or $\sim 10^{-10}$ Pa) can be free of physisorbed species. There is no significant redistribution of electron density either in the molecule or at the substrate surface, resulting in the association of water molecules in a quasi-liquid layer on the substrate surface. Thus, physisorption is reversible, and desorption can be induced simply by increasing temperature or decreasing vapor pressure.

The BET equation, as follows, is the most-used method for determining the monolayer and specific area values in various physicochemical areas:

$$\frac{x}{V(1-x)} = \frac{1}{V_m \cdot C_{BET}} + \frac{x \cdot (C_{BET} - 1)}{V_m \cdot C_{BET}}$$

Where V is the volume of adsorbed molecules, V_m is the monolayer volume, C_{BET} is the BET constant, and x is the relative pressure (P / P_0). The BET constant C_{BET} arises from the algebraic rearrangement of the series approximation for the determination of subsequent it layers adsorption volumes. C_{BET} is related to the adsorbate–adsorbent interaction strength and, therefore, to the heat of adsorption; the higher the value of C_{BET} , the stronger the interaction. In any case, the BET equation is generally used only

to give an apparent surface area related to the adsorption capacity of the solid. A straight line should be obtained by plotting $x / V (1 - x)$ as the ordinate and x as the abscissa over a certain $x (P / P_0)$ range. The data are considered acceptable if the correlation coefficient, (r), of the linear regression is not less than 0.9975; that is, if r^2 is not less than 0.995. By determining the slope and the intercept of the resulting linear plot, V_m , which is the amount of gas adsorbed if a monolayer were to form, can be determined.

Mesoporous materials have two stages in physisorption. In the first, monolayer adsorption, the surface layer of the adsorbent is covered by all adsorbed molecules. In multilayer adsorption, not all the adsorbed molecules are directly in contact with the adsorbent surface, and there is more than one layer of molecules in the adsorption space. Until now, IUPAC has recommended that the characteristic six types of isotherms are the most useful reference guides for the evaluation of the physisorption isotherms [43].

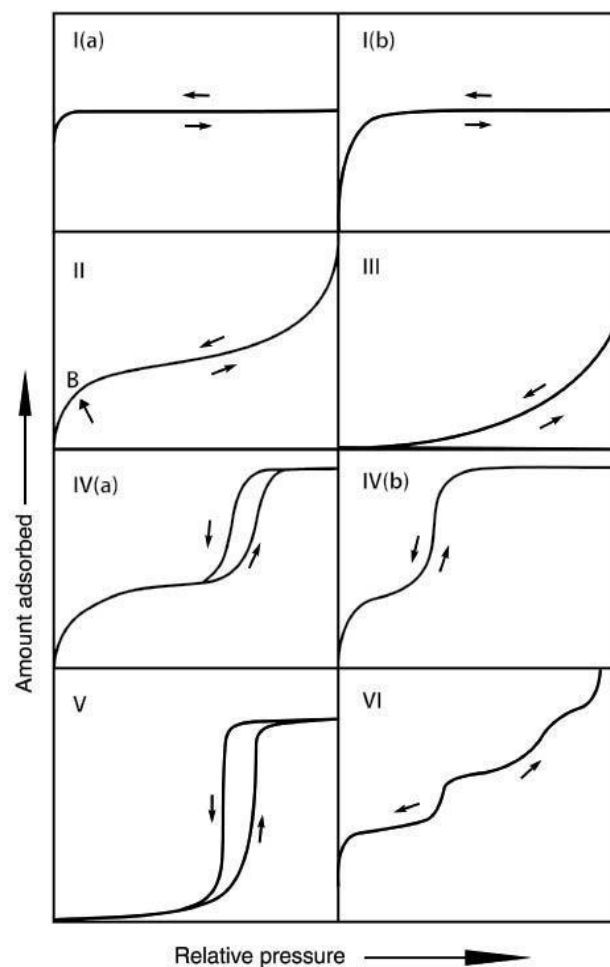


Figure 5: IUPAC recommended characteristic six types of physisorption isotherms.

The Langmuir Type I isotherm exhibits a rapid rise that approaches a maximum value asymptotically as the vapour pressure increases, indicating the completion of monolayer adsorption (Figure 5). From an energetic point of view, the monolayer capacity is defined as the number of adsorbed molecules at the maximum surface area of interaction with the adsorbent. The Type II BET isotherm describes reversible and unrestricted multilayer physical adsorption on nonporous (e.g., metal; alumina) or macroporous solids, with a point of inflection thought to be caused by the formation of a phase boundary, while the Type III BET isotherm is characterized by convexity toward the partial pressure axis, starting at the origin. It occurs in situations in which the interaction between the adsorbate molecules approaches that between adsorbate and adsorbent (i.e., the heat of adsorption is similar to the heat of condensation). Type IV isotherms are similar to Type II isotherms in that they have an inflection (or knee) in the monolayer formation. This isotherm is commonly exhibited by many mesoporous industrial adsorbents and inorganic oxide xerogels, in which the monolayer surface coverage of the pore walls is followed by capillary condensation or pore filling. The adsorption ceases once all the pores are filled. Type V isotherms are commonly observed for flat, homogeneous adsorbents. The initial pathway of this isotherm is similar to that of Type III. In this instance, the adsorbate preferentially interacts with the monolayer over the adsorbent surface due to the lower heat of adsorption compared to the heat of liquefaction. Meanwhile, a high-affinity isotherm is typical for very strong adsorption interactions. Thus, using the BET reference theory and recommended isotherms, it is possible to classify porous materials.

The concept of adsorption to an exposed surface was developed by *Langmuir* [42], who proposed that adsorption corresponds to a dynamic equilibrium between a gas and a solid surface, resulting in a surface layer that is only one molecule thick. The BET extended this theory and utilized statistical mechanics and simulations for reliable pore size distributions. Density functional theory (DFT) is the most widely used method for adsorptive/adsorbent systems and describes the phase and adsorption behaviour of fluids in pore structures [44].

1.3 Ordered Mesoporous Materials (OMMs): Historical Perspective and Recent Developments

The synthesis of ordered mesoporous polymeric materials has gained much attention due to their unique properties, such as high specific surface areas, uniform pore arrangements, and large pore volumes [45-47]. These features are important for various applications, including absorption, separation, catalysis, drug delivery, and energy storage/conversion [48]. OMMs include various materials, such as silica, metals, metal oxides, carbons, zeolites, and metal- and covalent-organic frameworks. In 1993, *Kuroda et al.* published that alkyltrimethylammonium ions with varying alkyl chain lengths can be used to expand interlayer spaces in layered polysilicates up to 4 nm [49]. This work foreshadowed a new era for nanoporous materials and paved the way to the discovery of OMMs.

The first synthesis of ordered mesoporous molecular sieves using a liquid crystal template method was published by *Kresge et al.* [50]. In their approach, positively charged surfactant micelles were directly introduced to the negatively charged silica phase via electrostatic interactions. After removing the surfactant by calcination, a mesoporous structure was obtained. Since then, researchers have developed various synthesis methods and materials. *Stucky et al.* reported the development of the triblock copolymer P123 strategy using the most promising SBA-15-type silica materials; various mesoporous structures and morphologies were developed [51]. Compared to their surfactant-templated siliceous counterparts, the polymer-templated silica materials showed high surface area, a broad mesoporous size range, and high hydrothermal stability.

The first ordered mesoporous organosilicas (OMOs) were reported in 1999. OMOs were synthesized by controlled hydrolysis and the condensation of alkoxysilanes, such as 1,2-bis(trimethoxysilyl)ethane, in the presence of surfactants [52]. *Olkhovyk and Jaroniec* developed a tris[3-(trimethoxysilyl)propyl] isocyanurate organosilica framework, with an ordered, mesostructure [53]. In the mid-1990s, the first mesoporous non-silica-based materials [55], notably, stable first-row transition metal oxides and oxophosphates were introduced to material science. Mesoporous, hexagonally packed titanium oxide frameworks were successfully obtained using

tetradecylphosphate as a soft template material via the interactions between the titania framework and phosphorus.

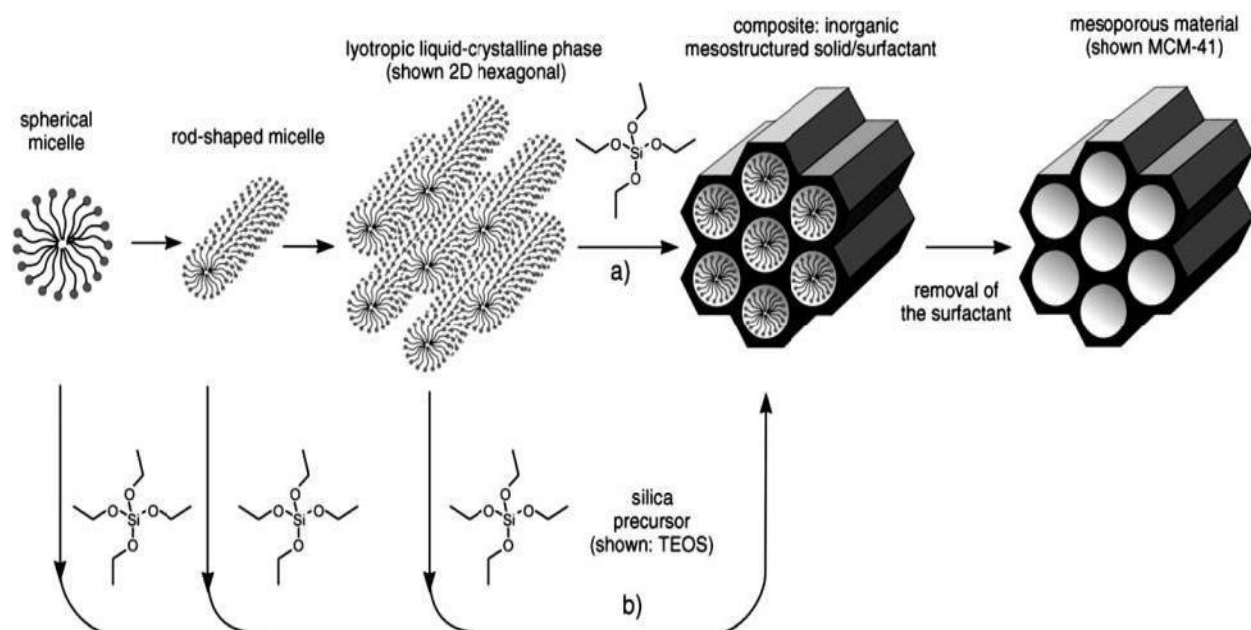


Figure 6: Formation of mesoporous silica template through a true liquid-crystal templating a) and a cooperative self-assembling mechanism b). Copyright 2006 Wiley-VCH Verlag GmbH & Co. KGaA, Weinheim [54].

During the synthesis of the ordered mesoporous metal-oxides (OMMOs), obtaining the desired mesoporous network and crystallinity is challenging, as the metal oxides are highly sensitive to phase transitions, hydrolysis, and redox reactions during the etching treatment, which is required to remove the templates. A modified precursor strategy and post-synthesis coating were developed to overcome this issue. The ordered crystalline titania mesostructure was post-modified into amorphous titania with ethylenediamine by thermal treatment and calcination steps.

Today, the synthesis of composite or modified OMMs using soft- and hard-templating strategies and related methods offers virtually limitless possibilities. The evolution of the leading OMM members e.g., silicas, organosilicas, metal oxides, carbons, metal-organic frameworks, and zeolites and the main factors affecting their development are briefly summarized, with special emphasis on the authors' accomplishments in this area. Additionally, recent advancements, applications, and prospects in the field of OMMs are presented.

1.3.1 Hard Templating

The hard templating method involves the use of an ordered porous material (e.g., silica) as a stable (hard) template in the foreground. The mesopore channels are then formed by removing them via either extraction, chemical etching, or calcination.

The most frequently used core templates are classified based on their chemical properties: polymer latex, carbon, and silica spheres. SiO₂ spheres are the best known and most suitable hard-core templates for preparing hollow mesoporous materials, polymers, and carbons. The manufacturing process usually consists of the following steps:

- I. Manufacture the ordered mesoporous silica with suitable surfactants (surface active agents, surfactants).
- II. Remove the surfactants by calcination, extraction, or other methods.
- III. Fill the pores of the hard template with the carbon precursor by wet impregnation, chemical vapor deposition, or a combination of these methods.
- IV. Carbonize the carbon precursor in the pores of the silica material.
- V. Remove the silica by etching (e.g., HF).

Knox et al. published the first successful synthesis of mesoporous, disordered materials in the 1980s. A phenol-hexamine mixture served as the carbon precursor, and a spherical silica gel served as a template for the synthesis of liquid chromatography carbon material [56].

The synthesis of the first ordered mesoporous carbon material, CMK-1, was developed by *Ryoo* [57] in 1999, using MCM-48 as a template. Three months later, *Hyeon* [58] published the making of another ordered mesoporous carbon (OMC), SNU-1, using the same template. For the fabrication of CMK-1, the cubically arranged (Ia $\bar{3}$ d) pores of MCM-48 were impregnated with a solution of sulfuric acid and sucrose, with the acid serving as a catalyst during the 1,073–1,373 °C carbonization. The silica framework was then coated with an ethanolic NaOH solution. The result was CMK-1, a cubically ordered mesoporous carbon with a mean pore diameter of about 3 nm [59].

Another important factor is stability, which is higher in a three-dimensional carbon skeleton than in a two-dimensional one. Thus, an MCM-41 with two-dimensional hexagonally arranged pores cannot be used to produce ordered carbon because the

connections between the individual “tunnels” are missing [60,62]. However, by fabricating the MCM-41 template in the microwave, *Tian et al.* were able to create small defects in the pore wall, which formed interconnections about 2 nm–long between the individual pores and provided the necessary stability in the final material [61].

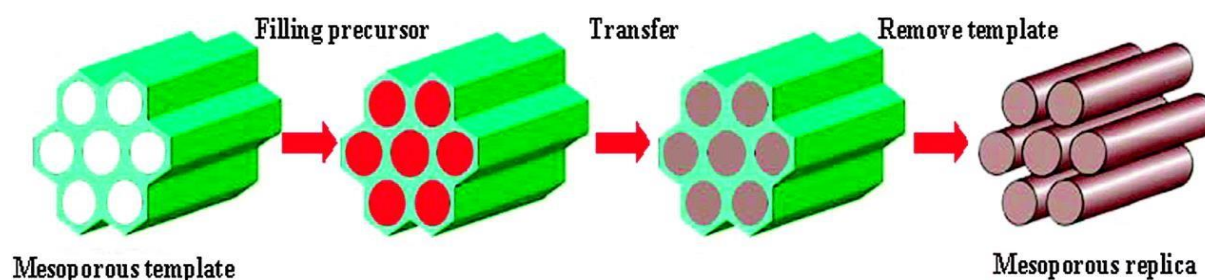


Figure 7: Schematic representation of the hard-templating (nanocasting) pathway leading to mesoporous non-siliceous materials. Reprinted with permission from Gu and Schuth (2014) [63].

Further improvement to this method came with the preparation of CMK-5, in which the bridges were replaced by nanotubes. This replacement can be achieved by incorporating of aluminium into the pore walls of SBA-15, as aluminum catalyzes the polymerization of furfuryl alcohol, which, in addition to carbonizing under vacuum, increases the quality of CMK-5. The interconnection of the individual cylindrical pores by the nanotubes can be visualized by XRD visualization: two pore maxima are indicated at 5.9 nm and 4.2 nm, with the former indicating the diameter of the cylindrical pores and the latter indicating that of the nanotubes [64]. The pore size of the OMCs depends on the wall thickness of the template materials, which produces a variety of ordered mesoporous carbon materials with varying structures, including body-centered cubic (Im3d), face-centered cubic (Fm3m), and 2D hexagonal (p6mm).

The hollow silica spheres with latex particles were first synthesized by *Qiu et al.* in 2001. Negatively charged colloidal PS particles were used to assist in the self-assembly of inorganic silica and surfactant micelles at $\text{pH} > 12$. High-temperature calcination was used to remove the PS particles and surfactant molecules to form the mesostructured silica spheres [65].

Recently, *Qi et al.* reported a method for preparing monodisperse hollow mesoporous silica. The researchers demonstrated that the experimental variations including the

concentration of the latex and surfactants, and the volume fraction of organic solvents precisely affected the dispersibility of the final material [66].

Carbon spheres are another hard-core template used to prepare uni-modal structures. The spheres have special functional groups (i.e., -OH, C=O groups) on the surface. The functional groups provide a favored chemical environment for the diffusion of the precursors. Based on this, Fe₃O₄@SiO₂ hollow mesoporous spheres were synthesized by using the carbon spheres as a hard-core template.

Following the hydrothermal synthesis of carbon spheres with iron precursors, TEOS and C18TMS are sol-gel fabricated to incorporate the silica shells on the carbon spheres, and the carbon templates are removed by a heating process. In the final stage, an Fe₂O₃ core is reacted with Fe₃O₄ nanoparticles under H₂ atmosphere [67]. In addition, the existence of OH groups on the surface of the carbon spheres enables anchoring the Pd nanoparticles to the outer surface possible. After removing the carbon template, Pd nanoparticles can be found inside the hollow spheres, which is critical for the high activity of Suzuki cross-coupling reactions [59].

1.3.2 Soft Templating

The second known method of producing mesoporous materials is soft templating. Unlike hard templating, soft templating does not depend on a silica template but instead benefits from the self-assembly of surfactants, such as amphiphilic ABA and BAB triblock copolymers as well as AB block copolymers. The soft-templating strategy was introduced to mesoporous carbon chemistry in 2004 [68]. With a dissolved polystyrene-*b*-poly-4-vinylpyridine (PS-P4VP) / resorcinol-formaldehyde system, subsequent solvent removal at 80 °C, followed by thermopolymerization of the resorcinols with formaldehyde gas and carbonization under protective gas resulted in the production of ordered mesoporous carbon (OMC). The diameters of the hexagonally arranged pores of the material were approximately 34 nm.

One year later, the *Ueyama et al.* published the preparation of a mesoporous carbon material with tunnel-shaped pores from the commercial F127 (PEO₁₀₆-PPO₇₀-PEO₁₀₆) Pluronic with resorcinol, formaldehyde, and triethyl orthoacetate as carbon precursors [69]. This mixture was dissolved in an ethanol-water mixture placed on a silicon wafer,

and it was evenly distributed using a spin-coating process. This was followed by thermopolymerization at 90 °C and carbonization, which yielded a hexagonally ordered carbon material with a pore diameter of about 6 nm.

Another important contribution to the preparation of mesoporous carbon materials was made by *Zhao's* working group in 2005 [70]. With F127 (PEO₁₀₀-PPO₆₅-PEO₁₀₀) as a surfactant, they produced two carbon materials in hexagonal (p6mm) or cubic (Im $\bar{3}$ m) order. This was also the first production of an OMC by dissolving an ABA block copolymer with phenolic resin oligomers (from phenol and formalin) in ethanol.

To meet the many requirements of mesoporous carbon materials and be applied in a wide variety of applications, the production of highly specialized materials is required. However, producing these materials requires controlling all parameters of the manufacturing process to ensure the reproducibility of the materials. These parameters include the purity and uniformity of the surfactants, since the polydispersity affects the self-assembly process [71], as well as the pH value, which along with the reaction temperature and duration has a major influence on the degree of polymerization or crosslinking of the phenolic resin oligomers and thus the self-assembly. It is therefore important to develop a process in which these and other parameters are kept constant.

However, effective control is only possible through a deeper understanding of the underlying parameters. *Naumann et al.* recently reported the soft-templating approach to preparing mesoporous carbon materials. A phenol-formaldehyde resin was used as an organic precursor, and well-defined, amphiphilic block copolyethers of the type PPO_{n/2}-PEO_m-PPO_{n/2} ("Reverse Pluronic," M_n up to 50, 000 g/mol, ĐM = 1.01–1.08, >100 examples) were used as structure-directing agents (SDAs) in a standard soft-templating process. The evaporation-induced triblock copolymer self-assembly (EISA) process, which is based on delivering films of OMC after thermal cross-linking, calcination, and carbonization, was used to make ordered OMC structures. A mesoporous carbon structure can be created by carefully selecting the SDA properties (total molar mass, n/m ratio, and PPO block length), resulting in monomodal and well-defined pore-size distributions in the 6–18 nm range. The evaporation-induced triblock copolymer self-assembly (EISA) process, which is based on delivering films of OMC after thermal cross-linking, calcination, and carbonization, was used to make ordered OMC structures. A mesoporous carbon structure can be created by carefully selecting the SDA

properties (total molar mass, n/m ratio, and PPO block length), resulting in monomodal and well-defined pore-size distributions in the 6–18 nm range [72].

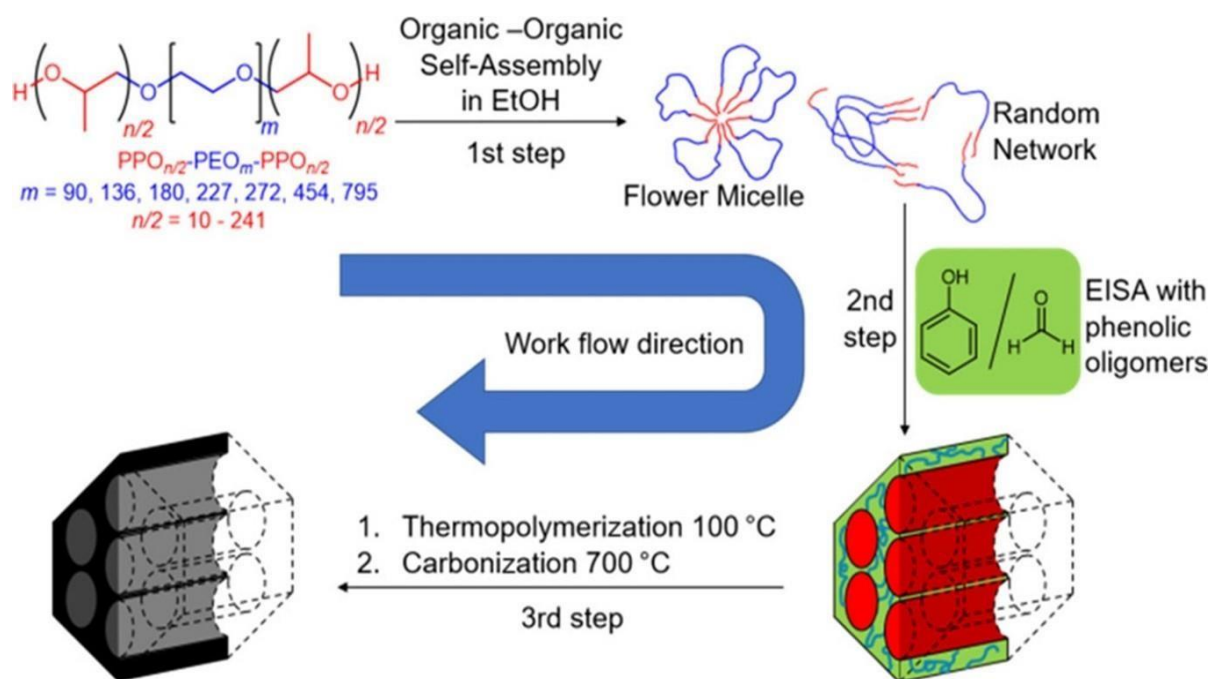


Figure 8: Preparation of OMC, Using “Reverse Pluronic” structure-directing agents (SDAs) [72].

1.3.3 Ordered Mesoporous Materials (OMMs): Prospects and Applications

Compared to microporous materials, mesopore structured materials consist of larger pores, which provide access to a variety of functionalized OMMs for specific applications. Interconnected mesoporous systems of functionalized OMMs facilitate the passage of larger molecules and are eminently suitable for various environmental applications, such as adsorption, separation, catalysis, electroanalysis, and energy storage/conversion [73]. Recent reports point out the potential use of OMMs in electroanalysis and sensors. Notably, energy conversion/storage uses the high and conductive surface areas of the OMMs. Practically, OMMs contribute to a broad range of areas, such as medicine and microelectronics.

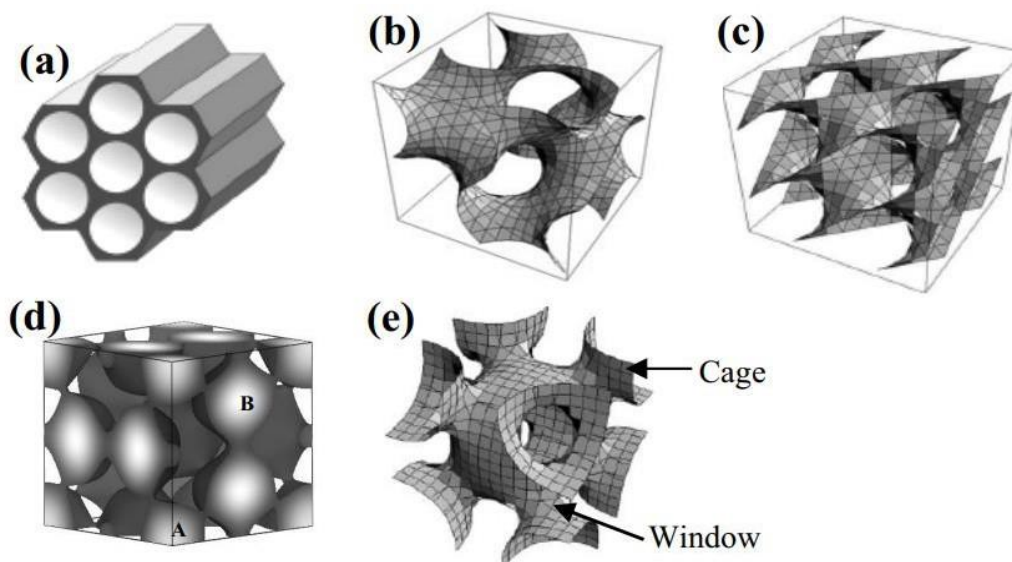


Figure 9: Various pore geometries of mesoporous structures, (a) 2D hexagonal $p6mm$, (b) bicontinuous cubic $Ia\bar{3}d$, (c) bicontinuous cubic $Pn\bar{3}m$, (d) cage type $Pm\bar{3}n$ and (e) cage type $Im\bar{3}m$ structures. Reprinted from ref [73-76].

OMMs can be classified according to their structural dimensions and pore geometry, e.g., either (2D- or 3D-) cylindrical pores or (3D-) interconnected cage type pores. Structures with cylindrical pores such as MCM-48 [50], AMS-6 [77], FDU-5 ($Ia\bar{3}d$), AMS-10 ($Pn\bar{3}m$) and MCM-41 [74,50], SBA-15 ($p6mm$) [78] possess uniform pore diameters (Figure 9 (a), (b), (c)). On the other hand, structures with interconnected cage type pores such as FDU-1 [79], FDU-12 [80], SBA-16 [79], ($Im\bar{3}m$), SBA-1, SBA-6 ($Pm\bar{3}n$) [81], SBA-2, SBA-12 ($P6_3/mmc$) [82] and AMS-8 ($Fd\bar{3}m$) [83] consist of spherical or ellipsoidal cages that are 3D connected by smaller cage-connecting pores called windows. These mesocaged materials possess features of both the microporous domain in the form of narrow windows and mesoporous voids in the form of cages (Figure 9 (d, e)).

Owing to the uniform and cylindrical mesopore structures, ordered mesoporous silicas M41S and SBA-n type mesoporous structures are the most promising candidates for supported heterogeneous catalysis [84]. They also offer advantages, such as high surface areas and narrow pore size distributions; reusability; efficient adsorption and mass diffusion; and thermal and mechanical stability [85]. SBA-15, SBA-16, MCM-41, and MCM-48 have been the most used mesoporous materials in catalysis. In this sense,

Joseph et al. [86] published the heterogenization of a chlorocarbonyl tris-(tri-phenylphosphine) ruthenium (II) complex on functionalized MCM-41 and SBA-15. The results showed that, in the hydrogenation reaction of styrene, while the pure Ru complex demonstrated catalytic activity values (TOF) of 16.6, the heterogenized Ru complex presented TOF values of 80.0 and 122.8 for MCM-41 and SBA-15, respectively. The higher activity of the heterogeneous catalysis system over the homogenous one was attributed to the transfer of electrons from the functional amine group to ruthenium.

In the last decades, catalytic reactions such as photocatalysis, transesterification, hydrogenation, oxidation, and hydroxylation of aromatics, among others, have attracted worldwide attention. *Cabrera-Munguia et al.* [87] published the esterification reaction of oleic acid, using SBA-15 as support in combination with acid catalysts. The SBA-15-SO₃H demonstrated the highest catalytic activity among the supported acid site catalysts, which was attributed to the high concentration of Lewis acid sites. *Zhou et al.* [88] developed Ni catalysts supported by APTES that functionalized MCM-41 for acetylene hydrogenation in ethylene, verifying that the Ni strongly interacts with the mesoparticles and is uniformly dispersed within the support. Moreover, the hydrogenation reaction showed that the conversion of acetylene was 100%, with a selectivity of 47%. *Samadi-Maybodi et al.* [89] reported that CdS@SBA-15 was a stable catalyst for alizarin dye degradation under solar irradiation, revealing that the semiconductor quantum dots (CdS) at SBA-15 showed good photocatalytic properties and more oxidation stability compared to the free quantum dots. In addition, catalyst structure, the morphology of the support material is crucial for catalytic reactions. Possible morphologies include spheres, thin films, fibers, and tubes.

In recent studies, synthesized materials with macro-mesoporous characteristics have been described as monoliths [73,90,62]. Porous monolithic structures which are, for example, required for bulk electrodes for energy storage devices can provide high storage capacity and a long lifetime. Hyper-crosslinking block-copolymer (BCP) assemblies is an effective approach to fabricating porous monoliths [91]. *Matyjaszewski et al.* [92] published mesoporous, carbonaceous-derived monoliths by hyper-crosslinking BCP micelles. In their work, PMMA-b-PS copolymers self-assembled as polymeric networks into spherical micelles, which consisted of a PMMA core and hyper-crosslinked PS chains. In the final step, cross-linked polymer agglomerates were converted to mesoporous carbons by pyrolysis. During the process, the PMMA core decomposed,

resulting in hollow structures, while the crosslinked PS domains were converted to a carbonaceous structure. The final mesoporous carbon monoliths obtained possessed a mean pore diameter of 16 nm, an average shell thickness of 6 nm, a surface area of 829 m² g⁻¹, and a total pore volume of 1.07 cm³g⁻¹.

Ordered mesoporous monoliths can also be synthesized by block-copolymer templating methods in solutions. *Wu et al.* [93] reported using self-assembled polyethylene glycol (PEG) homopolymers on phenol/ formaldehyde resol and Pluronic P123. The following step, with the decomposition of P123 and PEG, resulted in mesoporous monoliths with a 2D-hexagonal ordered mesoporous structure. The resulting carbon monoliths were obtained with an average pore size of 9 nm and surface areas of 563 m² g⁻¹.

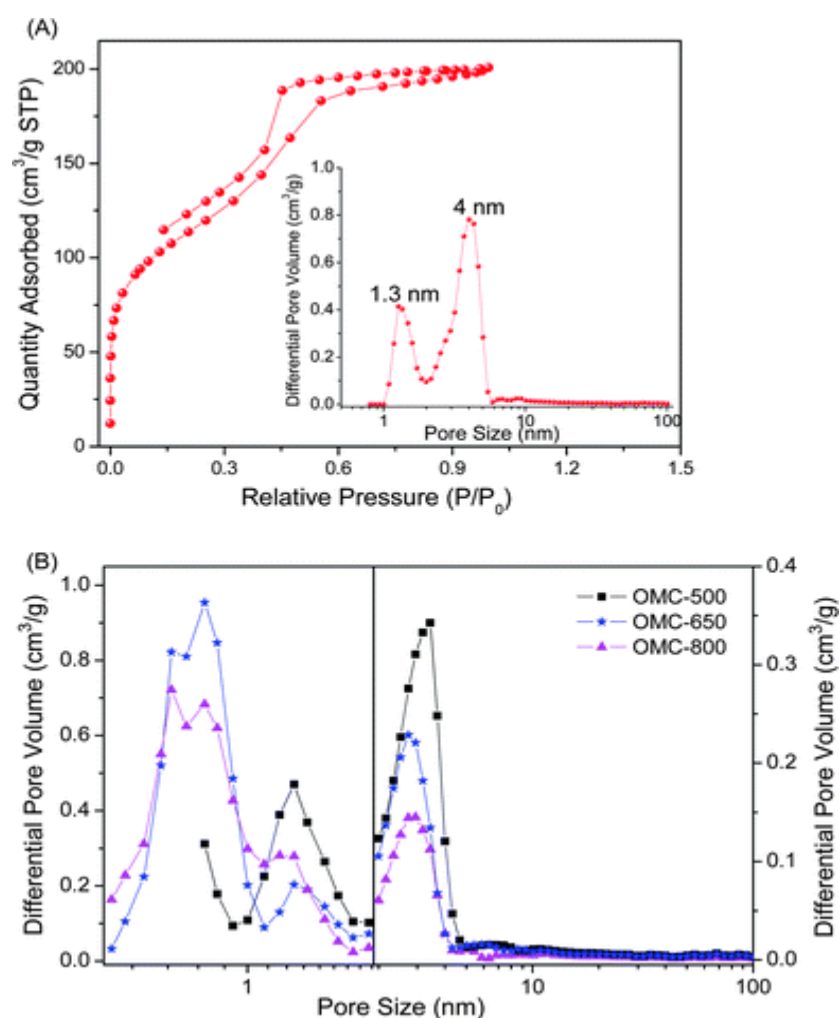


Figure 10: (A) N₂ adsorption–desorption isotherm of ordered mesoporous carbons (B) DFT pore size distributions of OMCs. Reprinted with permission from The Royal Society of Chemistry (2013) [93].

1.4 Polyurethanes: Prospects and Applications

Urethane was first synthesized by *Wurtz* in 1849 [94]. Later, the commercially important synthesis of isocyanates from amines and phosgene was discovered by *Hentschel* in 1884 [96]. In 1937, *Otto Bayer* synthesized polyurethanes (PUs) by reacting a polyester diol with a diisocyanate [94,95]. PUs are polymers that are formed by the reaction between the hydroxyl (OH) groups of a polyol with the isocyanate functional groups (NCO) of an isocyanate, and the name is associated with the polymerized urethane [96-98].

The application of PUs is diverse due to the tunability of the synthesis. Properties can be altered by adjusting the type and content of the polyol, isocyanate, catalyst, and additives. For example, increasing the polyol functionality without changing the molecular weight leads to a slight increase in the hardness and a small reduction in the tensile strength and elongation. In turn, by increasing the equivalent weight of the polyol, while maintaining the functionality of a polyol, increases the tensile strength and elongation [97].

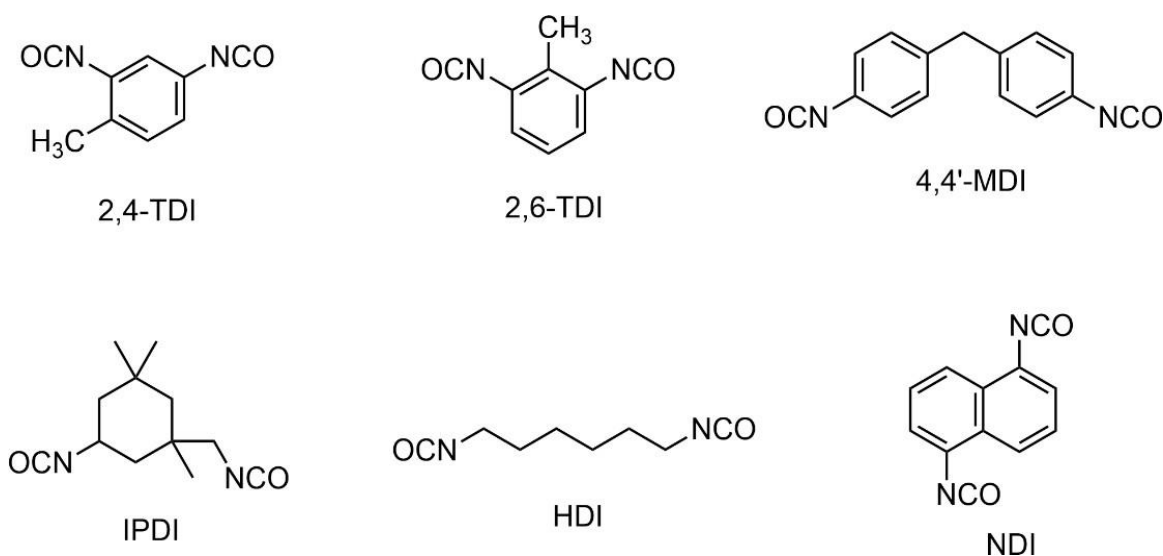


Figure 11: Common isocyanates

The nature of the isocyanate is equally significant as the impact of the type of polyol used. Methylene diphenyl diisocyanate (MDI) and toluene diisocyanate (TDI) represent ~90% of the total diisocyanate consumption [99]. Aliphatic isocyanates, such as isophoronediiisocyanate (IPDI) or hexamethylenediisocyanate (HMDI), are also used, but for other applications such as coatings. PUs derived from aromatic isocyanates

result in higher glass transition temperatures, modulus, and tensile strength. In turn, PUs derived from aliphatic isocyanates are rubbery materials with a higher elongation at break and lower tensile strength [100].

PUs are one of the most important classes of polymers that sustain the quality of human life through everyday products [94]. Among PU consumption, polyurethane foams (PUFs) correspond to 67% of global PU consumption. Due to the porous structure and excellent mechanical properties, PUFs have a variety of applications including thermal insulation, fire reaction, and sound absorption properties. Other properties of PUFs, such as the mechanical properties and electrical conductivity can be improved by the addition of functional fillers which increases the range of applications beyond building, construction, and automotive to radar absorbing and electromagnetic interference (EMI) shielding, oil absorbents, sensors, fire proofing, shape memory, and biomedical materials. *V. Ritleng et al.* showed the preparation of polydopamine-coated open-cell polyurethane foams (POPF) as robust catalyst support materials. Due to the remarkable adherence properties, POPF demonstrated high photodegradation activities for the noxious azo dye acid orange 7 (AO7) [101]. In 2021, *H. Taghvaei et al.* prepared 3D-PU foam with an interconnected porous structure to evaluate its effects on the conversion and efficiency of low-temperature CO₂ dissociation through a packed dielectric barrier discharge (DBD) plasma reactor [102]. Furthermore, various packing materials, including BaTiO₃, TiO₂, CeO₂, ZrO₂, CaO, Al₂O₃, Fe₃O₄, and SiO₂, are coated over the PU foam. According to the results, the highest attainable conversion for the BaTiO₃-coated configuration at the specific energy input (SEI) of 60 kJ/L is ~27.4 %, showing 124 and 203 % enhancement in comparison with foam-filled and empty plasma configurations, respectively [103].

1.5 Olefin Metathesis-Derived Polymers and Monoliths

Olefin metathesis is one of the few fundamentally new organic reactions that was developed in the late 1950s. This reaction was discovered serendipitously by *Banks* and *Bailey* at Phillips Petroleum Co. When using a supported molybdenum catalyst, they found that, e.g., instead of alkylating paraffin, the olefin molecules were split, and, furthermore, that propene can be catalytically converted into ethene and butene [103]. Because of the increasing demand for propylene, the reversible reaction process

became important over the years. This process, also known as the *Phillips triolefin process*, proceeds with various catalytic systems (such as WO_3 on SiO_2).

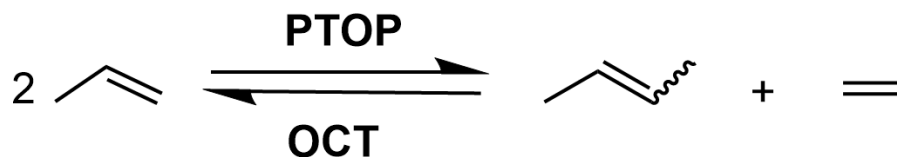


Figure 12: “Phillips Triolefin Process” (PTOP) and “Olefins Conversion Technology” (OCT).

The word "metathesis" is derived from ancient Greek and means "transposition." Olefin metathesis reactions are described as a metal-mediated reorganization of carbon–carbon (C–C) double-bond skeletons using well-designed catalysts [104]. Advances in catalytic complexes over the last three decades have transformed these reactions into powerful tools in many areas of chemistry. *Chauvin* proposed a general metathesis reaction mechanism involving metallacyclobutane in the 1970s (Figure 13) [105].

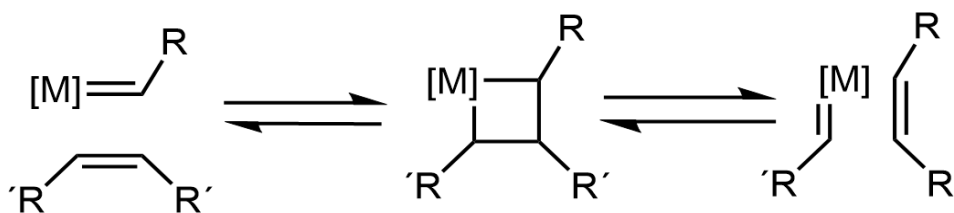


Figure 13: The principle of olefin metathesis according to Y. Chauvin.

The *Chauvin* mechanism involves a metal–carbene species, the coordination of the olefin to the metal atom of this species, a shift of the coordinated olefin to form a metallacyclobutane intermediate, and finally, a topologically identical shift of the new coordinated olefin in the metallacyclobutane in the opposite direction of the initial olefin shift. The most important advance has been the preparation of numerous well-defined metal carbene complexes, which can act directly as the initiators for all types of olefin metathesis reactions. These second-generation catalysts allow better control and a better understanding of the mechanism of the olefin metathesis reaction. Transition metal chlorides were first compounds used as catalysts for metathesis reactions. However, transition metal carbene catalysts developed by *Schrock* and *Grubbs* led to advanced control of catalytic activity by rearranging ligands.

In recent decades, several new catalytic systems based on metal alkylidenes have been developed and used in many areas of chemistry, such as organic chemistry, polymer chemistry, and material science. Thus far, all known types of metathesis reactions can be catalyzed using Grubbs and Schrock catalysts [106]. In ongoing research, scientists have developed a wide range of olefin metathesis reactions. Chauvin's mechanism applies to the entire range of these reactions, including cross-metathesis (CM), ring-closing metathesis (RCM), acyclic diene metathesis polymerization (AD-MEP), ring-opening metathesis polymerization (ROMP), enyne metathesis (EYM), and ring-opening cross-metathesis (ROCM). CM and RCM, which proceed at ambient conditions with high stereo- and regioselectivity using Ru- or Mo-based catalysts, are the most utilized reactions in chemistry. Recently, ROMP and the cyclopolymerization of 1,6-heptadiynes have become powerful reactions for polymer synthesis. Aside from providing excellent access to complex products, metathesis polymerization allows for the development of polymers with high stereo- and regioselectivity [104].

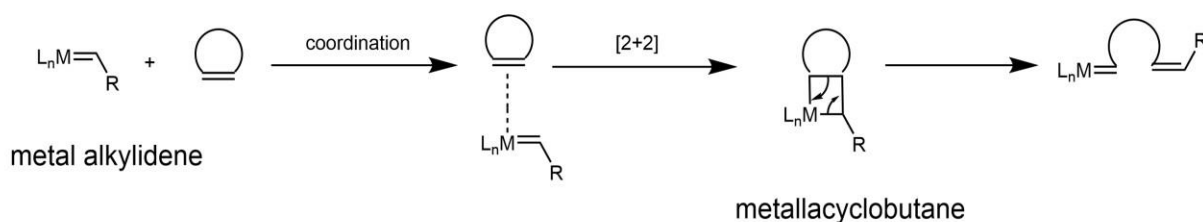
Living nature is another crucial feature of metathesis polymerization [106], which allows the synthesis of well-defined materials that can easily be post-functionalized using a "grafting-from" approach [107]. Because of these remarkable characteristics, this polymerization technique is a useful and broadly applicable method for synthesizing macromolecular materials. The following sections describe in detail the pathways for synthesizing and applying ROMP.

1.5.1 Ring-Opening Metathesis Polymerization (ROMP)

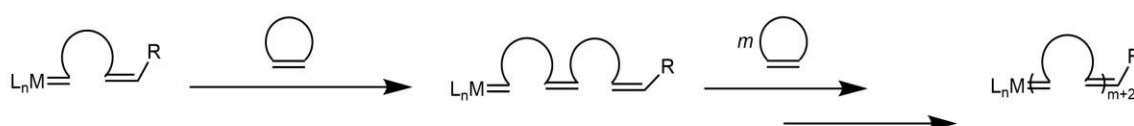
ROMP is a chain-growth polymerization process, where a mixture of unsaturated cyclic olefins is converted into polymeric materials. The reforming of the double bonds of the unsaturated cyclic olefins throughout the reaction results in polymers with double bonds in the polymer backbone. The general ROMP mechanism is shown in Figure 14. The initiation step involves coordinating a transition metal alkylidene to a cyclic olefin, followed by [2+2]-cycloaddition to form a stable metallocyclobutane intermediate (MCB), which starts the growing polymer chain process. The metallocyclobutane intermediate then undergoes cycloreversion to obtain a new metalalkylidene species. The reactivity of the new metalalkylidene is similar to that of the initiator. Consequently, the propagation stage continues until reaction equilibrium is reached. Living ROMP is

generally quenched by adding a suitable reagent to deactivate and remove the transition metal catalyst and install a peculiar functional group. Metal-mediated ROMP reactions have crucial features. First, the metal center in the growing polymer chain can be found in the metal alkylidene. This associated form depends on the reaction conditions, the transition metal, and its associated ligands [108]. Second, the olefin metathesis primary reaction mechanism is generally reversible. Third, the equilibrium-controlled reaction mechanism can be controlled by tuning the thermodynamics of the polymerization. Additionally, the formation of the polymer's tacticity, which results from the rearrangement of the chiral atom along the polymer chain, must also be considered crucial to the ROMP reaction. The most used monomers in ROMP are cyclic olefins such as norbornene derivatives, cyclobutenes, cyclopentenenes, and cis-cyclooctenes.

Initiation



Propagation



Termination

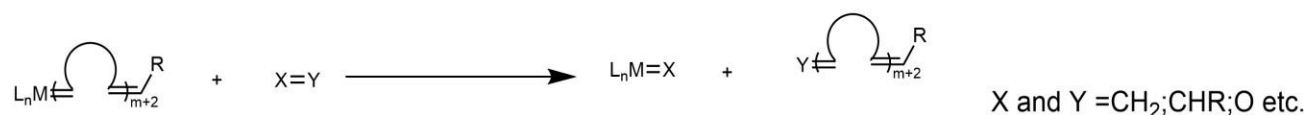


Figure 14: A general mechanism to a typical ROMP reaction [108].

The reaction parameters, such as temperature and concentration, also strongly influence the structure of the final ROMP product. The highest monomer concentration at the lowest temperature can be considered the most favorable condition for the general ROMP reaction mechanism. In addition to the general ROMP mechanism, the reaction equilibrium can also be determined by other pathways, including secondary metathesis reactions such as intermolecular and intramolecular chain transfer (backbiting). In an intermolecular chain transfer reaction, an active metal alkylidene-ended chain can react with another polymer chain in the reaction vessel. The molecular weight of the polymer increases accordingly. In a backbiting reaction, the active end functions of a polymer chain react with themselves to give cyclic components with reduced molecular weights. These secondary metathesis reactions broaden the polydispersity of the system. Another advantage of ROMP is its ability to form high-molecular-weight cyclic oligomers and polymers [109].

1.5.2 Living Ring-Opening Metathesis Polymerization (ROMP)

In 1956, the living polymerization system was introduced by Swarc [110,111]. The critical parameter of a living polymerization is its ability to provide polymers that have narrow molecular weight distributions (*polydispersity index (PDI) < 1.1*), which is generally defined following the equation: $PDI = M_w/M_n = 1 + 1/DP$, where M_w is the weight-average molecular weight, M_n is the number-average molecular weight, and DP is the degree of polymerization. To access well-defined, monodispersed materials, control is possible over the polymerization systems where the rate of initiation is similar or faster than the propagation rate. Thereby, the following characteristic features are required for a ROMP reaction to be considered “living:” (1) The rate of initiation needs to be similar to or faster than the rate of propagation. (2) The yields of polymerization vs. monomer consumption must be linear. (3) $PDI < 1.5$. Under these conditions, well-defined graft-, block-, and other types of polymers and polymeric materials with useful functions can be prepared. When considering the metal-mediated and equilibrium nature of most ROMP reactions, the need for very special metathesis catalysts to satisfy the requirements quickly becomes apparent. A catalyst should have these essential features: (1) exhibit fast initiation kinetics; (2) control the polymerization without chain termination or transfer; (3) facilitate selective end-functionalization by reacting with accessible terminating agents; and (4) show high stability toward air and

moisture. Recently, the development of catalysts with a well-defined structure has led to tremendous advances in olefin metathesis. Importantly, using olefin metathesis in polymer and petroleum chemistry has gained attention in recent years as, depending on the desired application, these catalyst complexes can be designed to make modifications and functionalization possible [112]. *Calderon et al.* reported a new catalyst system that was prepared from a mixture of AlEt_2Cl , WCl_6 , and ethanol. This mixture of catalysts creates opportunities for tremendous commercial applications and a potential for ROMP. In the late 1960s, a perfectly alternating copolymer of 1,4-butadiene and isoprene was synthesized by the ROMP of 1-methyl-1,5-cyclooctadiene [113].

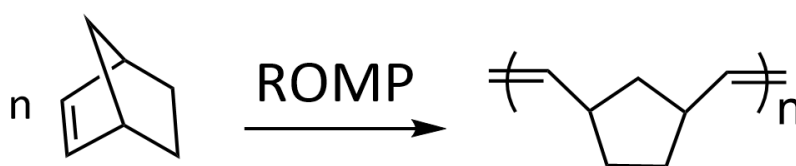


Figure 15: ROMP of norbornene.

Additionally, many catalyst systems based on transition metal complexes were discovered by *Natta, Michelotti, Dall'Asta, Banks, Rinehart, and others* [114]. The ROMP reactions using these catalyst systems provided a solid base for developing well-designed catalyst systems. In 1976, *Katz et al.* employed a well-defined catalyst series of tungsten complexes, $(\text{CO})_5\text{W}=\text{CPhR}$ (1, $\text{R}=\text{Ph}$ or OCH_3), which were previously reported by *Casey and Fischer* for ROMP [115]. The polymerization of various cyclic olefins, including cycloheptene, cyclobutene, and norbornene, was successfully achieved using tungsten–alkylidene complexes without needing a co-catalyst. Although the polydispersities of the resultant polymers were relatively broad (PDI: 41.85), the disubstituted methylidene moiety on the catalyst was found on the ends of the polymer chains. Thus, the catalyst appeared to suffer from either poor initiation characteristics or extensive secondary metathesis reactions.

Presently, depending on the desired application, there are well-designed metathesis catalysts with primary structural origins in the *ruthenium-based Grubbs-type* and the *molybdenum-based Schrock-type* catalysts. Recently the use of Ru catalysts has increased significantly in Olefin metathesis due to the low oxophilicity of Ru. Ru systems are generally more tolerant towards functional group and in some cases towards moisture and air.

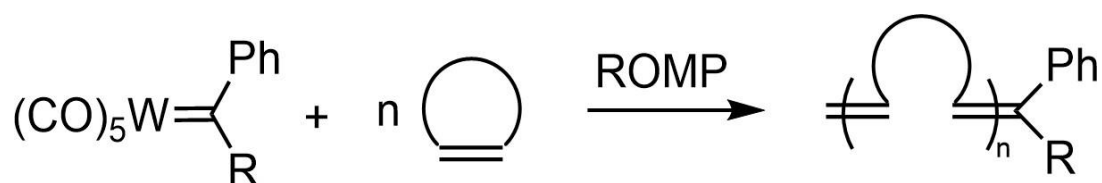


Figure 16: Polymerization of various cyclic olefins (cyclobutene, cycloheptene, cyclooctene, and norbornene) with well-defined tungsten-alkylidene complexes.

In the 1960s, the first reports based on ruthenium-based complexes (RuCl₃ salts in protic media) described facilitating the polymerization of various norbornene derivatives [113,116]. The first well-defined Ru complex that showed activity in the ROMP system was (PPh₃)₂Cl₂Ru=CH–CH=CPh₂ [117]. The synthesis of this complex was accomplished through the same synthetic pathway used to prepare W-based alkylidene complexes. Particularly, the reaction of (PPh₃)₃RuCl₂ or (PPh₃)₄RuCl₂ with 3,3-diphenylcyclopropene afforded this complex in nearly quantitative yields. This well-designed complex was successfully used to mediate the high activity living ROMP. The 1st-generation Grubbs catalyst [117,118] is synthesized by reacting of (PPh₃)₃RuCl₂ with diazobenzylidene, and the final complex is converted into its more active derivative complex via phosphine (e.g., PC_{y3}) exchange and converted to other alkylidene catalysts by adding the corresponding terminal olefin. Other Ruthenium-based catalysts are 1st-generation Grubbs catalyst derivatives. In the case of the 2nd-generation Grubbs catalyst, the phosphines are replaced by an *N*-heterocyclic carbene (NHC) [119]. The 3rd-generation Grubbs catalyst, octahedral complex [RuCl₂(3-Br-Py)₂(IMesH₂)(=CHC₆H₅)] (IMesH₂ = 1,3-dimesitylimidazol-2-ylidene), shows enhanced reactivity compared to the 2nd-generation Grubbs catalyst [120]. The activity of these catalysts are strongly affected by modifying the anionic ligands in the backbone. The Grubbs–Hoveyda type catalysts, including a chelating 2-isopropoxybenzylidene ligand, show enhanced stability [121,122]. Incorporating the more electron-withdrawing ligands, such as perfluorocarboxylates, increases the polarization of the Ru=C double bond, showing enhanced activity [123,124]. Modifying the benzylidene moiety of a Grubbs–Hoveyda type catalyst by introducing electron-donating functionalities allows for increased stability. In 2004, the *Buchmeiser* group introduced a new type of metathesis catalyst based on tetrahydropyrimidin-2-ylidenes [125,126]. Chiral Grubbs and Grubbs–Hoveyda-type catalysts have been prepared by introducing asymmetric NHC ligands to the backbone [127,128]. In the 1990s, well-defined Mo-

based alkylidenes were introduced by *Schrock* [129]. These catalysts can tolerate a broader range of functional moieties, including monomers containing esters, amides, imides, ketals, ethers, and cyano, trifluoromethyl, and primary halogen-containing functional groups. Additionally, a wide range of ligands, such as alkoxides and phenolates, can easily be attached to the metal center. The complex [Mo(N-2,6-*i*Pr₂C₆H₃)(CHCMe₂Ph)(OTf)₂(DME)] represents a universal Schrock-type catalyst precursor [130-132]. The incorporation of electron-withdrawing alkoxides generally increases the activity. Bisalkoxide- and bispyrrolide-type complexes are important precursors for synthesizing either bisalkoxide or monoalkoxide pyrrolide initiators, which possess four different tetrahedrally arranged ligands, thus creating a stereogenic metal center [133-135].

1.6 Supported Catalysts for Continuous Flow Synthesis

Flow chemistry and microreactor technologies have emerged as promising tools in modern organic synthesis, due to several advantages over traditional batch methods such as sustainability [136,137]. The breakthrough in continuous flow processing is because of the following features (I) large surface-to-volume ratios, (II) efficient mass and heat transfer, (III) precise mixing and intrinsic safety, (IV) reduced use of solvent and improved stoichiometry, (V) scalability, and (VI) reduced footprint and capital investment. The features make flow chemistry appealing for industrial production. Furthermore, flow chemistry might be considered a green technology, since the use of flow processing also allows for compliance with sustainability and environmental protection [138].

Heterogeneous catalysis plays a crucial role in chemical synthesis at both academic and industrial levels, as witnessed by vigorous research activity in this field. Both flow chemistry and heterogeneous catalysis hold incredible potential from a sustainability point of view and from a green perspective. Indeed, if heterogeneous catalysts are required by the chemical industry for efficiency, heterogeneous flow catalysis would enable greener and more efficient chemistry at the industrial level [139]. Heterogeneous flow catalysis has many benefits, such as safety, high efficiency, less waste, no build-up of dangerous chemicals, continuous product synthesis, and easy catalyst recovery and reuse.

Three general methods can be utilized to perform heterogeneous flow catalysis using microfluidic devices by using: (1) packed-bed flow reactors, (2) monolithic flow reactors, and (3) wall-coated flow reactors. In packed-bed flow reactors, the catalyst is covalently or non-covalently grafted onto an insoluble solid material [140,141]. Various types of catalysts (i.e., organic, organometallic, metallic, and enzymatic) can be supported by either organic or inorganic polymeric materials. Due to the superior properties of supported heterogeneous catalysts, such as the ease of characterization and quantification of the catalyst and the high catalyst loading, flow reactors can be used.

There are some advantages to using packed-bed flow reactors over classical batch reactor. The significantly higher catalyst loading affects the kinetics of the reaction, reducing reaction times. As the catalyst is supported by and confined to the flow hardware (i.e., column), separation or recovery of the catalyst from the reaction mixture is not required [142]. Monolithic flow reactors consist of a network (regular or irregular) of polymeric or inorganic materials with interconnected micro- or macropores. Flow reactors are preferred to packed-bed reactors, especially for their greater tolerance to high flow rates and efficient mass transfer, due to the porous nature of the catalytic material and the absence of interstitial spacing. In wall-coated reactors, the catalyst is immobilized on the inner walls of the channels of the microfluidic device. Generally, this type of microreactor has efficient good mass transfer and continuous flow of the reactants with minimal pressure drop or clogging of microchannels.

1.6.1 Packed Reactors

Microreactor technology has gained attention over the past 20 years. Microreactors minimize reagent consumption and energy waste due to their small dimensions, which in most cases do not exceed 1 mm in at least one dimension. The small volume of microreactors enables safe handling of reactions, including hazardous and/or highly exothermic reactions, while facilitating fast and easy parameter screening. Due to its small size, microreactors have a ratio of surface area to volume that is significantly higher than other reactors. This, in turn, affects other properties such as the flow regime, and mass, and heat transfer. Because high pressure and temperature can be handled much easier at a very small scale, microreactors unlock new process

windows. If a thin coating or a single layer of a catalyst is used, microreactors may have great potential in heterogeneous catalysis and, thus, in the petrochemical and pharmaceutical industries. As such, various methods to immobilize heterogeneous catalysts in microreactor structures and their applications for process development, data generation, and synthesis in continuous flow have been carefully evaluated [143-146]. The simplest way to incorporate a heterogeneous catalyst into a microreactor is to fill the channels with catalysts supported by beads, resins, or polymers with silicon dioxide being the preferred support material for continuous catalysis applications. Many studies have explored using polymer beads grafted with different ligands, coordinated with metals and tested, largely, in cross-coupling reactions and hydrogenations [144]. For example, *Ley et al.* reported using the polyurea encapsulated Pd(OAc)₂ for Suzuki–Miyaura cross-coupling reactions [145].

A. Moores et al. published the use of Fe nanoparticles (NPs) for the selective hydrogenation of alkenes and alkynes under continuous flow. All iron/polymer systems provided quantitative yields under continuous flow conditions. Selective hydrogenation of the styrene double bond served as a model reaction for the optimization of reaction conditions of 40 bar H₂, 100 °C, and a flow rate of 2 mL min⁻¹, resulting in a 92% yield of ethyl benzene [146].

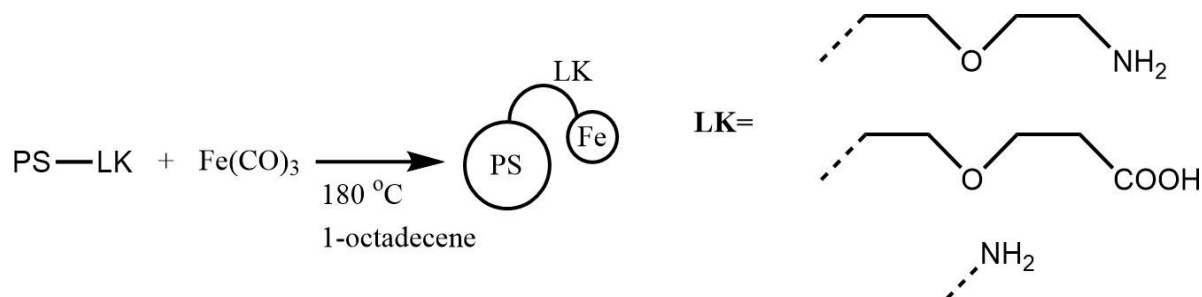


Figure 17: Schematic representation of the polymer supported iron nanoparticles [146].

G. Vilé and J. Pérez-Ramírez reported the three-phase hydrogenation of acetylenic compounds using silver and gold nanocatalysts loaded with different H-Cube flooded-bed microreactors (Al₂O₃, SiO₂, TiO₂, and carbon). It was found that NPs of <5 nm exhibited the highest activities [147]. Many studies have also reported the flow-through application of metal complexes on ionic-liquid phases (*SILP*), hyperbranched oligomers, and spherical siliceous mesocellular foams (MCF) [148-150]. *M. Buchmeiser et al.* recently reported the immobilization of a Hoveyda-Grubbs-type

inside mesoporous silica for use in the selective macro(mono)cyclization (MMC) of α , ω -dienes under spatially confined and continuous-flow conditions. The investigation revealed that working under continuous-flow conditions effectively suppresses the formation of higher oligomers and thus favors MMC [150].

1.6.1.1 Monolithic Flow-Through Reactors

The continuous-flow processes described to date utilize reactors with randomly packed beads, resulting in uncontrolled fluid dynamics, broad residence time distribution, low selectivity, and low process efficiency [33,151]. Monolithic structures have large void volumes and surface areas, resulting in a low-pressure drop along the microchannel and a large contact area of the reagent or catalyst with the liquid. Polymers, hybrid polymer/glass composites, and inorganic matrices (silica, zeolites) are the most used monolithic families for catalysis under continuous-flow conditions [152].

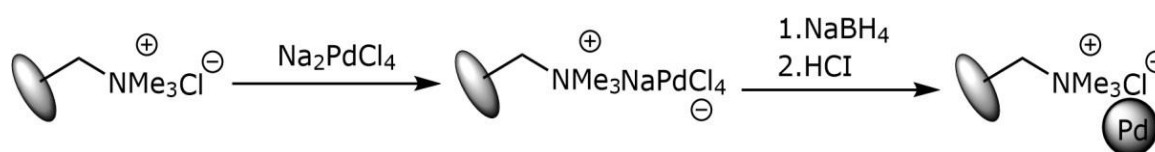


Figure 18: Immobilization of Pd NPs onto the monolithic phase inside a microreactor [139,153].

Kirschning et al. developed a polymer-assisted synthesis of monolithic materials in a flow-through process. In this way, poly (vinylbenzyl chloride) was synthesized within the glass rods to be used in continuous-flow processes. This system was used for transfer-hydrogenation and cross-coupling reactions. For that purpose, Pd NPs were immobilized within the monolithic structure. The vinylbenzyl chloride-based polymer was transformed into a quaternary ammonium ion-exchange resin. Thus, an aqueous solution of sodium tetrachloropalladate and subsequent reduction by means of a borohydride solution yielded Pd NPs of less than 10 nm in diameter. Borohydride reduction under flow conditions yielded smaller palladium clusters with a narrower particle size distribution and better dispersion in the polymer matrix compared with those obtained by reduction under diffusion control. The nature of monolithic composition was also a significant factor influencing Pd particle size [139,153].

F. Liguori developed a macroporous polymeric monolith that was composed of cation-exchange tetraphenylborate anions incorporated in a highly cross-linked divinylbenzene matrix. One of the advantages of this material is its reproducible microstructure, which guarantees high mechanical stability and high flow-through porosity. Palladium and rhodium NPs were immobilized onto the polymeric monolithic materials and used in the catalytic partial hydrogenation of alkynes under continuous flow. Excellent conversions (>98%) were obtained under mild conditions (1 bar H₂ and RT), with a selectivity towards cyclohexane of 99.9% [154,155].

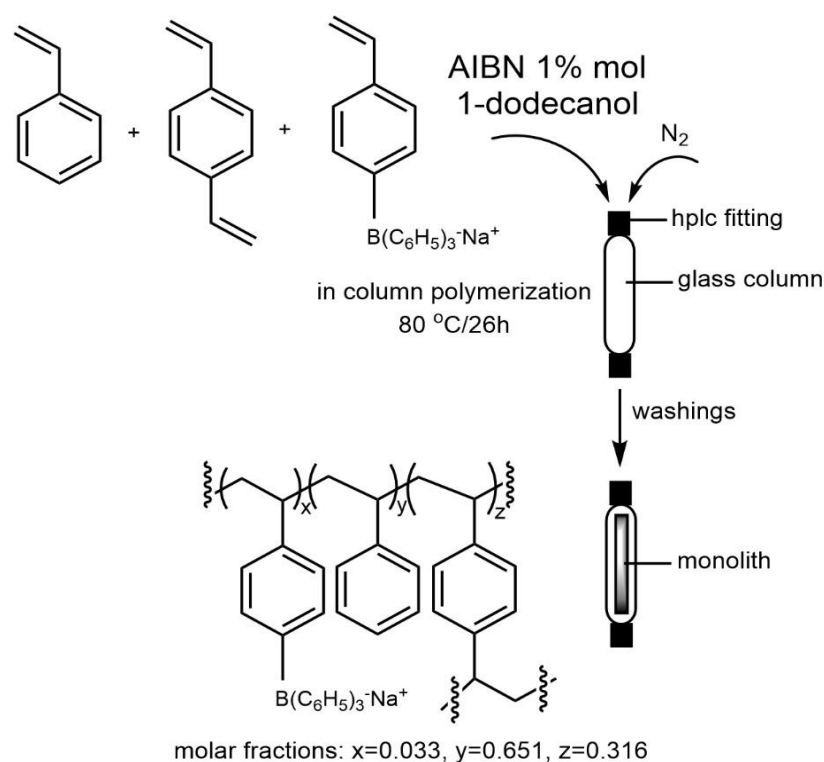


Figure 19: Sketch of the Procedure for the In-Column Preparation of the Monolithic Resin [154].

1.6.1.2 Silica-Based Monolith Reactors

The synthesis procedure for highly porous silica monoliths relies on the spinodal decomposition of the synthesis mixture. This phenomenon leads to phase separation into interpenetrating networks of a silica-rich phase and a solvent phase. Solid state-silica monoliths possess micro and meso-porosity. Generally, tetramethoxysilane (TMOS) or tetraethoxysilane are used as alkoxy silanes to produce monoliths.

Additionally, additives (i.e., surfactants) and water-soluble polymers induce the phase separation. The total pore volume can be adjusted by varying the volume fraction of the solvent phase in the starting solution. In chromatographic applications, the space between the column wall and the monolith is filled with a layer of PEEK polymer. These monoliths have an exceedingly high bimodal porosity of 80%. When compared to conventionally packed columns, the presence of macropore structure results in lower backpressure. Using high flow rates results in considerably reduced analysis times. In addition, meso- and micropores within the skeletal structure provide a large active surface area for high-efficiency separations. Such HPLC columns (4.6 mm x 100 mm) are commercially available even for semi-preparative work in a 10 mm x 100 mm format. Monolithic silica columns have also been produced using sol-gel technology. The silica gel structures can be attached to the tube wall by a chemical pre-treatment that activates the surface. Due to the larger surface-to-volume ratio contact areas, small-sized capillaries are generally preferable for the covalent bonding between the tube wall and the monolithic silica skeleton. For a larger capillary, a mixture of TMOS and methyltrimethoxysilane (MTMS) is used to minimize the shrinkage of the silica gel network. *Nakanishi et al.* reported a technique to tailor the mesoporosity by aging the monolith at 120 °C in an ammonia solution, which forms *in situ* by the hydrolysis of urea in the reaction mixture [156]. *M.T. Alotaibi et al.* studied gold nanoparticles incorporated in mesoporous silica monoliths by using direct impregnation of nanoparticles or functionalized monoliths with thiol groups prior to incorporation of the Au NPs. The thiol-functionalized Au NPs microreactor exhibited higher activity than the other material. Thiol-functionalized Au NPs were used to selectively oxidize cyclohexene to cyclohexene oxide with H₂O₂ or to 2-cyclohexen-1-ol when *tert*-butyl hydroperoxide was used as oxidant [157]. In 2016, *A. Koreniuk et al.* developed titania-silica microreactor monoliths for continuous flow. With this monolith, 2,3,6-trimethylphenol was oxidized to 2,3,5-trimethyl-1,4-benzoquinone by H₂O₂ with 85% conversion in 12 min, which is much faster than in a batch reaction, where the conversion after one hour was only about 75% [158]. *W. Song et al.* revealed that metal oxides (Al₂O₃, MgO) coating a hierarchically porous silica monolith could be employed for the base catalysed the Knoevenagel reaction [159]. *K. Szymańska et al.* reported the transesterification of neopentylglycol with ethyl acetate in an aqueous medium using the enzyme acyltransferase from *Mycobacterium smegmatis* (MsAct) that was immobilized in a hierarchical porous silica monolithic microreactor. Full

transesterification occurred within a very short time in comparison to other monoester formations using covalent bonding and functionalization methods [160]. Due to excellent chemical and thermal stability, controlled porosity, and sufficient reactivity to bind with different types of organic groups, many of the heterogeneous catalysts studied have used silica-derived monolith reactors.

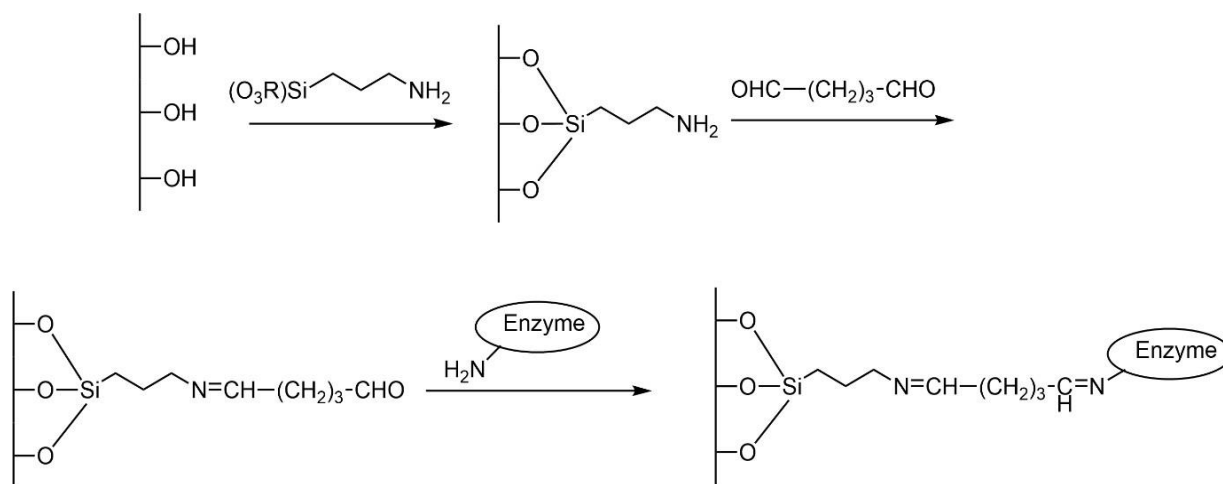


Figure 20: Functionalisation of silica monolith and immobilization of MsAcT by covalent bonding [160].

Brinker et al. reported the synthesis of CN-terminated mesoporous silica thin films by an evaporation-induced self-assembly (EISA) method using Brij56, a non-ionic surfactant, as a structure-directing agent [161]. The CN groups could be hydrolysed to produce a COOH-functionalized material with good enzyme binding properties.

1.6.1.3 Polymer-Based Monolith Reactors

Polymeric monolith reactors are characterized by a regular network of meso- and microporous channel structures. Polymeric carriers are generally used to immobilize organocatalysts and enzymes. *Gömann et al.* created poly(chloromethylstyrene-co-divinylbenzene) monoliths by combining 60% porogens, 24% monovinyl monomer, and 16% crosslinking monomer [162]. Prepared monoliths were subsequently functionalized by the covalent attachment of ligands. Pd was attached to the polymeric support using both 1,10-phenanthroline and imidazole/carbene binding for the Suzuki–Miyaura and Sonogashira reactions. Quantitative turnovers were achieved with most substrates and leaching of palladium was low in all cases. *A. Nagaki et al.* also published the preparation of a polymer monolith containing an immobilized Pd catalyst

from 1,3-bis-(*N,N*-diglycidylaminomethyl)cyclohexane, poly(ethylene glycol) (PEG, molecular mass = 200), 4,4'-diaminodicyclohexylmethane, and 6-(phenylamino)-1,3,5-triazine-2,4-dithiol [163]. A palladium acetate-THF solution was pumped through the column, followed by an aqueous solution of sodium borohydride, to reduce the amount of Pd (II) adsorbed on the surface of the monoliths. Recently, *C.-H. Pélisson et al.* reported the injection of a Pd²⁺ solution through a hierarchically porous, polymethylhydrosiloxane-grafted silica monolith. The functionalized, porous monolith was flushed with a strong Lewis acid (tris-(pentafluorophenyl)borane, B(C₆F₅)₃) in order to activate the Si-H bonds in the monolith, which were subsequently used to reduce the Pd²⁺ injected into the monolith [164]. It was found that the polymeric monolithic flow reactor performed exceptionally well in chemo- and stereoselective hydrogenation of alkynes.

The production of multifunctional chiral molecules is a promising application of monolithic microreactors. *V. Chirolì et al.* published the first example of a chiral organocatalyst immobilized on a monolithic reactor. Radical copolymerization of divinylbenzene and a properly modified, enantiomerically pure imidazolidinone inside a stainless-steel column in the presence of dodecanol and toluene (porogens) afforded the first example of a chiral organocatalyst immobilized onto a monolithic reactor. For cycloadditions between cyclopentadiene and cinnamic aldehyde under continuous-flow conditions, up to 90% ee at 25 °C and productivities higher than 0.3 mol(product) h⁻¹ mol(catalyst)⁻¹ were achieved [165].

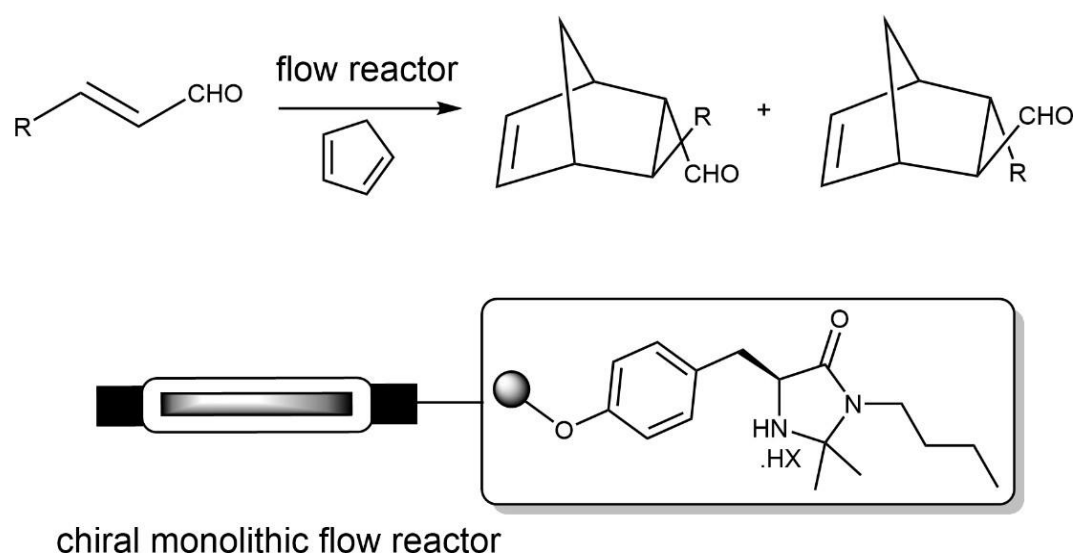


Figure 21: Enantioselective Diels-Alder reactions with different substrates under continuous-flow conditions catalyzed by imidazolidinone supported catalyst [165].

Metal-organic gels (MOGs) are also promising monolithic materials for catalysis applications and are produced via the assembly of metal ions and organic ligands through metal-organic coordination. Metal-organic gels (MOGs) consist of meso- and macropores for mass transfer and micro-size pores for the immobilization of catalysts. *Zhang et al.* recently described MOGs as monolithic supports for continuous catalysis flow reactions. In this study, fused-silica capillaries were functionalized with carboxyl groups for attachment to the gel monolith, followed by the addition of $[\text{Cr}(\text{NO}_3)_3]$ and 5-aminobenzene-1,3-dicarboxylic acid (H_2ADC) as precursors to develop the CrADC gel. Subsequently, Au NPs were stabilized within the gel monolith via *in situ* reduction, and 95% conversion was achieved in the oxidative coupling of phenylacetylene [166].

1.7 Hydrosilylation of Alkynes

In the last 30 years, functionalized organic and organometallic compounds facilitated new strategies for the development of organic chemistry and chemical technology. Owing to high stability, low toxicity, versatility, and highly selective reactivity towards electrophiles relative to other vinyl-metal species, vinylsilanes and their derivatives are highly valuable building blocks in reactions leading to functionalized organic compounds. The most straightforward, flexible, and powerful approach for the synthesis of vinyl silanes is the transition metal-catalyzed hydrosilylation of alkynes [167]. The silylative coupling reaction was first introduced by *B. Marciniak* in 1984 [168]. The control of regio- and stereoselectivity along the H-Si addition process is a vital parameter for the hydrosilylation of terminal alkynes (Figure 22). The reaction may proceed via *anti*-Markovnikov addition to afford the $\beta(E)$ - and $\beta(Z)$ -vinylsilane stereoisomers, while Markovnikov addition results in the formation of the α -vinylsilane isomer. Additionally, in catalyzed reactions, the formation of dehydrogenative side products, namely alkynylsilane and the corresponding alkene, have been observed.

The Chalk-Harrod mechanism, which is the widely accepted route for the hydrosilylation of olefins, was first proposed for the Pt-catalyzed hydrosilylation of alkenes [169]. In this mechanism, the Si-H oxidative addition of silane to the transition metal complex is followed by the Si – C reductive elimination to release the product. Later, the modified Chalk-Harrod mechanism, was proposed for Rh-, Co-, Fe-, and Ir-

catalyzed hydrosilylations of alkenes and alkynes. In this mechanism, the alkene and (-or alkyne) is inserted into the M-SiR₃ bond, followed by C-H reductive elimination. If β-H abstraction occurs after alkene addition into the M-SiR₃ bond, vinylsilane is produced, whereas vinylsilane is not produced in the Chalk-Harrod mechanism. Thereby, the formation of vinylsilane in the Rh-catalyzed hydrosilylation of alkene is a result of a modified Chalk-Harrod mechanism [169].

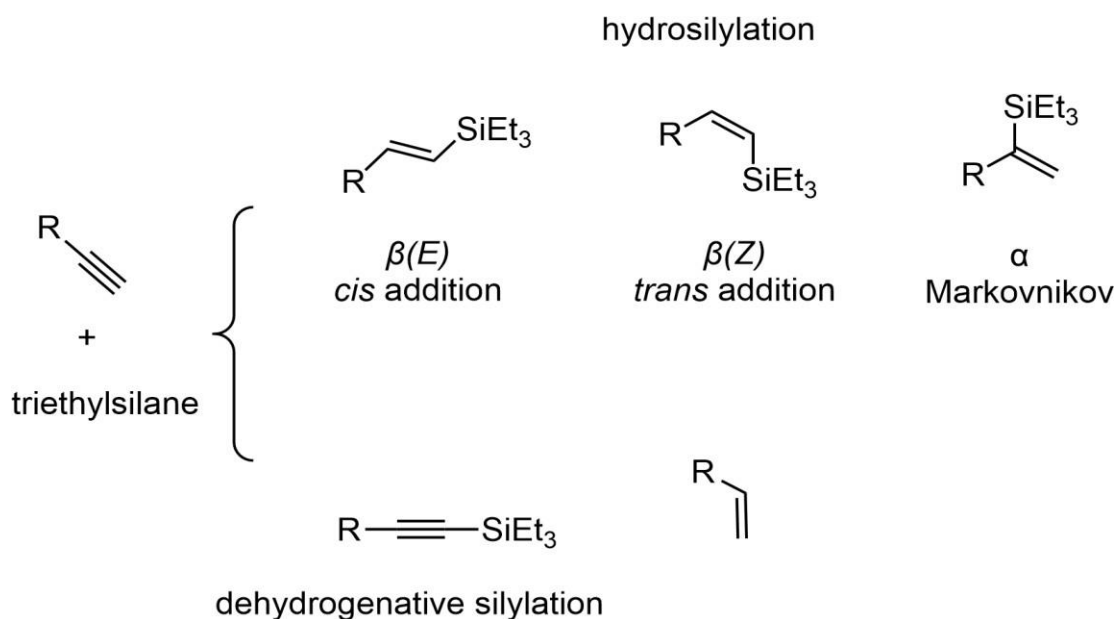


Figure 22: Possible products of the hydrosilylation of terminal alkynes.

The first hydrosilylation process was reported in 1947 [171]. Since then, Pt-based catalysts have dominated this field. Initially, the development of Speier's catalyst (H₂PtCl₆) was a significant advance. Later, *Karstedt et al.* enriched the field by creating a Pt complex with vinyl-siloxane ligands [172]. Today, the lipophilic complex serves as a benchmark catalyst for effective hydrosilylation procedures in the industrial sector. Despite the efficiency of this system, homogeneous Pt-based catalysts have some drawbacks in specific applications [173-175]. Additionally, it has been shown that up to 30% of the cost of silicones is attributed to platinum usage [176]. Therefore, from an industrial perspective, the high price of platinum fuels the need to create recyclable and less expensive catalysts. A long-standing goal of the silicone industry is to replace conventional platinum-based catalysts in alkene hydrosilylations with more affordable and sustainable metals [177,178]. Following this goal, various earth-abundant metal-

based molecularly defined catalysts (Fe, Co, Ni, etc.) have been created in the last ten years [179-182]. Furthermore, the regioselectivity can be controlled by the modification of ligands, leading to anti-Markovnikov or Markovnikov selective products. The resultant silane compounds are commonly employed as silicon fluids and silicon curing agents. The anti-Markovnikov silanes are also crucial molecules for many applications in the life sciences [182,183]. In 2017, *Deng et al.* published the anti-Markovnikov hydrosilylations of aliphatic alkenes with tertiary silanes using cobalt N-heterocyclic carbene (NHC)-catalyst systems [184]. The selective hydrosilylation of mono-substituted aliphatic alkenes with $\text{HSi}(\text{OEt})_3$ to linear products was achieved with a cobalt(II) amide/NHC catalyst system in moderate to very high yields (42-98%). In 2018, *Ge et al.* published a co-catalyzed anti-Markovnikov hydrosilylation of terminal alkynes with both primary and secondary hydrosilanes, $\text{PhR}'\text{SiH}_2$ [185]. A wide variety of alkynes with either aromatic or aliphatic substituents underwent this hydrosilylation process using $\text{Co}(\text{acac})_2$ and dpephos or xantphos as ligands to produce (E)-vinylsilanes in 59–91% yield with strong regioselectivity. *Zhu et al.* recently demonstrated a method for producing geminal bis(silanes) via Fe-catalysed dihydrosilylation of aliphatic terminal alkynes and primary silanes [186]. The corresponding geminal bis(silanes) were the only products of hydrosilylation produced by PhSiH_3 and $n\text{-C}_{12}\text{H}_{25}\text{SiH}_3$ reactions with a variety of aliphatic terminal alkynes, with yields of 85–95%.

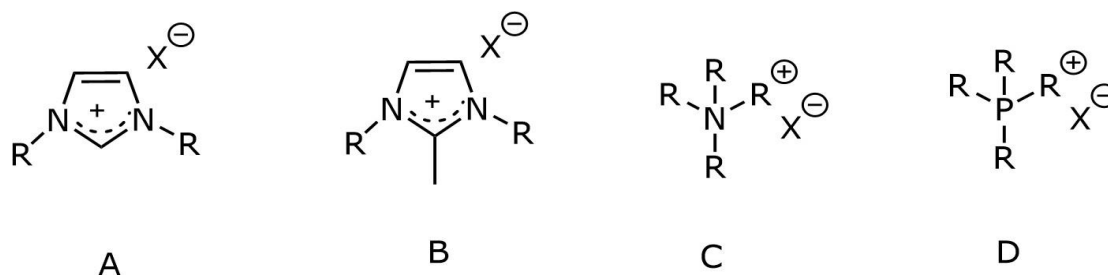
Heterogeneous catalysts can be recycled more easily than homogeneous ones in classical liquid-phase processes. For this reason, a growing number of heterogeneous catalysts have been studied recently. In 2017, *V.meille et.al* published the hydrosilylation of 1-octene with polymethylhydrosiloxane (PMHS) using Pt nanoparticles embedded in silica, mesostructured frameworks. The final products exhibited excellent catalyst turnover ($\text{TON} = 105$) and after recycling, Pt leaching was not detected [187]. Recently, *W.-J. Chun et al.* reported the immobilization of Rh^I complexes and tertiary amines on the surface of SiO_2 ($\text{SiO}_2/\text{Rh-NEt}_2$). $\text{SiO}_2/\text{Rh-NEt}_2$ demonstrated excellent turnover, with TON approaching 1.9 M over 24 h for the hydrosilylation of olefins with a wide range of substrates [188].

Another strategy under investigation in recent years involves the development of biphasic reaction systems with substrates in one phase and ILs in the second phase, in which the catalyst is dissolved. This concept, known as *SILP* catalysis, has been

successfully applied to several hydrosilylation reactions with different metal catalysts. In the following sections, the recent investigations of the *SILP* concept on hydrosilylation reactions are described in detail.

1.8 Ionic Liquids

Ionic liquids exhibit high viscosity, excellent thermal stability, low vapor pressure, and, most importantly, excellent solvation properties for the various polar and non-polar complexes. Owing to their unique properties, ILs have received considerable attention for applications as alternative solvents, particularly in catalysis. They are particularly suitable for activating and carrying out catalytic reactions involving ionic complexes [189,190].



R=alkyl, X = BF₄⁻, PF₆⁻, OTf⁻, Tf₂N⁻

Figure 23: Structures of ionic liquids.

The distinguishing feature of ILs over commercial molecular solvents is the wide temperature range between the melting and boiling points. Ethylammonium nitrate was the first discovered ionic liquid described by *P. Walden* in 1914 [190]. Subsequently, research on developing and characterizing novel ionic liquids increased rapidly.

In 1982, *J. S. Wilkes et al.* studied the ionic liquid system 1-ethyl-3-methylimidazolium chloride ([EMIM]Cl) + AlCl₃. The IL system had a melting point below room temperature and was found to be a suitable electrolyte for battery applications, as well as a good solvent and catalyst for Friedel-Crafts reactions [191]. However, since chloroaluminates are sensitive to moisture, water-soluble anions (i.e., tetrafluoroborate, hexafluorophosphate, nitrate, and sulfate) have been introduced into ILs.

Special attention has been focused on the development of alkyipyridinium-based cations and dialkylimidazolium halogenaluminates salts. ILs based on dialkylimidazolium cations ($[C_n\text{mim}^+]$ for 1-alkyl-3-methylimidazolium cations) are among the most used ionic liquids for solvent extraction. The interaction of these organic cations with fluorinated anions such as bis(trifluoromethylsulfonyl)imide (NTf_2^-) results in hydrophobic ionic liquids. In the application of the supported ionic liquid systems, the chosen ionic liquid within the pores of the solid support must be liquid at room temperature. *Kubota et al.* [192] published the preparation of a liquid membrane using $[C_n\text{mim}][\text{NTf}_2]$ ILs with various alkyl chain lengths. It was found that the membranes were highly selective for rare-earth magnets over iron-based magnets. *Özevci et al.* [193] reported the transport of lanthanum across a supported ionic liquid phase membrane made of a mixture of well-known extractants, tri-n-butyl phosphate (TBP), and $[C_4\text{mim}][\text{NTf}_2]$. The optimum transport rate of La (III) was obtained with a volume ratio of 50%/50% of IL/TBP. As such, the number of reports on ILs as powerful solvents and electrolytes (e.g., in battery and membrane applications) is growing [194].

1.9 Supported Ionic Liquid Phase (SILP) Catalysis

With the promising features of ILs in catalysis, *SILP* technology has gained popularity in chemistry. Application of the *SILP* approach to catalysis can preserve the main advantages of both homogeneous and heterogeneous catalysis, namely high reaction selectivity combined with low catalyst contamination of the products, respectively. ILs can be immobilized on the support's surface via covalent bonding or ionic interactions. In an ideal state, a biphasic liquid-liquid catalytic system must be capable of dissolving the active complex species while being partially miscible with the substrate. The final products should not be soluble in the ionic phase and can be simply removed by the solvents without affecting the catalyst. As an advantage of ILs, physisorption allows the recycling of the support material since the IL can be removed by flushing with polar solvents [195].

Hofmann et al. published a Pt-catalyzed hydrosilylation reaction where the IL phase was used in a continuous loop reactor, allowing for continuous operation for 48 h at constant activity and selectivity and a minimum of Pt leaching. After a series of repetitive batch experiments, the process indicated that the Pt leaching into the product

phase was significantly below 1 ppm. However, considering the mass transport limitations between phases in liquid/liquid processes, recent studies have focused on the investigation of the new possibilities for catalyst immobilization using ILs [196].

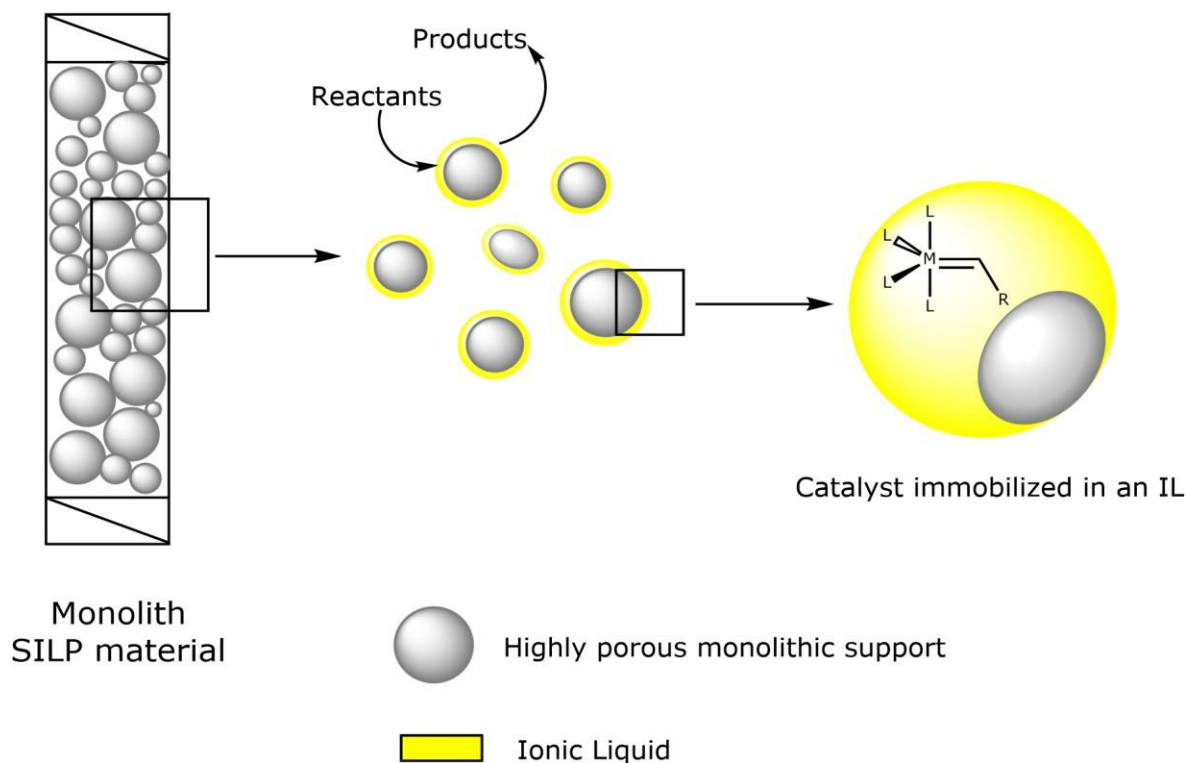


Figure 24: Schematic illustration of the SILP concept.

The adsorption of the catalyst on a highly porous solid substrate is one potential solution for the problem of limited mass transfer and it makes it easier to separate the catalyst after the reaction. In this case, *SILP* materials could be used, where transition metal complexes can be immobilized within a thin layer of IL deposited on a solid support such as silica, active carbon, or other mesoporous materials [197,198]. Due to the solid structure of these materials, the immobilized catalyst can be easily extracted from the reaction mixture, yields can be improved, and significant cost savings realized. Convincingly, *SILP* concept has a great potential for transition metal-catalyzed processes, and recent examples, including hydrogenation, hydrodeoxygenation, hydrosilylation, oxidation of alcohols, reforming of cellulose and many other organic reactions [199,200].

Due to the special properties, (i.e., high surface areas due to pores, high thermal stability of ILs and support material, adjustable solubility of the ILs, and improved mass

transport), *SILP* materials can be considered efficient and reusable catalysts for hydrosilylation reactions. *J. Li et al.* published the production of IL-modified silica using a "one-pot" reaction of activated silica, 3-chloropropyltriethoxysilane, and alkylimidazole or pyridine. The supported catalyst $\text{Rh}(\text{PPh}_3)_3\text{Cl}$ /ionic liquid-modified SiO_2 's catalytic activity and adduct selectivity for the hydrosilylation reaction of alkenes with triethoxysilane was significantly improved. The $\text{Rh}(\text{PPh}_3)_3\text{Cl}$ /modified- SiO_2 catalyst system was easily recovered and reused over ten times without significant loss of catalytic activity or selectivity [201]. In 2012, *M. R. Buchmeiser et al.* reported the ROMP-derived monolith-supported *SILP* system for continuous metathesis reactions. High TON values and exceptionally low catalyst leaching (0.1%) were observed under *SILP* conditions [15]. *R. Kukawka et al.* described slurry-phase hydrosilylation reactions carried out with novel *SILP* catalysts containing Rh-complexes immobilized in four phosphonium-based silica supports. In this work, the Rh-derived *SILP* catalyst proved to be much more efficient than the same catalyst under biphasic conditions. A TON of 74,270,000 was obtained, allowing for a reduction in catalyst amount of up to 1000 times that required in biphasic reactions [200].

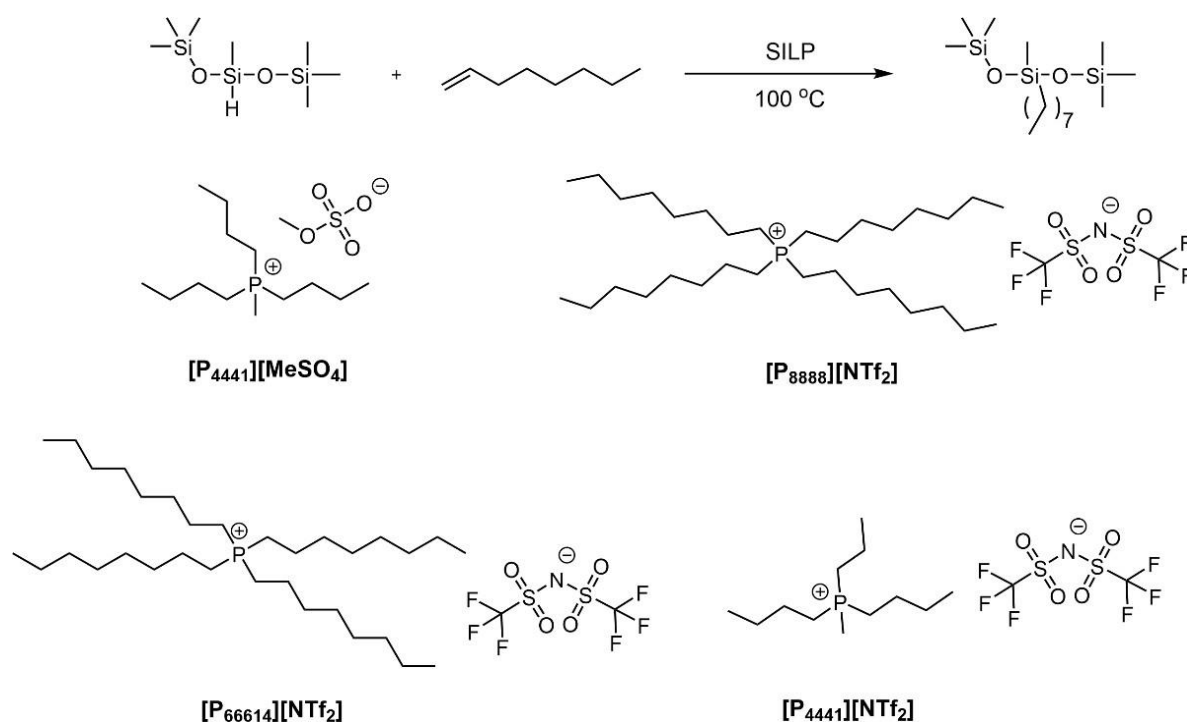


Figure 25: Model reaction of 1,1,1,3,5,5,5-heptomethyltrisiloxane and 1-octene (top) and structures of ILs used in experiments (bottom) [202].

In another study, *R. Kukawka et al.* investigated the synthesis and characteristics of new *SILP* materials and their catalytic activity in a hydrosilylation reaction using 1-octene (1-oct) and 1,1,1,3,5,5,5-heptamethyltrisiloxane (HMTS) as model substrates with three different Rh-catalysts. The most active *SILP* catalyst ($[\text{Rh}(\text{cod})(\text{OSiMe}_3)_2]/[\text{P}_{66614}][\text{NTf}_2]$ supported on silica) had a TOF value of $297,000,000 \text{ h}^{-1}$, allowing a 1000-fold reduction in catalyst amount when compared to biphasic reactions [202].

Chapter 2

2. RESULT AND DISCUSSION

2.1 Tailoring Mesoporosity in Poly(norborn-2-ene)-Based Monolithic Supports

2.1.1 Working hypothesis

Monolithic materials consist of a continuous skeleton with interconnected porosity throughout the column [34]. Aside from porosity, monoliths have large, micrometer-scale transport pores that allow convective flow at low backpressures and high flow rates. Monolithic polymeric supports can be synthesized by using different synthesis techniques. So far, *SIPS* has been used in the *Buchmeiser* research group [33] to synthesize monolithic support materials. *SIPS* allows the preparation of monolithic materials with the desired porosity by choosing the phase separation conditions. At the initial stage of the phase separation process, the polymer chains begin to grow and become insoluble, forming interconnected, porous solid structures. Upon completion of the phase separation, crosslinked surface globules are formed. One of the keys to successful *SIPS* is selecting the right quantity and type of monomers and porogenic systems. The onset of phase separation can be determined by the synthesis parameters and conditions, such as the reaction temperature, solvent mixtures, and degree of cross-linking. The phase separation is governed by the FH interaction parameter (χ_{FH}). According to FH theory [203], temperature and Hildebrand solubility values of the polymerization components are essential parameters to control *SIPS*. The FH theory is a mathematical model to determine the thermodynamics of polymer solutions, which considers the differences in molecular sizes in adapting the expression for the entropy of mixing increments. The phase separation phenomenon in polymer solutions depends on the free energy (ΔG_{mix}) change of the polymer solution. Generally, the microstructure of polymeric monoliths, in terms of porosity and size of the structure-forming microglobules, greatly depends on the onset of phase separation, which is dependent on both the solvents used and the degree of crosslinking at a given monomer conversion. Also, the process requires that phase separation is faster than gelation. According to the FH theory, the entropy term (ΔS_{mix}) is always positive since entropy increases upon mixing, due to the increase in randomness. Thereby, the sign of ΔG_{mix} depends on the magnitude and the sign of the enthalpy term (ΔH_{mix}), which arises from interactions between monomeric units. To

ensure phase separation, the ΔH_{mix} in equation (1) needs to be significantly positive to ensure a positive change in ΔG_{mix} .

The thermodynamic equation for the ΔG_{mix} accompanying mixing at constant temperature and (external) pressure is:

$$\Delta G_{mix} = \Delta H_{mix} - T\Delta S_{mix} \quad (1)$$

Initially, we determine the entropy of mixing which is the rise in uncertainty regarding the locations of the molecules when they are dispersed. When the solute is a macromolecular chain, it becomes impossible to express the entropy of the mixing of small molecules in terms of mole fractions. We assume that individual solvent molecules and polymer segments occupy locations on a lattice to account for the dissymmetry in molecule sizes. Because each site is occupied by exactly one solvent molecule or one monomer of the polymer chain, the total number of sites is: $N = N_1 + xN_2$. N_1 is the number of solvent molecules, and N_2 is the number of polymer molecules, each of which has x segments. We can determine the ΔS_{mix} through a random walk on a lattice. These are also the possibilities that a solvent molecule or a polymer segment will occupy a randomly chosen lattice location. Thus,

$$\Delta S_{mix} = -k[N_1 \ln(\Phi_1) + N_2 \ln(\Phi_2)] \quad (2)$$

Where k is Boltzmann's constant, $\Phi_1 = N_1 / N$ and $\Phi_2 = xN_2 / N$. The volume fractions reduce to molecular or mole fractions for a small solute, resulting in a value of one. As such, molecules occupy only one lattice site, and the entropy of mixing reverts to. In addition to the entropic effect, we can expect an enthalpy change. Solvent-solvent w_{11} , monomer-monomer w_{22} (not through covalent bonding, but between different chain sections), and monomer-solvent w_{12} are the three molecular interactions to consider. In addition to the entropic effect, an enthalpy change is to be anticipated. Each of the interactions occur at the expense of the average of the other two, resulting in an increase in energy per monomer-solvent contact is: $\Delta w = w_{12} - \frac{1}{2}(w_{11} + w_{22})$. The total number of such contacts is: $xN_2 z \Phi_1 = N_1 \Phi_2 z$. Where z is the coordination number, the number of nearest neighbours (chain segment or solvent molecule) for a lattice site. xN_2 is the total number of polymer segments (monomers) in the solution and $xN_2 z$ is the number of nearest-neighbor sites to all the polymer segments. Multiplying the values by probability (Φ_1) that any such site is occupied by a solvent molecule, we

obtain the total number of polymer-solvent molecular interactions. The ΔH_{mix} is equal to the energy change per polymer monomer-solvent interaction multiplied by the number of such interactions; $\Delta H_{mix} = N_1\Phi_2z\Delta w$. The polymer-solvent interaction parameter; $\chi_{12} = z\Delta w / kT$. The enthalpy change becomes:

$$\Delta H_{mix} = kTN_1\Phi_2\chi_{12} \quad (3)$$

In terms of the ΔH_{mix} , the condition for phase separation can be expressed as the χ_{12} and the ΔS_{mix} to mixing. The χ_{12} represents the degree of attraction between the polymer and solvent molecules, while the ΔS_{mix} reflects the increase in disorder that occurs when the two substances are mixed. When the attraction between the polymer and solvent is strong and the increase in disorder is small, the enthalpy of mixing becomes negative, indicating that energy is released when the two substances are mixed. However, when the attraction is weak and/or the increase in disorder is large, the enthalpy of mixing becomes positive, indicating that energy is required to mix the two substances. When the ΔH_{mix} is positive, phase separation occurs.

Assembling terms, the ΔG_{mix} is:

$$\Delta G_{mix} = RT[n_1 \ln \Phi_1 + n_2 \ln \Phi_2 + n_1 \Phi_2 \chi_{12}] \quad (4)$$

Where n_1 and n_2 are molecules N_1 and N_2 converted to moles by transferring the Avogadro constant N_A to the gas constant $R = kN_A$.

The χ_{12} is a measure of the strength of the interactions between the polymer and the solvent molecules and can be calculated using the Hildebrand solubility parameters δ_1 and δ_2 ; $\chi_{12} = V_{seg}(\delta_1 - \delta_2)^2 / RT$ where V_{seg} is the actual volume of a polymer segment. The solubility of a polymer with solubility parameter δ_1 in a solvent with solubility parameter δ_2 is favored when $\Delta\delta = |\delta_1 - \delta_2| / (\text{MPa}^{1/2})$ is minimized. When the interaction parameter is small, it indicates that the polymer and the solvent molecules have a strong tendency to mix with each other and form a single phase, which typically corresponds to high solubility of the polymer in the solvent.

The Hildebrand solubility parameter (δ) is a way of quantifying the cohesive energy density (CED) of the polymer and solvent. The solubility of the polymer in the solvent depends on the degree of similarity or compatibility between the CED s of the two substances. If the CED densities are similar, the polymer and solvent can mix and form

a homogeneous solution. However, if the cohesive energy densities are dissimilar, the mixing process becomes energetically unfavorable, and the polymer tends to separate from the solvent, resulting in phase separation.

2.1.2 ROMP-derived monoliths based on the reaction parameters

According to the hypothesis in 2.1.1, the size of the monolithic pores (d_{pore}) will be slightly larger than that of organometallic catalysts (1 nm), which ensures the confinement of the catalytic center and induces an affinity between the substrate and catalysts. As such, mesoporous materials ($2 < d_{\text{pore}}/\text{nm} < 50$) are the preferable supports over microporous materials ($d_{\text{pore}}/\text{nm} < 2$), due to the small nature of the pores that inhibit anchoring of the catalyst and enable efficient mass transport. Therefore, higher mesoporosity is required for ROMP-derived monolithic supports for catalysis. The aim in this study is to significantly shift the microporosity in the ROMP-derived monolithic structure towards the mesopore region by changing the reaction parameters (i.e., amounts and types of porogens and crosslinkers, type of monomer).

In 2000, *M. R. Buchmeiser* and *F. Sinner* introduced the first ROMP-derived monoliths. The living nature of the ROMP-derived monoliths offers the possibility of using functional monomers [204, 34, 28]. In this study, NBE-derived monoliths were prepared by ROMP using NBE as the monomer, 1,4,5,8,8a-hexahydro-1,4,5,8-exo,endo-dimethanonaphthalene (DMNH6) and $(\text{NBE-CH}_2\text{O})_3\text{SiCH}_3$ as crosslinkers, toluene and THF as the microporogens, and 2-propanol (IPA) as the macroporogen. A co-functional monomer, 5-norbornene-2-methanol, was used for the synthesis of hydroxyl-functionalized ROMP-derived monolithic supports. Table 1 includes a summary of the reagents. The pore-size distribution of the ROMP-derived monolithic supports was adjusted via the selection of a varying toluene:IPA ratio, while all other manufacturing parameters remain the same.

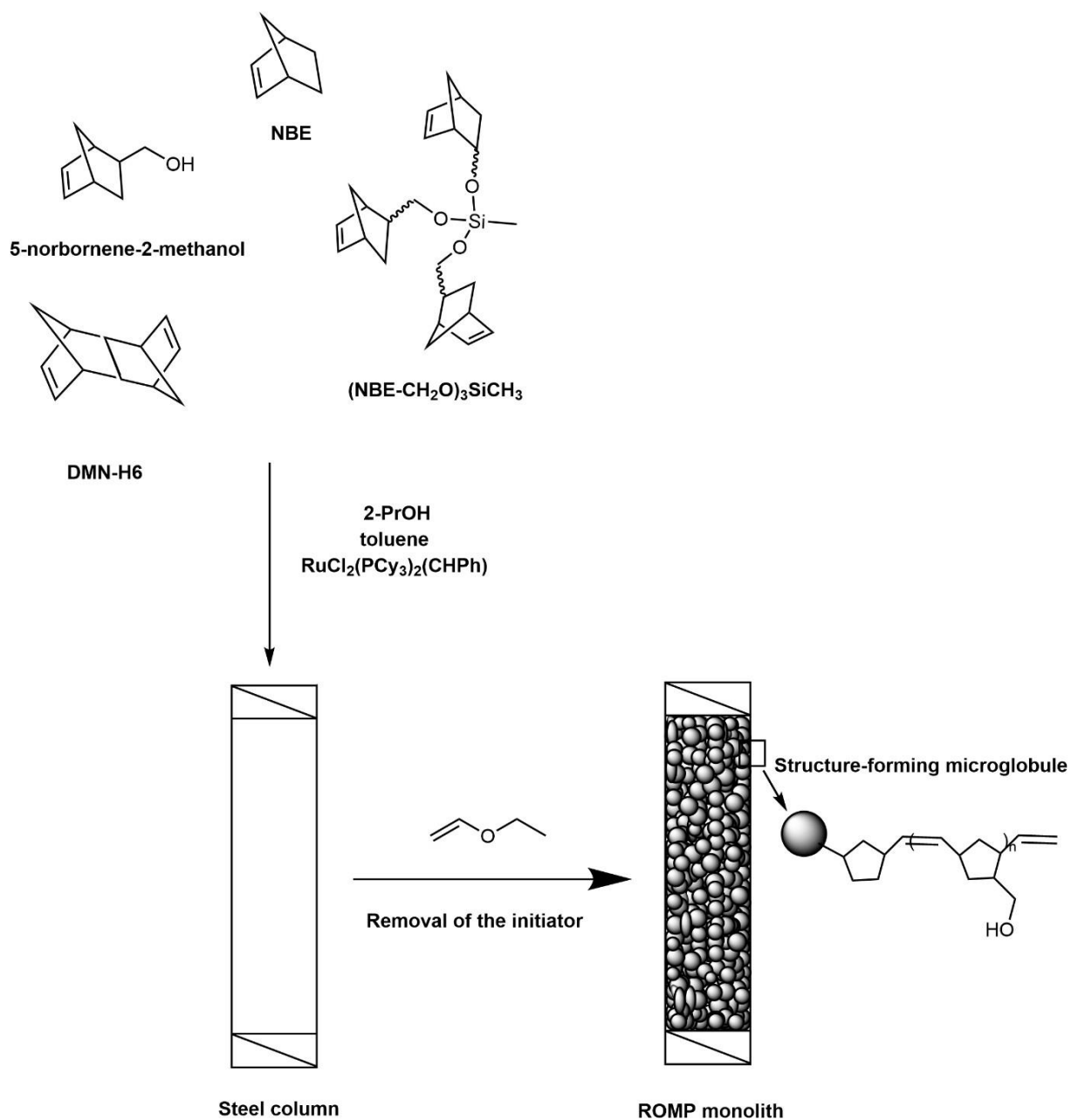


Figure 26: ROMP-derived monoliths using NBE as monomer, DMNH6 and (NBE-CH₂O)₃SiCH₃ as crosslinkers, toluene as microporogen, and 2-propanol as macroporogen.

Table 1: Physicochemical data for the ROMP-derived monoliths N1 - N7; 1: Grubbs' 1st-generation catalyst, CL-1; DMNH₆, CL-2; (NBECH₂O)₃SiCH₃.

#	Polymerization mixture [wt.-%]							
	NBE ¹⁾	NBE- CH ₂ OH ¹⁾	CL-1 ¹⁾	CL-2 ¹⁾	1 ¹⁾	Toluene ¹⁾	THF ¹⁾	2-Pr-OH ¹⁾
N1	22	-	11	11	2.3	2.9	-	50
N2	22	-	11	11	2.3	4.4	-	49
N3	22	-	11	11	2.3	11	-	42.3
N4	22	-	11	11	2.3	-	11	42.3
N5	22	-	11	11	2.3	-	17.6	35.7
N6	20	2	11	11	2.3	11	-	42.3
N7	20	2	11	11	2.3	-	11	42.3

¹⁾wt-%.**Table 2:** Physicochemical data for ROMP-derived monoliths, values for the pore volume, V_p ; the specific surface area, σ ; the volume fraction of pores, ϵ_p ; the volume fraction of intermicroglobule void volume (interstitial porosity), ϵ_z , and the total volume fraction, ϵ_t .

Structural data				
V_p [mL/g]	σ [m ² /g]	ϵ_p [%] ¹⁾	ϵ_z [%] ¹⁾	ϵ_t [%] ¹⁾
0.004	1.650	8	19	27
0.004	2.463	7	20	27
0.011	5.994	14	55	69
0.011	6.526	13	49	62
0.010	5.902	9	59	68
0.010	6.369	12	58	70
0.011	7.869	11	68	79

¹⁾Determined by ISEC in CHCl₃, flow rate: 2.0 mL/min, 35 °C, column: 8 x 300 mm.

ROMP-derived monolithic supports possess a substantial fraction (90%) of micro- and mesopores, as evidenced by ISEC [41] and N₂ sorption measurements [42]. By considering the elution volumes (V_e), the percentage of mesopores contributing to the total porosity of the monolithic columns is found to be constant and amounts to approx. 20%. Under *SIPS* conditions, the ISEC-distribution of the ROMP-derived monoliths makes it clear that micropores make up 70% of the structure of the monolithic support. As can be deduced from Table 2, the ϵ_p and the ϵ_z varied from 7-14% and 19-68 %, respectively. The different values for the ratio ϵ_p/ϵ_z are a consequence of the poor size distribution of the monolithic structure and result in improved discrimination of different molecular weights. Notably, a mixture of DMNH6 and (NBE-CH₂O)₃SiCH₃ allowed for sufficiently crosslinked and long-term stable monoliths during monolith synthesis. Monolith synthesis depends greatly on phase separation, which is dependent on both the precipitation and the cross-linking of growing polymer nuclei in solution. Many cross-linked microglobules are formed and precipitate at an early stage in the reaction, and their high cross-link density leads to a low probability of coalescence between globules as they continue to polymerize, resulting in smaller pore sizes. BET analysis found the specific surface area (σ) to be in the range of $1.65 < \sigma < 7.87 \text{ m}^2/\text{g}$ and pore volumes in the range of 0.004 - 0.011 mL/g (V_p). This increase in V_p coincides with an increase in σ (Table 2). Monoliths **N3 - N7** were characterized by higher pore volumes and specific surface areas than those in monoliths **N1 and N2**, which correlates with the increased microporogen concentration.

Adding a good solvent (*i.e.*, toluene, solvates free monomers) to the monomers lowers the local monomer concentration and this translates into early onsets of phase separation, into a large number of small nuclei as well as in a reduced capability of swelling of the formed nuclei with solvent and/or monomer. As shown in Figure 27, for monoliths, **N1**→**N2**, ISEC distribution confirmed the increase in microporogen concentration from 2.9 wt.% to 4.4 wt.% and the increase in ΔR from 2.6% to 3.7% in the 2.71 nm to 5.29 nm range (Figure S10). Further increments of toluene (11%) in the monolith formulation (**N3**) led to an increased mesoporosity (ΔR :7.3 %) in the range of 2.7 nm–5.64 nm (Figure S12). By changing the type of microporogen, from toluene to THF, while keeping the same monomer content, **N3**→**N4**, the ϵ_z decreased from 55 to 49, as well as the ΔR of the mesopores decreased from 14.9% to 11.6% in the range of 2.03–5.64 nm. (Figure S12), thus demonstrating that toluene produces improved microporogen qualities over THF.

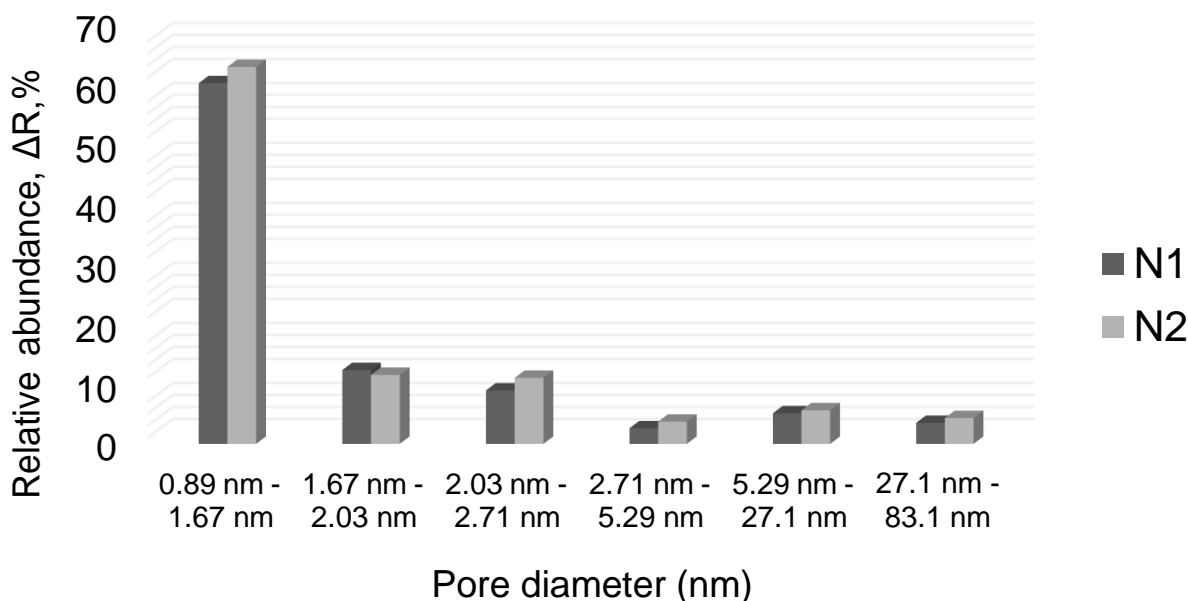


Figure 27: ISEC-derived distribution (relative abundance ΔR , %) of pore diameters (nm) of the ROMP-derived N1; N2.

According to the FH theory, the *SIPS* process can be controlled by temperature and the differences in the Hildebrand solubility parameters of 2-propanol ($\delta=23.8 \text{ MPa}^{1/2}$), toluene ($\delta=18.2 \text{ MPa}^{1/2}$), THF ($\delta=18.5 \text{ MPa}^{1/2}$), NBE- CH_2OH ($\delta\approx 19.5 \text{ MPa}^{1/2}$) as well as those of NBE and the crosslinkers content ($\delta\approx 16 \text{ MPa}^{1/2}$). As we mentioned earlier, the tendency for phase separation in a polymer-solvent system depends on the solubility parameter of the polymer and solvent. If the solubility parameter of the solvent is close to that of the polymer, the system will be more homogeneous and less likely to undergo phase separation. However, if the solubility parameter of the solvent is significantly different from that of the polymer, the system is more likely to undergo phase separation. The statement suggests that the better solubility of NBE and the crosslinkers in toluene compared to THF. This difference in solubility can affect the phase separation behaviour of the system. Hereby, when we use toluene as a microporogen, the concentration of the monomers and crosslinkers in the solution can reach the critical level for earlier onset phase separation in the polymerization process, leading to smaller pore dimensions in the final material.

Depending on the solubility parameters between the polymer and solvent, if the microporogen reaches a critical level, gel structures occur rather than phase separation. When a polymer network is formed, the polymer chains are usually in a swollen state, where the chains are expanded or separated from each other by a solvent or swelling

agents. This swelling allows the chains to move more freely and to occupy a larger volume, resulting in more porous structures. However, if the solvent or swelling agent is removed or evaporated, the polymer chains begin to pack more tightly together, which can lead to a more compact packing of the polymer chains and a lower porosity or gel structure. In the case of the ROMP-derived monolith, the critical amount of the IPA is important to expand or separate the polymer chains from each other for the porosity. Thus, the amount of toluene in the formulation can only be increased to 11% (Table 1). In the case of **N5**, increasing the amount of THF from 11% to 17.6%, **N4**→**N5**, caused the mesopores (ΔR) to decrease from 11.6% to 10.4% in the 2.03 nm to 5.64 nm range, while the micropores (ΔR) to increase from 74 to 77 (Figure S12;14) and a decrease from 6.52 to 5.90 m²/g in the surface area as well.

Other ways to control the porosity include changing the type of monomer. The hydrophilicity of the monomer and its degree of solvation in the porogenic solvents contribute greatly to the morphology of the monolith, and the resulting core monolith structure can be altered significantly with changes in monomer functionality. According to the FH theory, the solubility of a polymer with a solubility parameter δ_1 in a solvent with a solubility parameter δ_2 is favored when $\Delta\delta = |\delta_1 - \delta_2|$ (MPa^{1/2}) is minimized. This promotes the lower required energy (ΔH) to mix the components and creates more homogeneous structures. Adding 5-norbornene-2-methanol ($\delta \approx 19.5$ MPa^{1/2}) to the formulation (**N3**→**N6**) lowers the solubility parameter ($\Delta\delta$) and increases the solubility of the NBE-derivative monolith ($\delta \approx 16$ MPa^{1/2}) in toluene ($\delta = 18.2$ MPa^{1/2}). ISEC distribution confirmed the increase in the ΔR from 14.9% to 17.5% in the 2.03 nm to 5.64 nm range and an increase in the specific surface area (s) from 5.99 to 6.36 m²/g as determined by BET analysis (Figure S12-S16). Comparing the ΔR and s values for the monoliths **N6** and **N7** reveals that the latter has a greater specific surface area of 7.36 m²/g and a higher relative abundance (ΔR ; 18.6%) in the 2.03 nm to 5.64 nm range (Figure 28). Adding 5-norbornene-2-methanol ($\delta \approx 19.5$ MPa^{1/2}) to the formulation increases the polarity in the monolithic structure and using THF as a microporogen (**N7**) can cause swollen polymer chains and lead to increased porosity.

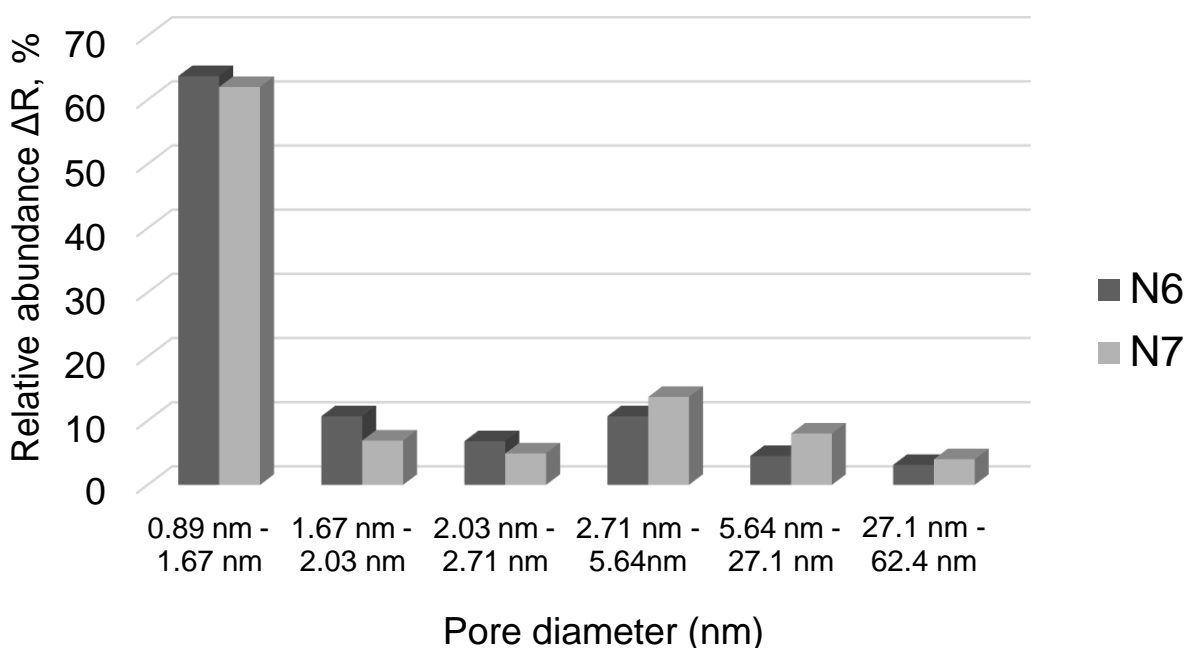


Figure 28: ISEC-derived distribution (relative abundance ΔR , %) of pore diameters (nm) of the ROMP-derived N6; N7 monoliths.

Production of monolithic capillary columns is remarkably simple. Either a bare or a surface-treated capillary is filled with a homogeneous polymerization mixture. The polymerization is initiated upon a thermostatic or ice bath to produce a rigid, monolithic porous polymer. Once the polymerization is complete, unreacted components such as the porogenic solvents are removed from the monolith using a syringe pump. There are many benefits to using this straightforward technique to synthesize monolithic capillary columns. For instance, the fused silica tubing may be used either directly as supplied without any chemical modification or after its functionalization with a suitable vinyl-containing moiety. All the chemicals may be used exactly as they are provided; however, proper purification improves batch-to-batch reproducibility.

In the case of column-to-column reproducibility, the pore size distribution effectively did not change, but larger differences were found for the retention times. The retention time increased based on number of injections (i.e., first injection of a PS standard produced a lower retention time peak than the second injection of the same PS standard). During the first injection of the PS standard, the standard blocks the corresponding pores causing increased retention time for the second injection. Because of this, the used column needs to be flushed with a solvent that can dissolve the PS standard

before subsequent injections. As previously stated, when calculating the elution volumes of the all-injected PS standards, there was no change in the relative pore size distribution even after the second injection throughout the columns.

2.1.3 ROMP-derived monoliths using Pluronic F-127 as an additive

Adding additives to polymer solutions is one of the most powerful strategies for controlling the pore structure of polymeric materials. In this study, the effect of a triblock copolymer, F-127, as an additive for ROMP-derived monolith formation was studied by examining the characteristics and performance of the resulting monoliths. ROMP-derived monoliths were prepared using NBE as monomer, DMNH6 and trimethylolpropane-tris-(5-norbornene-2-yl-carboxylate (TMPTNC) as crosslinkers, toluene as microporogen, and 2-propanol as macroporogen. A triblock copolymer, F-127, was used as an additive in the monolithic formulation.

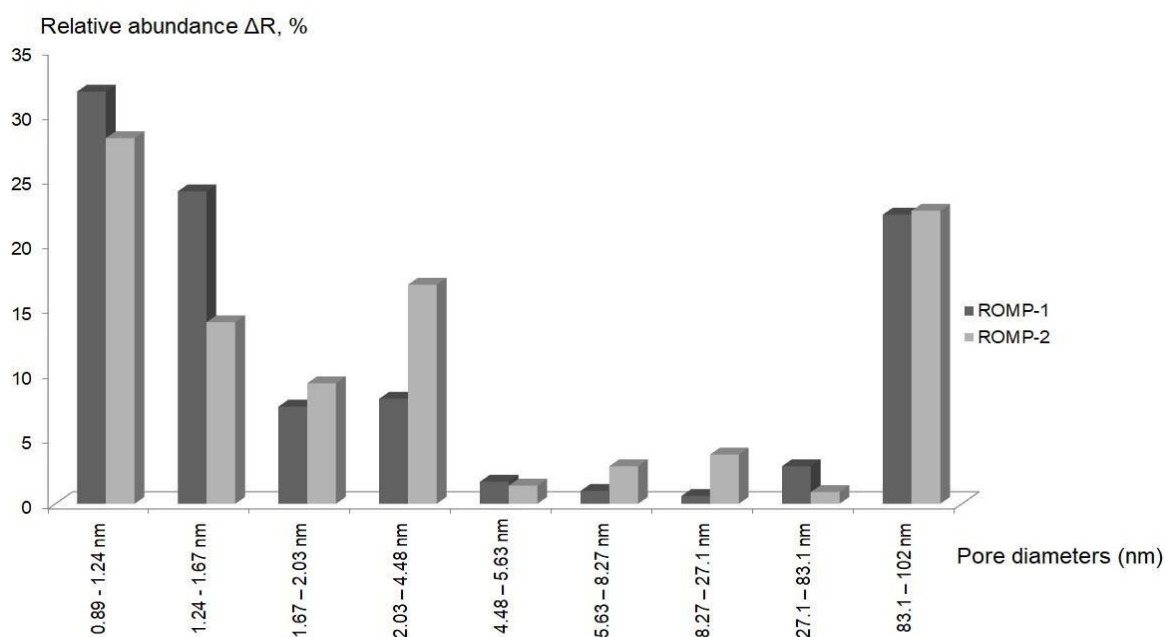


Figure 29: ISEC-derived distribution (relative abundance ΔR , %) of pore diameters (nm) of the surface-functionalized ROMP-derived monolithic supports. ROMP-1: 0.89 - 1.24 nm (ΔR : 31.8 %), 1.24 - 1.67 nm (ΔR : 24.1 %), 1.67 - 2.03 nm (ΔR : 7.5 %), 2.03 - 4.48 nm (ΔR : 8.1 %), 4.48 - 5.63 nm (ΔR : 1.7 %), 5.63 - 8.27 nm (ΔR : 1 %), 8.27 - 27.1 nm (ΔR : 0.6 %), 27.1 - 83.1 nm (ΔR : 2.9 %), 83.1 - 102 nm (ΔR : 22.3 %). ROMP-2: 0.89 - 1.24 nm (ΔR : 28.2 %), 1.24 - 1.67 nm (ΔR : 14 %), 1.67 - 2.03 nm (ΔR : 9.3 %), 2.03 - 4.48 nm (ΔR : 16.9 %), 4.48 - 5.63 nm (ΔR : 1.4 %), 5.63 - 8.27 nm (ΔR : 2.9 %), 8.27 - 27.1 nm (ΔR : 3.8 %), 27.1 - 83.1 nm (ΔR : 0.9 %), 83.1 - 102 nm (ΔR : 22.6 %).

When a surfactant such as Pluronic is added to a polymer solution, it can act as a micelle-forming agent. Micelles are tiny aggregates of surfactant molecules that have a hydrophilic "head" and a hydrophobic "tail." In a polymer solution, the hydrophobic tails of the micelles can interact with the hydrophobic regions of the polymer, causing them to form micelle-polymer complexes. These micelle-polymer complexes can act as nucleation sites for the formation of pores in the polymer matrix. As the polymer solution solidifies, the micelle-polymer complexes can be trapped in the solid, forming channels and pores. This can result in an increase in porosity in the final material. As shown in Fig. 29, it is confirmed that the inclusion of the Pluronic F-127 (2.5 wt.%) in the monolith composition shifts the pore size distribution of the entire monolith to the mesopore region; this impact is particularly noticeable for pore sizes between 2.03 nm-4.48 nm.

However, the structure of the ROMP-derived monoliths is primarily composed of micropores (55% frequency), with small mesopores making up roughly 15% of the total. Furthermore, macropores (83 nm–102 nm) outside the mesopore range occur with a frequency of 20%. ISEC data is listed in Table 3 and summarizes the values for the ϵ_p and the volume fraction of the ϵ_z . The presence of Pluronic F-127 (2.5 wt.%) in the monolith composition resulted in a very slight decrease in the ϵ_z and ϵ_T , which were 56% and 74%, respectively, indicating that the number of μm -range pores increased due to the accumulated Pluronic surfaces.

Table 3: Physicochemical data for ROMP-derived monoliths. Mobile phase: CHCl_3 , Flow Rate: 0.5 ml/min, Temperature: 35 °C, Column: d x l: 4.6 x 150 mm ($V_{\text{column}} = 2.49$ mL).

#	Polymerization mixture [wt.-%]							Structural data		
	NBE	NBE- CH ₂ OH	CL	IPA	Toluene	Grubbs ^{1t} Catalyst	Pluronic F-127	ϵ_p vol.-%	ϵ_z vol.-%	ϵ_t vol.-%
ROMP-1	20	0.8	21.8	40	14.5	1.1	-	0.18	0.60	0.78
ROMP-2	20	0.8	21.8	38	14.5	1.1	2.5	0.18	0.56	0.74

CL; DMN-H6, TMPTNC (1:1).

2.1.4 Summary and Outlook

By utilizing the living character of ROMP, we prepared NBE-derived monoliths with high linear flow rates (up to 8 mm/min) and low counter pressure (<9 bar). The preparation method for ROMP-derived monoliths, which is based on *SIPS*, is straightforward, regardless of batch size. Furthermore, this method is a highly effective route to the synthesis of durable monolithic supports. By varying the ratio and type of compounds used to prepare the monolithic support (i.e., the monomer, the crosslinker, the initiator, and the porogenic solvents). ROMP monoliths facilitate pore size distribution with pore sizes in the range of 2–10 nm. Most importantly, a precise control of the porosity, in particular pore dimensions, was achieved by exposing the synthesis mixtures to different amounts of microporogens. Increases in microporogen concentration from 2.9 wt. % to 11 wt. %, keeping the monomer content constant, increased the ϵ_p from 8 to 14, and improved the specific surface areas to the range of $1.65 < \sigma < 5.99 \text{ m}^2/\text{g}$ and pore volumes in the range of 0.004 - 0.011 mL/g. The degree of solvation of the monomers in the porogenic solvents and their hydrophilicity both had a significant impact on the morphology of the monoliths, and the resulting monolith porosity can be altered significantly with changes in monomer functionality. Adding 5-norbornene-2-methanol (2 wt. %) to the monolith formulation caused the pore size distribution to shift to smaller pore sizes between 2.7 and 5.6 nm and resulted in increased surface areas in the range of 6.36 m^2/g to 7.86 m^2/g . The inclusion of the surfactant Pluronic F-127 as an additive increased mesoporosity in the range of 2.0 - 4.4 nm. However, it is evident that ROMP-derived monoliths are predominately made up of micropores (55–70%), while the frequency of small mesopores is in the range of 15-20%. In addition, 5–20% of the monolith were macropores. In another study, the hard-templating technique was applied to raise the frequency of mesopores.

2.2 A Hard-Templating Approach to Functional Mesoporous Poly (Norborn-2-ene)-Derived Monolithic Supports

2.2.1 Introduction

Recently, OMMs have been the subject of substantial scientific interest in separation science and catalysis [71, 205-209]. In the field of molecular heterogeneous catalysis, the catalyst must be accessible to the reactants. Micropores are often too small to ensure the effective diffusion of reactants or to immobilize a catalyst; on the other hand, macropores are too large, leading to no significant differences in comparison to homogeneous catalysis. Given the dimensions of typical organometallic catalysts (*approx.* 1.5 nm), it is possible that the selective binding of a catalyst in the mesopores of a support material would provide a sufficient level of confinement to create constrained conditions during catalytic reactions [210,211]. This theory emphasizes the current need to develop OMMs.

In this respect, due to their regular, continuous pore arrangement, mesoporous monolithic materials are likely to help illuminate the role of confinement in catalytic activities and the development of a robust model. However, because of their lack of porosity, monolithic materials seen limited use in confinement research and catalytic applications. Recently, though, hard-templating approaches have been utilized; for such an approach, the incorporated template (i.e., silica, alumina) is etched via calcination, chemical etching, or extraction [55-64]. Based on the original hard templates, the resulting porous structures have well-defined, ordered porous architectures.

In this work, a similar principle is applied to polymeric, monolithic materials. These materials can be produced by using the *SIPS* synthesis technique. Accordingly, the first section of this work focuses on the homogeneous distribution of SiO₂ nanowires throughout the monolithic matrix with systematic variations in the reaction parameters. Submicrometric SiO₂ nanowires (d x l: 10 nm x 200 nm) were employed as a hard template for the synthesis of continuous monolithic structures. We demonstrated the synthesis of surface-embedded silica-ROMP hybrid monoliths by adjusting the porogen-to-monomer ratio. The existence of the surface-functionalized SiO₂ nanowires was observed using transmission electron microscopy (TEM) and scanning electron

microscopy (SEM) analyses. Energy dispersive X-ray (EDX) analysis was used to confirm the homogenous distribution of surface-functionalized SiO₂ nanowires within the ROMP-derived monolith matrix. During the second step, the SNWs were removed from the surface of the monolith without any mechanical deformation using *in situ* chemical etching. ISEC and N₂-sorption were used to analyze the pore size distribution of the polymeric monoliths. Ultimately, an uncomplicated manufacturing process was developed in which the pore diameter could be predicted by changing a single parameter while all the other properties of the material remained comparable.

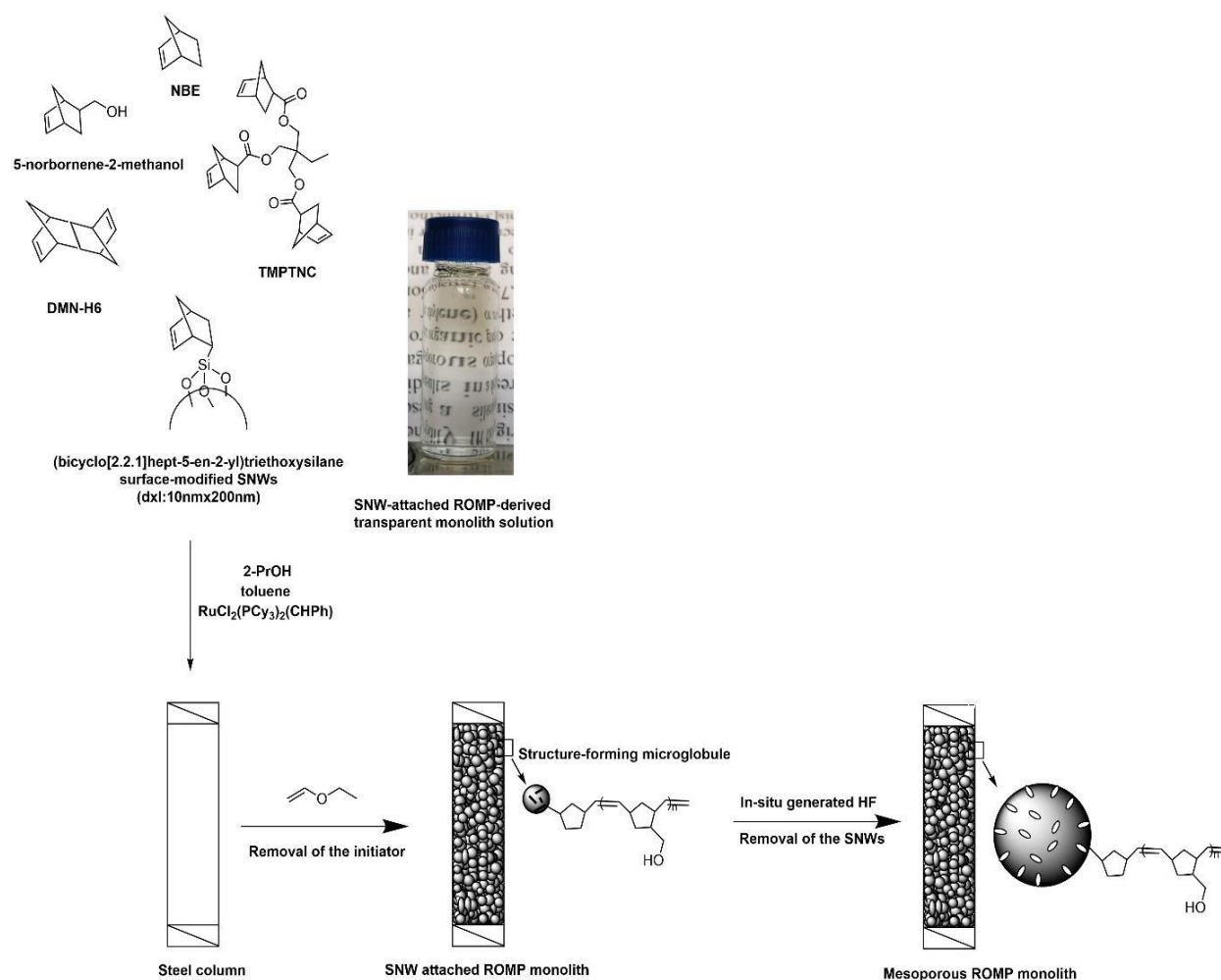


Figure 30: Monolith synthesis using a transparent polymerization mixture with fully dispersed SNWs.

2.2.2 Results and Discussion

Since living polymerization allows for *in situ* surface functionalization, ROMP proved to be particularly useful for preparing non-porous monolithic supports [28,108]. That way, surface-grafted functional group loadings of up to 1 mmol g^{-1} were accessible. However, recent studies on molecular heterogeneous catalysis demonstrated that ordered, mesoporous monolithic supports are urgently needed. The purpose of this research was to create the first ROMP-derived, poly(norborn-2-ene)-based monolithic supports with tailored mesoporosity via a hard-templating approach based on SiO_2 nanowires that would allow access to defined mesopores.

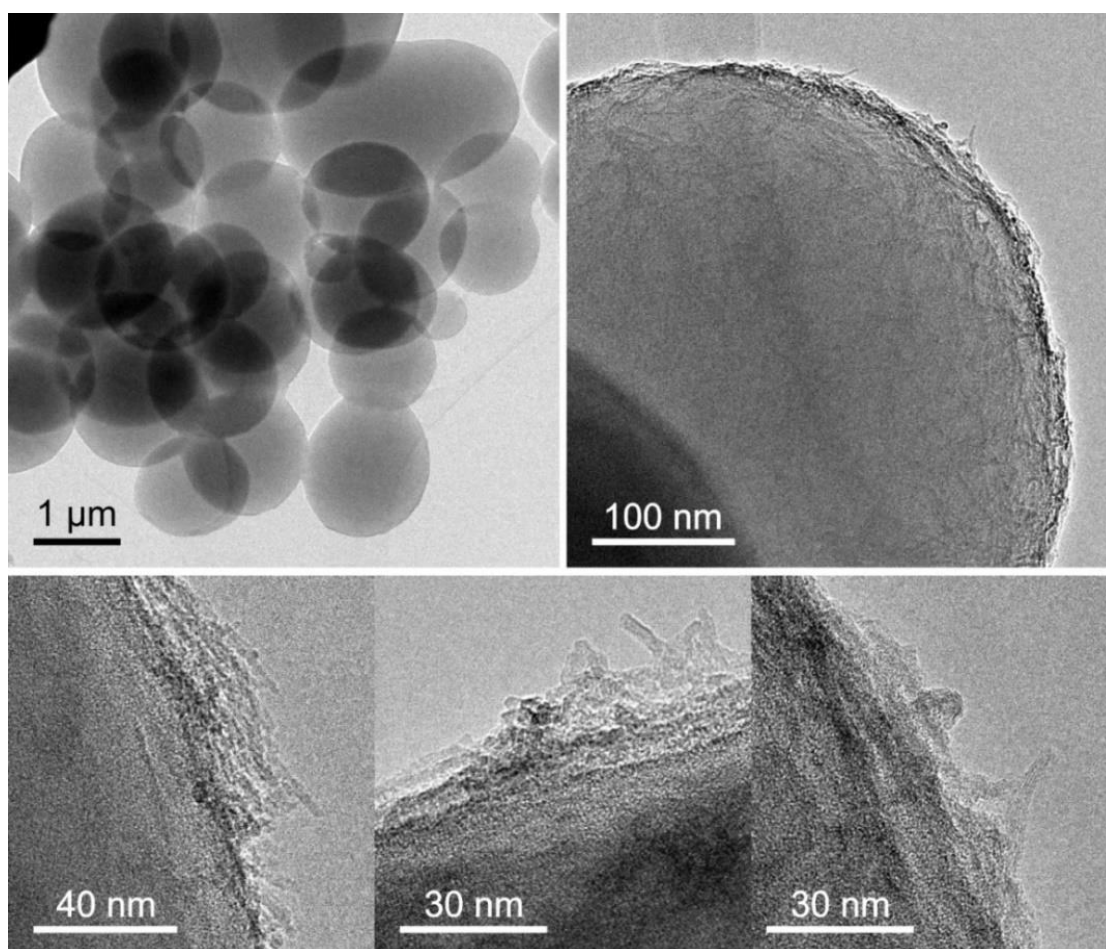


Figure 31: TEM images of the ROMP-derived monoliths containing $\text{AlO}(\text{OH})$ nanowire ($d \times l : 4 \text{ nm} \times 1 \mu\text{m}$) solution.

For the characterization of porous structures, pores must have specific dimensions in diameter and length. Thus, the nanomaterial must be chosen according to special sizes. The chosen nanomaterial must end up inside the structure-forming microglobules. For this purpose, ROMP-derived monolithic supports were synthesized

using NBE as the monomer, DMNH6 and $(\text{NBE-CH}_2\text{O}_3)_3\text{SiCH}_3$ as crosslinkers, toluene as a microporogen, and ethanol and 2-propanol as macroporogens. AIO(OH) nanowire (d x l : 4 nm x 1 μm) (~2 w.t%) dispersion in ethanol was used in the formulation as a hard-templating material. The TEM studies revealed the ROMP-derived monoliths with the AIO(OH) nanowires (d x l : 4 nm x 1 μm), as shown in Figure 31. On the surface of the structure-forming microglobules, it is easy to see that there are long, vein-like nanostructures. Regarding that, this study aimed to arrange these nanowires into the microglobules in a vertical position, but the controllability rate was exceptionally low. On the surface of the microglobules, there is an assembly of SiO_2 nanowires in both horizontal and vertical positions, as well as an accumulation of nanowires. Elemental EDX mapping is presented in Figure 32. The main constituents (namely, C and O) of the monolithic structure were successfully detected. During *SIPS*, AIO(OH) nanowires became immobilized within the monolithic structure. However, the polarity differences between the surface microglobules and the nanowires led to the accumulation of nanowires on the microglobule's surface. Since microglobules were mainly made of carbon (C), the given signal was much stronger than the signal for aluminum (Al) inside the microglobules (Point-analysis 3). In contrast, the accumulation of Al on the surface of the microglobule led to an increased Al signal intensity (Point-analysis 2), that indicated that a certain amount of Al nanowires was located inside the structure-forming microglobules.

The surface-modified AIO(OH) nanowire was removed using a continuous flow of acetic acid (5% wt.) solution at room temperature. As depicted in Figure 33, porous ROMP-derived monoliths were obtained that contained both micrometer-sized transport pores and micropores in the range between 1 nm and 5 nm, as evidenced by ISEC [204]. Since ISEC measurements are generally carried out under wet conditions, the non-permanent microporosity (<1 nm) became visible due to the swelling of the support during the mobile phase. Depending on the diameter of AIO(OH) NWs, a loading of 11 wt.% relative to the total polymerization mixture resulted in an increased mesopores ($\Delta R:6\%$) in the 2.03-5.29 nm range. However, because a higher concentration of porogen in the formulation led to the deterioration of the mechanical properties of the monolithic structure, the solution state of the suspended AIO(OH) nanowires limited the use of a higher concentration of nanowires in the monolithic formulation.

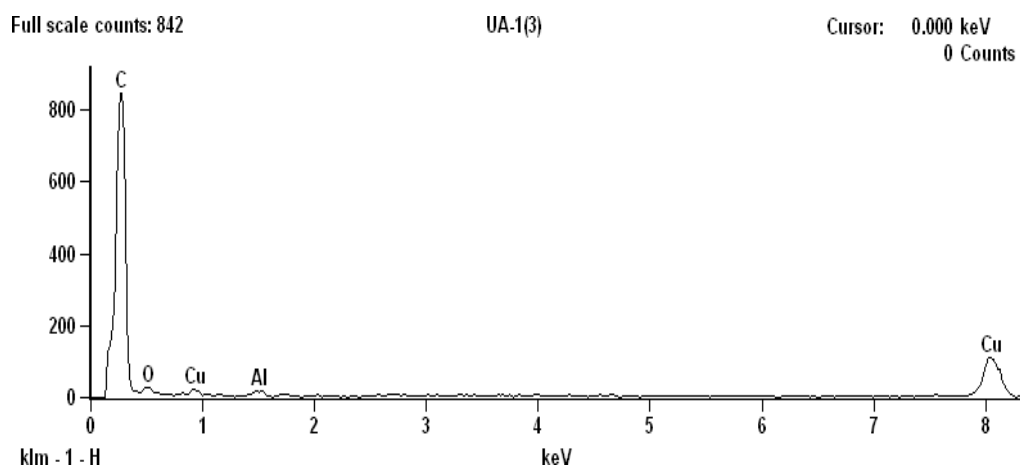
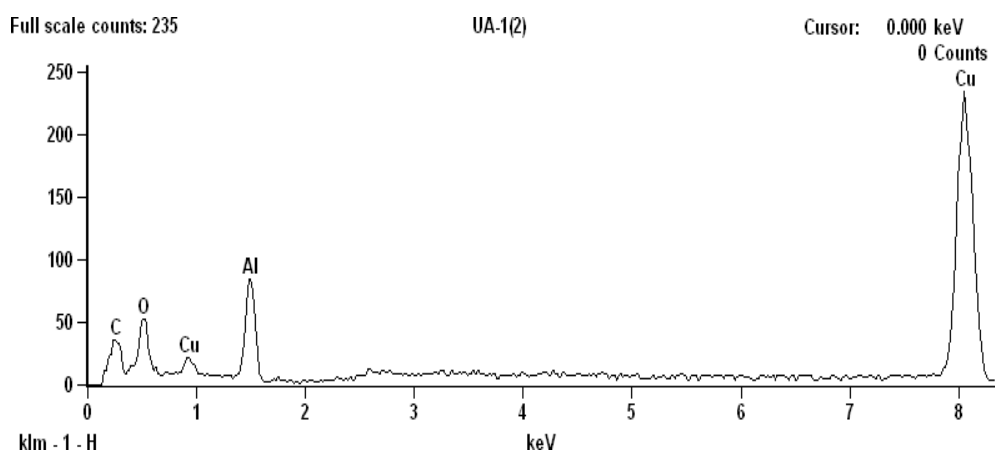
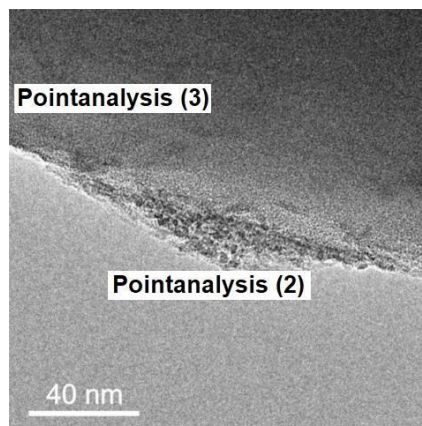


Figure 32: The EDX analysis of the ROMP-derived monolith with AlO(OH) nanowires.

Table 4: Physicochemical data for AlO(OH) nanowire-containing ROMP-derived monoliths. Mobile phase: CHCl₃. Flow Rate: 0.5 ml/min. Temperature: 35 °C, Column: d x l: 4.6 mm x 150 mm (V_{column} = 2.49 mL).

#	Polymerization Mixture [wt.-%]						Structural Data			
	NBE	NBE-CH ₂ OH	CL	2-Propanol	Toluene	Grubbs ^{1t} Catalyst	AlO(OH) Nanow. [2.5 wt. % in ethanol]	ε _p vol.-%	ε _z vol.-%	ε _t vol.-%
AL-1	20	2	22	30	14.5	2.3	11	0.05	0.60	0.65
AL-2	20	2	22	30	14.5	2.3	-	0.06	0.61	0.67

CL; DMNH₆, (NBECH₂O)₃SiCH₃ (1:1).

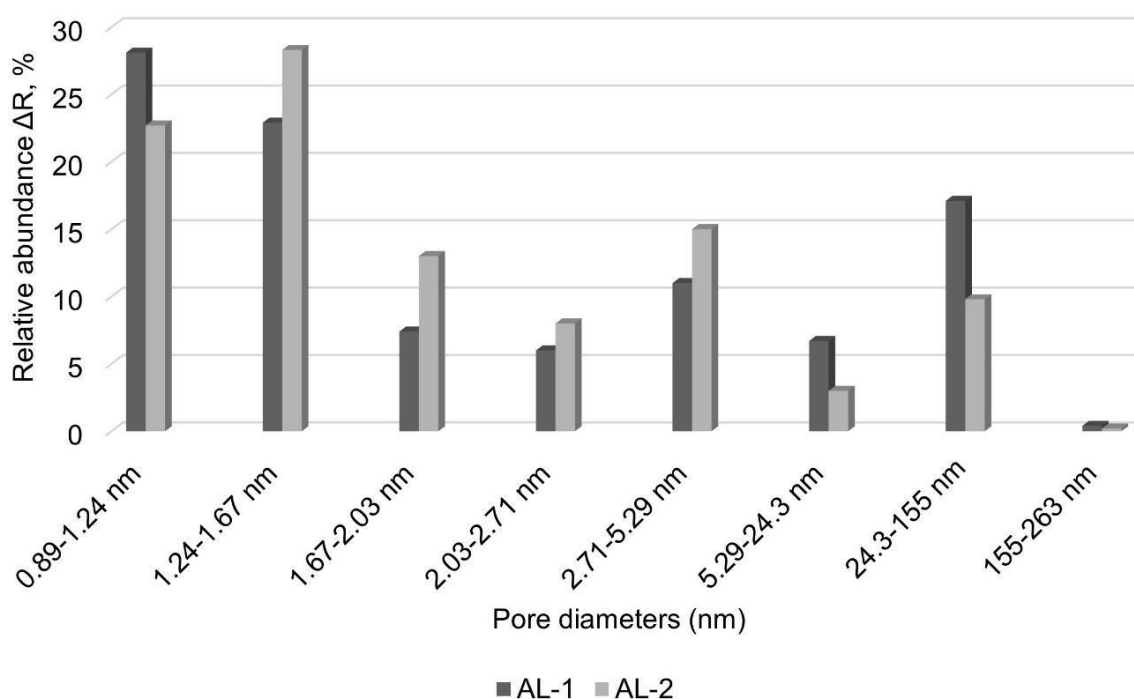


Figure 33: The ISEC-derived distribution (Relative abundance ΔR, %) of pore diameters (nm) of the surface-functionalized ROMP-derived monolithic supports: AL-1: 0.89 - 1.24 nm (ΔR: 28.1 %), 1.24 - 1.67 nm (ΔR: 22.9 %), 1.67 - 2.03 nm (ΔR: 7.4 %), 2.03 - 2.71 nm (ΔR: 6.0 %), 2.71 - 5.29 nm (ΔR: 11 %), 5.29 - 24.3 nm (ΔR: 6.7 %), 24.3 - 155 nm (ΔR: 17.1 %), 155 - 263 nm (ΔR: 0.4 %). AL-2: 0.89 - 1.24 nm (ΔR: 22.7 %), 1.24 - 1.67 nm (ΔR: 28.3 %), 1.67 - 2.03 nm (ΔR: 13 %), 2.03 - 2.71 nm (ΔR: 8.0 %), 2.71 - 5.29 nm (ΔR: 15 %), 5.29 - 24.3 nm (ΔR: 3 %), 24.3 - 155 nm (ΔR: 9.8 %), 155 - 263 nm (ΔR: 0.2 %).

Given the numerous benefits of silica-based nanomaterials, such as the ease of surface modification and dimensional variability, silica nanowires (SiO_2 , diameter \times length: 10 nm \times 200 nm) were next chosen as hard templates. Initially, oleic acid (OA), which is an emulsifying agent, was used to modify the surface of the silica nanowires. The effect of the OA emulsifier on the silica nanowires can be seen in Figure 34. The agglomerated silica nanowires became dispersed after the OA-surface modification of the SiO_2 nanowires.

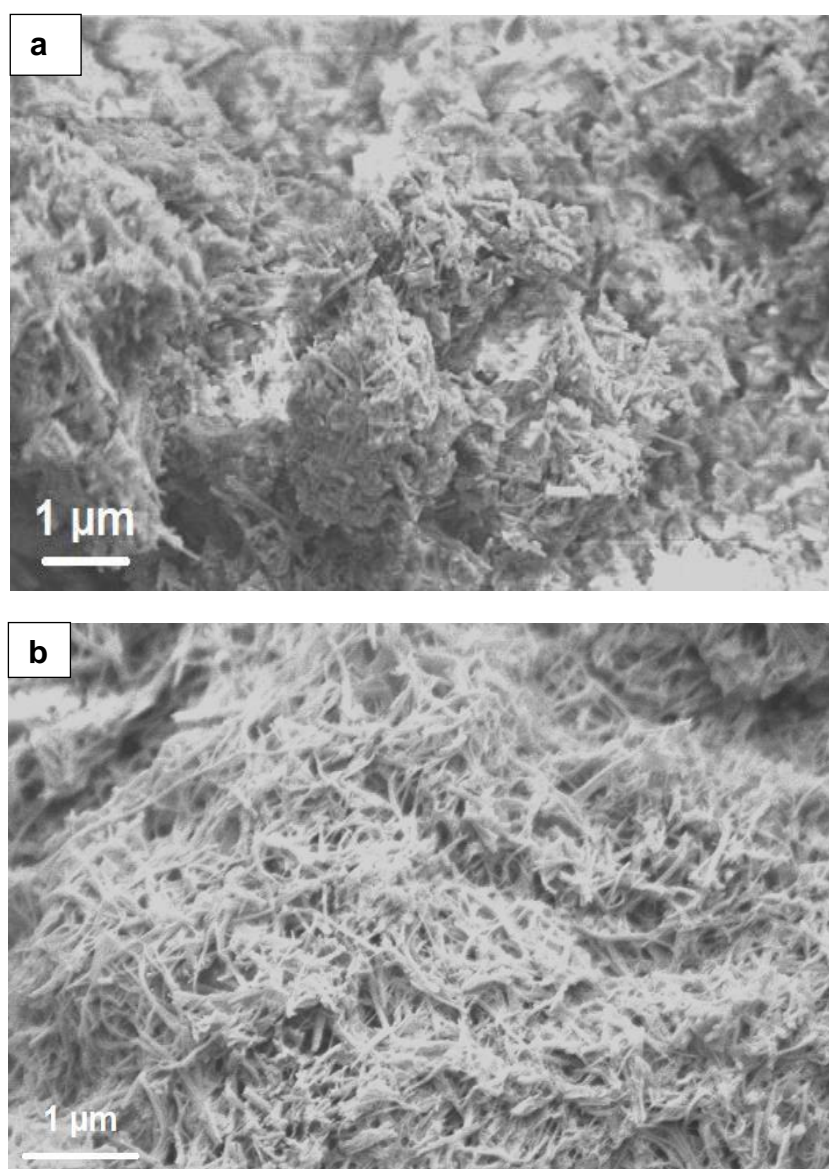


Figure 34: The SEM images of the neat SiO_2 nanowires (a) and OA-modified SiO_2 nanowires (b).

ROMP-derived monolithic supports were prepared using NBE as the monomer, DMNH6 and TMPTNC as crosslinkers, toluene as a microporogen, and 2-propanol as a macroporogen. Individually separated SiO₂ nanowires (diameter x length: 10 nm x 200 nm) that were surface-modified with OA were used as a hard-templating material. The OA emulsifier feature was beneficial for the homogenous distribution of the OA-surface-modified nanowires throughout the ROMP-derived matrix. According to EDX mapping, the OA modified silica nanowires were homogeneously distributed over the ROMP-derived polymeric matrix (Figure 35). However, the differences in the polarity factor (X_{FH}) value of the reaction mixture had to be considered during polymerization.

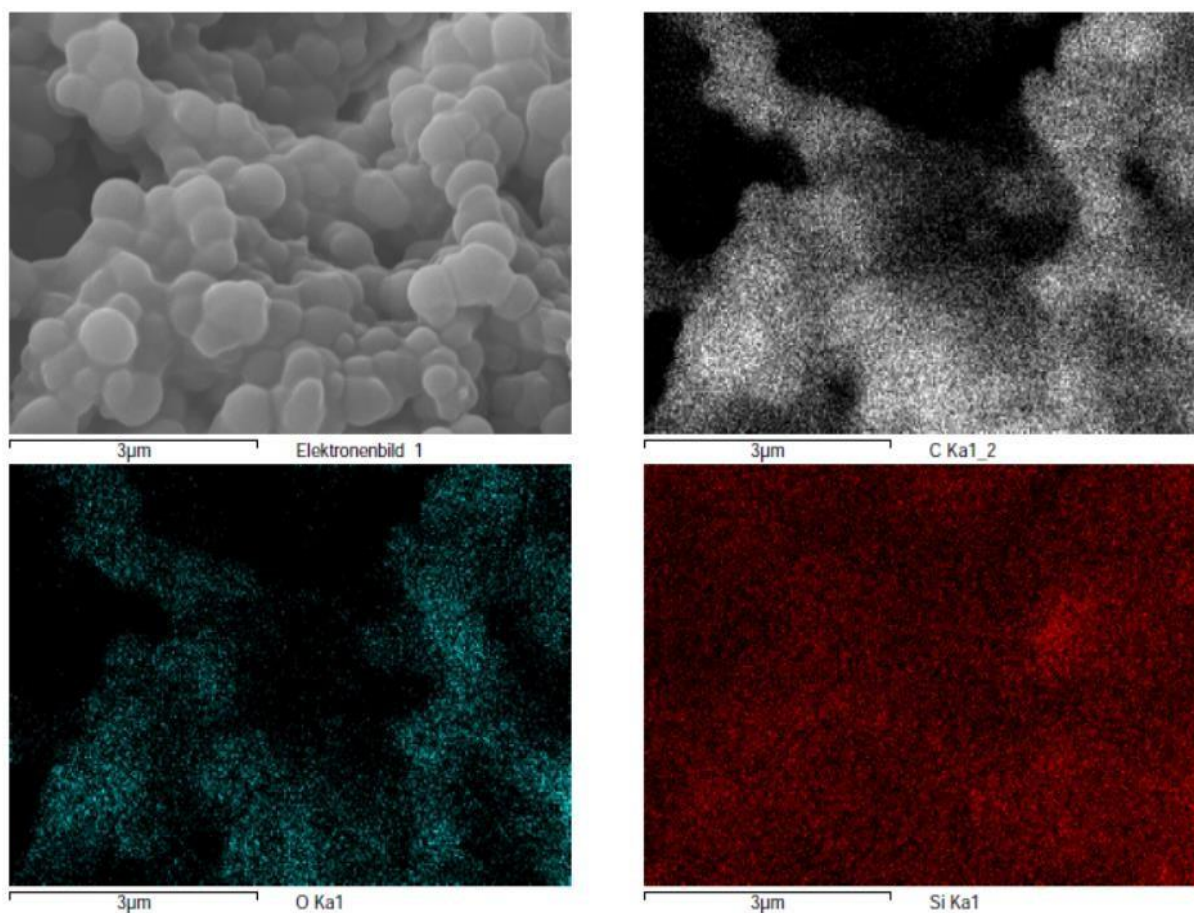


Figure 35: The EDX analysis of the OA-modified-SiO₂ nanowires that were attached to the ROMP-derived monoliths.

As presented in Figure 36, a high-resolution structural image of the ROMP-derived monolith that contained OA-modified SiO₂ nanowire on the micrometer scale was obtained. The SiO₂ nanowires were visible on the surface of the microglobules. Because the polarity of the polymerization mixture changed drastically during polymerization, nanomaterials accumulated throughout the polymer matrix.

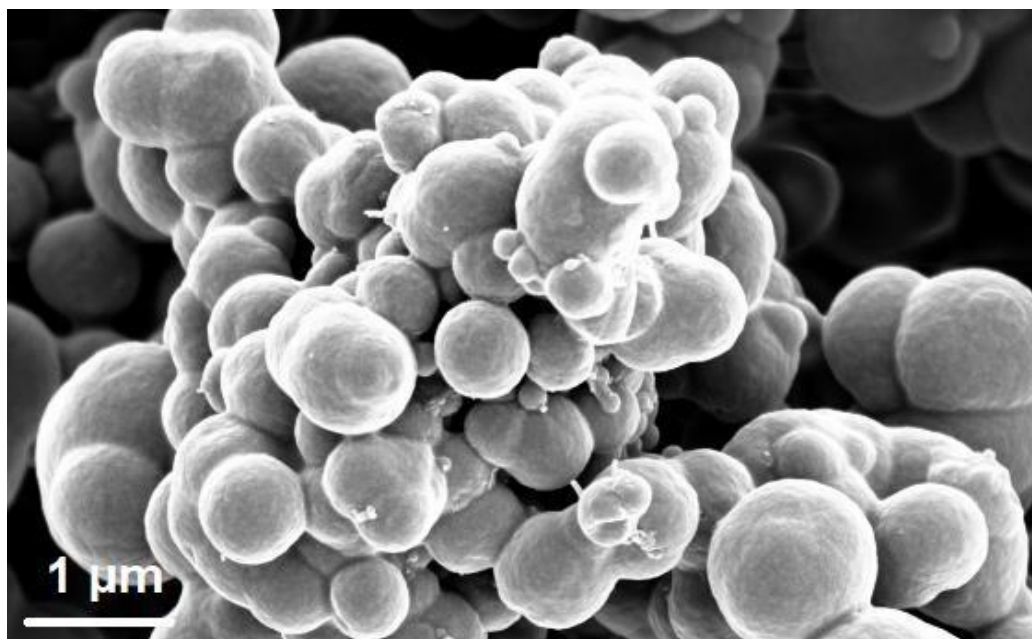


Figure 36: The SEM images of OA-modified-SiO₂ nanowires attached ROMP-based monoliths.

Thus, we concluded that the specific attachment of nanomaterials to microglobules is of enormous importance for pore formation. Therefore, creating a bond between the monolithic material and nanomaterial is essential for attaching the nanomaterial to a monolithic matrix. This can be accomplished via treatment with (bicyclo[2.2.1]hept-5-en-2-yl)triethoxysilane. NBE moieties were introduced throughout the ROMP-derived monolith matrix via covalent bond formation (Figure 37). The dimensions of the silica nanowires (diameter x length: 10 nm x 200 nm) were specifically chosen to obtain microglobules with a mesoporous structure. This helped us understand the connections between the size of silica nanowires and the formation of pores in a deeper and possibly more useful way.

In general, both the size and morphology of the pores depended strongly on several factors, including the solubility of the resulting polymer in the solvent mixture that was used and the polymerization kinetics. The entire process, which was determined by using the FH interaction parameter (X_{FH}), had to be set up so that phase separation would happen faster than gelation. The FH theory states that the *SIPS* process can be controlled not only through temperature and differences in the Hildebrand solubility parameters of 2-propanol (= 23.8 MPa^{1/2}), toluene (= 18.2 MPa^{1/2}), NBE-CH₂OH (= 19.5 MPa^{1/2}), and NBE and the crosslinkers (16 MPa^{1/2}), but also through crosslinker content. ROMP-derived monoliths that lack SNWs are characterized by specific

surface areas of $0.74 \text{ m}^2/\text{g}$. The monomers and crosslinkers chosen here enabled the complete dispersion of the functionalized SNWs. The surface of the SNWs was functionalized using the (bicyclo[2.2.1]hept-5-en-2-yl) triethoxysilane functional group to incorporate it throughout the ROMP-derived skeleton. Indeed, this surface modification turned out to be a prerequisite for any homogeneous distribution of the nanowires throughout the ROMP-derived monolithic matrix. ROMP derived, poly(norborn-2-ene)-based monolithic supports were prepared under *SIPS* conditions using the 1st generation Grubb's initiator $\text{RuCl}_2(\text{PCy}_3)_2(\text{CHPh})$ (1, Cy = cyclohexyl), and NBE, DMNH6, and TMPTNC as monomers and crosslinkers, respectively. 2-Propanol and toluene were used as macro- and microporogens. SNWs that were surface modified with NBE moieties were used as hard templates. *Exo*, *endo*-Norborn-5-ene-2-ylmethanol (NBE- CH_2OH) was used as a functional co-monomer. The tailored porogenic system and the surface functionalized SNWs allowed for a full dispersion of the SNWs in the polymerization mixture.

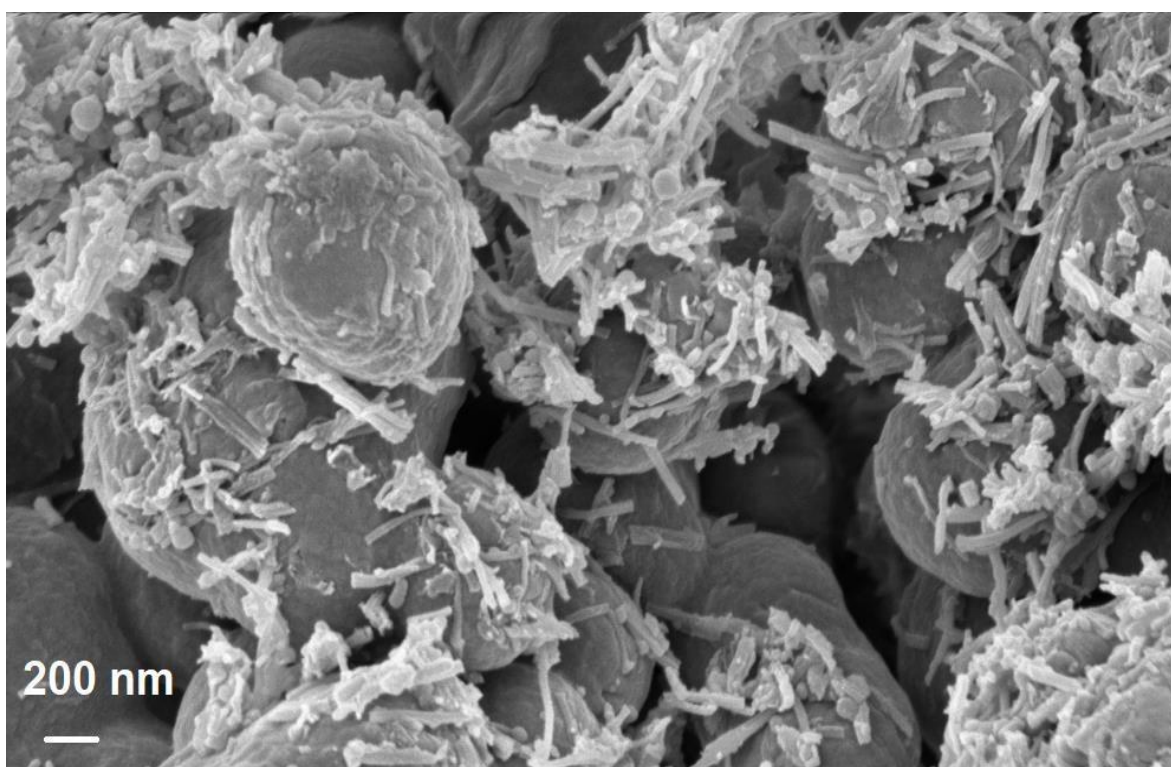


Figure 37: The SEM of the structure-forming microglobules of a ROMP-derived monolith covered with (bicyclo[2.2.1]hept-5-en-2-yl)triethoxysilane-modified SNWs.

The generation of mesoporous channels was accomplished via treatment with *in-situ* generated HF. The final ROMP-derived support materials were fully characterized using standard N₂-sorption and ISEC techniques.

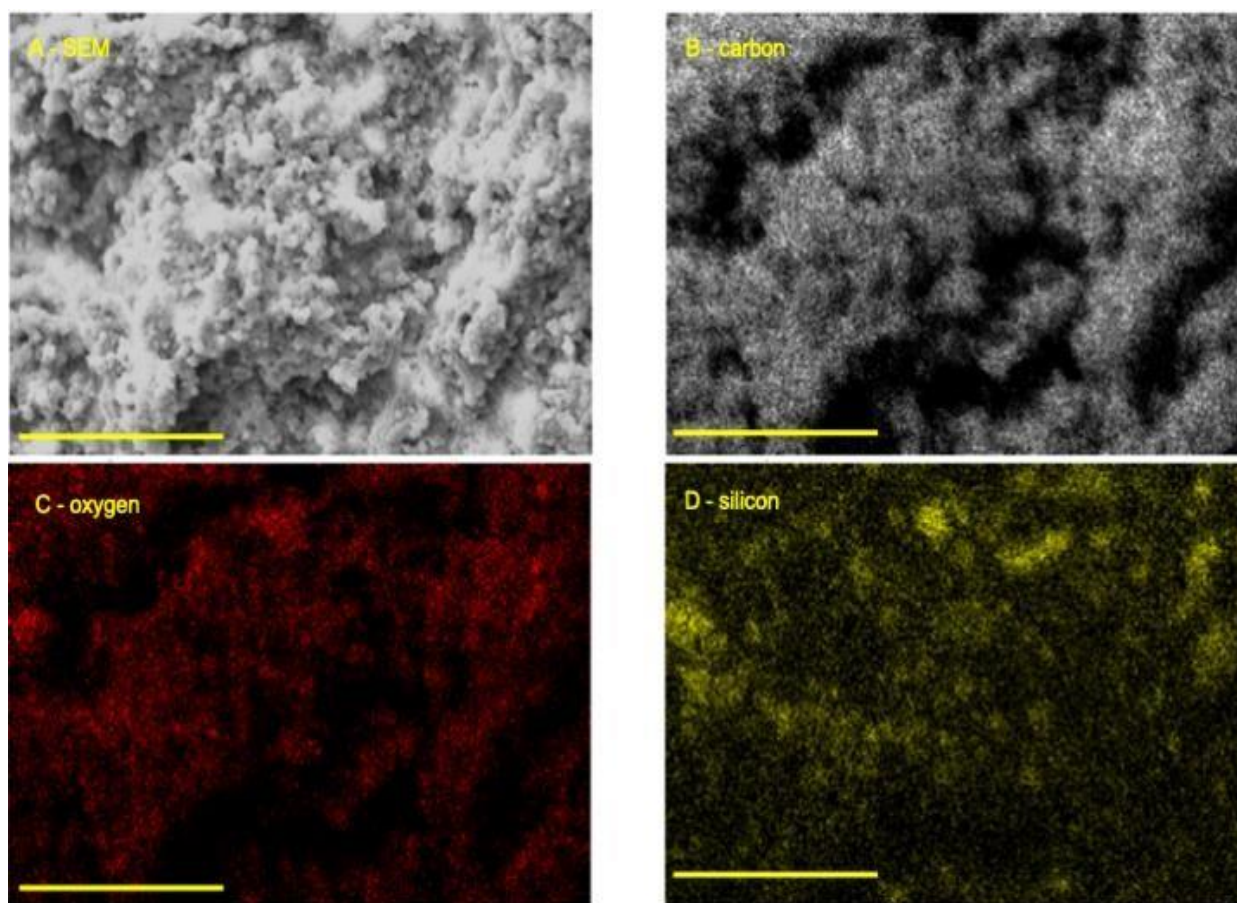


Figure 38: a) SEM, b - d) EDX mapping of the SNW-loaded mesoporous monolith M1 prior to etching. Scale bar = 20 μm .

The *SIPS* resulted in the formation of polymeric monoliths. Scanning electron microscopy (SEM, Figure 38 a, b) of the hard-templated ROMP-derived monoliths **M1a** and **M2a** revealed monolithic structures with microglobules in the 0.5 – 1 μm range along with large transport pores in the micrometer range. EDX mapping confirmed the presence of Si along with C and O throughout the polymeric matrix (Figure 38 b, d); the Si was homogeneously distributed over the entire polymeric matrix. Therefore, we concluded that most of the SNWs inside the monoliths remained fully dispersed inside the polymeric matrix. TEM images of the (bicyclo[2.2.1]hept-5-en-2-yl)triethoxysilane-modified SNWs (d x l : 10 nm x 200 nm) that contained ROMP-derived monoliths are depicted in Figure 39. The TEM samples were made from thin layers of ROMP-based monoliths that were approximately 100 nm thick. In addition to the silica nanowires

located at the interface between the pore and microglobules, one can see that the silica nanowires were embedded inside the polymeric monolithic matrix.

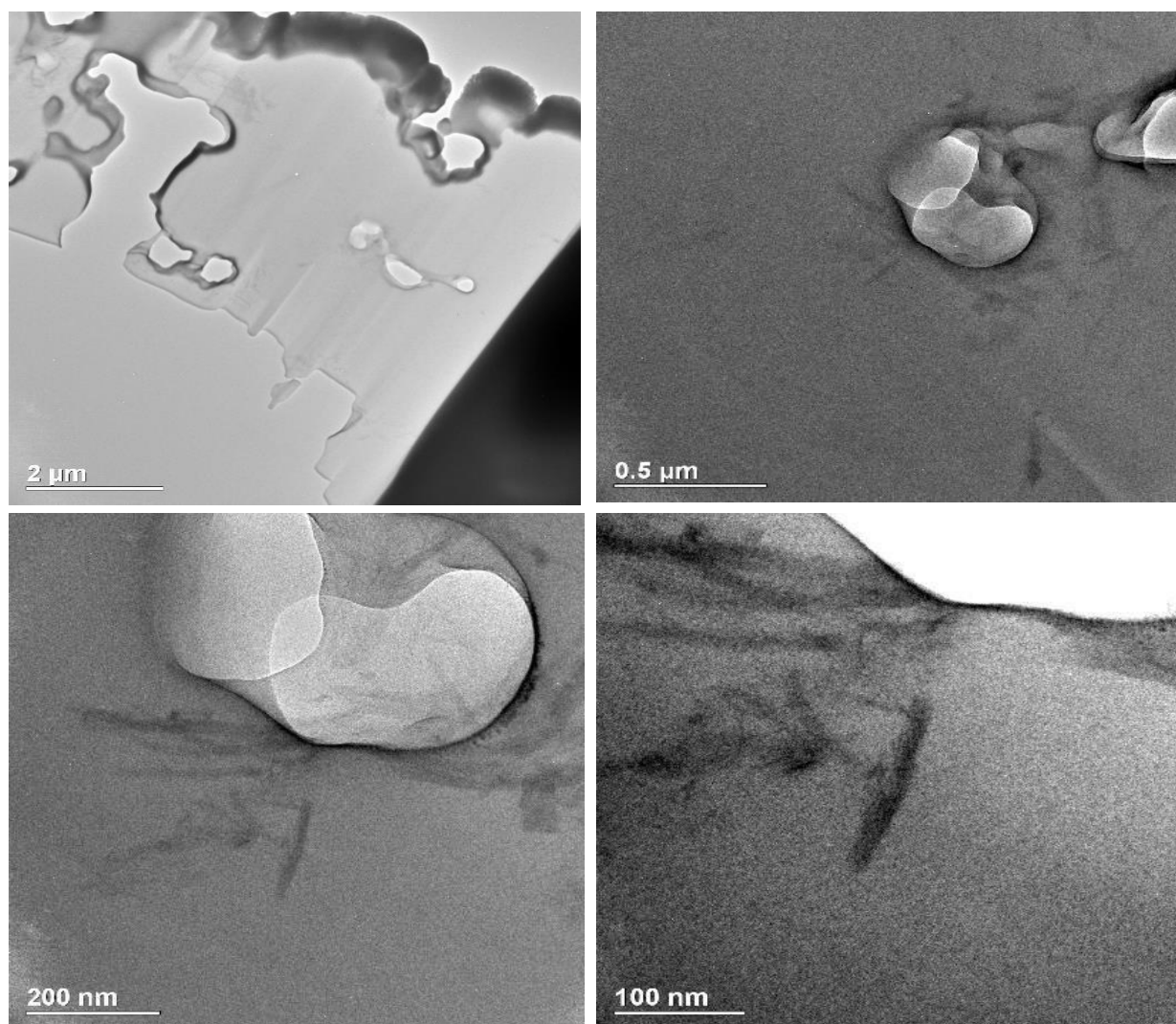


Figure 39: The TEM images of the (bicyclo[2.2.1]hept-5-en-2-yl)triethoxysilane-modified SNW containing ROMP-derived monoliths.

The type of etching technique noticeably influenced the characteristics of the porous materials. The chemical etching technique created the porosity based on structural differences between the template and the matrix material [212,213]. Silica etching chemistry [209] is classified into two categories. The first uses reversible etching at high temperatures in alkaline (e.g., NaOH, Na₂CO₃, ammonia) or strong acid (e.g., HCl, H₂SO₄) mediums, which includes chemically reversing less condensed silica oligomers. The second etching technique, which uses HF, is a fast and irreversible process, and the main product is gaseous silicon tetrafluoride (SiF₄) [214].

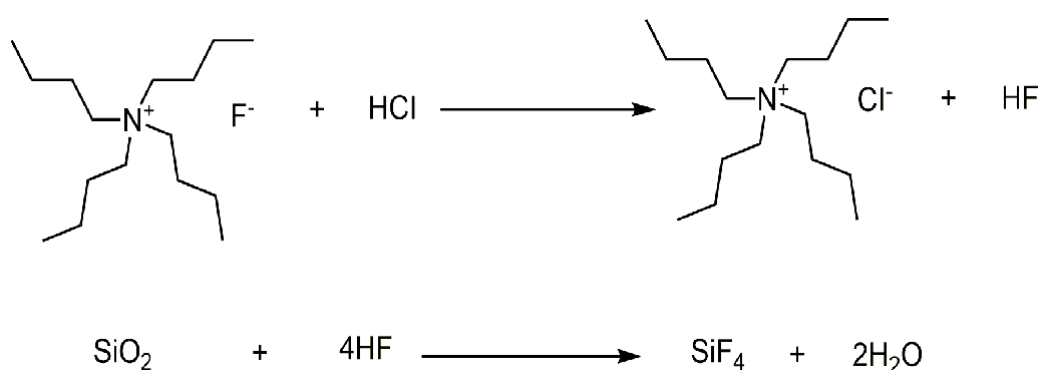


Figure 40: In situ generation of HF.

Following the incorporation of the SiO_2 nanowires into the monolithic structure, the surface-modified SNWs were removed using *in-situ*-generated HF in continuous flow at room temperature, which allowed for high linear flow rates (> 2 mm/s) at low back pressure (< 6 bar). The *in-situ* chemical etching procedure was successfully achieved using several steps. For the first step, to completely remove the covalently bonded SNWs from the structure-forming microglobules, the porosity had to be adjusted using the different solvent mixtures. For example, after ISEC characterization, chloroform had to be replaced with methanol for the chemical etching process. For that purpose, the ROMP-derived monolithic columns were initially flushed using a mixture of both chloroform and methanol. Later, the methanol was used to rinse the monolithic column under a continuous flow using a syringe pump. After the chemical etching process was completed, the methanol was removed from the column, which was then flushed with CHCl_3 for further ISEC measurements. Controlling the monolithic structure's mechanical stability during solvent exchange was the crucial point. Especially during the ISEC characterization step, all pores in the monolithic structure had to be filled with CHCl_3 because the remaining solvent caused high back pressures. Second, the mechanical processes (such as flow rates, temperatures, etc.) had to be designed to keep the monolithic structures stable and solid.

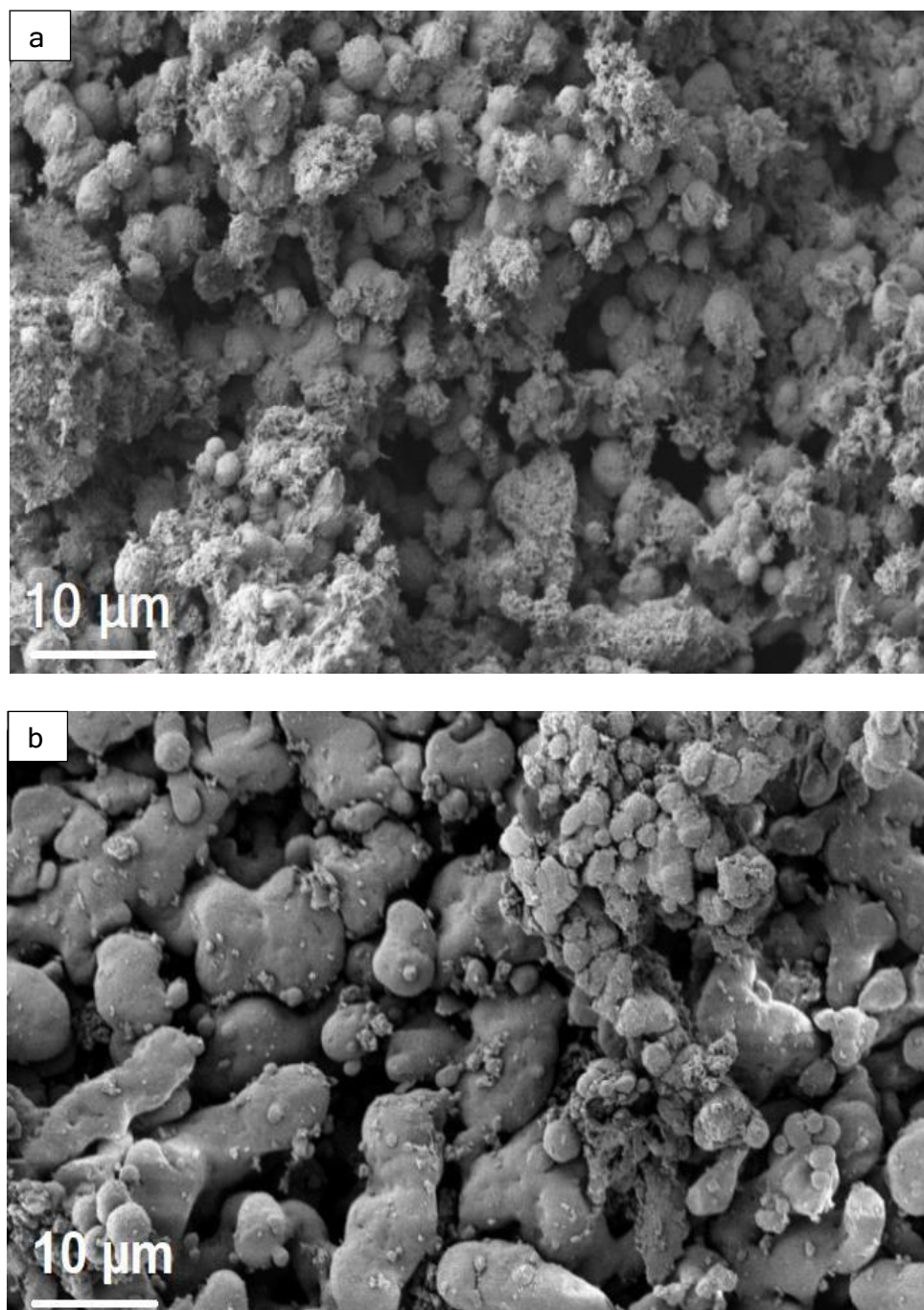


Figure 41: The SEM of the structure-forming microglobules of a ROMP-derived monolith covered with (bicyclo[2.2.1]hept-5-en-2-yl)triethoxysilane-modified SNWs. (a) prior to etching and (b) after etching.

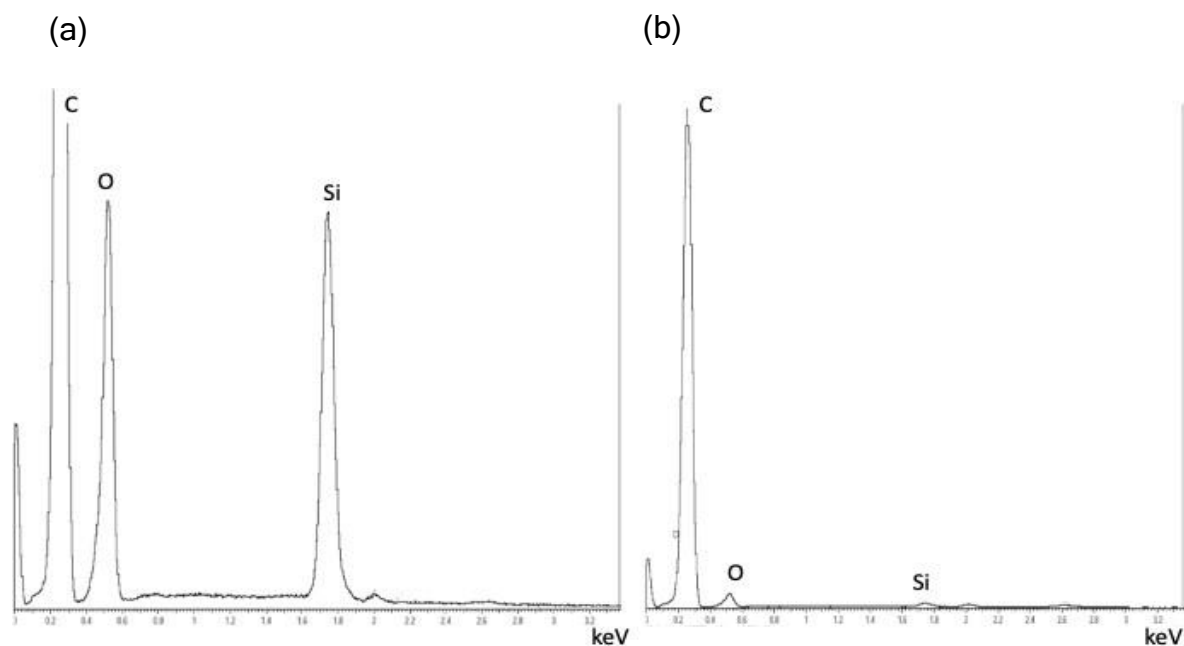


Figure 42: The EDX analysis spectrum of the SNW-loaded mesoporous monolith M2 prior to etching (a) and (b) after etching.

The EDX analysis (Figure 42) confirmed the quantitative removal of the SNWs with low intensities for remaining Si. The surface of the microglobules was dominated by C, with small amounts of O.

Table 5: Physicochemical data for the ROMP-derived monoliths M0 - M2; 1: Grubbs' 1st-generation catalyst, CL-1; DMNH₆, CL-2; TMPTNC.

#	<u>Polymerization Mixture [wt.-%]</u>							
	NBE ¹⁾	NBE-CH ₂ OH ¹⁾	CL-1 ¹⁾	CL-2 ¹⁾	1 ¹⁾	Toluene ¹⁾	2-Pr-OH ¹⁾	SNW
M0	19.8	1.1	10.4	10.4	2.2	16.8	39.1	-
M1a	19	1.1	10	10	2.1	16.1	37.5	4
M1b	-	-	-	-	-	-	-	-
M2a	19	1.1	10	10	2.1	16	37.4	4.3
M2b	-	-	-	-	-	-	-	-

¹⁾wt-%.

Table 6: Physicochemical data for the ROMP-derived monoliths M0 - M2; values for the pore volume, V_p ; the specific surface area, s ; the volume fraction of pores, ϵ_p ; the volume fraction of intermicroglobule void volume (interstitial porosity), ϵ_z , and the total volume fraction, ϵ_t .

<u>Structural Data</u>					
ϵ_p	ϵ_z	ϵ_t	V_p	V_p	s
[%] ¹⁾	[%] ¹⁾	[%] ¹⁾	[mL/g] ¹⁾	[mL/g] ²⁾	[m ² /g] ²⁾
6	51	57	0.165	0.006	0.74
23	60	83	0.581	0.020	2.41
33	61	94	0.823	0.022	3.7
18	62	80	0.446	0.016	2.55
18	58	76	0.452	0.029	3.00

¹⁾Determined by ISEC in CHCl₃. ²⁾ Determined by N₂-sorption

Porous monoliths were obtained that contained both micrometer-sized transport pores and mesopores in the range between 1 nm and 10 nm, as evidenced by the ISEC [41] and N₂-sorption measurements [42], which we used the BET method for to conduct the data evaluation. The differences in pore size distribution were the result of the different conditions under which these measurements were carried out. N₂-sorption was performed under dry conditions while ISEC was run under wet conditions. In the latter case, a non-permanent microporosity (<1 nm) became visible due to the swelling of the support during the mobile phase. When up to 4.3 w.t% SNWs were used, the specific surface areas as well as the ϵ_p and ϵ_z , increased for all the monoliths in comparison to the SNW-free monolith *M0*. Monolith *M1a*, which contained 4.0 w.t% SNWs, exhibited the highest increase in specific surface area (3.7 m²g⁻¹) and pore fraction (33%). Higher SNW loadings of up to 4.5 w.t% resulted in lower specific surface areas and pore volumes than 3.2 w.t% SNWs. This can tentatively be attributed to the more pronounced allocation of the surface-modified SNWs at the solid-liquid interface during polymerization and, thus, to additional immobilization on the microglobules' surfaces. Based on the density of the SNWs (1.87 g cm⁻³), a loading of 4.3 wt.% with respect to the entire polymerization mixture translated into an additional theoretical pore volume of 5.4 vol.-% (0.054 mL g⁻¹) in the polymeric monolith. Experimentally, a pore volume of 0.029 mL g⁻¹ (54% of theory) was found. The lower pore volume was consistent, as a slightly wider pore size distribution was present in

the monoliths after the *in-situ* chemical etching process, which was probably due to the formation of some larger pores that were created by small agglomerates of the modified SNWs during the phase separation process. As demonstrated in Figure 43, when the concentration of silica nanowires was raised to 5%, the surface characterization became challenging. During N₂-sorption characterization, lower surface area values were detected after the *in-situ* etching procedure because the SNWs had become entangled on the surface of the monolith, which created additional surface area.

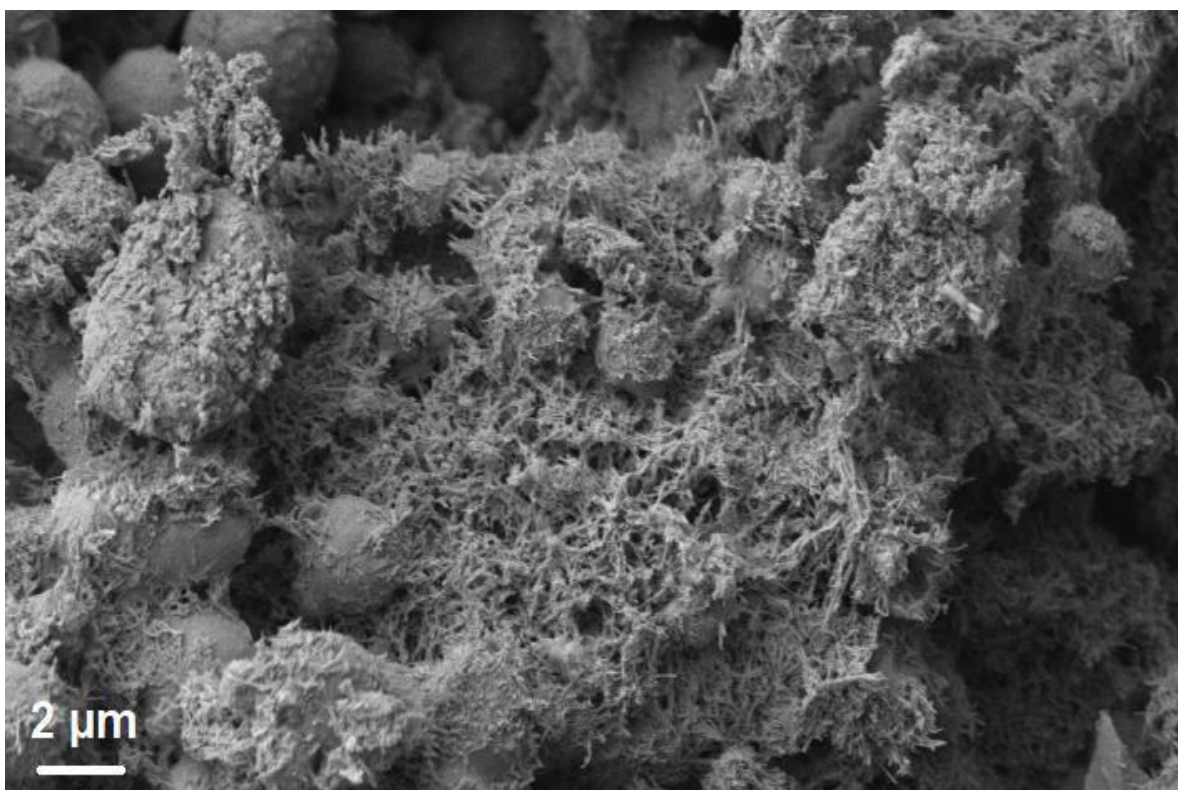


Figure 43: The SEM image of ROMP-derived monoliths that contain the (bicyclo[2.2.1]hept-5-en-2-yl)triethoxysilane-modified SNW.

The hydroxyl groups (-OH) provided by the norborn-5-ene-2-methanol co-monomer can be used for a reaction with suitable functional groups such as iso(thio)cyanates, anhydrides, carboxylic acids, or entire catalysts. In particular, the conversion of norborn-5-ene-2-methanol was quantitative. Much like the catalyst, during the phase separation process, similar to the catalyst, the polar comonomer stayed close to the 2-propanol phase, which resulted in the accumulation of the hydroxyl groups on the microglobules' surfaces, which rendered them accessible for further functionalization.

Indeed, for a typical functional monolith, we found on average, 56% of the OH groups to be accessible to titration with benzylmagnesium chloride using back titration techniques.

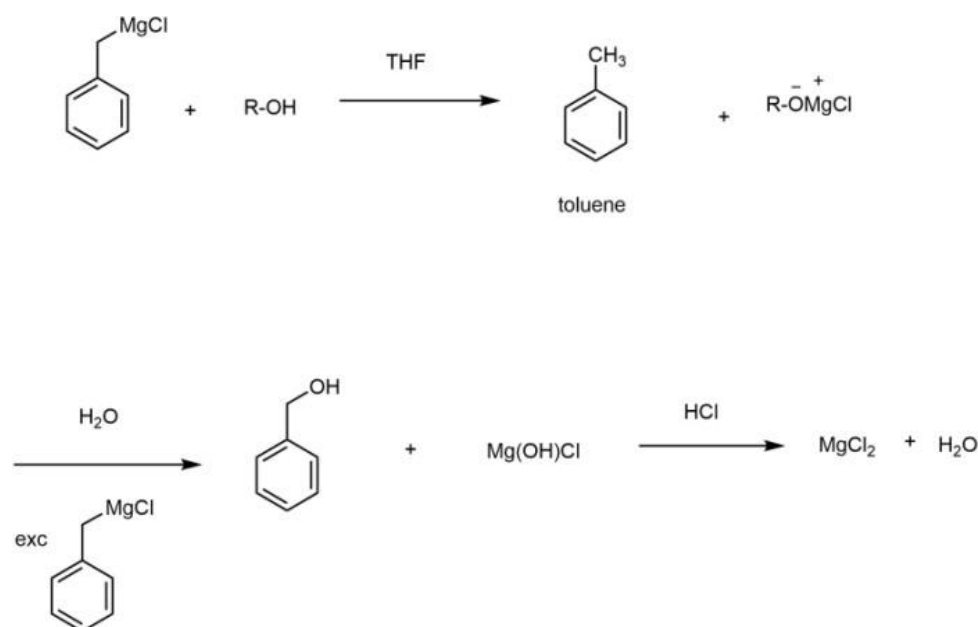
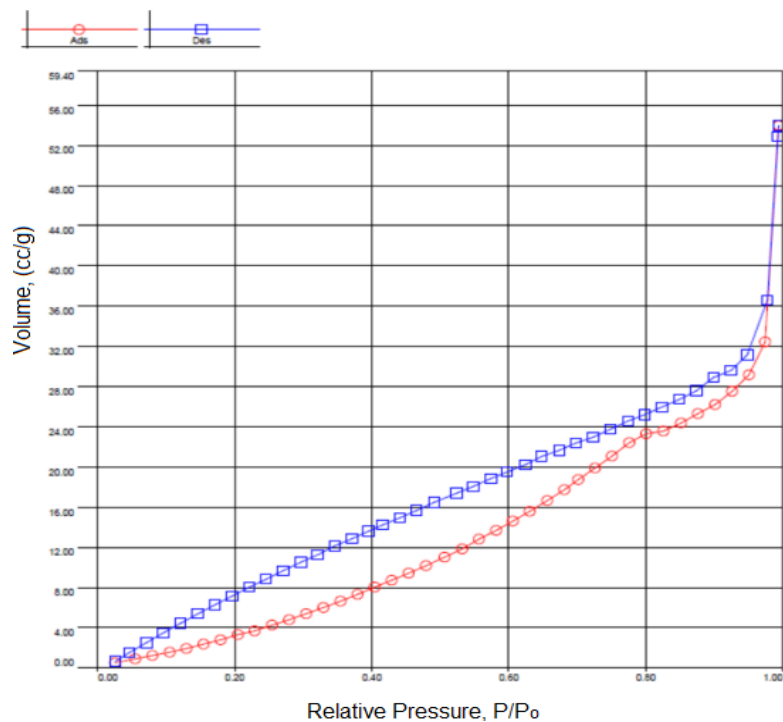


Figure 44: Hydroxyl group (-OH) determination using back-titration method.

As can be observed in Figure 45, in comparison to the N₂-sorption isotherms, Argon (Ar)-isotherms provided a better adsorption-desorption fitting line. Typically, the measurements are performed with nitrogen gas since it is less expensive than other inert gasses such as argon or helium. Due to the non-porous nature of the ROMP-derived monolith, the surface areas that resulted from both N₂ and Ar- measurements were almost identical. This also indicates the consistency of the non-local NLDFT model. Additionally, the pore size distribution that was obtained from the measurement using argon BET-characterization technique is illustrated in Figure 46.

a)



b)

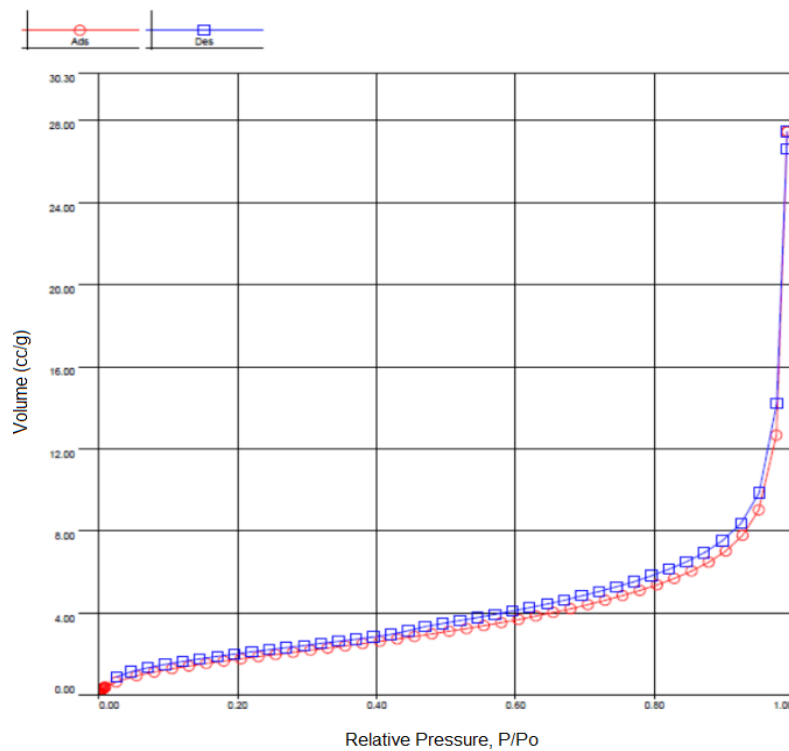


Figure 45: The (a) N₂-derived, (b) Ar-derived pore size distribution of a ROMP-derived monolith (M1b)

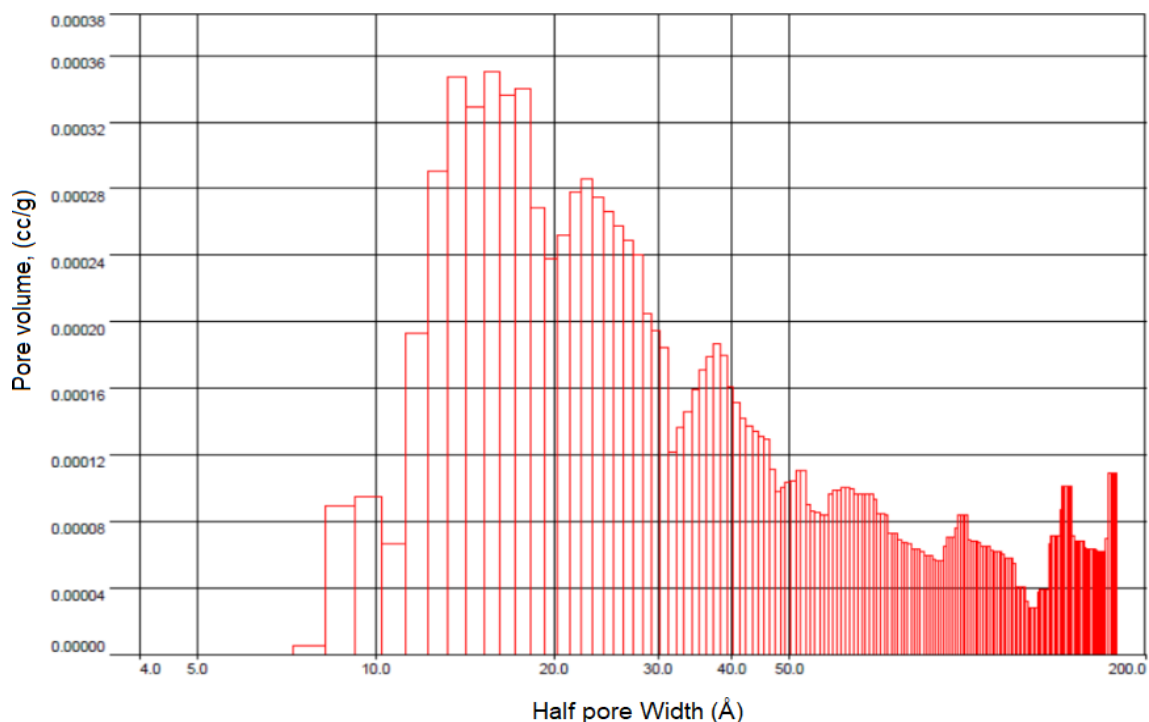


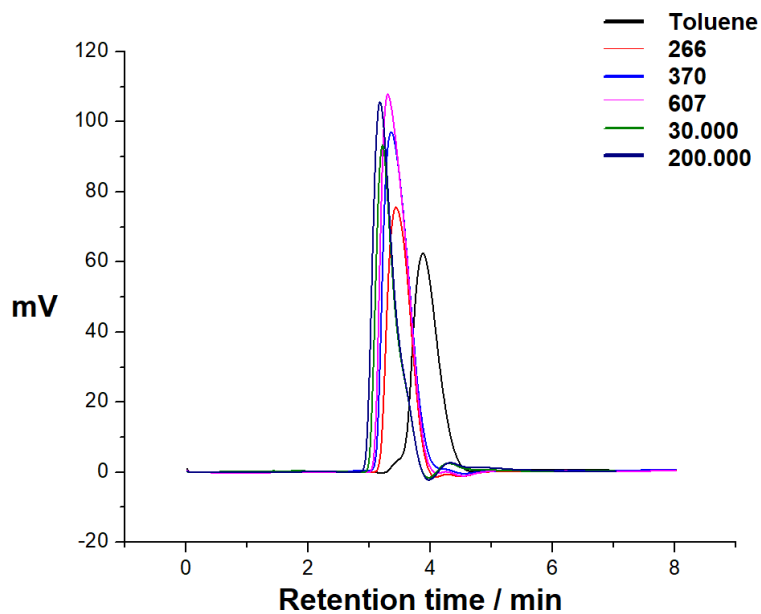
Figure 46: The volume histogram of the Ar-derived pore size distribution of a ROMP-derived monolith (M1b).

We notice again that, unlike the ISEC characterization, which was performed in wet conditions, even in dry conditions, the monolith was mostly composed of swell-induced pores (< 2 nm). The comparison of the ISEC-derived retention times obtained for the raw-derived monolith (a) and the silica-NW-added monolith (b) is depicted in Figure 47. The inclusion of silica nanowires throughout the ROMP-derived monolith matrix blocked the interstitial pores, which resulted in higher retention times and back pressures during the characterization.

Table 7: The effect of the SiO_2 nanowire distribution on the ISEC-derived pore size distribution of a ROMP-derived monolith.

ROMP-derived monolith without nanowire (a)	ROMP-derived monolith with nanowire (b)
0.5 ml / min – 6 bar $< x < 10$ bar	0.3 ml / min – 68 bar $< x < 90$ bar
Retention time (min) : 3 min $< x < 4$ min	Retention time (min) : 6 min $< x < 7$ min

(a)



(b)

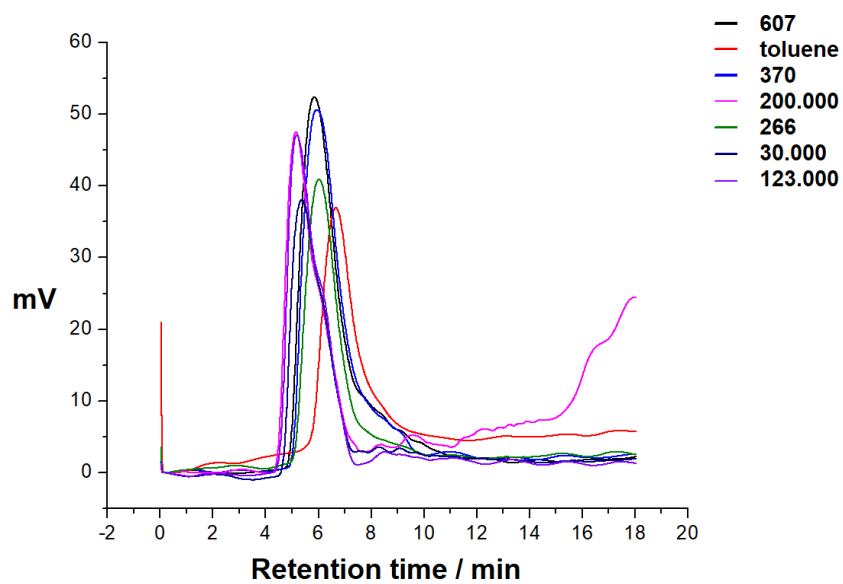


Figure 47: The ISEC-distribution of the PS standards for a ROMP-derived monolith (M1b).

2.2.3 Summary and Outlook

This work has demonstrated that the attachment of silica-derived inorganic nanowires within the matrix of a monolithic material is possible and, therefore, fundamentally applicable under the scope of the CRC project. This was demonstrated using a ROMP-derived monolithic material, which has advantages such as a living nature and functional group tolerance that is comparable to polymeric monoliths. As previously mentioned, the hard-templating process, in combination with the *SIPS* process, offers access to hybrid monolithic structures. The *SIPS* synthesis technique permitted the tailoring of conditions such as polarity and temperature to prepare hydroxyl-functionalized, SNW-loaded ROMP monoliths. To ensure the incorporation of the SNWs during polymerization, the SNWs were surface-functionalized with (bicyclo[2.2.1]hept-5-en-2-yl)triethoxysilane. Indeed, this surface modification turned out to be a prerequisite for any homogeneous distribution of the nanowires throughout the ROMP-derived monolithic matrix. We determined that, the NBE-functionalized SNWs, which were 10 nm in diameter and 200 nm in length, could be fully dispersed in the reaction mixtures as evidenced by the formation of clear and fully transparent solutions. Accordingly, the monomers and crosslinkers used here allowed for the complete dispersion of (bicyclo[2.2.1]hept-5-en-2-yl)triethoxysilane-functionalized SNWs. The EDX mapping proved the existence of Si along with C and O throughout the polymeric matrix; Si was homogeneously distributed over the entire polymeric matrix, illustrating that the SNWs had been fully dispersed throughout the polymeric matrix. The removal of the SNWs was accomplished with *in-situ* generated HF acid under continuous flow at room temperature, which allowed for high linear flow rates ($> 2\text{ mms}^{-1}$) at low backpressure ($< 6\text{ bar}$). The quantitative elimination of the SNWs was confirmed with low intensities for residual Si using EDX analysis. In comparison to the other hybrid monoliths, the monolith M1a, which contained 4.0% SNWs, exhibited the highest increase in specific surface area ($3.7\text{ m}^2\text{g}^{-1}$) and the highest percentage of pores (33%). However, due to the more pronounced allocation of surface-modified SNWs at the solid-liquid interface during polymerization, higher SNW loadings of up to 4.5 wt.% resulted in lower specific surface areas and pore volumes. Furthermore, 56% of the hydroxyl groups on the surface of the monolith were accessible and could be used in reactions with the suitable functional groups, such as iso(thio)cyanates, anhydrides, carboxylic acids, or entire catalysts.

2.3 Tailoring Mesoporosity in Poly(urethane)-Derived Monolithic Supports

2.3.1 Introduction

In recent years, functional porous organic frameworks (POFs) composed of simple molecular building blocks have gained significant interest due to their potential applications in gas storage and separation, catalysis, optoelectronics, and nanotechnology [94,95,98]. It has become more crucial than ever to create new functional POFs with high specific surface area, catalytically active pore surfaces, and exceptional chemical and thermal stability. A variety of covalent linkages can be created by using various synthetic reactions on a wide variety of molecular building blocks. Even though impressive progress has been achieved in the field of heterogeneous catalysis using modified zeolites and metal–organic frameworks (MOFs), improving the functionality of the pores in POFs for better catalytic performance and selectivity remains difficult.

Recently, porous polyurethanes (PURs) have attracted a lot of attention. Because of its high elastance, biocompatibility, and biodegradability, PURs are ideal materials for tissue engineering, biosensors, and enzyme immobilization applications. The interest in mesopore materials, especially within the framework of confinement for molecular heterogeneous catalysis has led our team to evaluate mesopore polyurethane monoliths. Herein we report a new mesoporous polyurethane (MPU) monolith, synthesized by the condensation of hexamethylene diisocyanate-trimer (HMDI-trimer), 1,1,1-tris(hydroxymethyl)propane (THP) and triethylene glycol (TEG) with using dibutyltin dilaurate (DBTDL) as catalyst in a mixture of dioxane and methyl *tert*-butyl ether (MTBE) at 50°C. For the synthesis of PUR monoliths, reaction parameters such as monomers, crosslinkers, and porogens were used to control the relative rates of isocyanate with polyols. The proportions of the components affect the stability of the structure and determining the appropriate ratio allows for custom monolith synthesis. In addition, polyurea monoliths were synthesized to investigate the impact of the crosslinker on the monolith's structure by switching THP to 1,3,5-tris (4-aminophenoxy)benzene. The successful formation of the crosslinked, continuous structure of the monoliths was verified by SEM. N₂-sorption and ISEC further confirmed the presence of a solid-state crosslinked structure. The polymeric supports also supply

all general requirements for polymeric monolith supports, such as mechanical stability, micro-meter range transport pores, optimum linear flow rates, and back pressures.

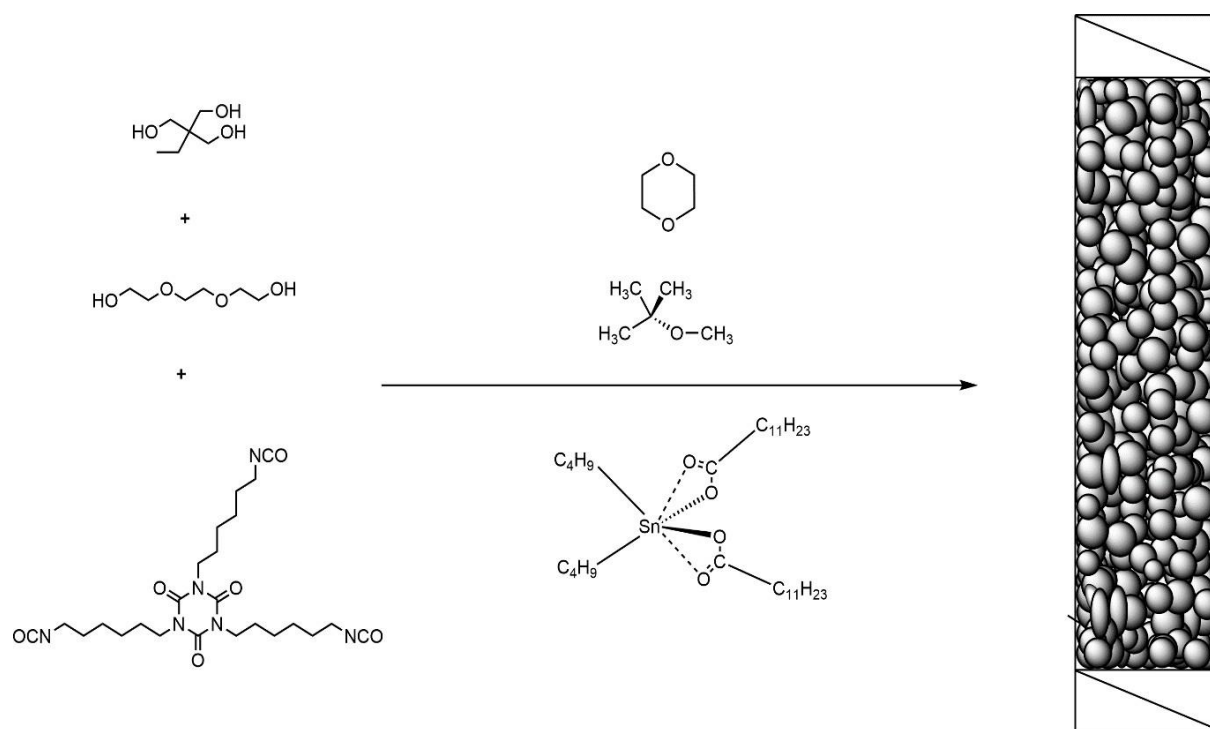


Figure 48: Synthesis of a PUR-derived monolithic support based on THP, TEG and HMDI using DBTDL as catalyst in a mixture of dioxane and MTBE.

2.3.2 Result and Discussion

Monolithic supports possess small pores to achieve a large functional surface area for catalysis and large flow-through pores that prevent high back pressures. However, it is crucial to adjust the counter-pressure for characterization of the porosity in the polymeric and monolithic support materials. To find the most suitable PUR-derived monolithic support material, the resulting back pressures were recorded using the CHCl_3 solvent system. For ISEC measurements, PUR-derived monoliths were connected to an HPLC-pump, which allowed for adjusting the flowrate and monitoring the resulting backpressures. To heat the columns and the solvent tubing, an HPLC-column oven was used. The results are summarized in Table 8. The chemical composition of PUR-derived monoliths A-D were not suitable, due to high backpressures in low flow rates. The polarity was too high, and the monolith's structure, to a large extent, was dominated by swelling-induced micropores. Lowering the TEG

content and decreasing the polarity resulted in lower back pressures (e.g., monolith *E* exhibited the lowest backpressure of all the monoliths).

Table 8: Composition of TEG, THP, HMDI-trimer, DBTDL and the mol ratio of THP to TEG, porogens.

PUR-derived Monoliths	THP/TEG [Mol Ratio] [wt.-%]	THP [wt.-%]	TEG [wt.-%]	Cat. [wt.-%]	HMDI [wt.-%]	Porogens [Dioxane, MTBE] [wt.-%]	Counter Pressure
A	-	4.1	-	2.5	15	77.5	-
B	5.2	4.1	1.3	2.4	18	73.6	<100 bar
C	10.5	4.4	0.7	2.4	18	73.8	<100 bar
D	39.5	4.7	0.1	2.4	18	73.9	<100 bar
E	80	4.8	0.08	2.4	18	73.9	6-7 bar

Solvent system: CHCl₃.

Table 9: Chemical compositions for the poly(urethane)-derived monoliths PUR1 - PUR4; 1; DBTDL.

Polymerization mixture [wt.-%]								
#	THP ¹⁾	TEG ¹⁾	MDI ¹⁾	HMDI ¹⁾	1 ¹⁾	MTBE ¹⁾	1,4-dioxane ¹⁾	diglyme ¹⁾
PUR1	4.7	-	13.4	-	3.9	53.4	24.3	-
PUR2	4.8	0.08	-	18	2.4	34.5	39.4	-
PUR3	4.8	0.08	-	18	2.4	32	42.1	-
PUR4	4.8	0.08	-	18	2.4	32	-	42.1

¹⁾ wt-%.

The chemical composition of the polymerization mixtures is listed in Table 9. The PUR monoliths, *PUR1–PUR4*, were produced by reacting TEG, THP, MDI and HMDI-trimer as monomers with DBTDL as catalyst. Depending on the solubility factor, 1,4-dioxane and diethylene glycol dimethyl ether (diglyme) were chosen as microporogens and MTBE as macroporogen.

Monolith *PUR1* with an MDI content of 13.4% exhibited an ε_z value of 75.3 %. Due to the relatively rigid structure of MDI, structure-forming microglobules begin to form larger pores during phase separation, resulting in higher ε_z in *PUR1* as compared to other *PUR*-derived monoliths. The tri-functional structure of the HMDI-trimer allowed for flexible, long cross-linked polymer chains, which resulted in early onset phase-separation and increased micro-/mesoporosity. Monolith *PUR2* with a microporogen content (dioxane) of 39.4 wt.% exhibited ε_p value of 20 %. With increasing dioxane content, monolith *PUR3* (42.1 wt. % dioxane) exhibited an ε_p value of 28 %. The mesoporosity of *PUR1* (ΔR : 7.5 %) was in the range of 2.0 - 4.4 nm (Figure S21). For monoliths, *PUR2* and *PUR3*, switching from MDI to HMDI resulted in increased mesoporosity (ΔR) of 14% and 11.5%, respectively, in the range of 2.0 - 5.2 nm (Figure S23).

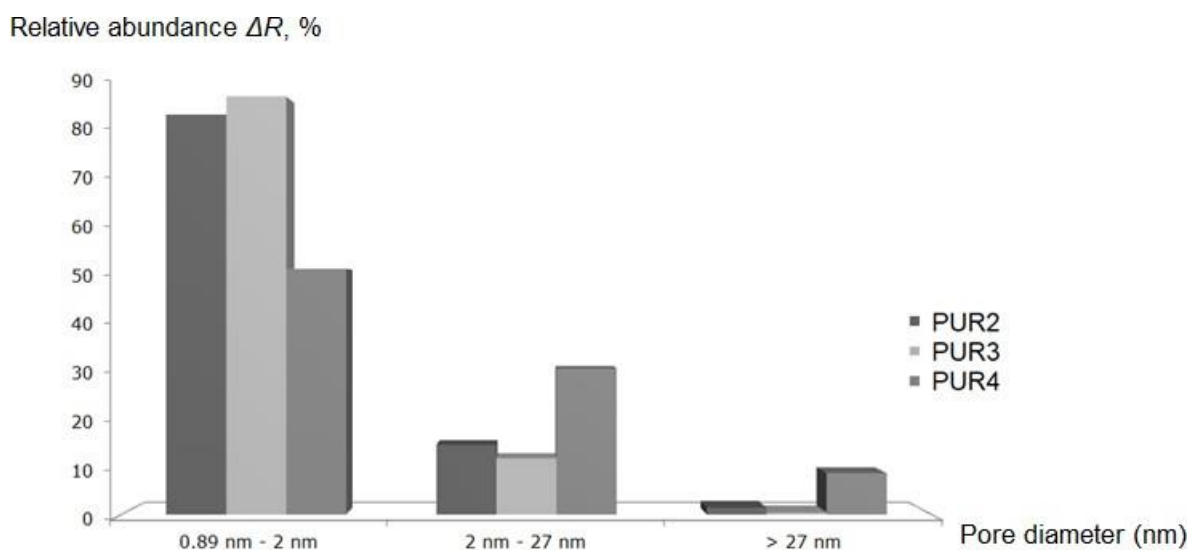


Figure 49: ISEC-derived (ΔR , %) pore size distribution (nm) of *PUR2*; *PUR3*; *PUR4* monoliths.

As shown in Figure 49, compared to the *PUR2* and *PUR3* monoliths, the relative mesopore contribution (ΔR : 2-27 nm) of *PUR4* is three times higher (Figure S23, S26). According to the FH theory, the *SIPS* process can be controlled by temperature and the differences in the Hildebrand solubility parameters of dioxane ($\delta = 10 \text{ cal}^{1/2} \text{ cm}^{-3/2}$), MTBE ($\delta = 7.4 \text{ cal}^{1/2} \text{ cm}^{-3/2}$), diglyme ($\delta = 8.4 \text{ cal}^{1/2} \text{ cm}^{-3/2}$) as well as

poly(urethane) ($\delta = 8.9 \text{ cal}^{1/2} \text{ cm}^{-3/2}$). By switching the microporogen from dioxane to diglyme (**PUR3** → **PUR4**), the solubility of poly(urethane) increases in diglyme compared to the dioxane, causes the onset phase separation, leading to the smaller pores in the structure (Figure S23, S26). However, the inclusion of diglyme (d:1,03 g/cm³) (**PUR4**) to the PUR monolith lowered the ϵ_p value to 8% and the ϵ_z to 26%. This can be attributed to the higher solubility of the diglyme in MTBE compared to the dioxane. The inclusion of diglyme throughout the monolith matrix caused a lower amount of MTBE and caused the polymer chains to pack more tightly together, which leads to a more compact packing of the polymer chains and a lower porosity or gel structure.

Table 10: Physicochemical data for PUR-derived monoliths PUR1 - PUR4.

#	Structural data				
	V_p [mL/g]	σ [m ² /g]	ϵ_p [%] ¹	ϵ_z [%] ¹	ϵ_t [%] ¹
PUR1	0.001	0.54	4.1	75.3	79.4
PUR2	0.004	1.92	20.3	30.1	50.4
PUR3	0.004	2.07	28.2	30.2	58.4
PUR4	0.003	1.86	8.1	26.4	34.5

¹)Determined by ISEC in CHCl₃, flow rate: 2.0 mL/min, 35 °C, column: 8 x 300 mm.

According to N₂-sorption analysis, **PUR1** had a specific surface area (s) of 0.54 m²/g and a pore volume of 1 μ L/g. In addition, the replacement of MDI by the more flexible HMDI-trimer (**PUR2-PUR4**) resulted in an increased volume fraction of pores and the desired porosity with specific surface areas in the range of $1.86 < \sigma < 2.07 \text{ m}^2/\text{g}$ and pore volumes in the range of 3 – 4 μ L/g.

Different experimental conditions explain the discrepancy between the two analytical methods. N₂-sorption analysis was performed under dry conditions, which caused the micropores to collapse; the ISEC method was performed in the presence of a solvent (e.g., CHCl₃), which resulted in non-permanent swelling-derived microporosity. However, even with the low surface areas, as clearly seen in Figure 50, under the dry conditions, **PUR1** revealed 70% microporosity in its structure.

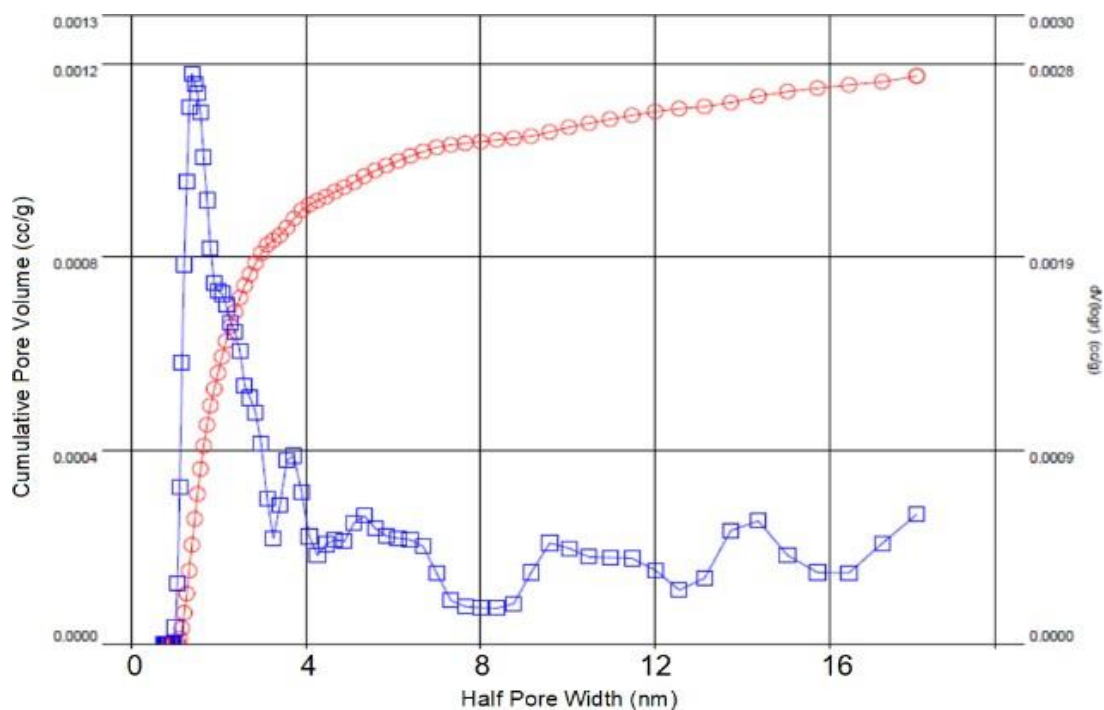


Figure 50: N₂-derived-pore size distribution of Poly(urethane)-derived monolith (*PUR1*).

As shown in Figure 51, the structure-forming microglobules are seen on a scale of 2–12 μm , demonstrating the non-porous surface structure of the PUR-derived monolith supports.

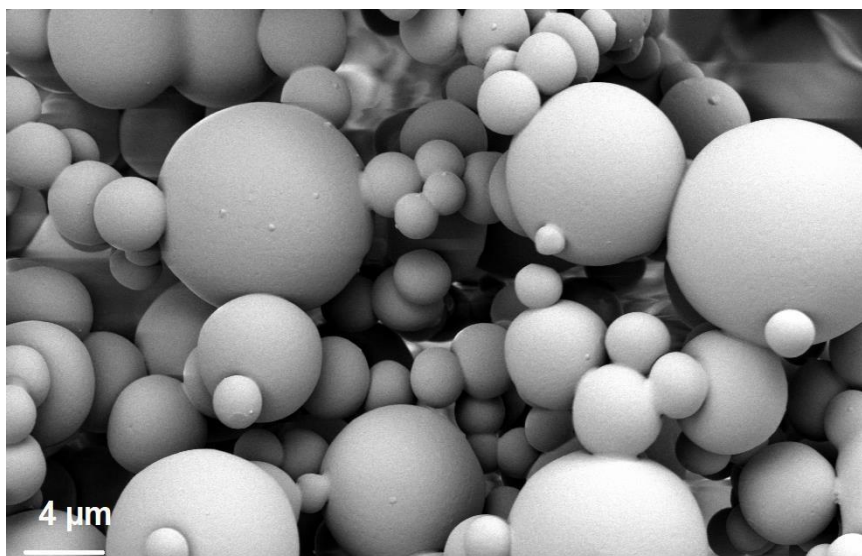


Figure 51: SEM picture of non-porous PUR-derived monolith support *PUR1*.

2.3.3 Tailoring Mesoporosity in Polyurea-Derived Monolithic Supports

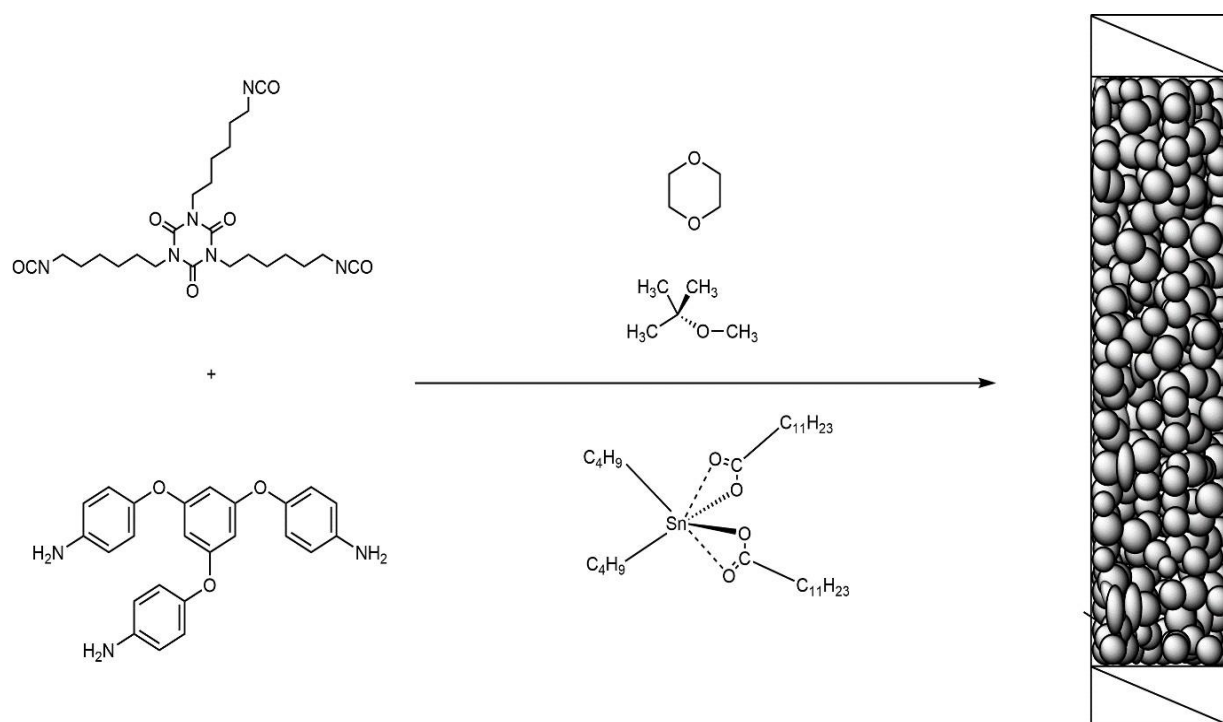


Figure 52: Synthesis of a polyurea-derived monolith based on 1,3,5-tris(4-aminophenoxy)benzene and HMDI with DBTDL as catalyst in dioxane and MTBE.

Polyurea-type polymers are known to have chemical resistance, strong abrasion resistance, high impact resistance, good flexibility, fast curing, etc. [55]. The formation of urea (NH-CO-NH) involves the reaction between amines (-NH₂) and isocyanate groups (-NCO). Furthermore, the chemical reaction between isocyanate groups (-NCO) and water, which produces carbon dioxide, can convert isocyanates to amine groups. Polyurea is then synthesized by the addition polymerization of isocyanates and the *in-situ* produced amines [221,222].

In this study, polyurea-derived monoliths were produced by reacting HMDI-trimer with long-chain trifunctional triamines (i.e., 1,3,5-tris(4-aminophenoxy)benzene) in the presence of DBTDL as catalyst in dioxane and MTBE under *SIPS*. Changing the type and amount of crosslinker agent had a significant impact on the final porous monolithic structure. Here, we studied the crosslinker effect on the pore morphology with an HMDI concentration of 18 wt.% in the first set of polymerizations.

ISEC data is listed in Table 11 and summarizes the values for the ϵ_p , and the ϵ_z . Switching the crosslinker from THP to 1,3,5-tris(4-aminophenoxy)benzene resulted in

an increase of ϵ_z : 68% and ϵ_t : 79% indicating that the number of large pores decreased, while that of small ones was increased.

Table 11: Physicochemical data for polyurea-derived monoliths ($V_{\text{column}} = 2.49 \text{ mL}$).

#	Polymerization mixture [wt.-%]						Structural data		
	HMDI	TEG	CL	Dioxane	MTBE	DBTDL	ϵ_p vol.-%	ϵ_z vol.-%	ϵ_t vol.-%
A	18	0.08	4.8	39	34.5	2.4	0.19	0.34	0.53
B	18	-	4.8	39	34.5	2.4	0.11	0.68	0.79

A; Poly(urethane) monoliths; CL; Trimethylolpropane (THP), B; Poly(urea) monoliths; CL; 1,3,5-tris(4-aminophenoxy)benzene.

A comparative study on ISEC-derived pore size distribution of polyurea and PUR monolith samples is given in Figure 53. The pore size distribution also greatly depends on the degree of crosslinking [215, 216]. Polyurea monoliths contained ~20% mesopores (pores <27 nm). Many cross-linked microglobules are formed and precipitate at an early stage in the reaction, and their high crosslink density leads to a low probability of coalescence between globules as they continue to polymerize (Figure S27).

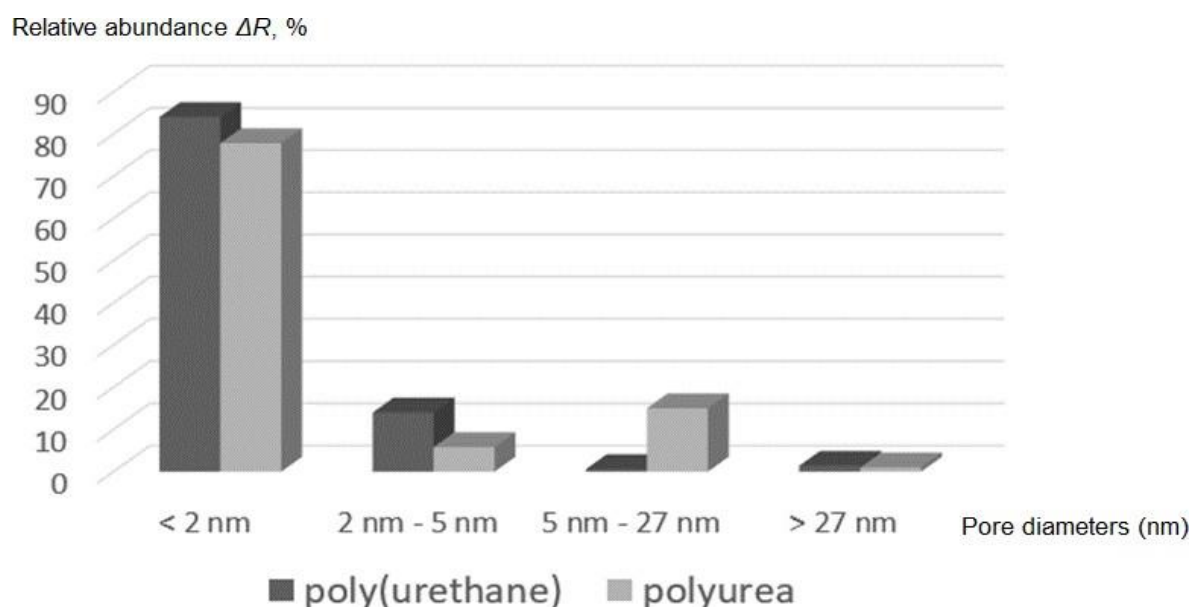


Figure 53: ISEC-derived (relative abundance ΔR , %) pore size distribution (nm) of polyurea and poly(urethane) monoliths.

2.3.4 Summary and Outlook

In this study, a simple approach to fabricating PUR-derived monolithic materials with tailored porosity was shown. The pore diameter can vary from $\varnothing_{\text{Pore}} = 2\text{--}27$ nm selectively by adjusting the ratio and nature of the compounds used for monolithic support preparation, namely the monomer, crosslinker, initiator, and porogenic solvents. PUR-derived monolithic supports meet the general requirements for polymeric monoliths such as unitary structure, in-compressibility, transport pores in the micrometer range, and high linear flow (> 2 mm/s) at low back pressure (< 2 bar) while having a tailored mesoporosity in the low-nm range. It was essential to adjust the back pressure to carry out the ISEC measurements. Adjusting the THP/TEG ratio resulted in lower backpressures in the CHCl_3 solvent system. The tri-functional structure of the HMDI-trimer allowed for flexible, long cross-linked polymer chains, which resulted in early onset phase-separation and increased micro-/mesoporosity. The mesoporosity of *PUR1* (ΔR : 7.5 %) was in the range of 2.0 - 4.4 nm. For monoliths, *PUR2* and *PUR3*, switching from MDI to HMDI resulted in increased mesoporosity (ΔR) of 14% and 11.5%, respectively, in the range of 2.0 - 5.2 nm. The microporogen change from dioxane to diglyme (*PUR3* \rightarrow *PUR4*) increased the solubility of poly(urethane) in diglyme compared to the dioxane, caused the earlier onset phase separation, led to the smaller pores in the structure and enabled a shift in the ΔR : 30.7% throughout the mesopores region (2-27 nm). However, the inclusion of diglyme (*PUR4*) to the PUR monolith lowered the ϵ_p value to 8% and the ϵ_z to 26%. The lack of macroporogen (MTBE) caused the polymer chains to pack more tightly together, which led to a more compact packing of the polymer chains and a lower porosity. *PUR1* was characterized with a specific surface area of 0.54 m²/g and a pore volume of 1 $\mu\text{L/g}$ by the N₂-sorption analysis. Furthermore, switching from MDI to the more flexible HMDI-trimer (*PUR2-PUR4*) resulted in an increased volume fraction of pores and pore volumes, with specific surface areas ranging from 1.86 m²/g to 2.07 m²/g and pore volumes ranging from 3 $\mu\text{L/g}$ to 4 $\mu\text{L/g}$. However, even under dry conditions, the *PUR1*-derived monolith revealed 70% microporosity in its structure. SEM of the surface of *PUR1* confirmed the non-porous surface structure of the PUR-derived monolith supports with microglobule diameters in the range of 2–12 μm . In the polyurea-derived monoliths, switching the crosslinker from THP to 1,3,5-tris(4-aminophenoxy)benzene resulted in an increase in mesoporosity (ΔR : ~20%) by enhancing the crosslinkability of the monolith structure.

2.4 Hydrosilylation of Alkynes Using Surface-Functionalized Monolithic Supports with Tailored Mesoporosity

2.4.1 Introduction

SILP is a synthetic concept that combines the benefits of ILs with those of heterogeneous support materials [195-199]. Immobilization of ILs on a solid, insoluble support can be performed via physical adsorption. The IL creates a thin layer of liquid on the carrier, which allows for the use of less IL in comparison to the reaction in the bulk. It also improves mass transfer to the catalytic centers on the fluid-fluid phase boundary and facilitates separation of the catalyst from the reaction mixture. Moreover, a heterogeneous *SILP* can be successfully employed in both batch and flow processes, including continuous reactors.

During our activities in the area of molecular heterogeneous catalysis in confined geometries [58,61,63], we were interested in synthesizing polyurethane-based monolithic supports that fulfill the general requirements for polymeric monoliths such as unitary structure, incompressibility, transport pores in the micrometer range, high linear flow (up to 20 mm s⁻¹) at low back pressure (<10bar), and a tailored mesoporosity in the 2–10 nm range. We successfully prepared surface-functionalized PUR-derived monoliths under *SIPS* conditions using MDI, TEG, and THP as monomers; DBTDL as a catalyst; as well as dioxane and MTBE as solvents. We prepared monoliths using a 10% excess of hydroxyl groups with respect to the isocyanate groups inside a stainless-steel column (d x l: 4.6 mm x 150 mm, V_{column} = 2.49 mL) and characterized them by means of ISEC. To determine the distribution and accessibility of excess hydroxyl groups on the monoliths, we conducted confocal laser scanning microscopy (CLSM) investigations with representative fluorescent probe molecules, namely a non-covalent polymeric pore-filling agent (Rhodamine B-PEG, RhB-PEG, M_n=5000 g mol⁻¹) and the organosilane 3-(2,4-dinitrophenylamino)propyltriethoxysilane (DPPS), capable of covalently binding to the hydroxyl groups. We then surface-functionalized the mesoporous monoliths with quaternary ammonium groups [NCO-C₆H₄-NMe₃⁺] [BF₄⁻] and subsequently immobilized an ionic Rh-catalyst-containing IL for use in heterogeneous, biphasic, continuous catalysis using the mesopores as confinements [64,66] that ultimately govern the reactivity of the Rh-catalyst. EDX characterized the existence of the

immobilized ionic monomer within the monolithic structure. We performed the hydrosilylation of both aromatic and aliphatic 1-alkynes (i.e., phenylacetylene, 4-ethynyltoluene, 4-ethynylanisole, 1-hexyne, 1-octyne, and 1-nonyne) with HSiMe_2Ph under continuous biphasic conditions at 55 °C using $[\text{BMIM}^+][\text{BF}_4^-]$ as the monolith-supported IL phase, MTBE as the second liquid transport phase, and the cationic Rh-NHC complex $[1-(\text{Pyrid-2-yl})-3\text{-mesityl-imidazol-2-ylidene}](\eta^4\text{-1,5-cyclooctadiene})\text{Rh(I) tetrafluoroborate}$ [170] dissolved in the IL phase, applying a linear flow of 0.2 mL min^{-1} . For comparison, we also carried out hydrosilylation reactions at 55 °C under batch- biphasic conditions using 1 mol-% of the cationic Rh(I) NHC complex with respect to the 1-alkyne dissolved in $[\text{BMIM}^+][\text{BF}_4^-]$, employing MTBE as the secondary liquid phase. Reactions were monitored by ^1H nuclear magnetic resonance (NMR) and gas-chromatography-mass spectroscopy (GC-MS) using n-dodecane as the internal standard.

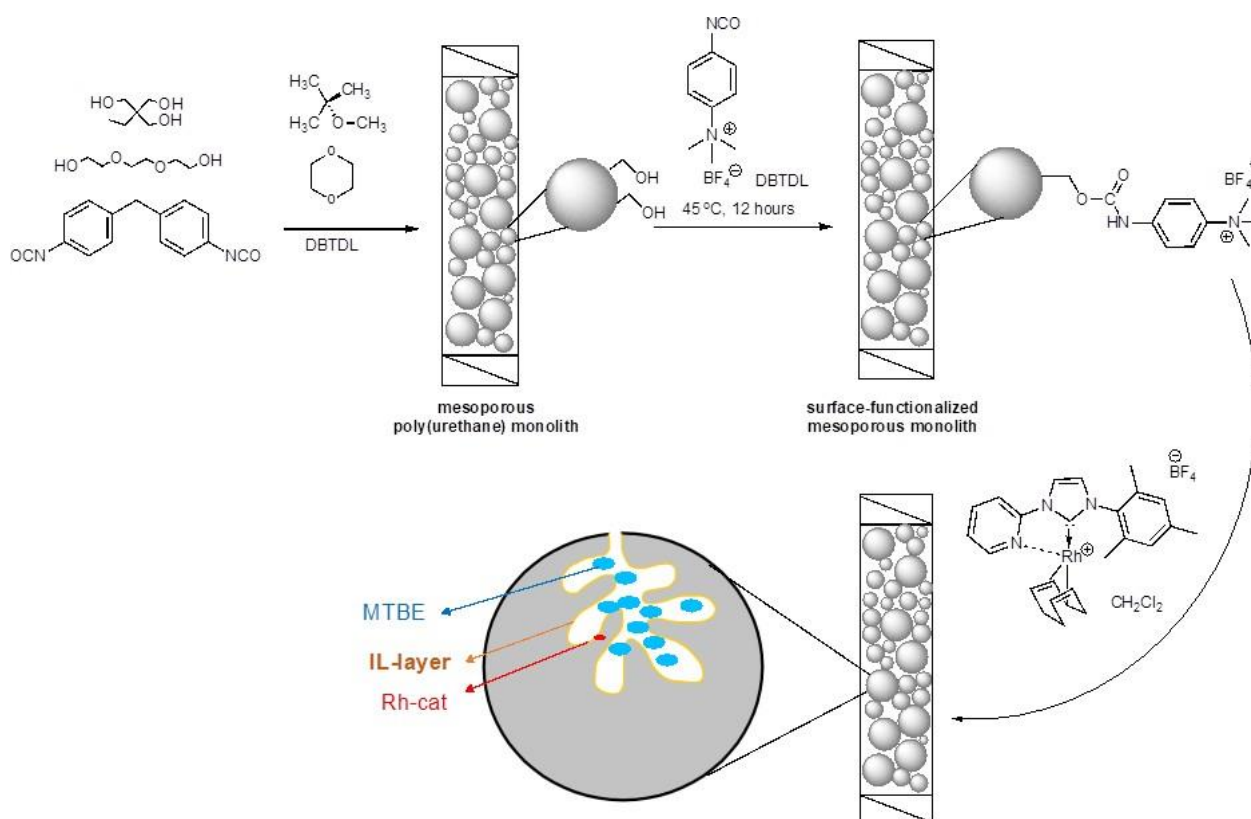


Figure 54: Surface functionalization and immobilization of $[\text{BMIM}^+][\text{BF}_4^-]$, containing a cationic Rh(I)-NHC complex onto the surface of a hydroxyl-containing polyurethane-based monolith.

We conducted the same study, *SILP*-based hydrosilylation reactions, using ROMP-derived monolithic supports. Here, we prepared surface-functionalized ROMP-derived monoliths by reacting NBE monomer with the cross-linkers TMPTNC and DMNH6 in the presence of the two porogenic solvents 2-propanol and toluene. We used NBE-CH₂OH as a functional *co-monomer* and [RuCl₂(PCy₃)₂(CHC₆H₅)] (*G1*, Cy = cyclohexyl) as the initiator. Surface grafting was accomplished by simply passing a solution of the ionic monomer ([NCO-C₆H₄-NMe₃][BF₄]) throughout the ROMP monolith immediately after its synthesis. In the final step, the living Ru-alkylidene was completely removed by treatment with ethyl vinyl ether. We carried out the hydrosilylation of terminal alkynes at 55 °C under biphasic conditions using 1 mol-% of the cationic Rh-NHC complex[1-(Pyrid-2-yl)-3-mesityl]-imidazol-2-ylidene)(η⁴-1,5-cyclooctadiene)rhodium (I) tetrafluoroborate] [170] with respect to the 1-alkyne dissolved in [BMIM⁺][BF₄], employing MTBE as secondary liquid phase. Homogenous conditions: catalyst: substrate (1:200); CDCl₃ was also used to determine the confinement efficiency in the ROMP-derived porous system.

2.4.2 Result and Discussion

2.4.2.1 Preparation and Characterization of Surface-Functionalized Poly(urethane)-Derived Monolithic Supports

During our activities in the area of molecular heterogeneous catalysis in confined geometries, we prepared non-porous polyurethane-based monoliths under *SIPS* conditions. We used MDI, polyethylene glycol (PEG₃₀₀), and THP as monomers, DBTDL as a catalyst, and dioxane and MTBE as solvents. The tailored monomer-to-crosslinker ratio offered access to non-porous polyurethane monoliths that allowed for high linear flow rates ($\leq 13 \text{ mm min}^{-1}$) at low counter back pressure (6-7 bar). The polyaddition reaction was carried out in a vertically oriented steel column (8 × 300 mm) at 45 °C over 18 h. Once the reaction was complete, we flushed the columns with CHCl₃ at a flow rate of 2.0 mL min⁻¹ for 3 h to remove the catalyst, the solvents, and any unreacted monomer. The volume fraction of the intermicroglobule void volume (interstitial porosity) as determined by ISEC was 63%, which explains the good permeability of the monoliths, resulting in the above-mentioned low back pressures at high linear flow rates.

To increase the accessible surface area, we modified the *SIPS* conditions used for the synthesis of the non-porous polyurethane monoliths outlined such that mesoporosity was generated. To this end, PEG₃₀₀ was substituted by TEG to increase the polarity of the polymerization mixture, facilitate mixing of the components, and allow for larger amounts of the macroporogen.

To reduce the complexity of the *SIPS* process, all variations in the polymerization mixture were restricted to changes in the solvent mixture. An increase in the amount of MTBE ($\delta = \text{ca. } 14.5 \text{ MPa}^{0.5}$) from 39.5 to 45.4 wt.-% at the expense of dioxane ($\delta = 20.3 \text{ MPa}^{0.5}$), whose content was reduced from 39.5 to 33.5 wt.-%, led to a decrease in the average Hildebrand solubility parameter, which enabled the onset of phase separation to shift to an earlier stage of polymerization. This in turn changed the ISEC-derived pore size distribution and resulted in a strong reduction of the volume fraction of micropores ($\leq 2 \text{ nm}$) from ca. 70% to ca. 40% (Figures S34 – S41, S.I.). At the same time the volume fraction of mesopores in the range of 2 – 10 nm almost doubled (22% \rightarrow 41%) while the volume fraction of larger mesopores up to 50 nm remained almost constant. The volume fraction of the pores (ϵ_p) and the volume fraction of the inter-microglobule void volume (ϵ_z) were 4-6% and 50-75% respectively (Table 13). These values resulted in a total porosity of (ϵ_t) 55-79%. Considering monolith *P5*, prepared from excess THP, the high porosity of the monolith is mainly caused by the interstitial porosity ($\epsilon_z = 75\%$) and guarantees a low backpressure under continuous flow. Pore volumes (V_p) were in the range of 1 - 7 mL/g as determined via N₂-sorption analysis, compared with 920, 100, 120, and 110 mL/g for *P2* – *P5*, and as determined by ISEC. This finding illustrates the importance of non-permanent (swelling) porosity in these monoliths in “good” polymer solvents such as CHCl₃. The drop from 920 to 100–120 mL/g is in line with increased mesoporosity in monoliths *P3* – *P5*. Notably, complementary to a recently reported template-based approach [73], this is the first successful report on the tuning of the pore diameters of monolithic materials in the low mesopore region via *SIPS*.

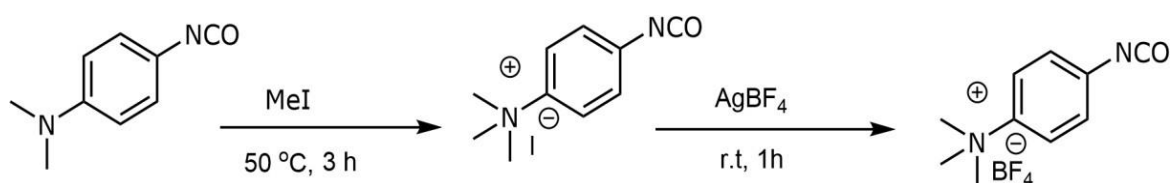


Figure 55: Synthesis of ionic [NCO-C₆H₄-NMe₃][BF₄].

We prepared monolith P5 using a 10 % excess of hydroxyl groups with respect to the isocyanate groups. The use of this comparably small excess of hydroxyl groups allowed us to retain a high maximum possible conversion of the polyaddition reaction while still providing ca. 40% mesoporosity in the range of 2-40 nm. The excess hydroxyl groups were then reacted with $[\text{NCO-C}_6\text{H}_4\text{-NMe}_3^+][\text{BF}_4^-]$ in the presence of DBTDL to introduce ionic groups at the monolith's surface, followed by flushing with CH_2Cl_2 to remove excess $[\text{NCO-C}_6\text{H}_4\text{-NMe}_3^+][\text{BF}_4^-]$. Finally, we introduced the cationic Rh-NHC catalyst and $[\text{BMIM}^+][\text{BF}_4^-]$ dissolved in CH_2Cl_2 into the monolithic column, and we applied a vacuum to remove all solvents and to immobilize both the catalyst and the IL on the monolith's surface. Finally, the support was flushed with heptane to remove any excess $[\text{BMIM}^+][\text{BF}_4^-]$.

Table 12: Recipes for the synthesis of the polyurethane-based monoliths P1 - P5 (all wt.-%).

#	THP ¹⁾	PEG ₃₀₀	TEG ¹⁾	MDI ¹⁾	DBTDL ¹⁾	MTBE ¹⁾	dioxane ¹⁾
P1	4.2	1.8		13.1	3.9	53	24
P2	4.8		0.08	13.6	2.4	39.6	39.6
P3	4.8		0.08	13.6	2.4	43.6	35.6
P4	4.8		0.08	13.6	2.4	45.5	33.7
P5	5.1		0.08	13.3	2.4	45.5	33.7

¹⁾wt-%.

Table 13: Values of the pore volume, V_p , the specific surface area, the volume fraction of pores, ϵ_p , the volume fraction of intermicroglobule void volume (interstitial porosity), ϵ_z , and the total volume fraction, ϵ_t of monoliths P1-P5.

#	ϵ_p [%] ¹⁾	ϵ_z [%] ¹⁾	ϵ_t [%] ¹⁾	V_p [mL/g] ¹⁾	V_p [mL/g] ²⁾	σ [m ² /g] ²⁾
P1	4	63	67	0.62	0.002	1.01
P2	6	71	77	0.92	0.007	0.69
P3	4	51	55	0.10	0.001	0.15
P4	6	50	56	0.12	0.003	0.40
P5	4	75	79	0.11	0.004	0.50

¹⁾Determined by ISEC in CHCl_3 , flow rate: 2.0 mL/min, 35 °C, column: 8 x 300 mm. ²⁾ Determined by N_2 -sorption.

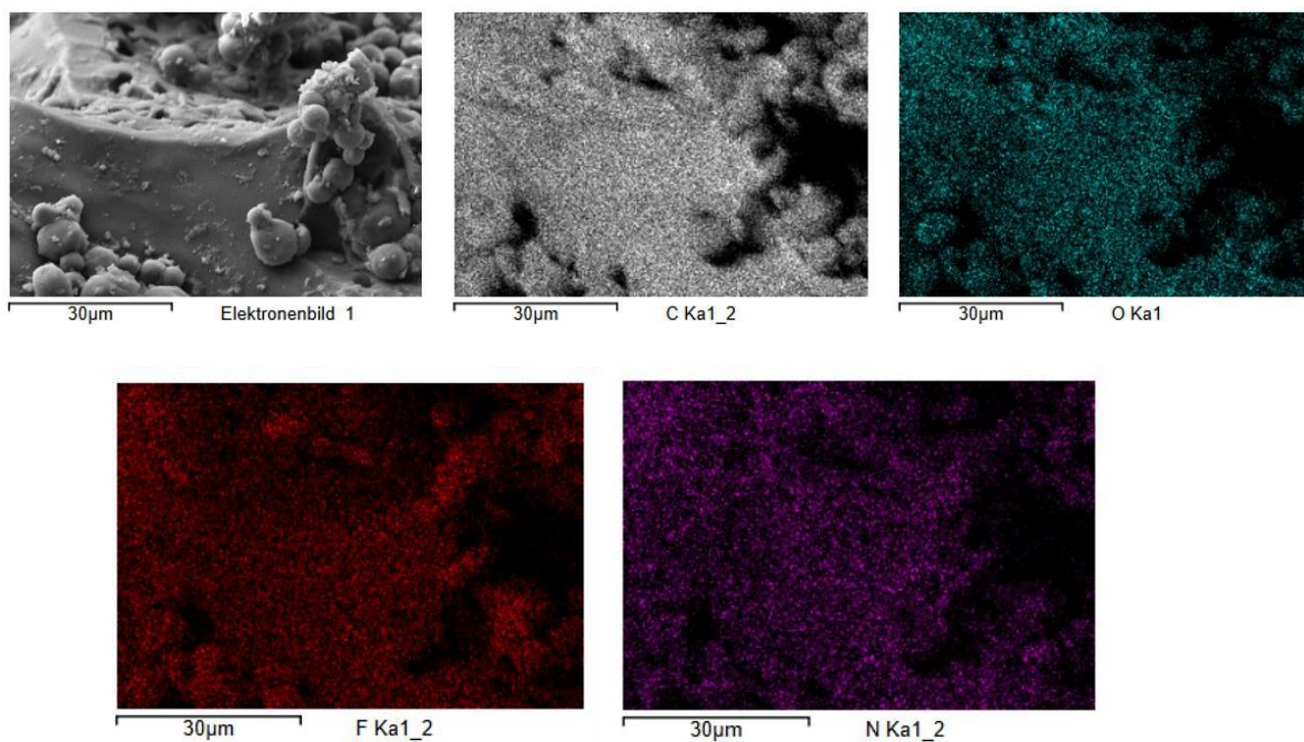


Figure 56: EDX mapping of $[\text{NCO-C}_6\text{H}_4\text{-NMe}_3][\text{BF}_4]$ -surface-functionalized PUR monolith P5.

EDX mapping confirmed the presence of F along with C, O, and N throughout the polymeric matrix (Figure 56); F was homogeneously distributed over the entire PUR-polymeric matrix. The ionic monomer, $[\text{NCO-C}_6\text{H}_4\text{-NMe}_3][\text{BF}_4]$, was hence successfully covalently attached to the PUR-derived polymeric matrix.

2.4.2.1.1 Confocal Laser Scanning Microscopy (CLSM) Measurements

To determine the distribution and accessibility of excess hydroxyl groups on the monoliths, we conducted CLSM investigations with representative fluorescent probe molecules, namely a non-covalent polymeric pore-filling agent (Rhodamine B-PEG, RhB-PEG $M_n = 5000 \text{ g mol}^{-1}$) and the organosilane 3-(2,4-dinitrophenylamino)propyltriethoxysilane (DPPS), capable of covalently binding to the hydroxyl groups. We first treated monolith P5 with RhB-PEG and subsequently functionalized it with DPPS. Since RhB-PEG and DPPS fluoresce at different wavelengths, their spatial distributions can be resolved by using different excitation lasers. Figure 57 depicts the CLSM image of a representative optical slice from the middle of the sample.

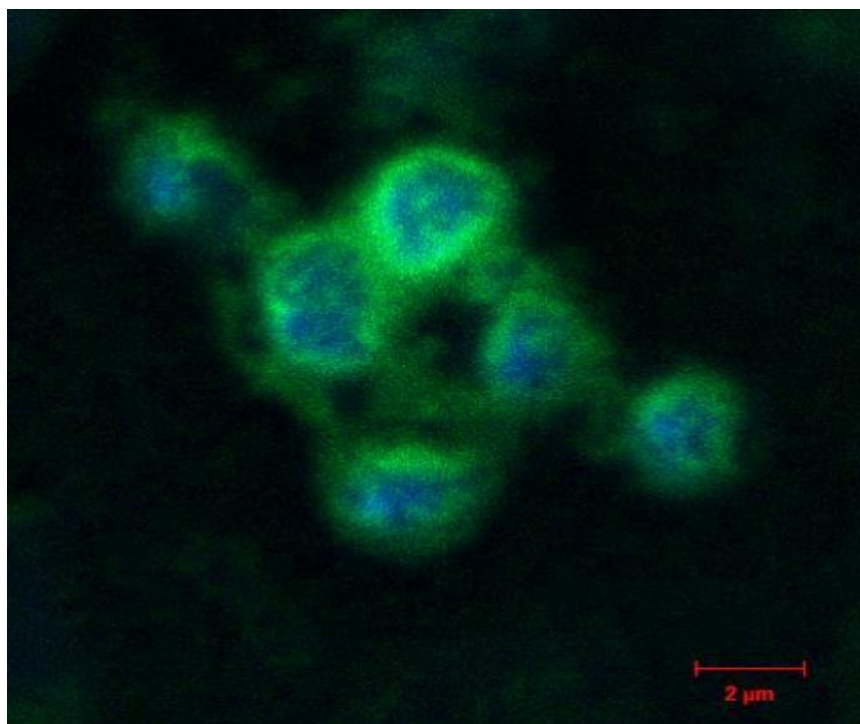


Figure 57: CLSM image of monolith P5 first filled with rhodamine B - PEG (green), then functionalized with DPPS (blue).

The green and blue regions correspond to the spatial distributions of RhB-PEG and DPPS, respectively. According to the CLSM image, RhB-PEG is largely constrained to the surface of the structure-forming microglobules, while DPPS is distributed far more substantively across the porous matrix. A precise visualization of the micropore and mesopore domains was not achieved due to the diffraction-limited resolution of CLSM. However, a qualitative interpretation of the spatial permeation behavior of the two probe molecules can be made based on their molecular size. On the one hand, since RhB-PEG is much larger than DPPS, its diffusion into the microporous domain is restricted, and thus its localization is constrained to the external surface of the microstructure-forming microglobules. On the other hand, the relatively smaller DPPS can permeate into the microporous domain as well. We also prepared reference samples in which P5 was only treated with RhB-PEG and DPPS, and we observed a similar trend in their spatial distribution (data not shown). Since the covalently binding DPPS permeates extensively across the microstructure of P5, it can be surmised that excess hydroxyl groups exist throughout the monolithic structure and can thus offer sites for subsequent functionalization. The presence of excess hydroxyl groups in the

micropore domain also explains the substantial non-permanent (swelling) porosity observed due to the swelling of the monolith structure in “good” polymer solvents such as CHCl_3 (vide supra).

2.4.2.1.2 Continuous Hydrosilylation of Alkynes Using Surface-Functionalized Poly(urethane)-Derived Monolith-Supported Ionic Liquids (ILs)

For continuous flow applications, it is essential to develop a system in which the ionic catalyst used is selectively soluble in the IL phase but not in the solvent/reactant phase. The ILs must show non-miscibility with common non-polar, organic solvents as well as a liquid state of matter at the reaction temperature. Therefore, the IL must have a melting point below 40°C . The reactants must show high solubility in both phases, and the reaction products must preferentially dissolve in the mobile phase. The hydrosilylation of both aromatic and aliphatic 1-alkynes, (i.e., phenylacetylene, 4-ethynyltoluene, 4-ethynylanisole, 1-hexyne, 1-octyne, and 1-nonyne), with HSiMe_2Ph was performed under continuous biphasic conditions at 55°C . We used $[\text{BMIM}^+][\text{BF}_4^-]$ as the monolith-supported IL phase and MTBE as the second liquid transport phase, and we used the cationic Rh-NHC complex $[\text{1-(pyrid-2-yl)-3-mesityl-imidazol-2-ylidene}](\eta^4\text{-1,5-cyclooctadiene})\text{Rh(I) tetrafluoroborate}$ [170] dissolved in the IL phase applying a linear flow of $0.2 \text{ mL}\cdot\text{min}^{-1}$.

In general, the choice of IL proved to be a crucial for the supported ILs catalysis applications [217,218]. We chose the BF_4^- anion to prevent anion metathesis with the catalyst and to ensure immiscibility with the second transport phase (i.e., with MTBE). For comparison, we also carried out hydrosilylation reactions at 55°C under biphasic conditions using 1 mol-% of the cationic Rh(I) NHC complex with respect to the 1-alkyne dissolved in $[\text{BMIM}^+][\text{BF}_4^-]$, and we employed MTBE as the secondary liquid phase. Reactions were monitored by ^1H NMR and GC-MS using *n*-dodecane as the internal standard. With all substrates, we observed a clear preference for the thermodynamically more stable $\beta(E)$ -isomer in the range of 55-85% (Table 14, Figure 58).

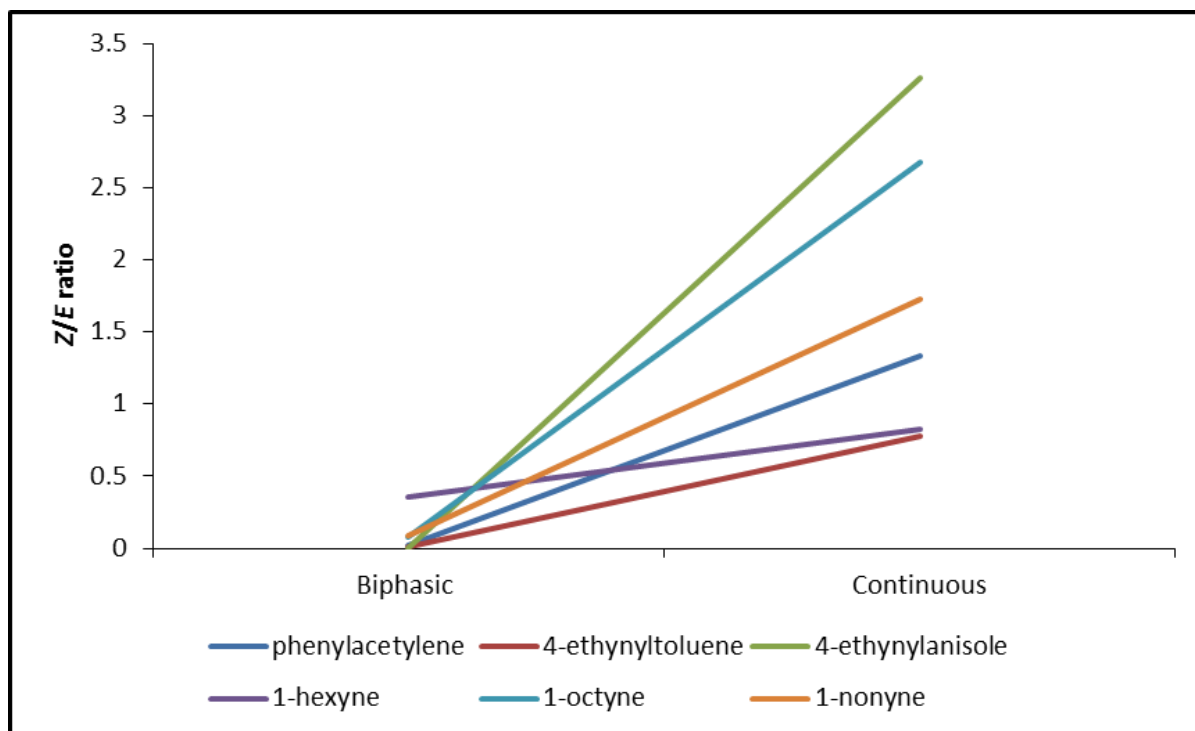


Figure 58: Z/E ratio under biphasic and continuous conditions.

As Figure 58 illustrates, the Z/E ratio (Z -content) of the hydrosilylation products increased substantially up to 3.26:1 for 4-ethynylanisole (62% Z -isomer) when the reactions were performed under monolith supported, biphasic continuous flow conditions compared with reactions carried out under biphasic conditions. This increase in Z -selectivity is attributed to a confinement effect [170] created by the constrained geometry inside the small mesopores, which affects the transition state of the Rh-catalyst, favoring a Z -arrangement. In line with that are the lower conversions with the monolith supported catalyst, which are a consequence of the slower diffusion inside the pores. Notably, the monitoring of the hydrosilylation of 4-ethynyltoluene and 1-octyne with dimethylphenylsilane under biphasic conditions revealed the formation of the $\beta(E)$ -isomer from the beginning of the reaction, suggesting a lack of $Z \rightarrow E$ isomerization (Figure S56, Supporting Information).

Table 14: Hydrosilylation of terminal alkynes.¹ 1 mol% Rh-catalyst, [BMIM⁺][BF₄⁻]:MTBE = 1:5, 55 °C, 12 h. ²Rh@[BMIM][BF₄] immobilized on surface grafted monolith P5, MTBE, 55 °C, 0.2 mL·min⁻¹, 24 – 48 h, catalyst loading 8 mg/monolith.

Substrate	Biphasic conditions ¹			Continuous conditions ²		
	$\beta(Z)/\beta(E)/\alpha$	Z/E	Conversion (%)	$\beta(Z)/\beta(E)/\alpha$	Z/E	Conversion (%)
phenylacetylene	2/80/18	0.02	45	40/30/30	1.33	34
4-ethynyltoluene	1/85/14	0.01	67	35/45/20	0.78	39
4-ethynylanisole	-/75/25	0	78	62/19/19	3.26	24
1-hexyne	20/55/25	0.36	45	35/42/23	0.83	24
1-octyne	6/75/19	0.08	29	59/22/19	2.68	12
1-nonyne	7/73/20	0.09	42	52/30/18	1.73	19

2.4.2.2 Preparation and Characterization of Surface-Functionalized ROMP Derived Monolithic Supports

We prepared functionalized ROMP-derived monoliths by reacting NBE monomer with the cross-linkers TMPTNC and DMNH6 in the presence of the two porogenic solvents 2-propanol and toluene. NBE-CH₂OH was used as a functional co-monomer, and we chose [RuCl₂(PCy₃)₂(CHC₆H₅)] (*G1*, Cy=cyclohexyl) as the initiator. Surface grafting was accomplished by simply passing a solution of the ionic monomer ([NCO-C₆H₄-NMe₃][BF₄]) throughout the ROMP monolith immediately after its synthesis. In the final step, the living Ru-alkylidene was completely removed by treatment with ethyl vinyl ether. As Figure 59 illustrates, the IL ([BMIM]⁺[BF₄]⁻) is homogeneously distributed throughout the ROMP-derived monolith structure. This functionalized ROMP-derived monolith was then used in hydrosilylation reactions.



Figure 59: ROMP-derived monolith structure after hydrosilylation reactions.

As shown in Table 15, we prepared the ROMP-derived monoliths using different amounts of NBE-CH₂OH to investigate the effects of the hydroxyl groups on the performance of the hydrosilylation reactions. The surface-functionalized monoliths were characterized using ISEC analysis. Corresponding to an NBE-CH₂OH content of 2 w.t%, monolith NbN1 exhibited an ϵ_z value of 44%. Similarly, monoliths NbN2 and NbN3, based on 2.6 w.t% and 4 w.t% NBE-CH₂OH, showed ϵ_z values of 67% and 49%, respectively. According to Figure 60, an increased number of hydroxyl groups on the monolithic surface (NbN3) results in an increased relative abundance of mesopores (ΔR : 12.2%) in the range of 2.72–5.30 nm (Figure S60, SI). As mentioned earlier, depending on the Hildebrand solubility parameters of the polymers and solvent system, the solubility of the ROMP-derived monolith skeleton in toluene increases with the addition of NBE-CH₂OH to the monolithic structure, resulting in an earlier onset of phase separation and smaller pore sizes.

Table 15: Physicochemical and structural data for the ROMP-derived monoliths NbN1 - NbN3; 1: Grubbs' 1st-generation catalyst, CL-1; DMNH6, CL-2; TMPTNC.

#	Polymerization mixture [wt.-%]							Structural data		
	NBE ¹⁾	NBE-CH ₂ OH ¹⁾	CL-1 ¹⁾	CL-2 ¹⁾	1 ¹⁾	Toluene ¹⁾	2-Pr-OH ¹⁾	ϵ_p [%] ¹⁾	ϵ_z [%] ¹⁾	ϵ_t [%] ¹⁾
NbN1	20	2	11	11	2.3	11	42.3	12	44	56
NbN2	19.4	2.6	11	11	2.3	11	42.3	12	67	79
NbN3	18	4	11	11	2.3	11	42.3	13	49	62

¹⁾wt-%.

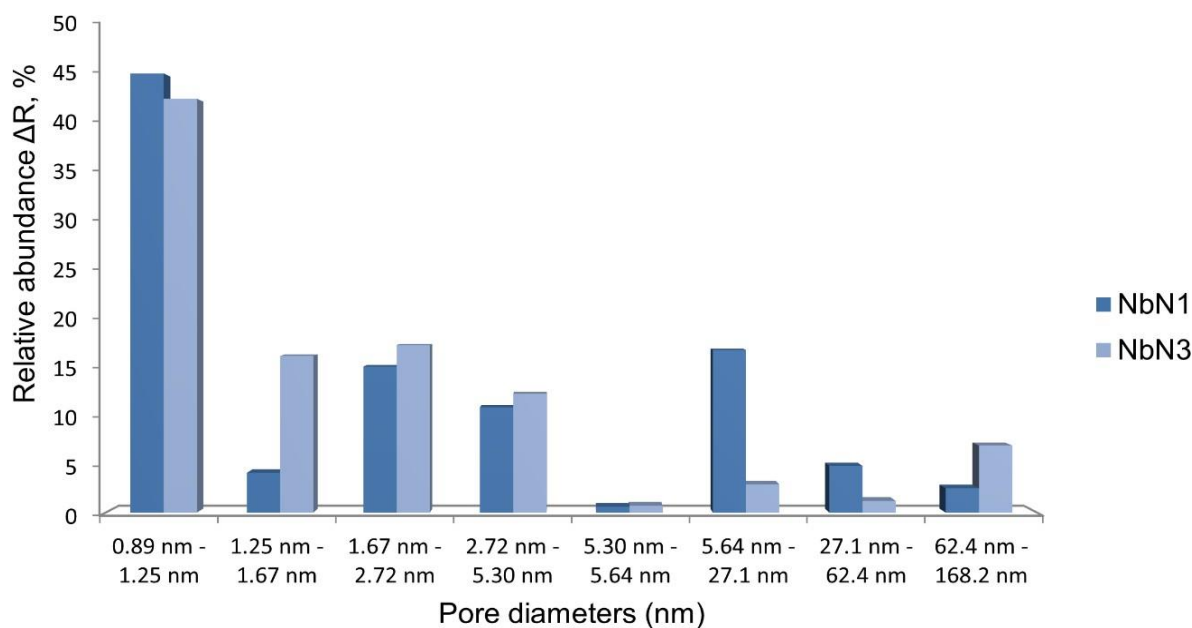


Figure 60: ISEC-derived distribution (Relative abundance ΔR , %) of pore diameters (nm) of the surface-functionalized ROMP-derived monolithic support.

2.4.2.2.1 Hydrosilylation of Alkynes Using Surface-Functionalized ROMP-Derived Monolith-Supported ILs

We carried out the hydrosilylation of terminal alkynes at 55 °C under biphasic conditions using 1 mol-% of the cationic Rh-NHC complex [1-(Pyrid-2-yl)-3-mesityl-imidazol-2-ylidene)](η^4 -1,5-cyclooctadiene)rhodium(I) tetrafluoroborate] [170] with respect to the 1-alkyne dissolved in [BMIM⁺][BF₄⁻], and we employed MTBE as the secondary liquid phase. Homogenous conditions: Catalyst:substrate (1:200), CDCl₃ also used to determine the confinement efficiency in the ROMP-derived porous system.

To understand the Chalk-Harrod [169] mechanism of the reactions catalyzed by Rh-NHC complex, we monitored the hydrosilylation of terminal alkynes with HSiMe₂Ph by ¹H NMR and GC-MS using n-dodecane as the internal standard. For the immobilization of Rh(I)-NHC using HSiMe₂Ph, we employed three different ROMP-derived monoliths with defined average pore diameters of 2.0 nm and 10 nm, respectively, referred to as *NbN1*, *NbN2*, and *NbN3*. As indicated in Figure 60, the increased percentage of hydroxyl groups (-OH) causes an increased ΔR of swell-induced micro- mesoporosity in the range of 1.25 – 5.30 nm. Table 16 shows that the Z/E ratio (Z-content) of the

hydrosilylation products increased substantially up to 1.92:1 for 4-ethynyltoluene (54% Z-isomer) when the reactions were performed under monolith-supported, biphasic conditions compared with reactions carried out under homogenous conditions. In addition, the reaction of HSiMe₂Ph with phenylacetylene under biphasic conditions catalyzed by Rh(I)-NHC yielded the corresponding β -(E)-alkylsilane accompanied by higher amounts (57-58 % α -isomer) of the Markovnikov silane addition product. Consequently, using the ROMP-derived supported catalysis system provides a sufficient steric confinement effect [170] created by the constrained geometry inside the small mesopores.

Table 16: Hydrosilylation reactions under biphasic and monolith-supported conditions. (Homogenous conditions: N0 Catalyst:substrate (1:200), CDCl₃, Biphasic conditions: IL:MTBE (1:5), Catalyst:substrate (1:200), Monolith Support: Rh-NHC_{monolith}, MTBE, Ionic Liquid: [BMIM]⁺[BF₄]⁻).

Selectivity profile for homogeneous conditions N0					
Substrate	Conversion (%) (48h)	Cis (%)	Trans (%)	Alpha (%)	Z/E
1-Hexyne	37	20	55	25	0.36
1-Octyne	35	6	75	19	0.08
1-Nonyne	16	7	73	20	0.09
Phenyl acetylene	72	2	80	18	0.02
4-Ethynyltoluene	58	1	85	14	0.01
4-Ethynylanisole	51	-	75	25	0
Selectivity profile for monolith NbN1					
Substrate	Conversion (%) (48h)	Cis (%)	Trans (%)	Alpha (%)	Z/E
1-Hexyne	28	44	24	32	1.83
1-Octyne	20	34	37	29	0.91
1-Nonyne	22	26	39	35	0.66
Phenyl acetylene	17	7	75	19	0.09
4-Ethynyltoluene	8	16	48	36	0.33
4-Ethynylanisole	15	14	54	32	0.25
Selectivity profile for monolith NbN2					
Substrate	Conversion (%) (48h)	Cis (%)	Trans (%)	Alpha (%)	Z/E
1-Hexyne	64	8	88	4	0.09
1-Octyne	18	11	81	8	0.13
1-Nonyne	30	6	88	6	0.06
Phenyl acetylene	15	4	39	57	0.10
4-Ethynyltoluene	12	54	28	18	1.92
4-Ethynylanisole	7	50	29	21	1.72

Selectivity profile for monolith NbN3					
Substrate	Conversion (%) (48h)	Cis (%)	Trans (%)	Alpha (%)	Z/E
1-Hexyne	50	4	93	3	0.04
1-Octyne	30	8	86	6	0.09
1-Nonyne	32	8	84	8	0.09
Phenyl acetylene	14	3	39	58	0.07
4-Ethynyltoluene	8	55	29	16	1.89
4-Ethynylanisole	7	49	32	19	1.53

¹⁾Determined by ISEC in CHCl₃.

2.4.3 Summary and Outlook

In summary, we prepared non-porous PUR-based monoliths. The rigid non-porous structure enabled high linear flow rates up to 13 mm/min with low counter pressure (< 7 bar). The pore size distribution obtained from ISEC confirms the non-porous nature of the monoliths but reveals some solvent-induced swelling propensity. We synthesized the first polyurethane-based monolith with tailored mesoporosity in the range of ≈ 2 –10 nm via *SIPS* by carefully changing the ratio of the porogenic solvents. We accomplished surface-functionalization of the poly(urethane)-derived monoliths via reaction with 4-isocyanatophenyltrimethylammonium tetrafluoroborate. To increase the accessible surface area, we changed the *SIPS* conditions utilized for the synthesis of the non-porous polyurethane monoliths described above such that mesoporosity was produced. The substitution of PEG₃₀₀ by TEG resulted in a strong reduction of the volume fraction of micropores (≤ 2 nm) from $\approx 70\%$ to $\approx 40\%$.

PUR-derived monolith *P5* was prepared using a 10% excess of hydroxyl groups with respect to the isocyanate groups. The use of a small excess of hydroxyl groups provided $\approx 40\%$ mesoporosity in the range of 2–40 nm. The distribution and accessibility of excess hydroxyl groups on the PUR-derived monoliths were confirmed through CLSM analyses. We then used polymeric monolithic supports in the application of *SILP* catalysts for the hydrosilylation reaction, thereby resolving the mass transport problem due to the thin film of ILs and a facile recycling of the immobilized catalyst from the reaction mixture. Excess hydroxyl groups were reacted with [NCO-C₆H₄-NMe₃⁺] [BF₄⁻] in the presence of DBTDL to introduce ionic groups at the surface of the PUR-derived monolith. Finally, immobilization of the IL [BMIM⁺][BF₄⁻] containing [1-(pyrid-2-yl)-3-mesityl]-imidazol-2-ylidene)) (η^4 -1,5-cyclooctadiene)

rhodium(I) tetrafluoroborate] on a mesoporous monolith allowed for hydrosilylation reactions under continuous polymer-supported biphasic conditions. The use of the Rh(I) catalyst supported on surface-modified PUR monoliths under continuous flow resulted in a significant improvement in selectivity toward -(Z)- vinylsilanes (62% Z-isomer), which can be attributed to a steric confinement effect produced by the mesoporous system.

SILP-based hydrosilylation reactions were also conducted on ROMP-derived monolithic supports. In that case, we prepared ROMP-derived monoliths with excess hydroxyl groups by using 5-norbornen-2-methanol as a functional co-monomer and $[\text{RuCl}_2(\text{PCy}_3)_2(\text{CHC}_6\text{H}_5)]$ (*G1*, Cy=cyclohexyl) as an initiator. The ROMP-derived monoliths were characterized with defined average pore diameters of 2.0 and 10 nm using ISEC. Surface grafting was accomplished by simply passing a solution of the ionic monomer ($[\text{NCO-C}_6\text{H}_4\text{-NMe}_3][\text{BF}_4]$) throughout the ROMP monolith directly after its synthesis. In the final step, the living Ru-alkylidene was completely removed by treatment with ethyl vinyl ether. Using the ROMP-supported Rh(I) catalyst under biphasic conditions provides a sufficient steric confinement effect and yielded substantially up to 1.92 for 4-ethynyltoluene (54% Z-isomer).

Chapter 3

3. EXPERIMENTAL AND SPECTROSCOPIC DATA

3.1 General

NBE (Fluka) and 5-norbornene-2-methanol (Sigma) were used without further purification. DMNH6 and TMPTNC were prepared according to the literature [33, 220]. Silica nanowires A10 (10 × 200 nm) and AIO(OH) nanowire (d × l : 4 nm × 1 μm) solution were purchased from Novarials. (Bicyclo[2.2.1]hept-5-en-2-yl)triethoxysilane (mixture of isomers) and tetrabutylammonium fluoride were obtained from TCI chemicals. Pluronic F-127 was obtained from Sigma-Aldrich. Triethylene glycol (TEG) (99%), 1,1,1-tris(hydroxymethyl)propane 98% (98%), 1,4-dioxane (99.8%), 4,4'-methylenebis(phenyl isocyanate) (98%) (MDI) were purchased from Sigma–Aldrich. Dibutyltin dilaurate (DBTDL) (95%), polyethylene glycol (PEG₃₀₀), diglyme (99.0%) were purchased from Tokyo Chemical Industry (TCI). Hexamethylene-1,6-diisocyanate trimer (HMDI) was supplied by Bayer. 1,3,5-Tris(4-aminophenoxy)Benzene was supplied by Tokyo Chemical Industry (TCI). 4-(Dimethylamino)phenyl isocyanate and 1-butyl-3-methylimidazolium tetrafluoroborate [BMIM][BF₄] were purchased from Sigma–Aldrich. Rh(I)-NHC complexes were prepared according to the literature by Dr. Pradeep Panyam [170].

Synthesis of ROMP-Derived Monoliths

The general synthetic procedure used was as follows: stainless steel columns (4.6 × 150 mm) were cleaned, rinsed, and sonicated in a 1:1 mixture of chloroform and acetone. Finally, they were dried for 3 h at 120 °C. For the preparation of the ROMP-derived monolith (**N3**), solution I consisted of NBE (0.75 g, 7.9 mmol), (NBECH₂O)₃SiCH₃ (0.375 g), and DMNH6 (0.375 g) dissolved in 2-PrOH (1.8 mL). Solution II contained Grubbs' 1st-generation catalyst RuCl₂(PPh₃)₂(CHPh) dissolved in toluene (0.4 mL). Both solutions were combined and thoroughly mixed. Then, the solution was filled into the vertically oriented steel column, which was closed at one end and polymerization was allowed to proceed for 30 min at 0 °C. After rod formation, each monolith was kept at room temperature for 2 h. For initiator removal, columns were flushed with a mixture of 40 vol.-% ethyl vinyl ether in CHCl₃ for 3 h at a flow rate of 0.5 ml/min. Finally, they were flushed with CHCl₃ for a further 3h at a flow rate of 0.5 ml/min. For functionalized monoliths, 5-norbornene-2-methanol (2 wt.%) was added to the monolith solution to be used in catalysis applications.

Synthesis of Pluronic F-127-containing, ROMP-derived porous monoliths

Pluronic-containing ROMP-derived monoliths were prepared from NBE, norborn-5-ene-2-methanol (NBE-CH₂OH), TMPTNC, DMNH6 and Grubbs' 1st-generation catalyst RuCl₂(PPh₃)₂(CHPh) (**1**) in a mixture of 2-propanol and toluene. A typical procedure for monolith synthesis was as follows: Solution I consisted of NBE (0.67 g, 7.1 mmol), 5-norbornene-2-methanol (0.026 g, 0.2 mmol), TMPTNC (0.365 g, 0.7 mmol) and DMNH6 (0.365 g, 2 mmol) dissolved in 2-PrOH (0.5 mL), and toluene (0.2 mL) and Pluronic F-127 (0.09 g) dissolved in 2-PrOH (0.5 mL) was added to the solution I at 0 °C. Solution II contained initiator **1** (0.03 g, 0.03 mmol) dissolved in toluene (0.2 ml) and was cooled to 0 °C. Both solutions were combined and thoroughly mixed. Then, the solution was filled into the vertically oriented stainless-steel column (V_k: 4.6 × 150 mm i.d.), closed at one end, and polymerization was allowed to proceed for 30 min at 0 °C. After rod formation, each monolith was kept at room temperature for 2 h. For initiator removal, columns were flushed with a mixture of 40 vol.-% ethyl vinyl ether in CHCl₃ for 3 h at a flow rate of 0.3 mL min⁻¹. Finally, they were flushed with CHCl₃ for a further 3 h at a flow rate of 0.3 mL min⁻¹.

Synthesis of SNW-containing, ROMP-derived porous monoliths

SNW-containing porous monoliths were prepared from NBE, norborn-5-ene-2-methanol (NBE-CH₂OH), (bicyclo[2.2.1]hept-5-en-2-yl)triethoxysilane surface-modified SNWs (10 × 200 nm), TMPTNC, DMNH6 and Grubbs' 1st-generation catalyst RuCl₂(PPh₃)₂(CHPh) (**1**) in a mixture of 2-propanol and toluene. A typical procedure for monolith synthesis was as follows: solution I consisted of NBE (0.71 g, 7.5 mmol), 5-norbornene-2-methanol (0.04 g, 0.3 mmol), TMPTNC (0.375 g, 0.75 mmol) and DMNH6 (0.375 g, 2.3 mmol) dissolved in 2-PrOH (1.7 mL), and toluene (0.4 mL). SNWs (0.17 g, 1.87 g cm⁻³) were added to solution I at 0 °C. Solution II contained initiator **1** (0.09 g, 0.1 mmol) dissolved in toluene (0.2 ml) and was cooled to 0 °C. Both solutions were combined and thoroughly mixed. Then, the solution was filled into the vertically oriented stainless-steel column (V_k: 4.6 × 150 mm i.d.), closed at one end, and polymerization was allowed to proceed for 30 min at 0 °C. After rod formation, each monolith was kept at room temperature for 2 h. For initiator removal, columns were flushed with a mixture of 40 vol.-% ethyl vinyl ether in CHCl₃ for 3 h at a flow rate of 0.3 mL min⁻¹. Finally, they were flushed with CHCl₃ for a further 3 h at a flow rate of 0.3 mL min⁻¹.

Synthesis of (bicyclo[2.2.1]hept-5-en-2-yl)triethoxysilane surface modification of SNWs

In a 25-mL pressure tube, 0.10 g dry SNWs were suspended in 2.25 mL of anhydrous toluene; 0.25 mL of (bicyclo[2.2.1]hept-5-en-2-yl)triethoxysilane was added and the mixture was refluxed for 23 h in an oil bath. Then the suspension was transferred into centrifuge bottles and centrifuged at 5000 rpm for 5 min. After three washes in toluene and two washes in acetone, the particle sediment was transferred to a glass beaker and dried for 24 h under vacuum at room temperature followed by 24 h at 115 °C.

***In Situ* Generation of HF for the chemical etching of SNW-containing monoliths**

In a typical procedure, hydrogen fluoride (*HF*) was synthesized in situ from tetra-*n*-butylammonium fluoride (TBAF, 1.74 g, 6.65 mmol) and HCl (6.65×10^{-1} M, 0.24 g, 6.65 mmol) in 10 mL methanol. This mixture was pumped through the SNW-loaded monolith under continuous flow using a monosyringe pump at flow rate of 0.03 mL/min. After etching, the methanol was removed from the column and the column was flushed with CHCl₃ for ISEC measurements.

Titration of the surface hydroxyl groups via back titration with benzylmagnesium chloride

In a typical procedure, 0.70 g monolith with a calculated (-OH) group content of 0.056 mmol OH g⁻¹ was placed in a 50 mL flask containing 10 mL anhydrous THF. Benzylmagnesium chloride (2.0 M in THF, 0.028 mL) was added to the monolith mixture with the aid of a microsyringe and the solution was stirred for 3 h. After filtration and washing with anhydrous THF, distilled water (5 mL) was added, and the solution was stirred for another 2 h. Excess Grignard reagent was titrated with 0.005 M HCl versus phenolphthalein revealing an accessible fraction of OH groups of 56%.

Synthesis of (NBE-CH₂O)₃SiCH₃ (CL)

Trichloromethylsilane (3.63 g, 0.024 mmol) was added dropwise to a solution of 5-norbornene-2-methanol (9.03 g, 0.072 mmol) in 50 mL of CH₂Cl₂ and 12 mL of triethylamine at 0 °C. The reaction mixture was stirred in an ice/water bath for a further 30 min, then at room temperature for a further 2h. The organic phase was washed with 2 x 100 ml portions of water, acetic acid, saturated aqueous sodium bicarbonate and

finally water and dried over magnesium sulfate. Finally, all volatiles were removed in vacuum at 50 °C [221].

¹H NMR (CDCl₃): 0.06, 0.08, 0.1 (s, CH₃Si), 0.43 (m, H⁷), 1.05 (m), 1.20 (s), 1.22 (s), 1.27 (s), 1.40 (m), 1.62 (m), 1.75 (m), 2.28 (m), 2.75 (s), 2.90 (s), 3.05-3.06 (m), 3.24-3.45 (m), 5.9 (m, H⁵, H⁶), 6.10 (m, H⁵, H⁶).

Synthesis of Trimethylolpropane-tris-(5-norbornene-2-yl-carboxylate) (CL)

A solution of (100 g, 0.33 mol) of trimethylolpropane triacrylate (TMPTA) in CH₂Cl₂ (400 mL) was flushed with nitrogen for 15 min. Then, freshly cracked cyclopentadiene (70 g, 1.06 mol) was added dropwise and the reaction mixture was stirred for 16 h at 40°C. The mixture was consecutively washed with 500 mL of saturated NaHCO₃ solution and with 500 mL of water. Finally, the organic layer was dried over anhydrous MgSO₄ and concentrated, then high vacuum was applied for 16 h to obtain the pure product. Yield: 155 g (93%) [33].

¹H-NMR (250 MHz, CDCl₃) δ=0.82-0.89 (m, 3H), 1.22-1.26 (m, 2H), 1.33-1.46 (m, 9H), 1.82-1.92 (m, 3H), 2.17-2.22 (m, 1H), 2.88-2.98 (m, 6H), 3.16 (s, 2H), 3.92-4.09 (m, 6H), 5.83-5.87 (m, 2H), 6.07-6.18 (m, 4H).

Oleic acid (OA)-surface modification of SNWs

A 100 mg sample of the SiO₂ nanowires was heated to ~90 °C under vacuum for 24 h to drive off any adsorbed water. n-Hexane (20 ml) and OA (0.02 g) were mixed under stirring, then the SiO₂ nanowires (0,1 g) were added to them. The mixture was heated under vigorous stirring at 60 °C for 4 h. The solution was then filtered, and the precipitate was rinsed thoroughly with the mixed solvent of ethanol and deionized water. The precipitate was kept in a vacuum desiccator for 24 h. A white powder was obtained, which was the surface-modified nanowires of SiO₂ with OA.

Synthesis of AlO(OH) nanowire (d x l : 4 nm x 1 μm) containing-ROMP-derived monoliths

AlO(OH) nanowire (d x l : 4 nm x 1 μm)-containing monoliths were prepared from NBE, norborn-5-ene-2-methanol (NBE-CH₂OH), AlO(OH) nanowires (d x l : 4 nm x 1 μm, ethanol solution), (NBE-CH₂O)₃SiCH₃, DMNH6 and the Grubbs' 1st-generation catalyst RuCl₂(PPh₃)₂(CHPh) (**1**) in a mixture of ethanol and toluene. A typical procedure for

monolith synthesis was as follows: solution I consisted of NBE (0.71 g, 7.5 mmol), 5-norbornene-2-methanol (0.04 g, 0.3 mmol), (NBE-CH₂O)₃SiCH₃ (0.375 g, 0.75 mmol) and DMNH₆ (0.375 g, 2.3 mmol) dissolved in ethanol (1.7 mL), and toluene (0.4 mL). SNWs (0.17 g, 1.87 g cm⁻³) were added to the solution I at 0 °C. Solution II contained initiator 1 (0.09 g, 0.1 mmol) dissolved in toluene (0.2 ml) and was cooled to 0 °C. Both solutions were combined and thoroughly mixed. Then, the solution was filled into the vertically oriented stainless-steel column (V_k: 4.6 × 150 mm i.d.), closed at one end, and polymerization was allowed to proceed for 30 min at 0 °C. After rod formation, each monolith was kept at room temperature for 2 h. For initiator removal, columns were flushed with a mixture of 40 vol.-% ethyl vinyl ether in CHCl₃ for 3 h at a flow rate of 0.3 mL min⁻¹. Finally, they were flushed with CHCl₃ for a further 3 h at a flow rate of 0.3 mL min⁻¹.

Chemical Etching of AlO(OH) nanowire (d × l : 4 nm × 1 μm) containing-ROMP-derived monoliths

In a typical procedure, acetic acid (CH₃COOH) solution (5 wt.%) was pumped through the AlO(OH) nanowire-loaded monolith under continuous flow using a monosyringe pump at flow rate of 0.03 mL/min. After chemical etching procedure, the etched monolith was flushed with CHCl₃ for further characterization using ISEC method.

Synthesis of Poly(urethane)-Derived Monoliths

The typical synthetic procedure used was as follows: stainless steel columns (8 × 300 mm) were cleaned, rinsed and sonicated in a 1:1 mixture of CHCl₃ and acetone. Finally, they were dried for 3 h at 120 °C. A stainless steel column (8 × 30 mm) was attached on top of a second stainless steel column that was closed on the lower end as an extension to compensate for the longitudinal volume shrinkage and was again removed after monolith synthesis. For non-porous polyurethanes, solution I consisted of PEG₃₀₀, THP, MTBE and DBTDL, all dissolved in dioxane. Solution II contained MDI dissolved in dioxane. Both solutions were combined and thoroughly mixed. Then, the solution was filled into the vertically oriented steel columns and polymerization was allowed to proceed for 18 hours at 45°C. For polyurethane monoliths with tailored mesoporosity, solution I consisted of TEG, THP, MTBE and DBTDL, all dissolved in dioxane. Solution II consisted of MDI dissolved in dioxane. Both solutions were combined and thoroughly mixed. Then, the solution was filled into the vertically

oriented steel columns and polymerization was allowed to proceed for 18 hours at 45°C. Once polymerizations were complete, all columns were flushed with CHCl₃ at a flow of 0.1 mL·min⁻¹ for 2 hours.

Synthesis of Polyurea-Derived Monoliths

Polyurea monolithic supports produced containing 1,3,5-tris(4-aminophenoxy)benzene and HMDI-trimer as monomer. DBTDL was used as catalyst, dioxane as a good and MTBE as a poor solvent. Reaction equation 1 shows the synthesis of the polyurea-based monolith. First, Solution I was prepared. For this purpose, 1,3,5-tris(4-aminophenoxy)benzene was dissolved in dioxane. Subsequently, MTBE and dibutyltin dilaurate were added. The mixture was shaken well, so that a homogeneous solution was obtained. For solution II, the monomer HMDI-trimer was dissolved in dioxane. Solution I was added to solution II then the mixture was filled into a vertically oriented steel column (d x l : 4.6 mm x 150 mm) and polymerized for 18h at 45 ° C. Finally, the column was flushed with CHCl₃ for 3 h at a flow rate of 1.0 mL/min.

Synthesis of the ([NCO-C₆H₄-NMe₃][BF₄])

4-(Dimethylamino)phenyl isocyanate (0.2 g, 1.2 mmol) and methyl iodide (1 g, 7 mmol) were stirred for 3 h at 50 °C. The product was purified by washing with diethyl ether, then dried in vacuo. AgBF₄ (0.7 mmol) was then added to [NCO-C₆H₄-NMe₃⁺][I⁻] (1.2 mmol) in CH₂Cl₂ at room temperature. The reaction mixture was stirred for 1 h, then the yellow precipitate of AgI was filtered off and the product was purified by washing with diethyl ether and dried in vacuo.

FT-IR (cm⁻¹): 2280 (s, NCO), 1736 (bs), 1041 (s), 722 (s), 568 (s)

¹H -NMR (CDCl₃): δ 8.0 (d, 2 H, J = 8 Hz), 7.33 (d, 2 H, J = 8 Hz), 4.06 (s, 9 H)

¹⁹F-NMR (CDCl₃) δ 148.2

¹³C NMR (CDCl₃): δ 144.9, 135.0, 126.7, 125.1, 122.5, 27.0

HRMS calculated for C₁₀H₁₃N₂O: 177.1022, found: 177.1021.

Synthesis of surface-grafted ROMP-derived monolithic supports

For the grafting of $[\text{NCO-C}_6\text{H}_4\text{-NMe}_3][\text{BF}_4]$ to the -OH functionalized monoliths, the column was flushed with CH_2Cl_2 for 2 h at a flow rate of $0.1 \text{ mL}\cdot\text{min}^{-1}$. The monomer $[\text{NCO-C}_6\text{H}_4\text{-NMe}_3][\text{BF}_4]$ (one equiv. with respect to the 5-norbornene-2-methanol) was dissolved in a 1:10 mixture of DMF and CH_2Cl_2 in the presence of DBTDL. This mixture was injected into the monolith using a syringe pump at a flow rate of $0.03 \text{ mL}\cdot\text{min}^{-1}$. The ionic monomer-loaded monolith was then sealed and kept at $45 \text{ }^\circ\text{C}$ for 12 h. To remove the DBTDL and excess $[\text{NCO-C}_6\text{H}_4\text{-NMe}_3^+][\text{BF}_4^-]$, the column was flushed with CH_2Cl_2 for 2 h at a flow rate of $0.1 \text{ mL}\cdot\text{min}^{-1}$.

Synthesis of the surface-grafted poly(urethane)-derived monolithic supports

For the grafting of $[\text{NCO-C}_6\text{H}_4\text{-NMe}_3^+][\text{BF}_4^-]$ to the -OH functionalized monoliths, the column was flushed with CH_2Cl_2 for 2 h at a flow rate of $0.1 \text{ mL}\cdot\text{min}^{-1}$. The ionic monomer (5 mg, one equiv. with respect to the excess hydroxyl groups) was dissolved in a 1:10 mixture of DMF and CH_2Cl_2 in the presence of DBTDL (11 mg). This mixture was injected into the monolith using a syringe pump at a flow rate of $0.03 \text{ mL}\cdot\text{min}^{-1}$. The ionic monomer-loaded monolith was then sealed and kept at $45 \text{ }^\circ\text{C}$ for 12 h. To remove the DBTDL and excess $[\text{NCO-C}_6\text{H}_4\text{-NMe}_3^+][\text{BF}_4^-]$, the column was flushed with CH_2Cl_2 for 2 h at a flow rate of $0.1 \text{ mL}\cdot\text{min}^{-1}$.

Immobilization of $[\text{BMIM}^+][\text{BF}_4^-]$ containing the ionic Rh-catalyst on the surface of the monoliths: The cationic Rh-NHC catalyst (8 mg) and $[\text{BMIM}^+][\text{BF}_4^-]$ (100 mg) were dissolved in CH_2Cl_2 . The solution was then introduced into the monolith. Vacuum was applied for 3 h to remove all solvents. Prior to use, the support was flushed with heptane overnight applying a flow rate of $0.1 \text{ mL}\cdot\text{min}^{-1}$.

Typical procedure for the Rh-catalyzed hydrosilylation of alkynes under biphasic conditions: The cationic Rh complex (1 mol% with respect to the 1-alkyne) was dissolved in $[\text{BMIM}][\text{BF}_4]$ (50 mg) and MTBE (0.5 mL) was added. The alkyne (1 equiv.) and dimethylphenylsilane (1.5 equiv.) were then added to the reaction mixture along with $10 \text{ }\mu\text{L}$ of the internal standard (dodecane) and the biphasic mixture was then vigorously stirred for 12 h. Conversion was determined by GC-MS analysis while the *Z/E* ratios were determined by NMR.

Typical procedure for the Rh-catalysed hydrosilylation of alkynes under continuous flow: Hydrosilylation reactions were performed using the 1-alkyne (140 μL 1.0 equiv) and dimethylphenylsilane (280 μL , 1.5 equiv) as the coupling partners in the presence of MTBE. An HPLC column (4.6 mm x 150 mm, $V_{\text{column}} = 2.49 \text{ mL}$) containing the monolith loaded with [BMIM⁺][BF₄⁻] with the ionic Rh-catalyst (8 mg) dissolved therein was used. Dodecane (10 μL) was used as internal standard. The HPLC monolith column was placed inside an oven and the reaction mixture was pumped through the monolith column at 55 °C for 48-60 hours at a flow rate of 0.2 ml/min.

Filling of monolith P5 with rhodamine B-PEG, followed by functionalization with DPPS: 4 mg of rhodamine B-PEG and 0.8 g of PEG were dissolved in 12 mL H₂O. Upon homogenization, 0.1 g of the **P5** were added and the mixture was stirred at room temperature for 24 h. The rhodamine B-PEG filled monolith was separated by filtration and dried *in vacuo* at 80°C for 24 h. 50 mg of the RhB-PEG filled monolith were treated with 1.015 mL of DPPS and reaction was allowed to proceed under solventless conditions for 1 h at room temperature. All unreacted DPPS was washed off with *n*-hexane (30 mL) and the sample was allowed to dry under air at room temperature.

Typical procedure for the preparation of monolith dispersions for CLSM: 15 mg of the monolith were dispersed in 5 mL of 2-propanol and then sonicated for 45 minutes. The dispersion was vortexed and 100 μL of the dispersion were drop cast on plasma-cleaned 25 mm round microscope glass slides.

3.2 Spectroscopic Data

Inverse Size Exclusion Chromatography (ISEC)

Narrow PS standards ($162\text{--}3280000\text{ g mol}^{-1}$) were purchased from PSS (Mainz, Germany). Hydrodynamic volumes of polymers were calculated as described in the literature [41]. For ISEC measurements [17], the retention times of toluene and PS standards ($\bar{M}_n \leq 1.02$) with $162 \leq \bar{M}_n \leq 2\,000\,000\text{ g mol}^{-1}$ were measured in CHCl_3 at $35\text{ }^\circ\text{C}$ applying a flow rate of 0.3 mL min^{-1} .

Nitrogen Sorption Measurements:

N_2 -sorption measurements were conducted at 77K on a Quantachrome Autosorb iQ MP automatic volumetric instrument. Monoliths were degassed for 17 h at $100\text{ }^\circ\text{C}$ under vacuum before the gas adsorption studies. Surface areas were evaluated using the Brunauer-Emmett-Teller (BET) model applied between p/p_0 ratios of 2.4×10^{-2} and 0.9 . Pore size distributions were calculated using the slit pore, non-local density functional theory (NLDFT) equilibrium model.

Scanning electron microscopy (SEM)

The surface morphology of the samples was analysed by scanning electron microscopy (SEM) using a Zeiss Auriga field emission scanning electron microscope; samples were sputtered with 10 nm Pt-Pd using an Oxford X-Max 50 device; samples were coated with 30 nm carbon.

Transmission electron microscopy (TEM)

Monolithic structures were characterized by transmission electron microscopy (TEM) using a *Philips* CM 200 FEG and a dual-beam FEI SCIOS FIB-SEM system. Monolith samples were sputtered with 50 nm Cu for the FIB (Focused Ion Beam): A lamella was cut out from the bulk material and attached to a TEM half grid using FIB Lift Out technique. Then the lamella was thinned to 100 nm for TEM analysis.

Infrared Spectroscopy (IR)

IR spectra were measured on a Bruker IFS 28 using ATR technology in NaCl cuvettes or as KBr pellets.

Nuclear Magnetic Resonance Spectroscopy (NMR)

NMR spectra were recorded on a Bruker Avance III 400 spectrometer or a Bruker DRX 250 spectrometer in the indicated solvent at 25°C and data are listed in parts per million downfield from tetramethylsilane (TMS) as an internal standard.

Gas-Chromatography Mass-Spectroscopy (GC-MS)

GC-MS data were obtained by using an Agilent Technologies 5975C inert MSD with a triple-axis detector, a 7693 autosampler, and a 7890A GC system equipped with an SPB-5 fused silica column (34.13 m x 0.25 mm x 0.25 µm film thickness). The injection temperature was set to 150°C. The column temperature ramped from 45 to 250°C within 8 min, and was then held for a further 5 min. The column flow was 1.05 mL min⁻¹.

4. REFERENCES

- [1] M. Beller, *Chem. Soc. Rev.* **2011**, 40, 10, 4891-4892.
- [2] S. Caron, A. Ghosh, S. G. Ruggeri, D. I. Nathan, D. J. Nelson, J. A. Ragan, *Practical Synthetic Organic Chemistry*, Wiley Hoboken N.J. **2020**.
- [3] J. E. Karroumi, H. Abderrahim, E. Manoury, A. Benharref, J. C. Daran, M. Gouygou, M. Urrutigoity, *J. Mol. Catal. A. Chem.* **2015**, 401, 18-26.
- [4] Z. J. Wang, K. N. Clary, R. G. Bergman, K. N. Raymond, F. D. Toste, *Nat. Chem.* **2013**, 5, 2, 100-103.
- [5] D. M. Vriezema, M. C. Aragonès, Johannes A. A. W. Elemans, Jeroen J. L. M. Cornelissen, Alan E. Rowan, Roeland J. M. Nolte, *Chem. Rev.* **2005**, 105, 4, 1445-1490.
- [6] M. Raynal, P. Ballester, A. Vidal-Ferran, Piet W. N. M. Van Leeuwen, *Chem. Soc. Rev.* **2014**, 43, 5, 1734-1787.
- [7] G. Sastre, A. Corma, *J. Mol. Catal. A. Chem.* **2009**, 305, 1, 3-7.
- [8] D. L. Pompliano, A. Peyman, J. R. Knowles, *Biochem.* **1990**, 29, 13, 3186-3194.
- [9] K. S. W. Sing, *Pure Appl. Chem.* **1985**, 57, 4, 603-619.
- [10] J. Wu, F. Xu, S. Li, P. Ma, X. Zhang, Q. Liu, R. Fu, D. Wu, *Adv. Mater.* **2019**, 31, 4, 1802922.
- [11] X. Yu, C. T. Williams, *Catal. Sci. Technol.* **2022**, 12, 19, 5765-5794.
- [12] F. Vermoortele, M. Vandichel, B. Van de Voorde, R. Ameloot, M. Waroquier, V. V. Speybroeck, Dirk E. De Vos, *Angew. Chem. Int. Ed.* **2012**, 51, 20, 4887-4890.
- [13] S. Royuela, R. Gil-San Millán, María J. Mancheño, M. M Ramos, José L. Segura, Jorge A. R. Navarro, F. Zamora, *Mater.* **2019**, 12, 12, 1974.
- [14] A. Choplin, F. Quignard, *Coord. Chem. Rev.* **1998**, 178-180, 1679-1702.
- [15] B. Autenrieth, W. Frey, M. R. Buchmeiser, *Chem. Eur. J.* **2012**, 18, 14069-14078.
- [16] P. H. Steinrück, P. Wasserscheid, *Catal. Lett.* **2015**, 145,1, 380-397.
- [17] P. J. Flory, *J. Chem. Phys.*, **1942**, 10, 1, 51-61.
- [18] D. L. Mould, R. L. M. Synge, *Analyst*, **1952**, 77, 921, 964-969.
- [19] D. L. Mould, R. L. M. Synge, *Biochem. J.*, **1954**, 58, 4, 571-85.
- [20] F. Svec, Jean M. J. Frechet, *Anal. Chem.* **1992**, 64, 7, 820-822.
- [21] I.M. Monich, B.P. Shtarkman, *Polym. Sci. U.S.S.R.* **1974**, 16, 4, 890-895.

- [22] W.D.Ross, R.T. Jefferson, *J. Chromatogr. Sci.* **1970**, 8, 7, 386-389.
- [23] B.G., Belenkii., A.M. Podkladenko, O.I. Kurenbin, V.G. Mal'tsev, D.G. Nasledov, S.A. Trushin, *J. Chromatogr. A.* **1993**, 645, 1, 1-15.
- [24] T.B. Tennikova, M. Bleha, F. Švec, T.V. Almazova, B.G. Belenkii, *J. Chromatogr. A.* **1991**, 555, 1, 97-107.
- [25] H. Minakuchi, K. Nakanishi, N. Soga, N. Ishizuka, N. Tanaka, *Anal. Chem.* **1996**, 68, 19, 3498-3501.
- [26] J. Urban, P. Jandera, *J. Sep. Sci.* **2008**, 31, 14, 2521-2540.
- [27] M.R. Buchmeiser, *Chem. Rev.* **2009**, 109, 2, 303-321.
- [28] M.Mayr, B. M. Mag, M.R. Buchmeiser, *Angew. Chem. Int. Ed.* **2001**, 40, 20, 3839-3842.
- [29] E.B. Anderson, M.R. Buchmeiser, *ChemCatChem* **2012**, 4, 1, 30-44.
- [30] C. Viklund, F. Svec, J. M. J. Fréchet, K. Irgum, *Chem. Mater.* **1996**, 8, 3, 744-750.
- [31] E.S. Sinitsyna, Yu. N. Sergeeva, E.G. Vlakh, N.N. Saprikina, T.B. Tennikova, *React. Funct. Polym.* **2009**, 69, 6, 385-392.
- [32] P. Holdšvendová, P. Coufal, J. Suchánková, E. Tesařová, Z. Bosáková, *J. Sep. Sci.* **2003**, 26, 18, 1623-1628.
- [33] R. Bandari, M. R. Buchmeiser, *Analyst* **2012**, 137, 14, 3271-3277.
- [34] M.R. Buchmeiser, *Polymer* **2007**, 48, 8, 2187-2198.
- [35] Z. Xu, L. Yang, Q. Wang, *J. Chromatogr. A* **2009**, 1216, 15, 3098-3106.
- [36] F. Svec, J.M.J. Frechet, *Chem. Mater.* **1995**, 7, 4, 707-715.
- [37] L. Trojer, C. P. Bisjak, W. Wieder, G. K. Bonn, *J. Chromatogr. A* **2009**, 1216, 35, 6303-6309.
- [38] H. Marsh, *Carbon* **1987**, 25, 1, 49-58.
- [39] Z. Hu, M.P. Srinivasan, Y. Ni, *Carbon* **2001**, 39, 6, 877-886.
- [40] X. Zhou, H. Yi, X. Tang, H. Deng, H. Liu, *J. Chem. Eng.* **2012**, 200-202, 399-404.
- [41] I. Halász, K. Martin, *Angew. Chem. Int. Ed.* **1978**, 17, 12, 901-908.
- [42] M. Naderi, *Progress in Filtr. and Sep.* **2015**, 585-608.
- [43] M. Thommes, K. Kaneko, A. V. Neimark, J. P. Olivier, F. R-Reinoso, J. Rouquerol, K. S.W. Sing, *Pure Appl. Chem.* **2015**, 87, 9-10, 1051-1069.
- [44] K. Kaneko, T. Itoh, T. Fujimori, *Chem. Lett.* **2012**, 41, 5, 466-475.

- [45] F. Zhang, Y. Meng, D. Gu, Yan, C. Yu, B. Tu, D. Zhao, *J. Am. Chem. Soc.* **2005**, 127, 39, 13508-13509.
- [46] J. Jang, J. Bae, *J. Non. Cryst. Solids* **2006**, 352, 38, 3979-3984.
- [47] A. S. Zalusky, R. Olayo-Valles, J. H. Wolf, M. A. Hillmyer, *J. Am. Chem. Soc.* **2002**, 124, 43, 12761-12773.
- [48] Z. Bin, L. Wanfang, W. Xiaoqiang, W. Shige, D. Qinyue, H. Mingxian *Chem. Asian J.* **2020**, 15, 8, 1248-1265.
- [49] S. Inagaki, Y. Fukushima, K. Kuroda, *J. Chem. Soc., Chem. Commun.* **1993**, 8, 680-682.
- [50] C. T. Kresge, M. E. Leonowicz, W. J. Roth, J. C. Vartuli, J. S. Beck, *Nature* **1992**, 359, 6397, 710-712.
- [51] D. Zhao, J. Feng, Q. Huo, N. Melosh, G. H. Fredrickson, B. F. Chmelka, G. D. Stucky, *Science*, **1998**, 279, 5350, 548-552.
- [52] S. Inagaki, S. Guan, Y. Fukushima, T. Ohsuna, O. Terasaki, *J. Am. Chem. Soc.* **1999**, 121, 41, 9611-9614.
- [53] O. Olkhoviyk, M. Jaroniec, *J. Am. Chem. Soc.* **2005**, 127, 1, 60-61.
- [54] F. Hoffmann, M. Cornelius, J. Morell, M. Fröba, *Angew. Chem. Int. Ed.* **2006**, 45, 20, 3216-3251.
- [55] A. Monnier, F. Schüth, Q. Huo, D. Kumar, D. Margolese, *Science* **1993**, 261, 5126, 1299-1303.
- [56] J. H. Knox, *J. Chromatogr. Sci.* **1980**, 18, 9, 453-461.
- [57] R. Ryoo, S. Hoon Joo, S. Jun, *J. Phys. Chem. B.* **1999**, 103, 37, 7743-7746.
- [58] J. Lee, S. Yoon, T. Hyeon, S. M. Oh, K. Bum Kim, *Chem. Comm.* **1999**, 21, 2177-2178.
- [59] Z. Chen, Z.M. Cui, F. Niu, L. Jiang, W.G. Song, *Chem. Comm.* **2010**, 46, 35, 6524-6526.
- [60] Z. Zhou, M. Hartmann, *Chem. Soc. Rev.* **2013**, 42, 9, 3894-3912.
- [61] T.-Y Ma, Lei Liu, Z.-Y. Yuan, *Chem. Soc. Rev.* **2013**, 42, 9, 3977-4003.
- [62] H Qin, R Jian, J Bai, J Tang, Y Zhou, B Zhu, D Zhao, *ACS Omega*, **2018**, 3, 1, 1350-1356.
- [63] D Gu, F. Schüth, *Chem. Soc. Rev.* **2014**, 43, 1, 313-344.
- [64] H. Nishihara, T. Kyotani, *Chem. Comm.* **2018**, 54, 45, 5648-5673.
- [65] G. Zhu, S. Qiu, O. Terasaki, Y. Wie, *J. Am. Chem. Soc.* **2001**, 123, 31, 7723-7724.

- [66] G. Qi, Y. Wang, L. Estevez, A.K. Switzer, X. Duan, X. Yang, E. P. Giannelis, *Chem. Mater.* **2010**, 22, 9, 2693-2695.
- [67] S.B. Yoon, K. Sohn, J.Y. Kim, C.-H. Shin, J.-S. Yu, T. Hyeon, *Adv. Mater.* **2002**, 14, 1, 19-21.
- [68] C. Liang, K. Hong, G. A. Guiochon, Jimmy W. Mays, S. Dai, *Angew. Chem. Int. Ed.* **2004**, 43, 43, 5785-9.
- [69] S. Tanaka, N. Nishiyama, Y. Egashiraa, K. Ueyama, *Chem. Comm.* **2005**, 16, 2125-2127.
- [70] Y. Meng, D. Gu, F. Zhang, Y. Shi, H. Yang, Z. Li, C. Yu, Bo Tu, D. Zhao, *Angew. Chem. Int. Ed.* **2005**, 44, 43, 7053-7059.
- [71] K. E. B. Doncom, L. D. Blackman, D. B. Wright, M. I. Gibson, R. K. O'Reilly, *Chem. Soc. Rev.* **2017**, 46, 14, 4119-4134.
- [72] F. Markus, C. Vogler, J. R. Bruckner, S. Naumann, *ACS Appl. NanoMater.* **2021**, 4, 4, 3486-3492.
- [73] Y. Zhai, Y. Dou, D. Zhao, P. F. Fulvio, R. T. Mayes, S. Dai, *Adv. Mater.* **2011**, 23, 42, 4828-4850.
- [74] S. Shen, A. E. Garcia-Bennett, Z. Liu, Q. Lu, Y. Shi, Yan, C. Yu, W. Liu, Y. Cai, O. Terasaki, D. Zhao, *Angew. Chem. Int. Ed.* **2005**, 45, 26, 4295-4298.
- [75] Y. Sakamoto, M. Kaneda, O. Terasaki, D. Y. Zhao, J. M. Kim, G. Stucky, H. J. Shin, R. Ryoo, *Nature*, **2000**, 408, 6811, 449-453.
- [76] Z. Yunfeng, Z. Daliang, Z. Lan, W. Guangchao, Z. Yihan, C. Amy, S. Junliang, Z. Xiaodong, H. Yu, *Chem. Mater.* **2011**, 23, 16, 3775-3786.
- [77] AE Garcia-Bennett, O. Terasaki, S. Che, T. Tatsumi. *Chem. Mater.* **2004**, 16, 813.
- [78] D. Zhao, P. Yang, Q. Huo, B. F. Chmelka, G. D. Stucky, *Curr Opin Solid State Mater Sci.* **1998**, 3, 1, 111-121.
- [79] D. Zhao, Q. Huo, J. Feng, B. F. Chmelka, G. D. Stucky, *J. Am. Chem. Soc.* **1998**, 120, 24, 6024-6036.
- [80] T. Yu, H. Zhang, X. Yan, Z. Chen, X. Zou, P. Oleynikov, D. Zhao, *J. Phys. Chem. B.* **2006**, 110, 43, 21467-21472.
- [81] M. Kaneda, T. Tsubakiyama, A. Carlsson, Y. Sakamoto, T. Ohsuna, O. Terasaki, S. H. Joo, R. Ryoo, *J. Phys. Chem. B.* **2002**, 106, 6, 1256-1266.
- [82] H. M. A. Hunter, A. E. Garcia-Bennett, I. J. Shannon, W. Zhou, P. A. Wright, *J. Mater. Chem.* **2002**, 12, 1, 20-23.

- [83] AE Garcia-Bennett, K. Miyasaka, O. Terasaki. *Chem. Mater.* **2004**, 16, 3597.
- [84] M. Kruk, M. Jaroniec, A. Sayari, *Langmuir* **1997**, 13, 23, 6267-6273.
- [85] P. Verma, Y. Kuwahara, K. Mori, R. Raja, H. Yamashita, *Nanoscale* **2020**, 12, 21, 11333-11363.
- [86] T. Joseph, S. S. Deshpande, S.B. Halligudi, A. Vinu, S. Ernst, M. Hartmann, *J. Mol. Catal. A. Chem.* **2003**, 206, 1, 13-21.
- [87] D. A. Cabrera-Munguia, H. González, E. Tututi-Ríos, A. Gutiérrez-Alejandre, J. L. Rico, *J. Mater. Res.* **2018**, 33, 21, 3634-3645.
- [88] S. Zhou, L. Kang, Z. Xu, M. Zhu, *RSC Adv.* **2020**, 10, 4, 1937-1945.
- [89] A. Samadi-Maybodi, M.-R. Sadeghi-Maleki, *J. Inorg. Organomet. Polym. Mater.* **2018**, 28, 6, 2620-2632.
- [90] S. Álvarez, A. B. Fuertes, *Mater. Lett.* **2007**, 61, 11, 2378-2381.
- [91] R. K. O'Reilly, Craig J. Hawker, K. L. Wooley, *Chem. Soc. Rev.* **2006**, 35, 11, 1068-1083.
- [92] Z. Li, D. Wu, X. Huang, J. Ma, H. Liu, Y. Liang, R. Fu, K. Matyjaszewski, *Energy Environ. Sci.* **2014**, 7, 9, 3006-3012.
- [93] Y. Liang, S. Lu, D. Wu, B. Sun, F. Xu, R. Fu, *J. Mater. Chem. A.* **2013**, 1, 9, 3061-3067.
- [94] M. Ionescu, *Chemistry and Technology of Polyols for Polyurethanes*, *Smithers Rapra Pub.* **2005**.
- [95] T. Ueda, S. Inoue, Thermoplasticity in Polyurethane-Imide Elastomers. *J. Polym. Sci.* **2018**, 8, 11-20.
- [96] M. Ates, S. Karadag, A. Akdogan Eker, B. Eker **2022**, *Polym Int*, 71, 1157-1163.
- [97] Kozakiewicz, J., *Polimery* **2015**, 60, 9, 525-535.
- [98] D. C. Allport, D.S. Gilbert, S. Outterside, *MDI and TDI: safety, health, and the environment: a source book and practical guide*, John Wiley & Sons. **2003**.
- [99] I. Javni, W. Zhang, Z.S. Petrović, *J. Appl. Polym. Sci.* **2003**, 88, 13, 2912-2916.
- [100] A. Kausar, *Polym. Plast. Technol. Eng.* **2018**, 57, 4, 346-369.
- [101] E. Pardieu, N. T. T. Chau, T. Dintzer, T. Romero, D. Favier, T. Roland, D. Edouard, L. Jierry, V. Ritleng, *Chem. Comm.* **2016**, 52, 4691-4693.
- [102] H. Taghvaei, E. Pirzadeh, M. Jahanbakhsh, O. Khalifeh, M.R. Rahimpour, *J. CO2 Util.* **2021**, 44, 101398.

- [103] R. L. Banks, G. C. Bailey, *Ind. Eng. Chem. Prod. Res. Dev.* **1964**, 3, 3, 170-173.
- [104] N. Calderon, E. A. Ofstead, W. A. Judy, *Angew. Chem. Int. Ed.* **1976**, 15, 7, 401-409.
- [105] J.L. Hérisson, P., Y. Chauvin, *Makromol. Chem.* **1971**, 141, 1, 161-176.
- [106] T.-L. Choi, R. H. Grubbs, *Angew. Chem. Int. Ed.* **2003**, 42, 15, 1743-1746.
- [107] M. G. Mayershofer, O. Nuyken, M. R. Buchmeiser, *Macromolecules* **2006**, 39, 7, 2452-2459.
- [108] C. W. Bielawski, R.H. Grubbs, *Prog. Polym. Sci.* **2007**, 32, 1, 1-29.
- [109] Z. R. Chen, J. P. Claverie, R. H. Grubbs, J. A. Kornfield, *Macromolecules*, **1995**, 28, 7, 2147-2154.
- [110] M. Szwarc, M. Levy, R. Milkovich, *J. Am. Chem. Soc.* **1956**, 78, 11, 2656-2657.
- [111] T. R. Darling, T. P. Davis, M. Fryd, A. A. Gridnev, D. M. Haddleton, S. D. Ittel, R. R. Matheson, G. Moad, E. Rizzardo, *J. Polym. Sci., Part A: Polym. Chem.* **2000**, 38, 10, 1706-1708.
- [112] O.W. Webster, *Science*, **1991**, 251, 4996, 887-893.
- [113] N. Calderon, H.Y. Chen, K.W. Scott, *Tetrahedron Lett.* **1967**, 8, 34, 3327-3329.
- [114] F.W. Michelotti, W.P. Keaveney, *J. Polym. Sci., Part A: Gen. Pap.* **1965**, 3, 3, 895-905.
- [115] E.O. Fischer, A. Maasböl, *Angew. Chem. Int. Ed.* **1964**, 3, 8, 580-581.
- [116] T.M. Trnka, R.H. Grubbs, *Acc. Chem. Res.* **2001**, 34, 1, 18-29.
- [117] S. T. Nguyen, L. K. Johnson, R. H. Grubbs, J. W. Ziller, *J. Am. Chem. Soc.* **1992**, 114, 10, 3974-3975.
- [118] P. Schwab, M. B. France, J. W. Ziller, R. H. Grubbs, *Angew. Chem. Int. Ed.*, **1995**, 34,18, 2039-2041.
- [119] T. Weskamp, W. C. Schattenmann, M. Spiegler, W. A. Herrmann, *Angew. Chem. Int. Ed.* **1998**, 37, 2490-2493.
- [120] J. A. Love, J. P. Morgan, T. M. Trnka, R. H. Grubbs, *Angew. Chem. Int. Ed.* **2002**, 41, 4035-4037.
- [121] S. B. Garber, J. S. Kingsbury, B. L. Gray, A. H. Hoveyda, *J. Am. Chem. Soc.* **2000**, 122, 8168-8179.

- [122] J. S. Kingsbury, J. P. A. Harrity, P. J. Bonitatebus, A. H. Hoveyda, *J. Am. Chem. Soc.* **1999**, 121, 791-799.
- [123] T. S. Halbach, S. Mix, D. Fischer, S. Maechling, J. O. Krause, C. Sievers, S. Blechert, O. Nuyken, M. R. Buchmeiser, *J. Org. Chem.* **2005**, 70, 4687-4694.
- [124] S. Naumov, M. R. Buchmeiser, *Organometallics* **2012**, 31, 847-856.
- [125] P. S. Kumar, K. Wurst, M. R. Buchmeiser, *Organometallics* **2009**, 28, 1785-1790.
- [126] L. Yang, M. Mayr, K. Wurst, M. R. Buchmeiser, *Eur. J. Chem.* **2004**, 10, 5761-5770.
- [127] T. J. Seiders, D. W. Ward, R. H. Grubbs, *Org. Lett.* **2001**, 3, 3225-3228.
- [128] J. J. Van Veldhuizen, S. B. Garber, J. S. Kingsbury, A. H. Hoveyda, *J. Am. Chem. Soc.* **2002**, 124, 4954-4955.
- [129] R. R. Schrock, J. S. Murdzek, G. C. Bazan, J. Robbins, M. DiMare, M. O'Regan, *J. Am. Chem. Soc.* **1990**, 112, 3875-3886.
- [130] R. R. Schrock, *Chem. Rev.* **2009**, 109, 3211-3226.
- [131] J. B. Alexander, D. S. La, D. R. Cefalo, A. H. Hoveyda, R. R. Schrock, *J. Am. Chem. Soc.* **1998**, 120, 4041-4042.
- [132] G. C. Bazan, E. Khosravi, R. R. Schrock, W. J. Feast, V. C. Gibson, M. B. O'Regan, J. K. Thomas, W. M. Davis, *J. Am. Chem. Soc.* **1990**, 112, 8378-8387.
- [133] I. Ibrahim, M. Yu, R. R. Schrock, A. H. Hoveyda, *J. Am. Chem. Soc.* **2009**, 131, 3844-3845.
- [134] E. S. Sattely, S. J. Meek, S. J. Malcolmson, R. R. Schrock, A. H. Hoveyda, *J. Am. Chem. Soc.* **2009**, 131, 943-953.
- [135] S. J. Malcolmson, S. J. Meek, E. S. Sattely, R. R. Schrock, A. H. Hoveyda, *Nature* **2008**, 456, 933-937.
- [136] X. Li, E. Mastan, W.J. Wang, B.G. Li, S. Zhu, *React. Chem. Eng.* **2016**, 1, 1, 23-59.
- [137] T Junkers, *J. Flow Chem.* **2017**, 7, 3, 106-110.
- [138] K. Jähnisch, V. Hessel, H. Löwe, M. Baerns, *Angew. Chem. Int. Ed.* **2004**, 43, 4, 406-446.
- [139] R. Munirathinam, J. Huskens, W. Verboom, *Adv. Synth. Catal.* **2015**, 357, 6, 1093-1123.

- [140] K. G. Maskill, J. P. Knowles, L. D. Elliott, R. W. Alder, K. I. Booker-Milburn, *Angew. Chem. Int. Ed.* **2013**, 52, 5, 1499-1502.
- [141] M. Colella, C. Carlucci, R. Luisi, *J. Flow. Chem.* **2018**, 29-65.
- [142] A. Tanimu, S. Jaenicke, K. Alhooshani, *J. Chem. Eng.* **2017**, 327, 792-821.
- [143] R.D. Arrua, M.C. Strumia, C.I. Alvarez Igarzabal, *Materials* **2009**, 2, 4, 2429-2466.
- [144] N. Jeddi, N.W.J. Scott, I.J.S. Fairlamb, *ACS Catal.* **2022**, 12, 19, 11615-11638.
- [145] C. Ramarao, S. V. Ley, S. C. Smith, I. M. Shirley, N. DeAlmeida, *ChemComm* **2002**, 1132-1133.
- [146] R. Hudson, G. Hamasaka, T. Osako, Y. M. A. Yamada, C.-J. Li, Y. Uozumi, A. Moores, *Green Chem.* **2013**, 15, 2141-2148.
- [147] G. Vilé, J. Pérez-Ramírez, *Nanoscale* **2014**, 6, 13476-13482.
- [148] U. Hintermair, T. Höfener, T. Pullmann, G. Franciò, W. Leitner, *ChemCatChem* **2010**, 2, 150-154.
- [149] M. Beigi, R. Haag, A. Liese, *Adv. Synth. Catal.* **2008**, 350, 919-925.
- [150] F. Ziegler, T. Roider, M. Pyschik, C. P. Haas, D. Wang, U. Tallarek, M. R. Buchmeiser, *ChemCatChem* **2021**, 13, 2234-2241.
- [151] A. Kirschning, W. Solodenko, K. Mennecke, *Eur. J. Chem.* **2006**, 12, 5972-5990.
- [152] R. M. Heck, S. Gulati, R. J. Farrauto, *Chem. Eng. J.* **2001**, 82, 149-156.
- [153] A. Kirschning, C. Altwicker, G. Dräger, J. Harders, N. Hoffmann, U. Hoffmann, H. Schönfeld, W. Solodenko, U. Kunz, *Angew. Chem. Int. Ed.* **2001**, 40, 3995-3998.
- [154] F. Liguori, S. Coiai, E. Passaglia, P. Barbaro, *Macromolecules* **2013**, 46, 5423-5433.
- [155] F. Liguori, P. Barbaro, *Catal. Sci. Technol.* **2014**, 4, 3835-3839.
- [156] K. Nakanishi, N. Soga, *J. Non. Cryst. Solids* **1992**, 139, 1-13.
- [157] M. T. Alotaibi, M. J. Taylor, D. Liu, S. K. Beaumont, G. Kyriakou, *Surf. Sci.* **2016**, 646, 179-185.
- [158] A. Koreniuk, K. Maresz, K. Odrozek, J. Mrowiec-Białoń, *Microporous Mesoporous Mater.* **2016**, 229, 98-105.
- [159] W. Song, D. Shi, S. Tao, Z. Li, Y. Wang, Y. Yu, J. Qiu, M. Ji, X. Wang, *J. Colloid Interface Sci.* **2016**, 481, 100-106.

- [160] K. Szymańska, K. Odrozek, A. Zniszczoł, G. Torrelo, V. Resch, U. Hanefeld, A. B. Jarzębski, *Catal. Sci. Technol.* **2016**, 6, 4882-4888.
- [161] N. Liu, R. A. Assink, C. J. Brinker, *ChemComm* **2003**, 370-371.
- [162] A. Gömann, J. A. Deverell, K. F. Munting, R. C. Jones, T. Rodemann, A. J. Canty, J. A. Smith, R. M. Guijt, *Tetrahedron* **2009**, 65, 1450-1454.
- [163] A. Nagaki, K. Hirose, Y. Moriwaki, K. Mitamura, K. Matsukawa, N. Ishizuka, J. Yoshida, *Catal. Sci. Technol.* **2016**, 6, 4690-4694.
- [164] C.-H. Péliesson, T. Nakanishi, Y. Zhu, K. Morisato, T. Kamei, A. Maeno, H. Kaji, S. Muroyama, M. Tafu, K. Kanamori, T. Shimada, K. Nakanishi, *ACS Appl. Mater. Interfaces* **2017**, 9, 406-412.
- [165] V. Chiroli, M. Benaglia, A. Puglisi, R. Porta, R. P. Jumde, A. Mandoli, *Green Chem.* **2014**, 16, 2798-2806.
- [166] J. Chen, Y. Xin, J. Wu, P. Liao, L. Chen, J. Zhang, *ChemNanoMat* **2021**, 7, 334-340.
- [167] B. Marciniak, K. Szubert, R. Fiedorow, I. Kownacki, M. J. Potrzebowski, M. Dutkiewicz, A. Franczyk, *J Mol Catal A Chem* **2009**, 310, 9-16.
- [168] B. Marciniak, J. Guliński, *J. Organomet. Chem.* **1984**, 266, 19-21.
- [169] A. J. Chalk, J. F. Harrod, *J. Am. Chem. Soc.* **1965**, 87, 16-21.
- [170] P. K. R. Panyam, B. Atwi, F. Ziegler, W. Frey, M. Nowakowski, M. Bauer, M. R. Buchmeiser, *Eur. J. Chem.* **2021**, 27, 17220-17229.
- [171] L. H. Sommer, E. W. Pietrusza, F. C. Whitmore, *J. Am. Chem. Soc.* **1947**, 69, 188.
- [172] B. D. Karstedt, *General Electric Company, US3775452A* **1973**.
- [173] I. E. Markó, S. Stérin, O. Buisine, G. Mignani, P. Branlard, B. Tinant, J. P. Declercq, *Science* **2002**, 298, 204-206.
- [174] I. E. Markó, S. Stérin, O. Buisine, G. Berthon, G. Michaud, B. Tinant, J. P. Declercq, *Adv. Synth. Catal.* **2004**, 346, 1429-1434.
- [175] P. Gigler, M. Drees, K. Riener, B. Bechlars, W. A. Herrmann, F. E. Kuhn, *J. Catal.* **2012**, 295, 1-14.
- [176] M. Y. Hu, P. He, T. Z. Qiao, W. Sun, W. T. Li, J. Lian, J. H. Li, S. F. Zhu, *J. Am. Chem. Soc.* **2020**, 142, 16894-16902.
- [177] O. Buisine, G. Berthon-Gelloz, J. F. Briere, S. Sterin, G. Mignani, P. Branlard, B. Tinant, J. P. Declercq, I. E. Marko, *Chem. Commun.* **2005**, 3856-3858.
- [178] C. M. Downing, H. H. Kung, *Catal. Commun.* **2011**, 12, 1166-1169.

- [179] C. Chen, M. B. Hecht, A. Kavara, W. W. Brennessel, B. Q. Mercado, D. J. Weix, P. L. Holland, *J. Am. Chem. Soc.* **2015**, 137, 13244 – 13247.
- [180] I. Buslov, J. Becouse, S. Mazza, M. Montandon-Clerc, X. Hu, *Angew. Chem. Int. Ed.* **2015**, 54, 14523 – 14526; *Angew. Chem.* **2015**, 127, 14731-14734.
- [181] L. B. Junquera, M. C. Puerta, P. Valerga, *Organometallics* **2012**, 31, 2175-2183.
- [182] E. Remond, C. Martin, J. Martinez, F. Cavelier, *Chem. Rev.* **2016**, 116, 11654-11684.
- [183] E. Langkopf, D. Schinzer, *Chem. Rev.* **1995**, 95, 1375-1408.
- [184] Y. Liu, L. Deng, *J. Am. Chem. Soc.* **2017**, 139, 1798-1801.
- [185] C. Wu, W. J. Teo, S. Ge, *ACS Catal.* **2018**, 8, 5896 – 5900.
- [186] M. Y. Hu, J. Lian, W. Sun, T. Z. Qiao, S. F. Zhu, *J. Am. Chem. Soc.* **2019**, 141, 4579-4583.
- [187] T. Galeandro-Diamant, R. Sayah, M. L. Zanota, S. Marrot, L. Veyre, C. Thieuleux, V. Meille, *Chem. Commun.* **2017**, 53, 2962-2965.
- [188] K. Motokura, K. Maeda, W.-J. Chun, *ACS Catal.* **2017**, 7, 4637 – 4641.
- [189] P. Wasserscheid, *Chem. Unserer Zeit* **2003**, 37, 52-63.
- [190] P. Walden, *Bull. Acad. Imper. Sci.* **1914**, 1800.
- [191] J. S. Wilkes, J. A. Levisky, R. A. Wilson, C. L. Hussey, *Inorg. Chem.* **1982**, 21, 1263-1264.
- [192] Y. Baba, F. Kubota, N. Kamiya, M. Goto, *Solvent Extr. Res. Dev., Jpn.* **2011**, 18, 193-198.
- [193] G. Özevci, Ş. Sert, M. Eral, *Chem. Eng. Res. Des.* **2018**, 140, 1-11.
- [194] M. Armand, F. Endres, D. R. MacFarlane, H. Ohno, B. Scrosati, *Mater. Renew. Sustain Energy* **2010**, 129-137.
- [195] J. Scholz, S. Loekman, N. Szesni, W. Hieber, A. Görling, M. Haumann, P. Wasserscheid, *Adv. Synth. Catal.* **2011**, 353, 2701-2707.
- [196] N. Hofmann, A. Bauer, T. Frey, M. Auer, V. Stanjek, P. S. Schulz, N. Tacca-
rdi, P. Wasserscheid, *Adv. Synth. Catal.* **2008**, 350, 16, 2599-2609.
- [197] T. Selvam, A. Machoke, and W. Schwieger, *Appl. Catal. A: Gen.* **2012**, 445-446, 92-101.
- [198] C. Van Doorslaer, J. Wahlen, P. Mertens, K. Binnemans, D. De Vos, *Dalton Trans.* **2010**, 39, 36, 8377-8390.
- [199] M.R. Axet, K. Philippot, *Chem. Rev.* **2020**, 120, 2, 1085-1145.

- [200] R. Kukawka, A. P. Zygarowicz, J. Dzialkowska, M. Pietrowski, H. Maciejewski, K. Bica, M. Smiglak, *ACS Sustain. Chem. Eng.* **2019**, 7, 5, 4699-4706.
- [201] J. Li, J. Peng, Y. Bai, Y. Hu, H. Qiu, G. Lai, X. Li, *Phosphorus Sulfur Silicon Relat. Elem.* **2010**, 185, 484-490.
- [202] R. Kukawka, A. Pawlowska-Zygarowicz, R. Januszewski, *Catalysts* **2020**, 10, 12, 1414.
- [203] P. J. Flory, *Proc. R. Soc. A: Math. Phys. Eng. Sci.* **1956**, 234, 73-89.
- [204] F. Sinner, M. R. Buchmeiser, *Macromolecules* **2000**, 33, 5777-5786.
- [205] V. P. Taori, R. Bandari, M. R. Buchmeiser, *Eur. J. Chem.* **2014**, 20, 3292-3296.
- [206] A. El Kadib, R. Chimenton, A. Sachse, F. Fajula, A. Galarneau, B. Coq, *Angew. Chem. Int. Ed.* **2009**, 48, 4969-4972.
- [207] A. Sachse, A. Galarneau, B. Coq, F. Fajula, *New J Chem* **2011**, 35, 259-264.
- [208] U. Tallarek, J. Hochstrasser, F. Ziegler, X. Huang, C. Kübel, M. R. Buchmeiser, *ChemCatChem* **2021**, 13, 281-292.
- [209] Y. Chen, H. Chen, L. Guo, Q. He, F. Chen, J. Zhou, J. Feng, J. Shi, *ACS Nano* **2010**, 4, 529-539.
- [210] G. Yang, N. Tsubaki, J. Shamoto, Y. Yoneyama, Y. Zhang, *J. Am. Chem. Soc.* **2010**, 132, 8129-8136.
- [211] J. Yuan, A. M. Fracaroli, W. G. Klemperer, *Organometallics* **2016**, 35, 2149-2155.
- [212] Y. Chen, P. Xu, H. Chen, Y. Li, W. Bu, Z. Shu, Y. Li, J. Zhang, L. Zhang, L. Pan, X. Cui, Z. Hua, J. Wang, L. Zhang, J. Shi, *Adv. Mater.* **2013**, 25, 3100-3105.
- [213] Y. Chen, Y. Gao, H. Chen, D. Zeng, Y. Li, Y. Zheng, F. Li, X. Ji, X. Wang, F. Chen, Q. He, L. Zhang, J. Shi, *Adv. Funct. Mater.* **2012**, 22, 1586-1597.
- [214] S. Alexander, G. Anne, F. François, Francesco, C. Patrice, C. Bernard, *Microporous Mesoporous Mater.* **2011**, 140, 58-68.
- [215] S. Jun, S. H. Joo, R. Ryoo, M. Kruk, M. Jaroniec, Z. Liu, T. Ohsuna, O. Terasaki, *J. Am. Chem. Soc.* **2000**, 122, 10712-10713.
- [216] D. S. Su, J. J. Delgado, X. Liu, D. Wang, R. Schlögl, L. Wang, Z. Zhang, Z. Shan, F.-S. Xiao, *Chem.: Asian J.* **2009**, 4, 1108-1113.
- [217] Y. S. Vygodskii, A. S. Shaplov, E. I. Lozinskaya, O. A. Filippov, E. S. Shubina, R. Bandari, M. R. Buchmeiser, *Macromolecules* **2006**, 39, 7821-7830.

- [218] P. Śledź, M. Mauduit, K. Grela, *Chem. Soc. Rev.* **2008**, 37, 2433-2442.
- [219] M. R. Buchmeiser, N. Atzl, G. K. Bonn, *J. Am. Chem. Soc.* **1997**, 119, 9166-9174.
- [220] S. Lubbad, M. R. Buchmeiser, *Macromol. Rapid Commun.* **2003**, 23, 617-621.
- [221] O. Franke, J. Rathousky, G. Schulz-Ekloff, J. Stárek, A. Zúkal, *Stud. Surf. Sci. Catal.* **1994**, 84, 77-84.
- [222] M. Marszewski, J. Marszewska, S. Pylypenko, M. Jaroniec, *Chem. Mater.* **2016**, 28, 7878-7888.

5. APPENDIX

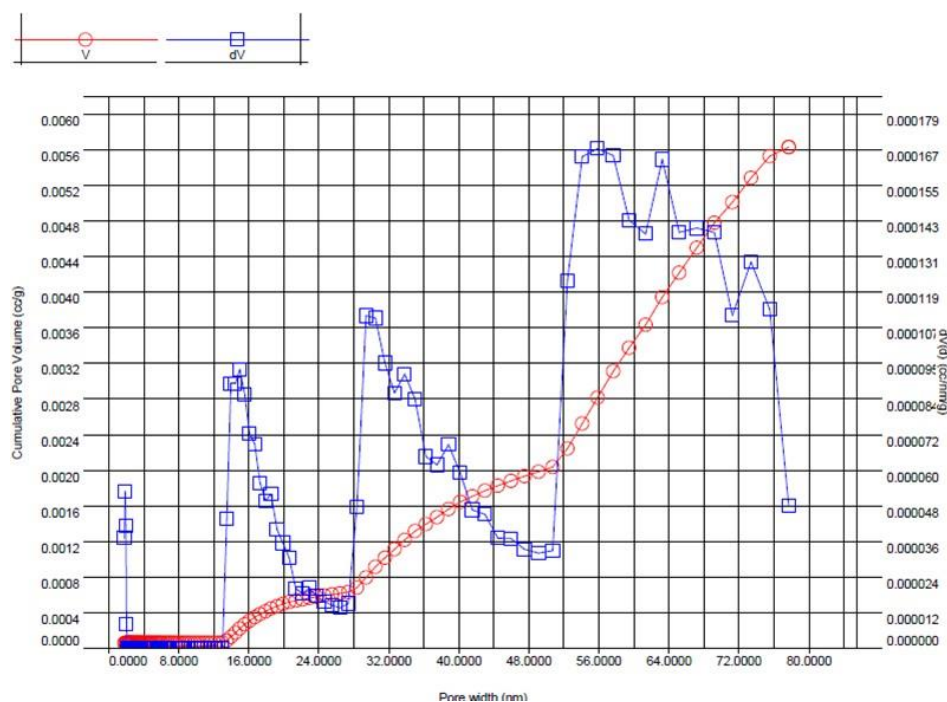


Figure S1: N₂ - adsorption results (BET method) - pore size distribution of M0.

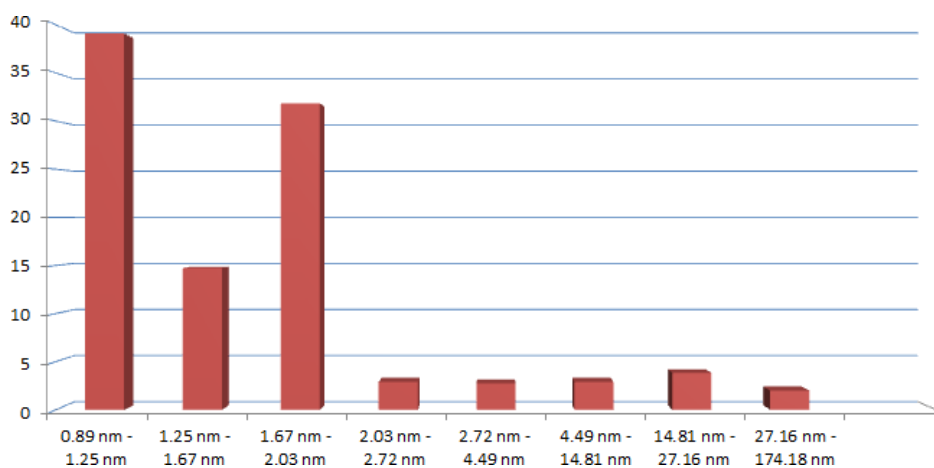


Figure S2: ISEC-derived distribution (relative abundance ΔR , %) of pore diameters (nm) of monolith M0 (ΔR of the pore range): 0.89 - 1.25 nm (ΔR : 39.0 %), 1.25 - 1.67 nm (ΔR : 14.7 %), 1.67 - 2.03 nm (ΔR : 31.8 %), 2.03 - 2.72 nm (ΔR : 2.9 %), 2.72 - 4.49 nm (ΔR : 2.7 %), 4.49 - 14.81 nm (ΔR : 2.9 %), 14.81 - 27.16 nm (ΔR : 3.8 %), 27.1 - 174.18 nm (ΔR : 2 %).

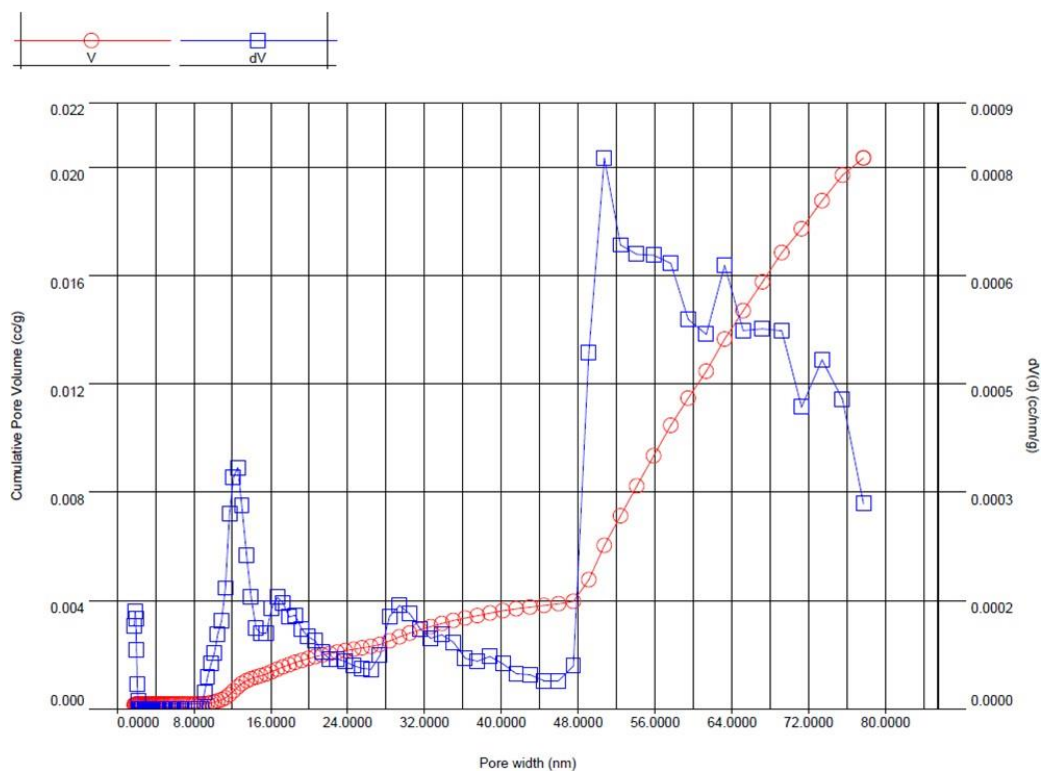


Figure S3: N₂ - adsorption results (BET method) - pore size distribution of M1a.

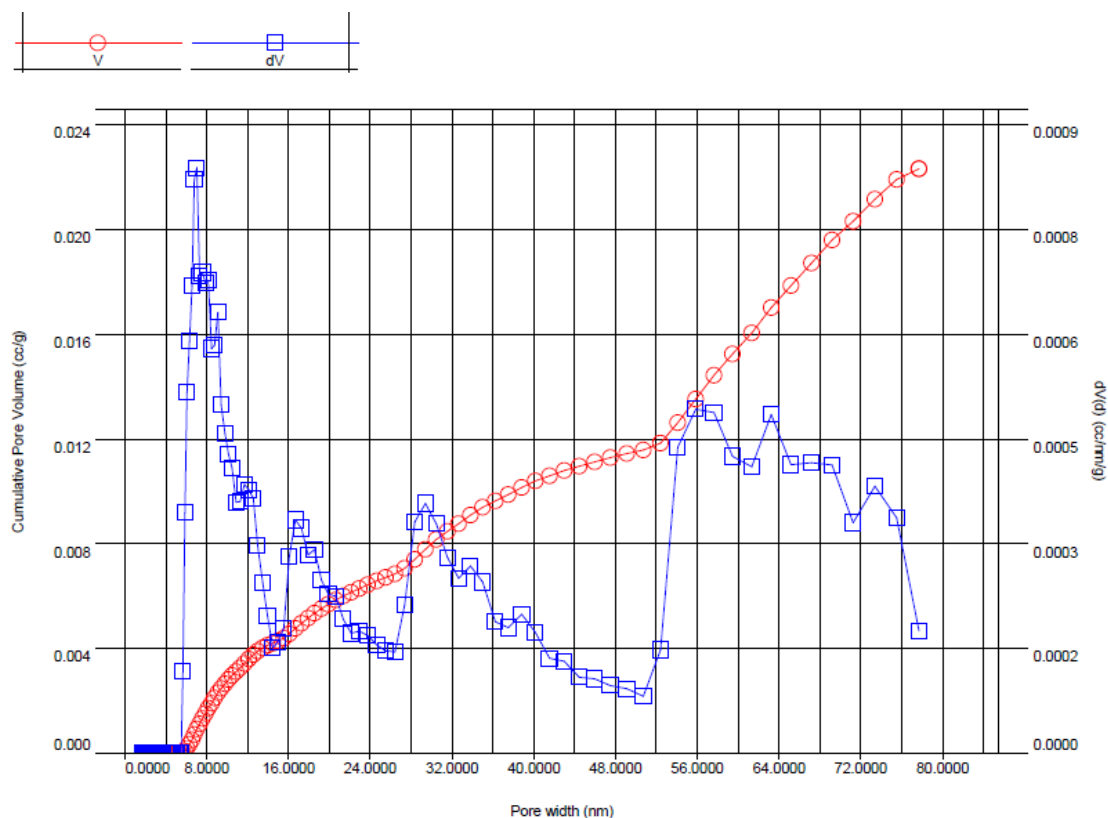


Figure S4: N₂ - adsorption results (BET method) - pore size distribution of M1b.

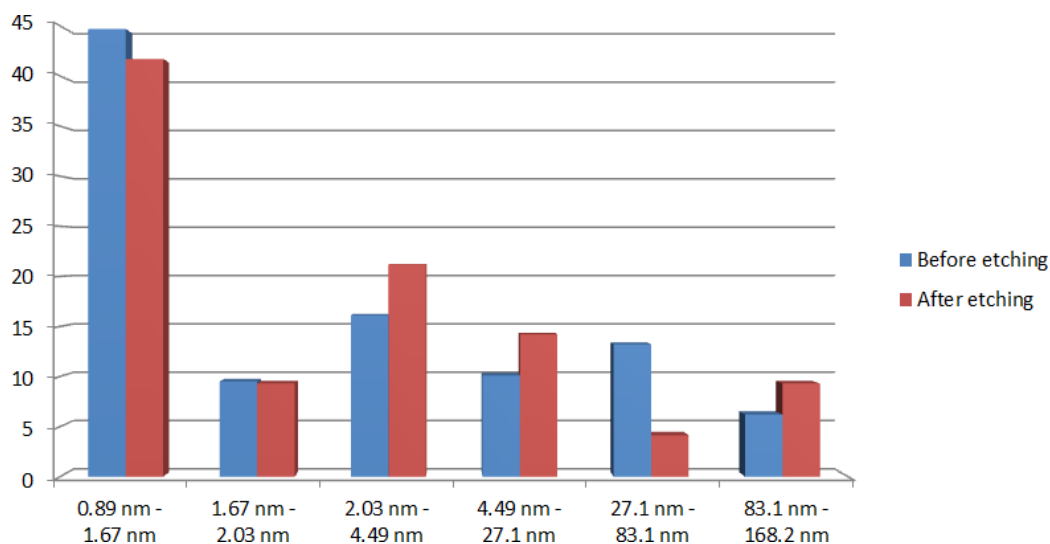


Figure S5: ISEC-derived distribution (relative abundance ΔR , %) of pore diameters (nm) of the ROMP monoliths M1a and M1b. M1a (ΔR of the pore range): 0.89 - 1.67 nm (ΔR : 44.7 %), 1.67 - 2.03 nm (ΔR : 9.5 %), 2.03 - 4.49 nm (ΔR : 16.1 %), 4.49 - 27.1 nm (ΔR : 10.1 %), 27.1 - 83.1 nm (ΔR : 13.2 %), 83.1 - 168.2 nm (ΔR : 6.2 %). M1b (ΔR of the pore range): 0.89 - 1.67 nm (ΔR : 41.7 %), 1.67 - 2.03 nm (ΔR : 9.3 %), 2.03 - 4.49 nm (ΔR : 21.2 %), 4.49 - 27.1 nm (ΔR : 14.2 %), 27.1 - 83.1 nm (ΔR : 4.1 %), 83.1 - 168.2 nm (ΔR : 9.3 %).

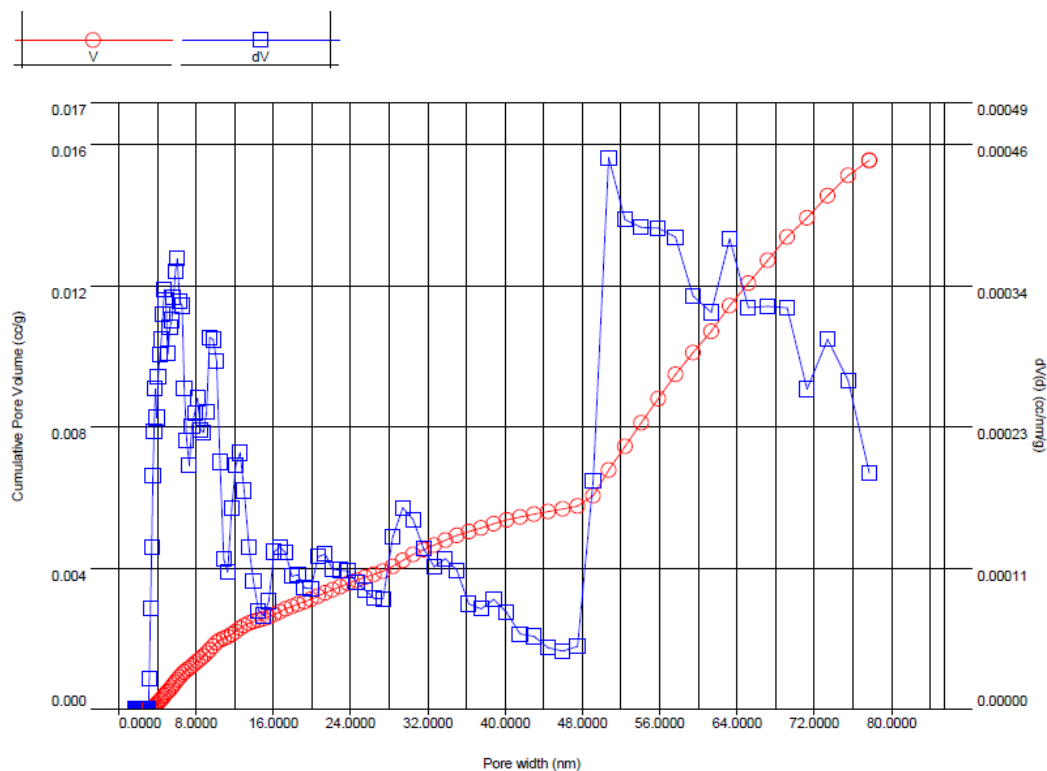


Figure S6: N_2 -adsorption results (BET method) - pore size distribution of M2a.

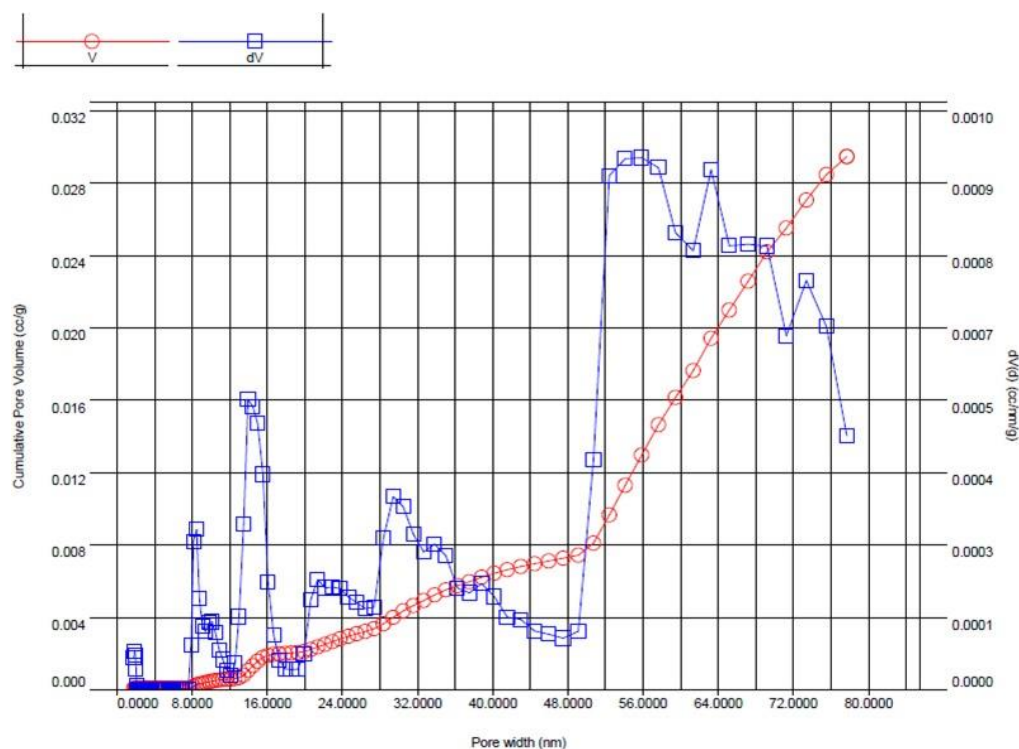


Figure S7: N₂-adsorption results (BET method) - pore size distribution of M2b.

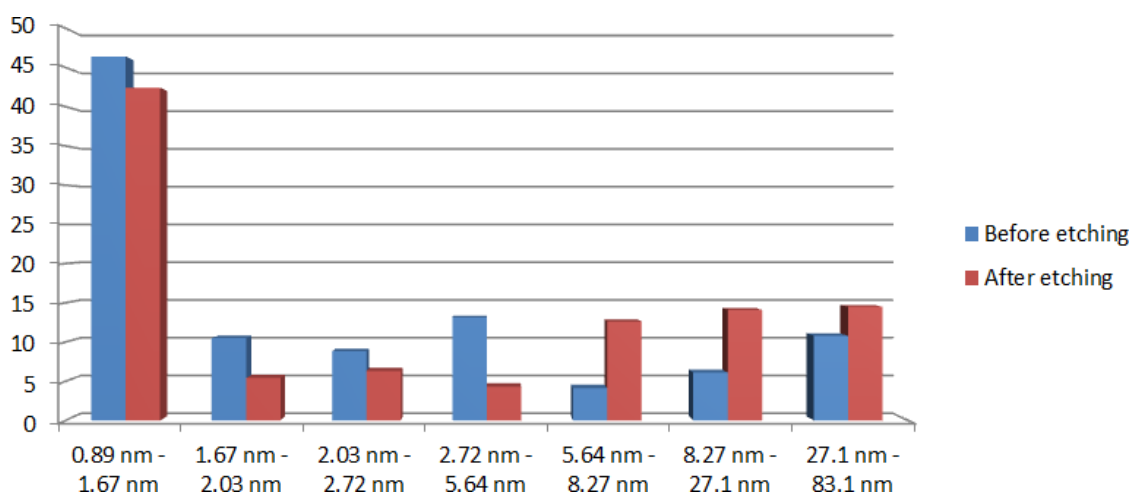


Figure S8: ISEC-derived distribution (relative abundance ΔR , %) of pore diameters (nm) of the ROMP monoliths M2a and M2b. M2a (ΔR of the pore range): 0.89 - 1.67 nm (ΔR : 46.4 %), 1.67 - 2.03 nm (ΔR : 10.5 %), 2.03 - 2.72 nm (ΔR : 8.8 %), 2.72 - 5.64 nm (ΔR : 13.1 %), 5.64 - 8.27 nm (ΔR : 4.1 %), 8.27 - 27.1 nm (ΔR : 6.1 %), 27.1 - 83.1 nm (ΔR : 10.8%). M2b (ΔR of the pore range): 0.89 - 1.67 nm (ΔR : 42.4 %), 1.67 - 2.03 nm (ΔR : 5.4 %), 2.03 - 2.72 nm (ΔR : 6.3 %), 2.72 - 5.64 nm (ΔR : 4.3 %), 5.64 - 8.27 nm (ΔR : 12.6 %), 8.27 - 27.1 nm (ΔR : 14.1 %), 27.1 - 83.1 nm (ΔR : 14.5 %).

Table S1: PS standards and elution volumes (M0).

M_w	Φ [Å]	Retention time [min]	V_e [μ L]	R [%]	ΔV_e [μ L]	ΔR [%]	Φ_{av} [nm]
Toluene	8.9	5.117	1445	100	65	39.0	1.06
162	12.4	4.902	1381	60.9	24	14.7	1.43
266	16.7	4.821	1356	46.1	52	31.8	1.84
370	20.3	4.646	1304	14.3	5	2.9	2.34
607	27.2	4.630	1299	11.4	5	2.7	3.49
1420	44.9	4.615	1295	8.7	5	2.9	8.14
10730	148.1	4.599	1290	5.8	6	3.8	20.0
30000	271.6	4.578	1283	2	3.3	2.0	68.7
700000	1741.81	4.567	1280	0			

Table S2: PS standards and elution volumes (M1a).

M_w	Φ [Å]	Retention time [min]	V_e [μ L]	R [%]	ΔV_e [μ L]	ΔR [%]	Φ_{av} [nm]
Toluene	8.9	7.364	2089	100	260	44.7	1.22
266	16.7	6.497	1829	55.2	55	9.5	1.84
370	20.3	6.313	1774	45.7	94	16.1	3.01
1420	44.9	6.000	1680	29.5	59	10.1	11.0
30000	271.6	5.804	1621	19.4	77	13.2	47.4
200000	831.8	5.548	1544	6.2	36	6.2	118.0
660000	1682.4	5.427	1508	0			

Table S3: PS standards and elution volumes (M1b)

M_w	Φ [Å]	Retention time [min]	V_e [μ L]	R [%]	ΔV_e [μ L]	ΔR [%]	Φ_{av} [nm]
Toluene	8.9	8.226	2348	100	344	41.7	1.22
266	16.7	7.08	2004	58.2	77	9.3	1.84
370	20.3	6.825	1928	48.9	175	21.2	3.01
1420	44.9	6.243	1753	27.6	117	14.2	11.0
30000	271.6	5.852	1636	13.4	34	4.1	47.4
200000	831.8	5.739	1602	9.3	77	9.3	118.0
660000	1682.4	5.484	1525	0			

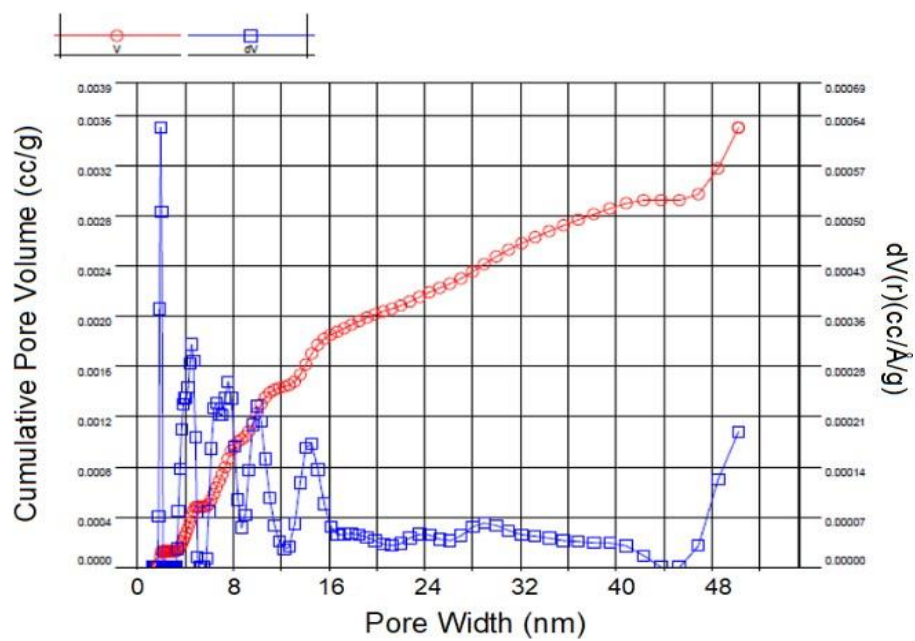
Table S4: PS standards and elution volumes (M2a).

M_w	Φ [Å]	Retention time [min]	V_e [μ L]	R [%]	ΔV_e [μ L]	ΔR [%]	Φ_{av} [nm]
Toluene	8.9	7.029	1989	100	207	46.4	1.22
266	16.7	6.339	1782	53.5	47	10.5	1.84
370	20.3	6.182	1735	43	39	8.8	2.34
607	27.2	6.051	1695	34	59	13.1	3.90
2090	56.4	5.856	1637	21	18	4.1	6.82
4000	82.7	5.795	1619	17	27	6.1	14.9
30000	271.6	5.704	1591	10.8	49	10.8	47.4
200000	831.8	5.542	1543	0			

Table S5: PS standards and elution volumes (M2b).

M_w	Φ [Å]	Retention time [min]	V_e [μ L]	R [%]	ΔV_e [μ L]	ΔR [%]	Φ_{av} [nm]
Toluene	8.9	6.640	1902	100	192	42.4	1.22
266	16.7	6.000	1710	57.5	25	5.4	1.84
370	20.3	5.918	1685	52.1	29	6.3	2.34
607	27.2	5.822	1657	45.7	20	4.3	3.90
2090	56.4	5.756	1637	41.3	57	12.6	6.82
4000	82.7	5.565	1580	28.7	64	14.1	14.9
30000	271.6	5.351	1515	14.5	66	14.5	47.4
200000	831.8	5.132	1450	0			

a)



b)

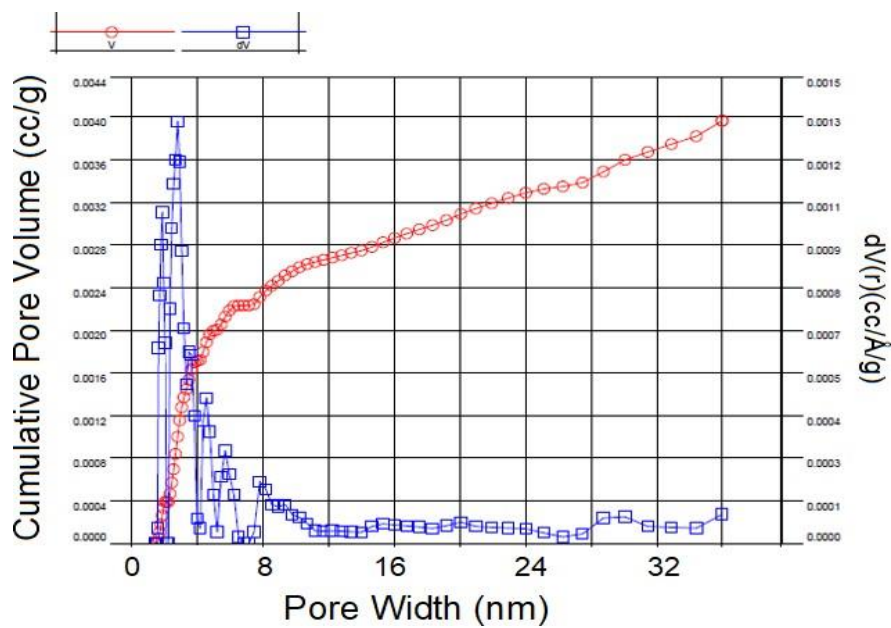
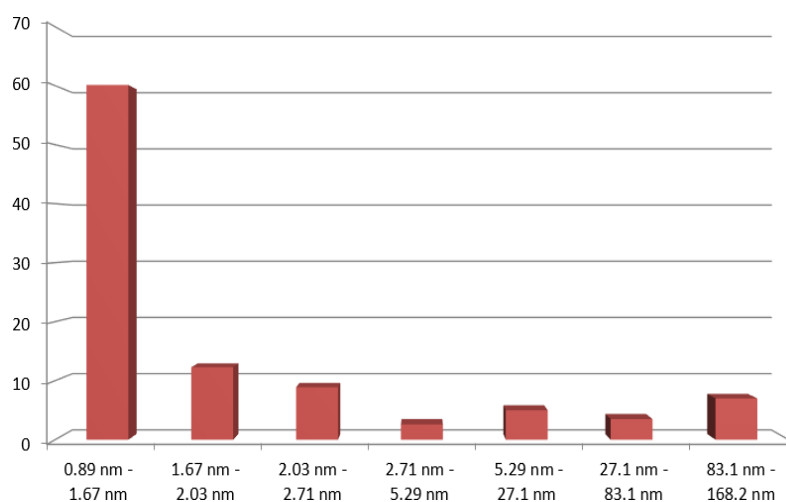


Figure S9: Pore size distribution of NBE-based monoliths. a) N1, b) N2.

a)



b)

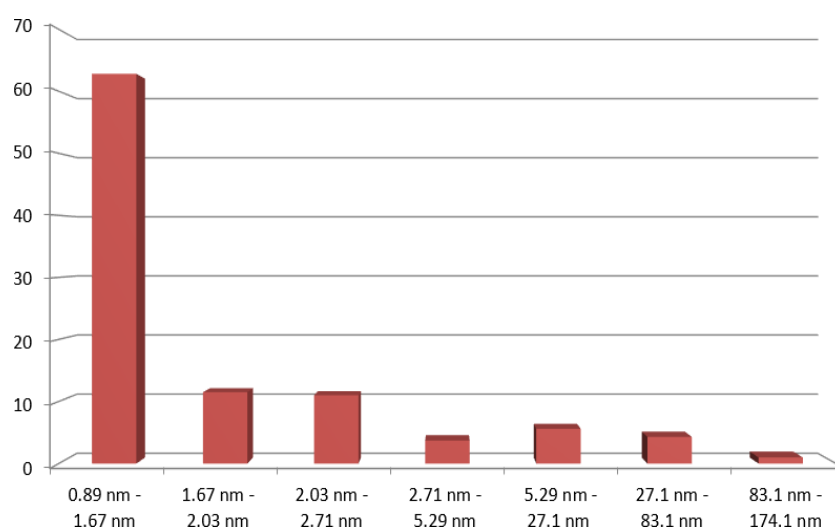
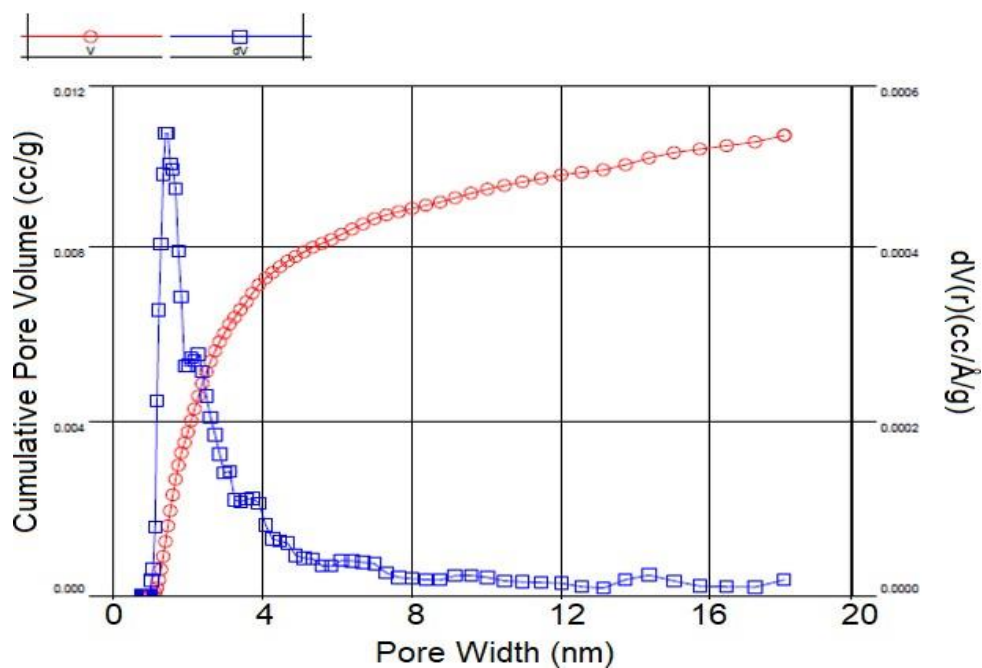


Figure S10: ISEC-derived distribution (relative abundance ΔR , %) of pore diameters (nm) of the ROMP-derived monoliths. a) N1. ΔR of the pore range: 0.89 - 1.67 nm (ΔR : 60.1 %), 1.67 - 2.03 nm (ΔR : 12.3 %), 2.03 - 2.71 nm (ΔR : 8.9 %), 2.71 - 5.29 nm (ΔR : 2.6 %), 5.29 - 27.1 nm (ΔR : 5.1 %), 27.1 - 83.1 nm (ΔR : 3.5 %), 83.1 - 168.2 nm (ΔR : 7.1 %), b) N2. ΔR of the pore range (nm): 0.89 - 1.67 nm (ΔR : 62.8 %), 1.67 - 2.03 nm (ΔR : 11.5 %), 2.03 - 2.71 nm (ΔR : 11 %), 2.71 - 5.29 nm (ΔR : 3.7%), 5.29 - 27.1 nm (ΔR : 5.6%), 27.1 - 83.1 nm (ΔR : 4.3 %), 83.1 - 174.1 nm (ΔR : 1.0%)

a)



b)

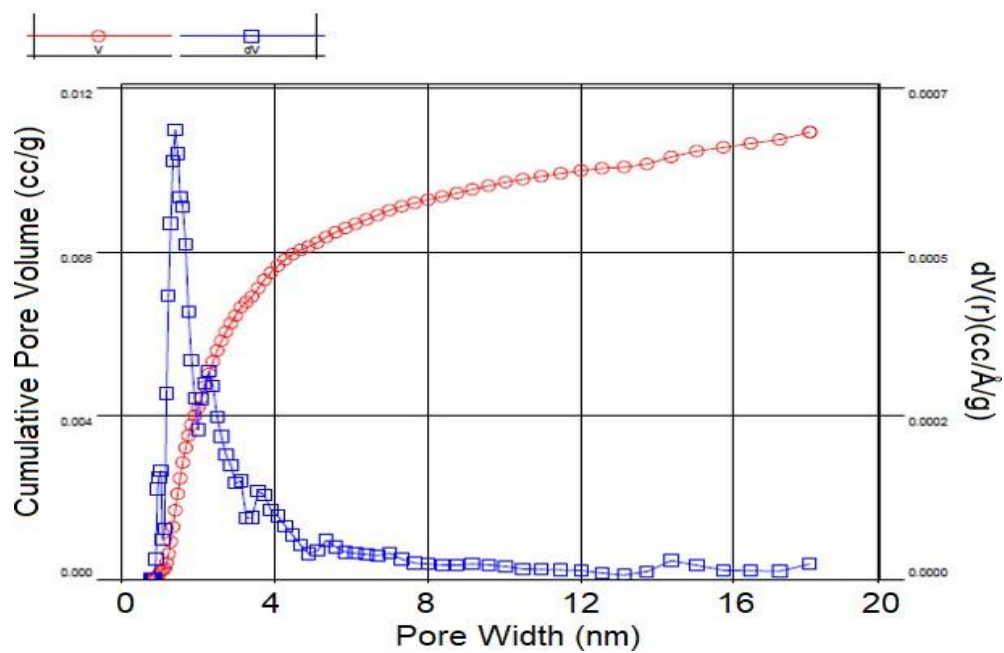
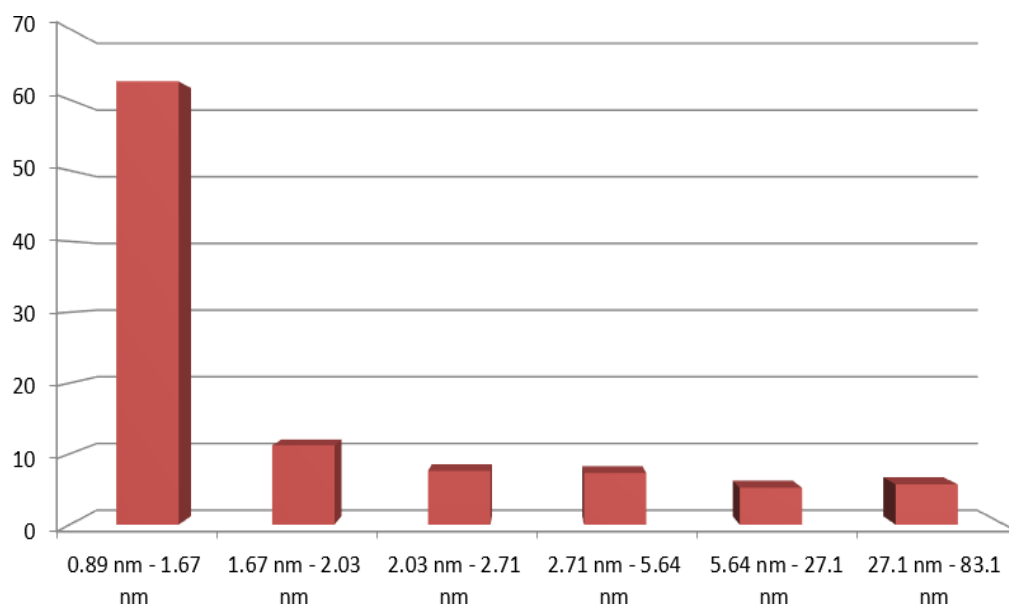


Figure S11: Pore size distribution of NBE-based monoliths. a) N3, b) N4.

a)



b)

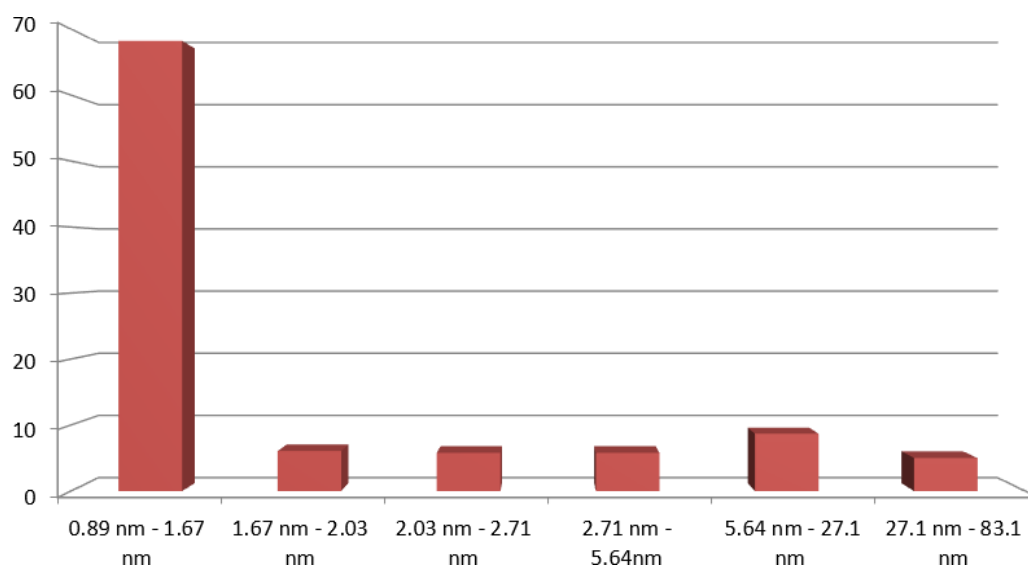


Figure S12: ISEC-derived distribution (relative abundance ΔR , %) of pore diameters (nm) of the ROMP-derived monoliths. a) N3. ΔR of the pore range: 0.89 - 1.67 nm (ΔR : 62.6 %), 1.67 - 2.03 nm (ΔR : 11.2 %), 2.03 - 2.71 nm (ΔR : 7.6 %), 2.71 - 5.64 nm (ΔR : 7.3 %), 5.64 - 27.1 nm (ΔR : 5.2%), 27.1 - 83.1 nm (ΔR : 5.7 %). b) N4. ΔR of the pore range (nm): 0.89 - 1.67 nm (ΔR : 68.2 %), 1.67 - 2.03 nm (ΔR : 6.07 %), 2.03 - 2.71 nm (ΔR : 5.8 %), 2.71 - 5.64 nm (ΔR : 5.8 %), 5.29 - 27.1 nm (ΔR : 8.7%), 27.1 - 83.1 nm (ΔR : 5 %).

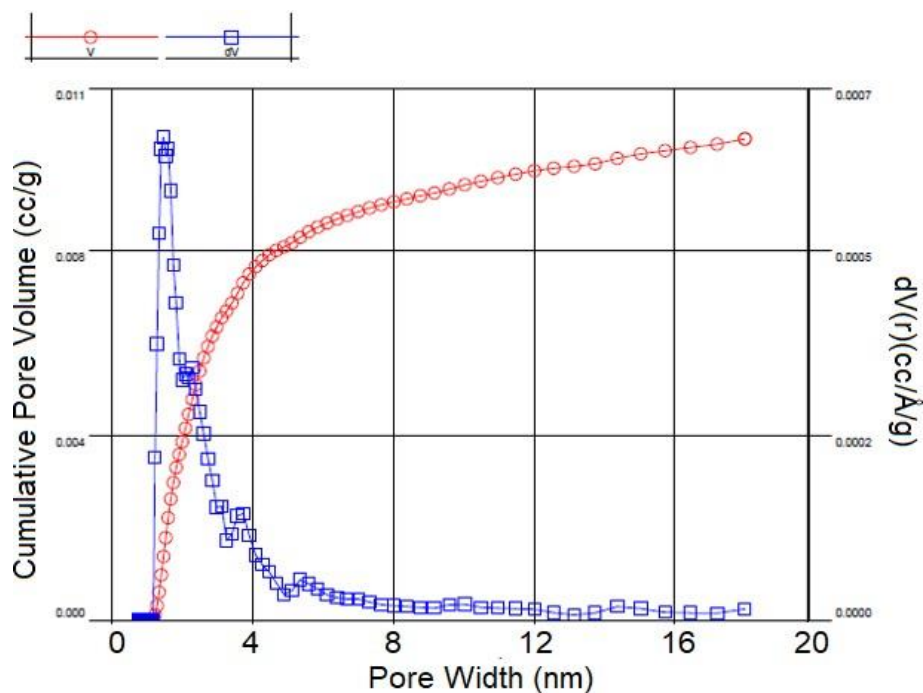


Figure S13: Pore size distribution of NBE-based monoliths N5.

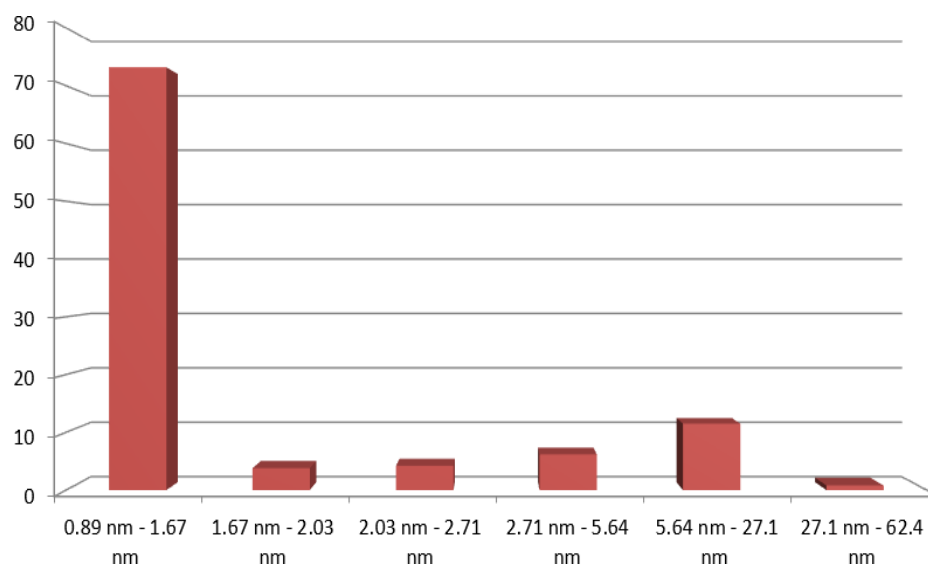
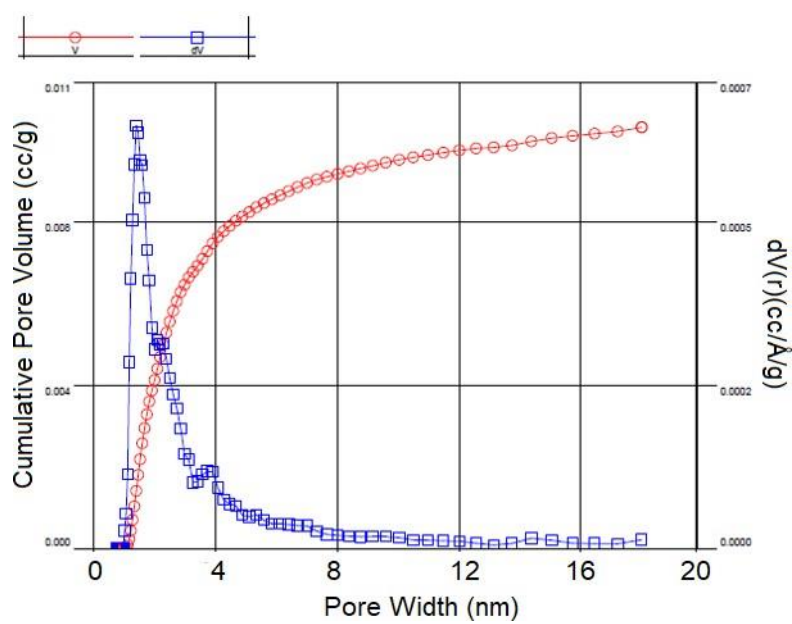


Figure S14: ISEC-derived distribution (relative abundance ΔR , %) of pore diameters (nm) of the ROMP-derived monoliths. N5. ΔR of the pore range: 0.89 - 1.67 nm (ΔR : 73.2 %), 1.67 - 2.03 nm (ΔR : 3.8 %), 2.03 - 2.71 nm (ΔR : 4.2 %), 2.71 - 5.64 nm (ΔR : 6.2 %), 5.64 - 27.1 nm (ΔR : 11.5%), 27.1 - 62.4 nm (ΔR : 0.8 %).

a)



b)

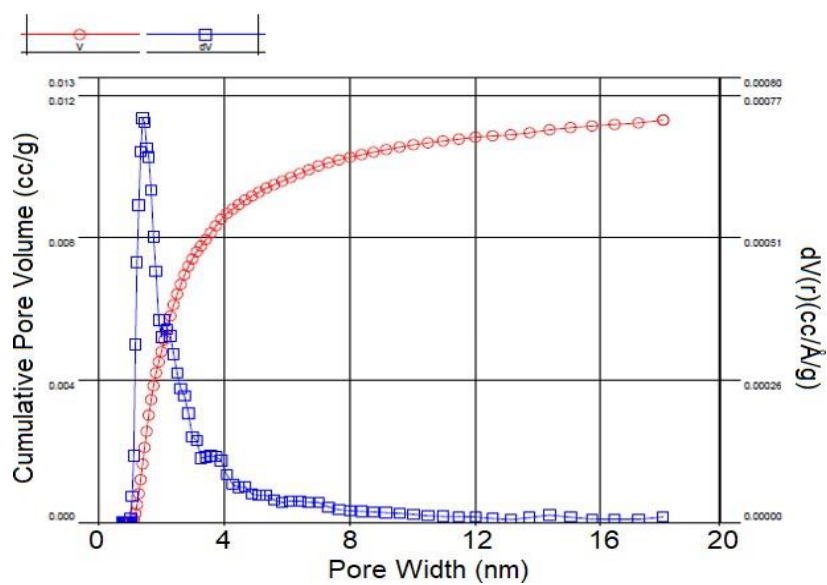
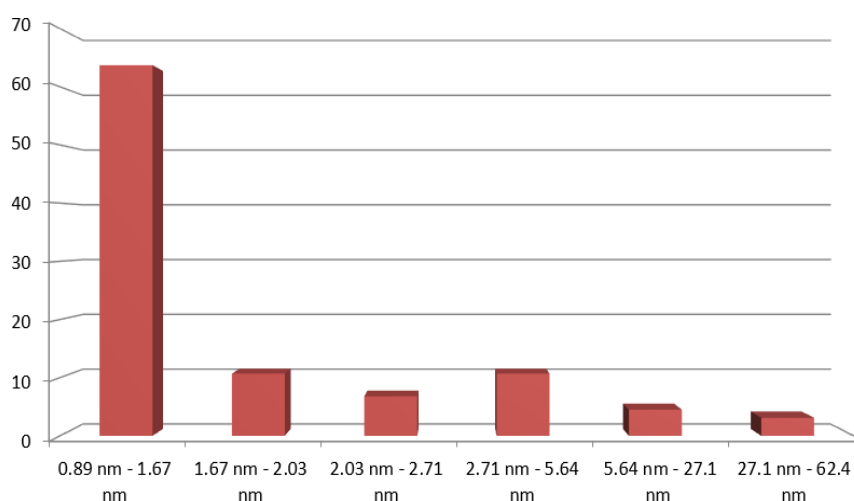


Figure S15: Pore size distribution of NBE-based monoliths. a) N6, b) N7.

a)



b)

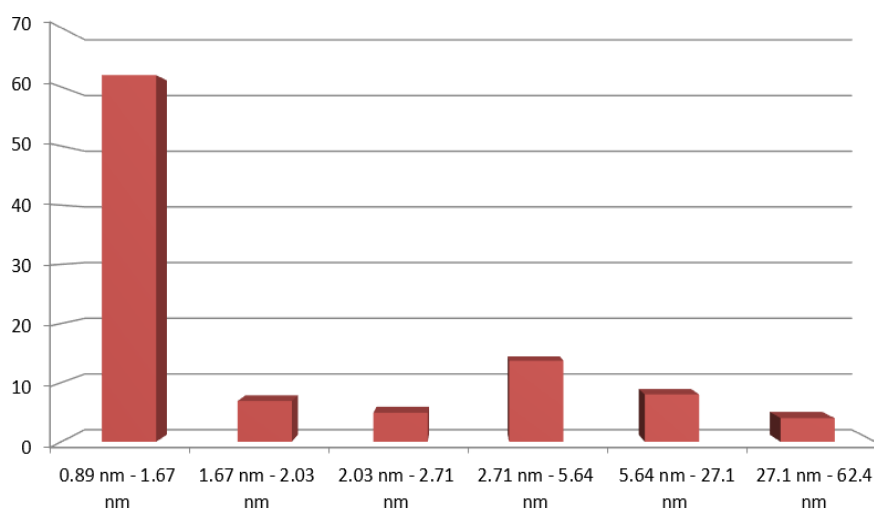


Figure S16: ISEC-derived distribution (relative abundance ΔR , %) of pore diameters (nm) of the ROMP-derived monoliths. a) N6. ΔR of the pore range (nm): 0.89 - 1.67 nm (ΔR : 63.7 %), 1.67 - 2.03 nm (ΔR : 10.7 %), 2.03 - 2.71 nm (ΔR : 6.8 %), 2.71 - 5.64 nm (ΔR : 10.7 %), 5.64 - 27.1 nm (ΔR : 4.5%), 27.1 - 62.4 nm (ΔR : 3.1 %). b) N7. ΔR of the pore range: 0.89 - 1.67 nm (ΔR : 62 %), 1.67 - 2.03 nm (ΔR : 6.9 %), 2.03 - 2.71 nm (ΔR : 4.9 %), 2.71 - 5.64 nm (ΔR : 13.7 %), 5.64 - 27.1 nm (ΔR : 8%), 27.1 - 62.4 nm (ΔR : 4 %)

Table S6: PS Standards and elution volumes (N1).

M_w	Φ [Å]	Retention time [min]	V_e [μ l]	R [%]	ΔV_e [μ l]	ΔR [%]	Log Φ_{av} [Å]
Toluene	8.9	1.608	604	100	77	34.4	1.027
162	12.4	1.454	527	65.5	57	25.7	1.158
266	16.7	1.339	469	39.8	28	12.3	1.265
370	20.3	1.284	442	27.5	20	8.9	1.374
607	27.1	1.244	422	18.5	6	2.6	1.577
1880	52.9	1.232	416	15.8	12	5.1	2.078
30000	271.5	1.209	404	10.7	8	3.5	2.676
200000	831.7	1.193	396	7.1	16	7.1	3.072
660000	1682.3	1.161	380	0			

Table S7: PS Standards and elution volumes (N2).

M_w	Φ [Å]	Retention time [min]	V_e [μ l]	R [%]	ΔV_e [μ l]	ΔR [%]	Log Φ_{av} [Å]
Toluene	8.9	1.583	592	100	71	36.0	1.027
162	12.4	1.442	521	63.9	52	26.8	1.158
266	16.7	1.337	468.5	37.0	23	11.5	1.265
370	20.3	1.292	446	25.5	21.5	11	1.374
607	27.1	1.249	424.5	14.5	0	0.2	1.484
912	34.5	1.249	424.5	14.5	7	3.5	1.630
1880	52.9	1.235	417.5	10.9	11	5.6	2.078
30000	271.5	1.213	406.5	5.3	9	4.3	2.676
200000	831.7	1.196	398	1.0	2	1.0	3.079
700000	1741.8	1.192	396	0			

Table S8: PS Standards and elution volumes (N3).

M_w	Φ [Å]	Retention time [min]	V_e [μ l]	R [%]	ΔV_e [μ l]	ΔR [%]	Log Φ_{av} [Å]
Toluene	8.9	3,877	1739	100	220	62.6	1.087
266	16.7	3,437	1518	37.3	40	11.2	1.265
370	20.3	3,358	1479	26.0	27	7.6	1.371
607	27.1	3,304	1452	18.3	24	6.8	1.543
1420	44.9	3,256	1428	11.5	2	0.5	1.701
2090	56.4	3,252	1426	10.9	8	2.2	1.834
4000	82.7	3,236	1418	8.6	5	1.2	2.008
8140	125.8	3,227	1413.5	7.4	0	0	2.135
10730	148.1	3,227	1413.5	7.4	6	1.7	2.302
30000	271.6	3,215	1407.5	5.6	20	5.7	2.676
200000	831.8	3,175	1387.5	0			

Table S9: PS Standards and elution volumes (N4).

M_w	Φ [Å]	Retention time [min]	V_e [μ l]	R [%]	ΔV_e [μ l]	ΔR [%]	Log Φ_{av} [Å]
Toluene	8.9	3,404	1552	100	191	68.2	1.087
266	16.7	3,022	1311	31.7	17	6.0	1.265
370	20.3	2,988	1294	25.7	16	5.8	1.371
607	27.1	2,955	1277	19.8	14	4.8	1.543
1420	44.9	2,928	1264	15.0	3	1.0	1.701
2090	56.4	2,922	1261	13.9	8	2.6	1.834
4000	82.7	2,907	1253	11.2	1	0.3	2.008
8140	125.8	2,905	1252	10.8	6	2.1	2.135
10730	148.1	2,893	1246	8.7	11	3.7	2.302
30000	271.6	2,872	1236	5.0	14	5.0	2.676
200000	831.8	2,844	1222	0			

Table S10: PS Standards and elution volumes (N5).

M_w	Φ [Å]	Retention time [min]	V_e [μ l]	R [%]	ΔV_e [μ l]	ΔR [%]	Log Φ_{av} [Å]
Toluene	8.9	3,830	1715	100	174	73.2	1.087
266	16.7	3,483	1541	26.7	9	3.8	1.265
370	20.3	3.465	1532	22.9	10	4.2	1.371
607	27.1	3.445	1522	18.7	9	3.5	1.543
1420	44.9	3.428	1514	15.1	7	2.7	1.701
2090	56.4	3.415	1507	12.4	17	6.9	1.834
4000	82.7	3.382	1491	5.4	1	0.4	2.044
10730	148.1	3.380	1490	5.0	10	4.2	2.302
30000	271.6	3.360	1480	0.8	2	0.8	2.614
123000	624.4	3.356	1478	0			

Table S11: PS Standards and elution volumes (N6).

M_w	Φ [Å]	Retention time [min]	V_e [μ l]	R [%]	ΔV_e [μ l]	ΔR [%]	Log Φ_{av} [Å]
Toluene	8.9	3,889	1745	100	191	63.7	1.087
266	16.7	3,508	1554	36.2	32	10.7	1.265
370	20.3	3.444	1522	25.5	21	6.8	1.371
607	27.1	3.403	1501	18.7	20	6.6	1.543
1420	44.9	3.363	1481	12	13	4.1	1.701
2090	56.4	3.338	1469	7.8	2	0.8	1.834
4000	82.7	3.333	1466	7.0	8	2.6	2.008
8140	125.8	3.317	1458	4.3	4	1.1	2.266
30000	271.6	3.310	1455	3.1	10	3.1	2.614
123000	624.4	3.291	1445	0			

Table S12: PS Standards and elution volumes (N7).

M_w	Φ [Å]	Retention time [min]	V_e [μ l]	R [%]	ΔV_e [μ l]	ΔR [%]	Log Φ_{av} [Å]
Toluene	8.9	4,403	2002	100	182	62.0	1.087
266	16.7	4,038	1819	37.9	21	6.9	1.265
370	20.3	3.997	1798	30.9	15	4.9	1.371
607	27.1	3.968	1784	26	23	7.8	1.543
1420	44.9	3.922	1761	18.1	18	5.9	1.701
2090	56.4	3.887	1743	12.2	17	5.7	1.834
4000	82.7	3.853	1726	6.4	7	2.3	2.175
30000	271.6	3.839	1719	4.0	12	4.0	2.614
123000	624.4	3.815	1707	0			

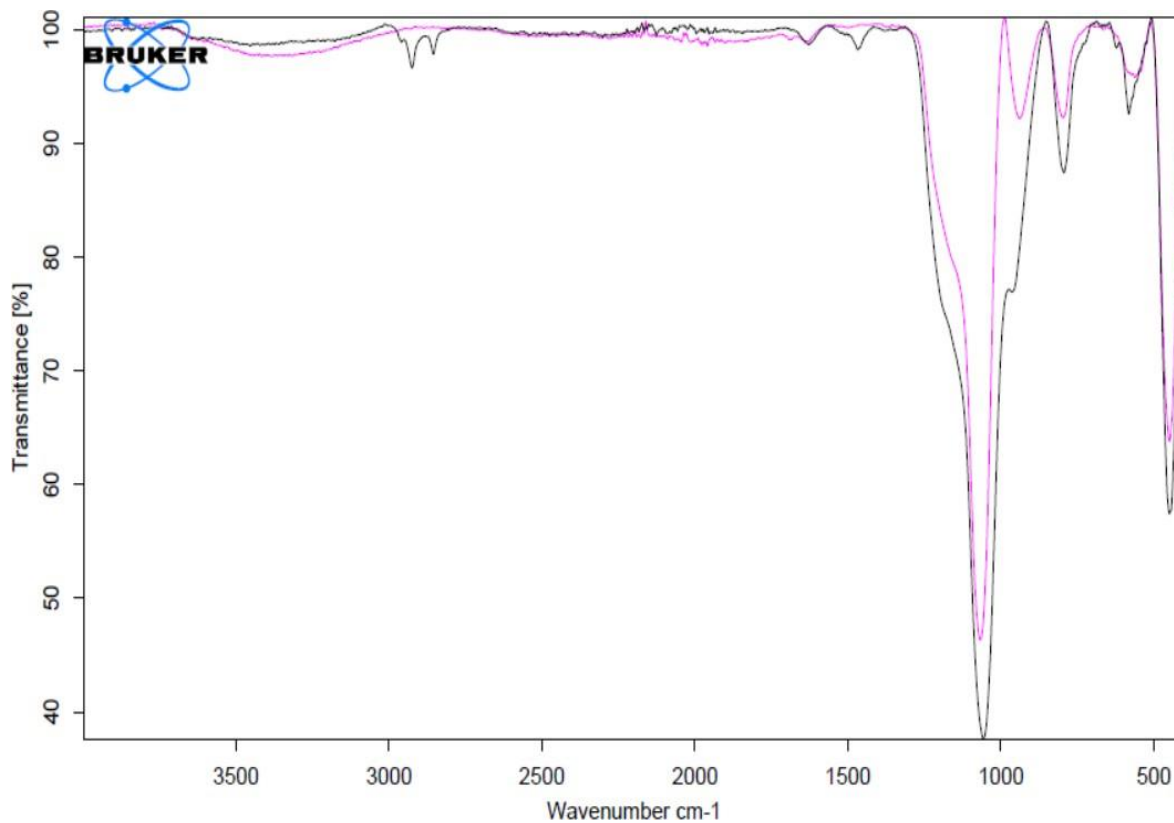


Figure S17: The comparison of FT-IR spectra of non-modified, neat SiO₂ nanowires and Oleic acid (OA)-modified SiO₂ nanowires.

The peaks at 2926 and 2855 cm⁻¹ show that a long alkyl chain is present in the OA-modified nanowire. The peak at 1590 cm⁻¹ corresponding to carboxylate appears. Thus, it can be concluded that the OA, -COOH has reacted with -OH on the surface of SiO₂, and the product is a carboxylate.

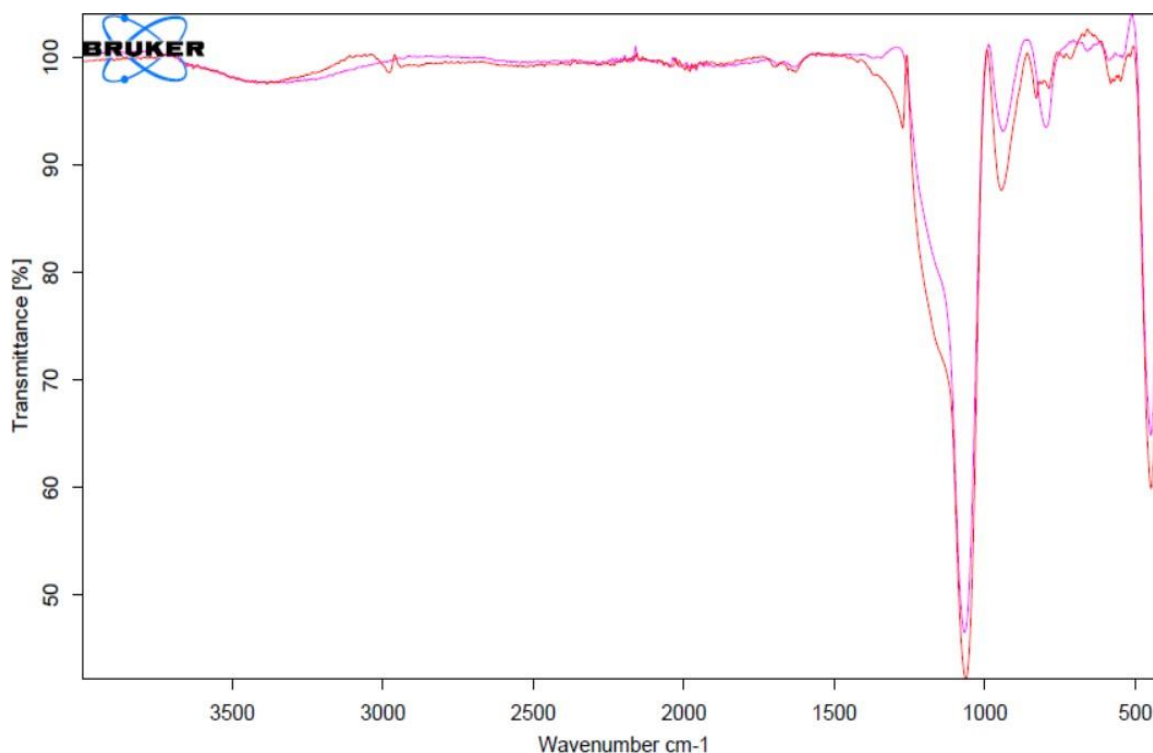
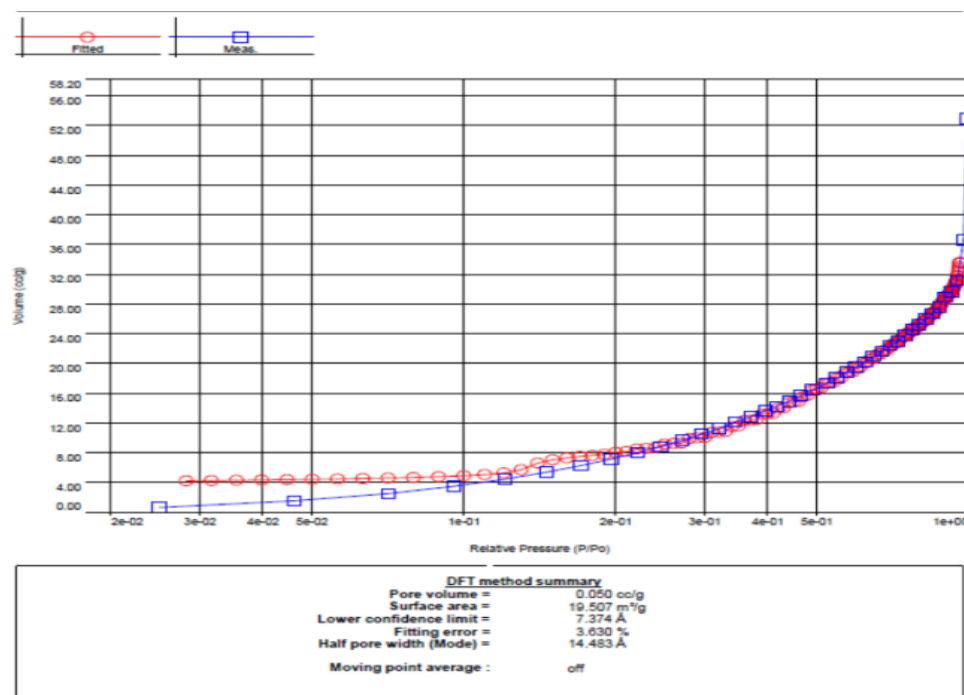


Figure S18: The comparison of FT-IR spectra of non-modified SNWs and (bicyclo[2.2.1]hept-5-en-2-yl)triethoxysilane-modified SNWs.

The peak near 3000 cm⁻¹ shows that -CH is present in the (bicyclo[2.2.1]hept-5-en-2-yl)triethoxysilane-modified SiO₂ nanowire. The peak at 1590 cm⁻¹ corresponding to carboxylate appears. Thus, it can be concluded that the triethoxysilane norbornene, -COOH has reacted with -OH on the surface of SiO₂, and the product is a carboxylate.

a)



b)

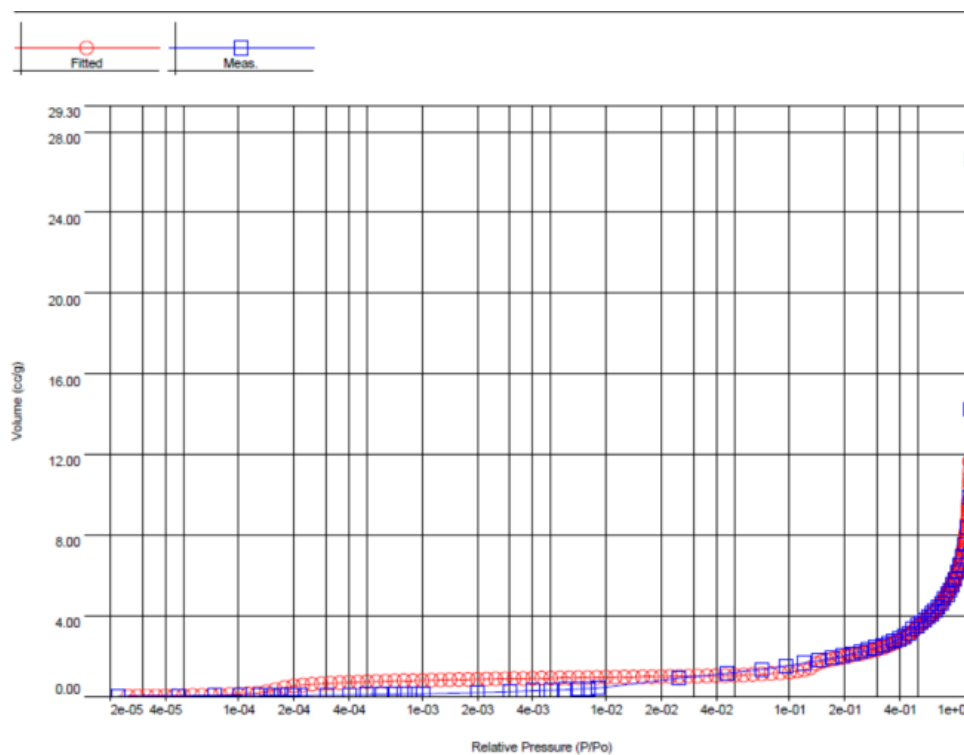


Figure S19: Comparison of the (a) N₂-derived, (b) Ar-derived pore size distribution of the ROMP-derived monolith (M1b).

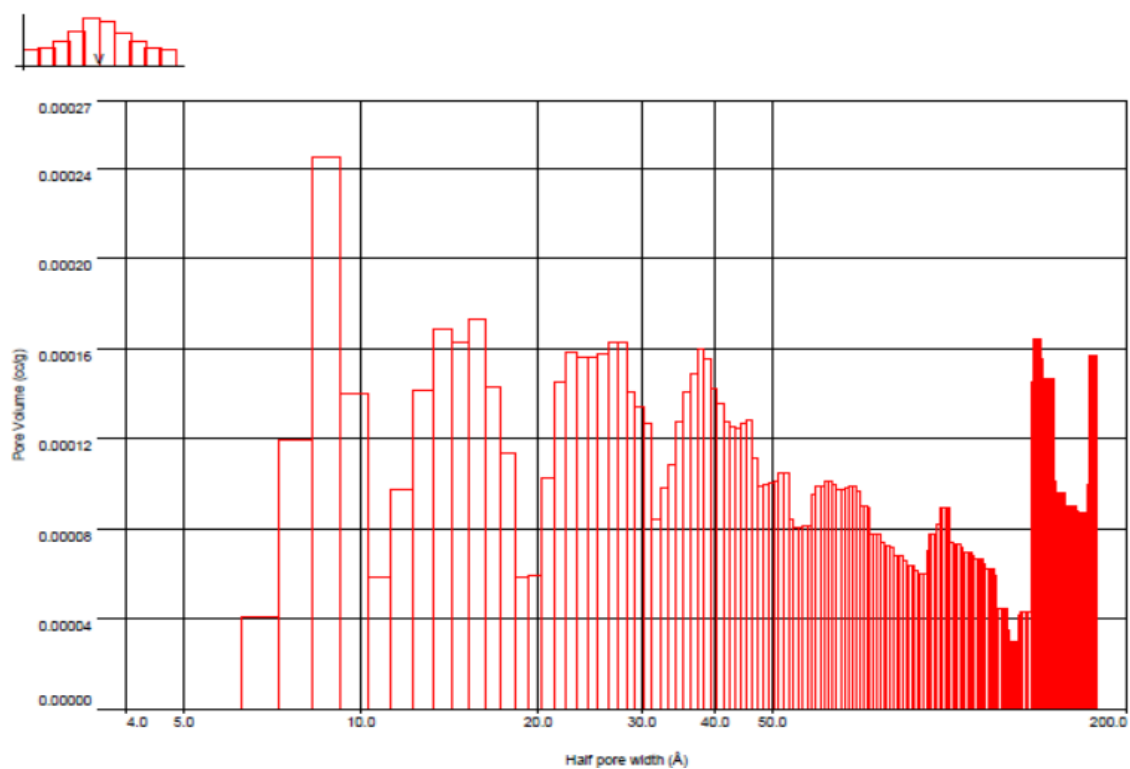


Figure S20: Volume histogram of Ar-derived pore size distribution of the ROMP-derived monolith (M2b).

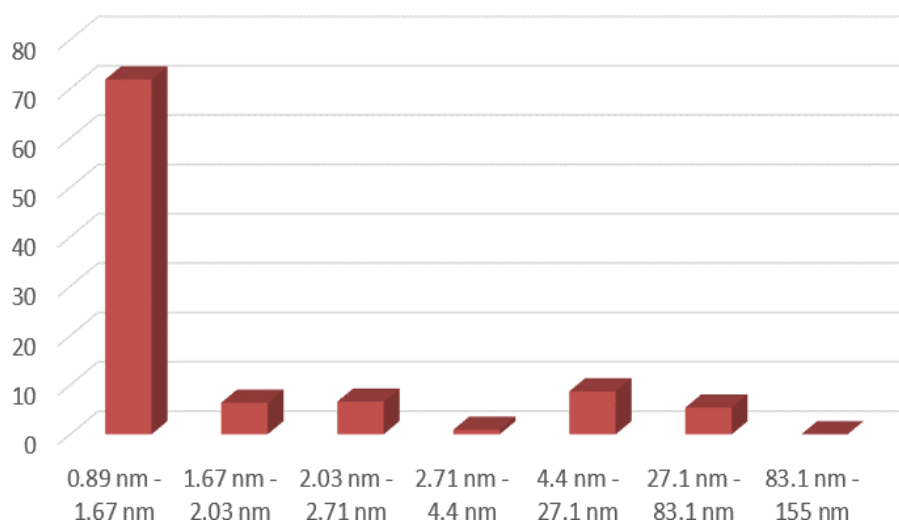


Figure S21: ISEC-derived distribution (relative abundance ΔR , %) of pore diameters (nm) of the polyurethane-based monolith PUR1. ΔR of the pore range: 0.89 - 1.67 nm (ΔR : 71.9 %), 1.67 - 2.03 nm (ΔR : 6.4 %), 2.03 - 2.71 nm (ΔR : 6.6 %), 2.71 - 4.4 nm (ΔR : 0.9 %), 4.4 - 27.1 nm (ΔR : 8.7 %), 27.1 - 83.1 nm (ΔR : 5.4 %), 83.1 nm - 155 nm (ΔR : 0%).

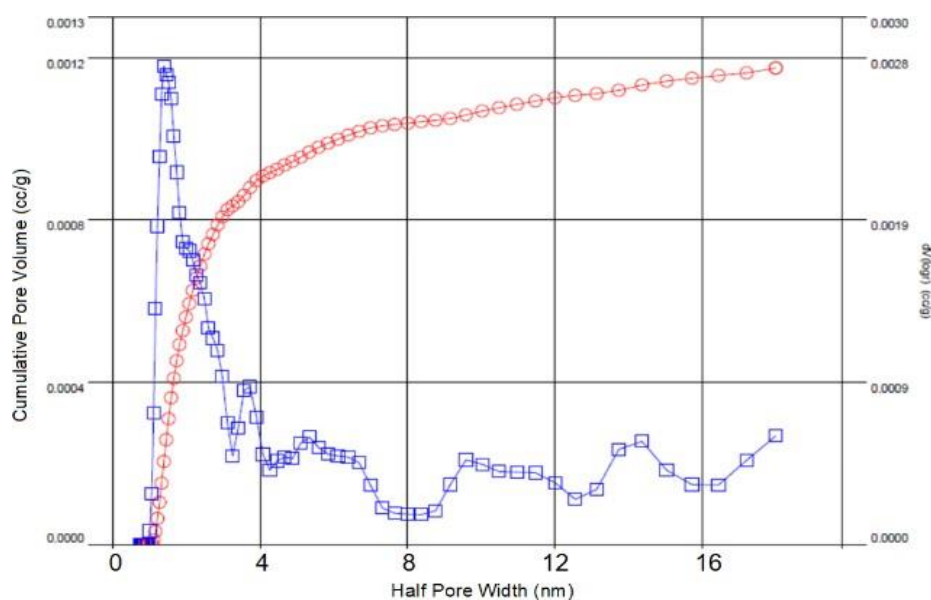
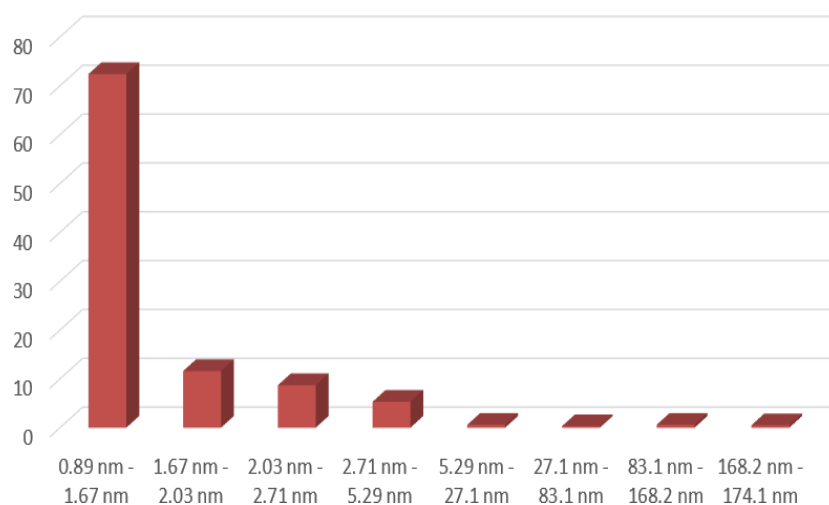


Figure S22: N₂ derived-pore size distribution of poly(urethane)-derived monoliths. PUR1.

a)



b)

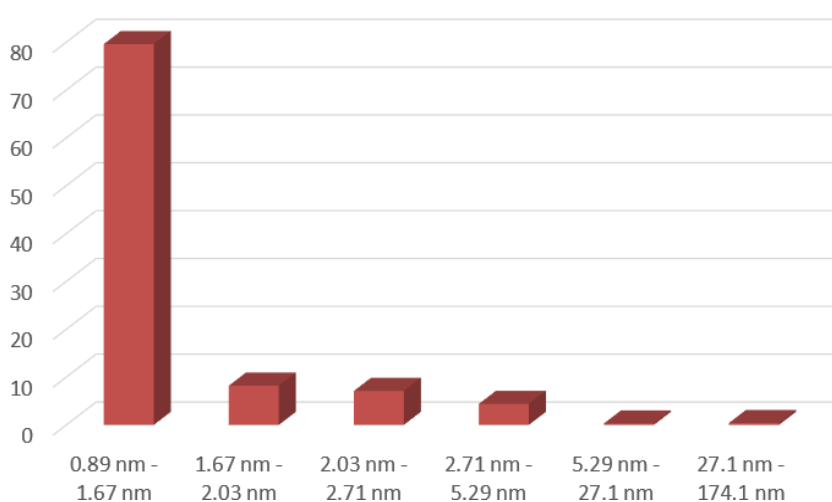
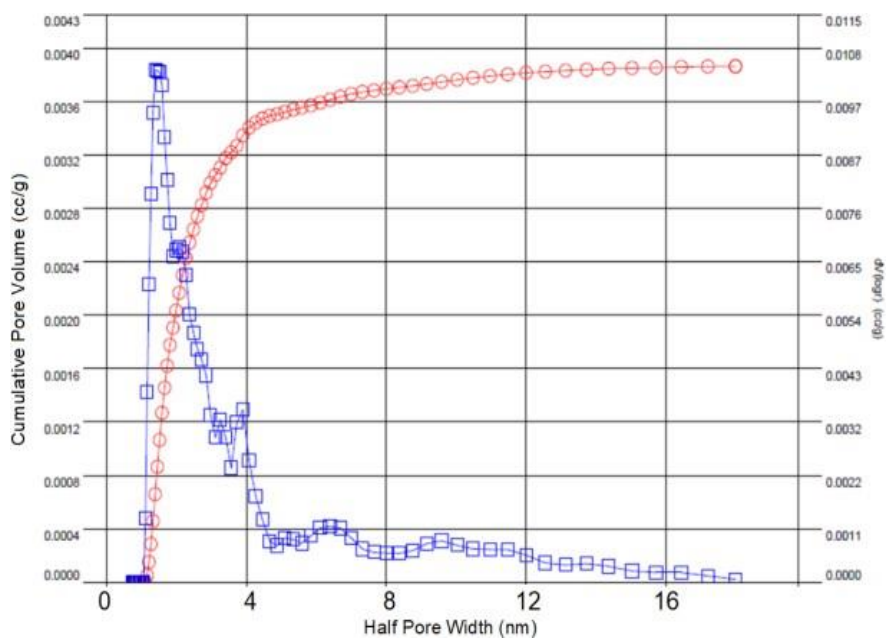


Figure S23: ISEC-derived distribution (relative abundance ΔR , %) of pore diameters (nm) of the polyurethane-based monolith a) PUR2. ΔR of the pore range: 0.89 - 1.67 nm (ΔR : 72.4 %), 1.67 - 2.03 nm (ΔR : 11.6 %), 2.03 - 2.71 nm (ΔR : 8.7 %), 2.71 - 5.29 nm (ΔR : 5.3 %), 5.29 - 27.1 nm (ΔR : 0.6 %), 27.1 - 83.1 nm (ΔR : 0.3 %), 83.1 nm - 168.2 nm (ΔR : 0.6 %), 168.2 nm - 174.1 nm (ΔR : 0.5 %) b) PUR3. ΔR of the pore range (nm): 0.89 - 1.67 nm (ΔR : 79.6 %), 1.67 - 2.03 nm (ΔR : 8.2 %), 2.03 - 2.71 nm (ΔR : 7.1 %), 2.71 nm - 5.29 nm (ΔR : 4.4 %), 5.29 nm - 27.1 nm (ΔR : 0.3 %), 27.1 nm - 174.1 nm (ΔR : 0.4 %).

a)



b)

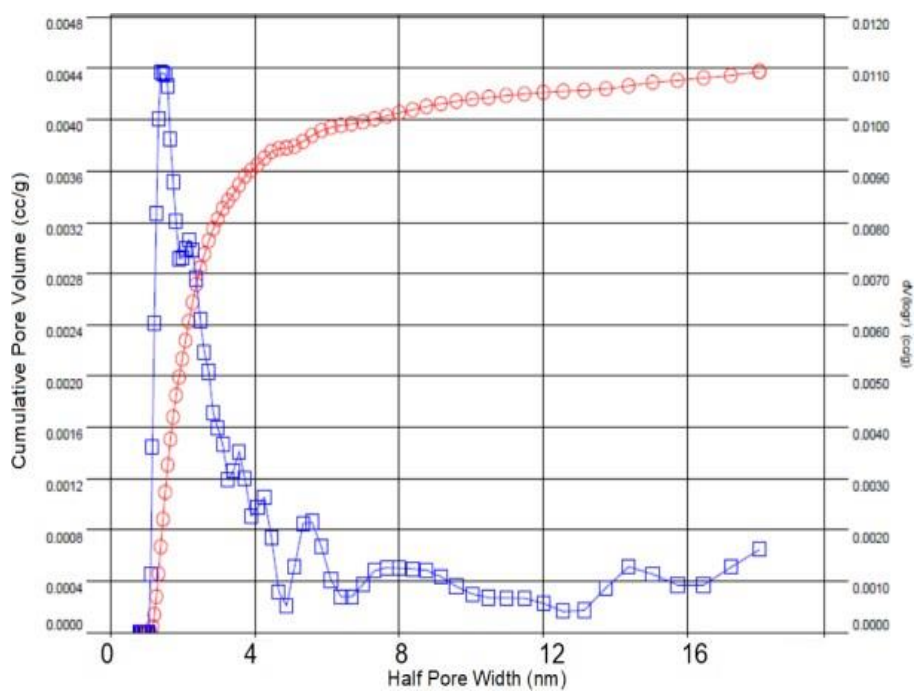


Figure S24: Pore size distribution of poly(urethane)-derived monoliths. a) PUR2, b) PUR3

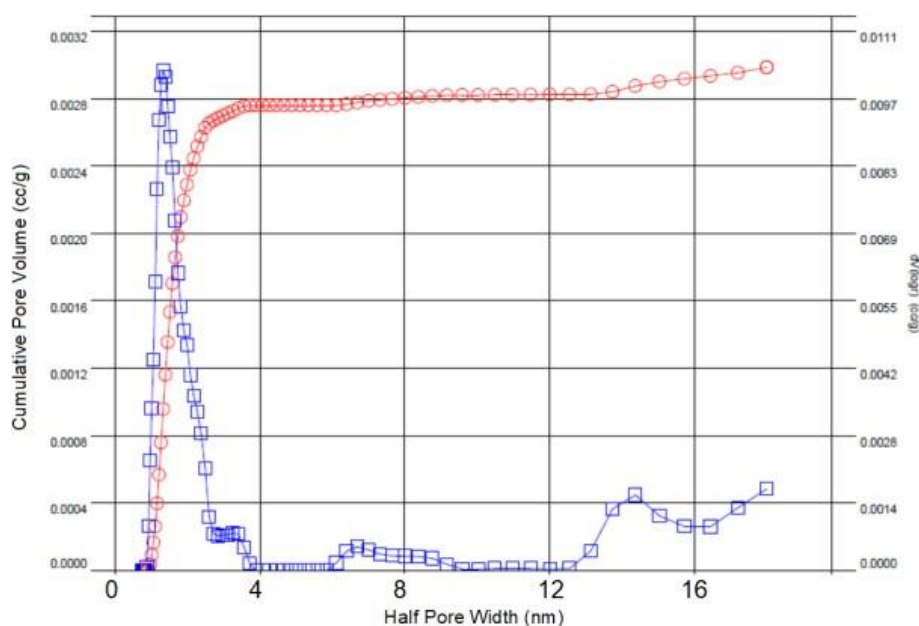


Figure S25: Pore size distribution of poly(urethane)-derived monoliths. PUR4

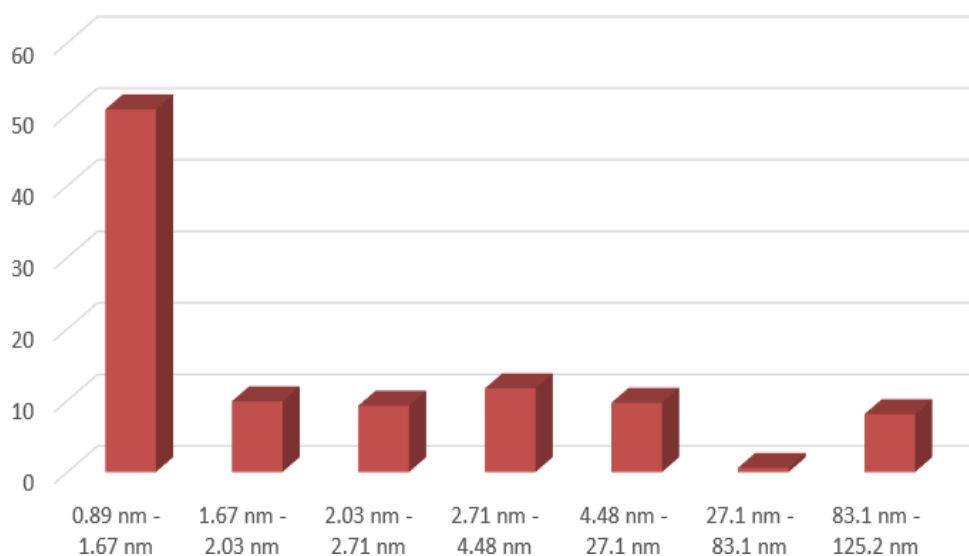


Figure S26: ISEC-derived distribution (relative abundance ΔR , %) of pore diameters (nm) of the poly(urethane)-based monolith PUR4. ΔR of the pore range: 0.89 - 1.67 nm (ΔR : 50.7 %), 1.67 - 2.03 nm (ΔR : 9.9 %), 2.03 - 2.71 nm (ΔR : 9.3 %), 2.71 - 4.48 nm (ΔR : 11.7 %), 4.48 - 27.1 nm (ΔR : 9.7 %), 27.1 - 83.1 nm (ΔR : 0.6 %), 83.1 nm - 125.2 nm (ΔR : 8.1 %).

Table S13: PS Standards and elution volumes (PUR1).

M_w	Φ [Å]	Retention time [min]	V_e [μl]	R [%]	ΔV_e [μl]	ΔR [%]	Log Φ_{av} [Å]
Toluene	8.9	6.161	11988	100	328	52.2	1.021
162	12.4	5.997	11660	47.8	124	19.7	1.158
266	16.7	5.935	11536	28.1	40	6.4	1.265
370	20.3	5.915	11496	21.7	42	6.6	1.370
607	27.1	5.894	11454	15.0	6	0.9	1.541
1420	44.8	5.891	11448	14.1	54	8.7	2.041
30.000	271.5	5.863	11394	5.4	34	5.4	2.676
200.000	831.7	5.847	11360	0	0	0	3.050
575.000	1550.9	5.846	11360	0	-	-	-

Table S14: PS Standards and elution volumes (PUR2).

M_w	Φ [Å]	Retention time [min]	V_e [μl]	R [%]	ΔV_e [μl]	ΔR [%]	Log Φ_{av} [Å]
Toluene	8.9	3.969	7604	100	1452	47.4	1.021
162	12.4	3.243	6152	52.6	766	25	1.158
266	16.7	2.860	5386	27.6	354	11.6	1.265
370	20.3	2.683	5032	16	266	8.7	1.370
607	27.1	2.550	4766	7.3	162	5.3	1.577
1880	52.9	2.469	4604	2.0	20	0.6	2.078
30000	271.5	2.459	4584	1.4	8	0.3	2.676
200000	831.7	2.455	4576	1.1	20	0.6	3.072
660000	1682.3	2.445	4556	0.5	16	0.5	3.232
700000	1741.8	2.437	4540	0	-	-	-

Table S15: PS Standards and elution volumes (PUR3).

M_w	Φ [Å]	Retention time [min]	V_e [μ l]	R [%]	ΔV_e [μ l]	ΔR [%]	Log Φ_{av} [Å]
Toluene	8.9	4.572	8810	100	2236	52.6	1.021
162	12.4	3.454	6574	47.4	1148	27	1.158
266	16.7	2.880	5426	20.4	348	8.2	1.265
370	20.3	2.706	5078	12.2	302	7.1	1.370
607	27.1	2.555	4776	5.1	188	4.4	1.577
1880	52.9	2.461	4588	0.7	14	0.3	2.078
30.000	271.5	2.454	4574	0.4	18	0.4	2.836
700.000	1741.8	2.445	4556	0	-	-	-

Table S16: PS Standards and elution volumes (PUR4).

M_w	Φ [Å]	Retention time [min]	V_e [μ l]	R [%]	ΔV_e [μ l]	ΔR [%]	Log Φ_{av} [Å]
Toluene	8.9	2.775	5216	100	468	38.2	1.021
162	12.4	2.541	4748	61.8	154	12.5	1.158
266	16.7	2.464	4594	49.3	122	9.9	1.265
370	20.3	2.403	4472	39.4	114	9.3	1.370
607	27.1	2.346	4358	30.1	144	11.7	1.541
1420	44.8	2.274	4214	18.4	118	9.7	2.041
30.000	271.5	2.215	4096	8.7	8	0.6	2.676
200.000	831.7	2.211	4088	8.1	100	8.1	3.008
400.000	1252.0	2.161	3988	0	-	-	-

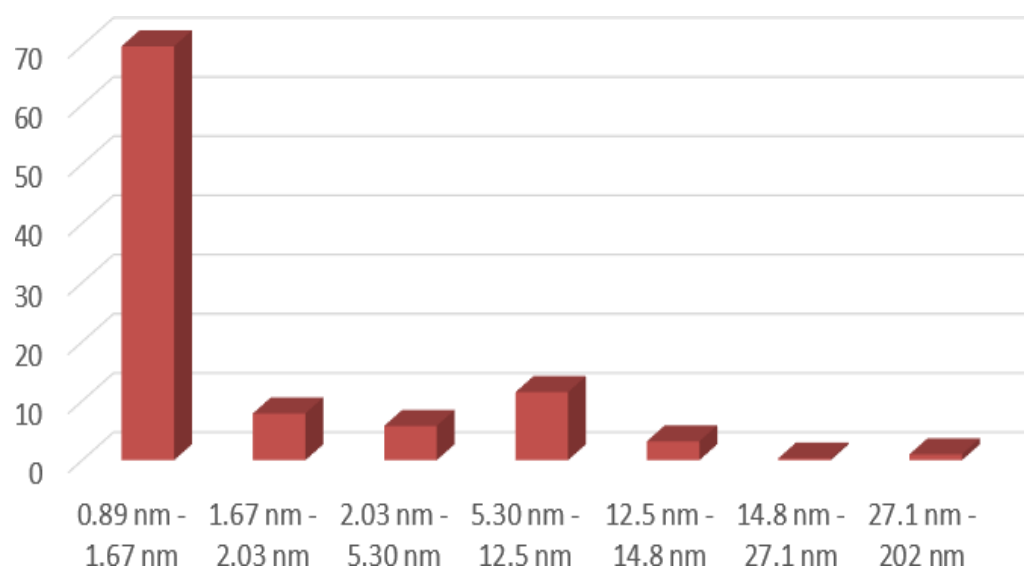
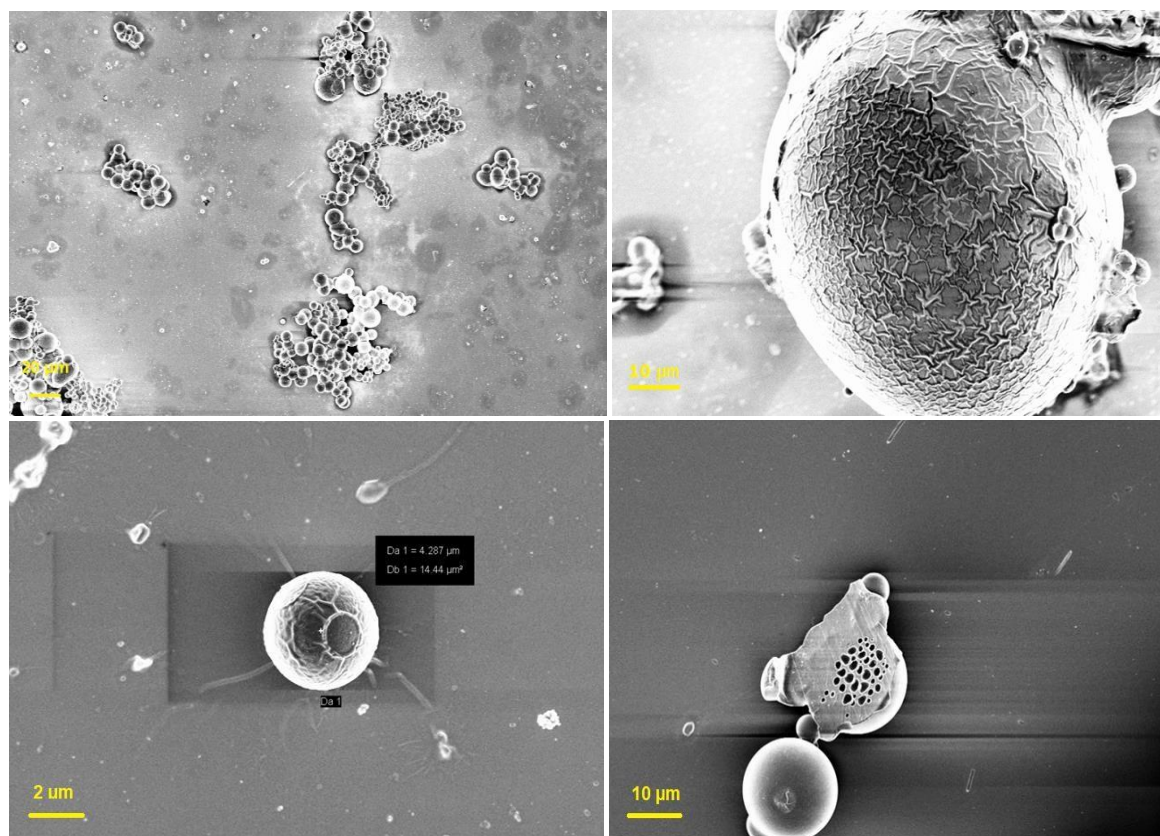


Figure S27: ISEC-derived distribution (relative abundance ΔR , %) of pore diameters (nm) of the polyurea-derived monolith. ΔR of the pore range: 0.89 - 1.67 nm (ΔR : 69.9 %), 1.67 - 2.03 nm (ΔR : 7.9 %), 2.03 - 5.30 nm (ΔR : 5.8 %), 5.30 - 12.5 nm (ΔR : 11.5 %), 12.5 - 14.8 nm (ΔR : 3.2 %), 14.8 - 27.1 nm (ΔR : 0.3 %), 27.1 - 202 nm (ΔR : 1.0).

Table S17: PS Standards and elution volumes of Polyurea-derived monolith.

M_w	Φ [Å]	Retention time [min]	V_e [μ l]	R [%]	ΔV_e [μ l]	ΔR [%]	Log Φ_{av} [Å]
Toluene	8.9	2.283	1983	100	135	48.9	1.021
162	12.4	2.148	1848	51.0	58	21.0	1.158
266	16.7	2.090	1790	30.0	22	7.9	1.265
370	20.3	2.068	1768	22.1	16	5.8	1.515
1880	53.0	2.052	1752	16.3	32	11.5	1.911
8140	125.8	2.020	1720	4.7	9	3.2	2.135
10730	148.1	2.011	1711	1.4	1	0.3	2.302
30000	271.6	2.010	1710	1.0	3	1.0	2.869
900000	2020.0	2.007	1707	0			

**Figure S28:** SEM pictures of isolated, poly(urethane)-derived microglobules.

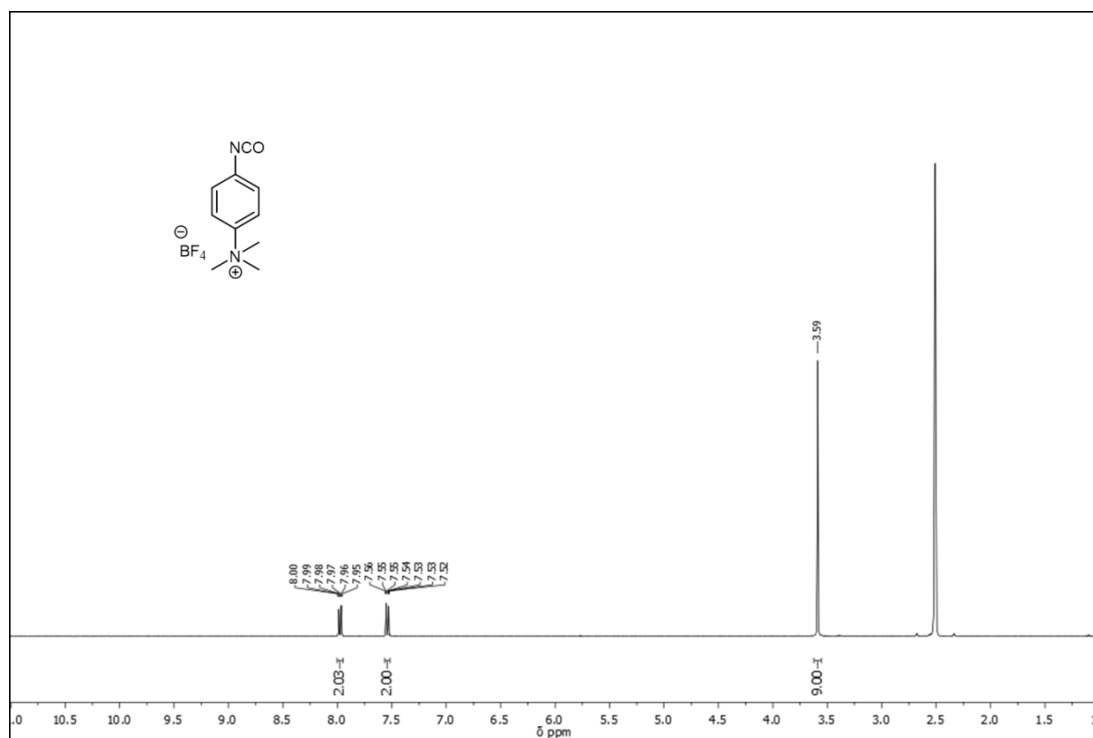


Figure S29: ^1H NMR spectrum of $[\text{NCO-C}_6\text{H}_4\text{-NMe}_3^+][\text{BF}_4^-]$ in DMSO-d_6 .



Figure S30: ^{19}F NMR spectrum of $[\text{NCO-C}_6\text{H}_4\text{-NMe}_3^+][\text{BF}_4^-]$ in DMSO-d_6 .

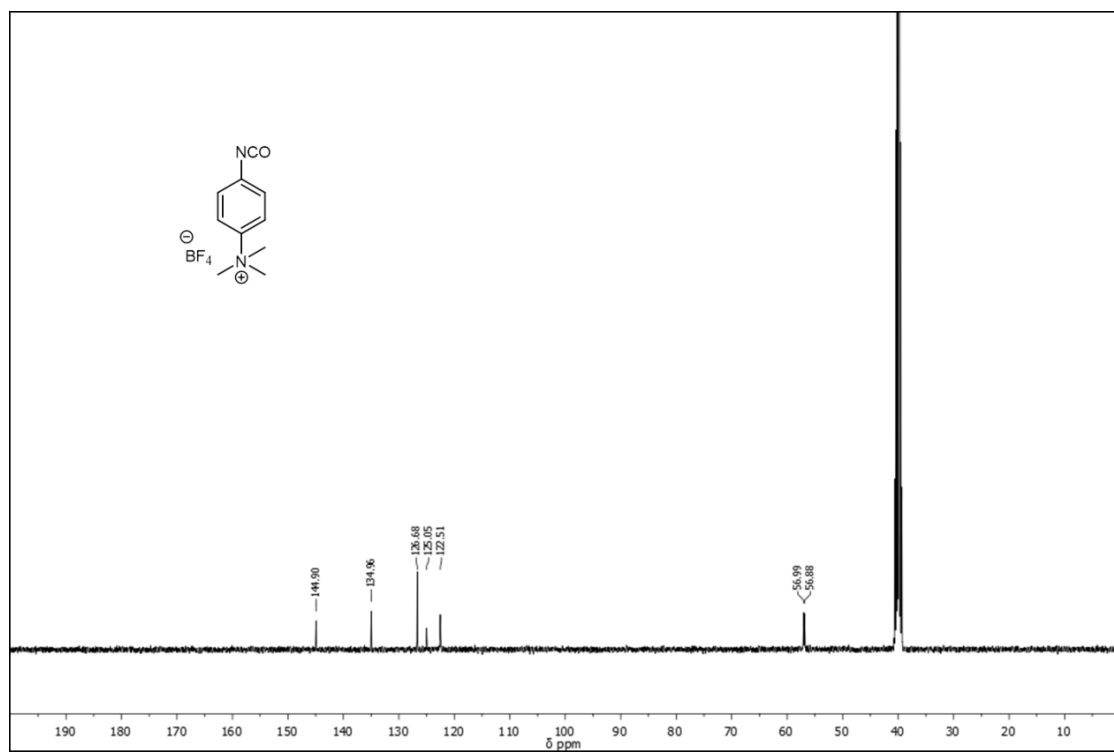


Figure S31: ^{13}C NMR spectrum of $[\text{NCO-C}_6\text{H}_4\text{-NMe}_3^+][\text{BF}_4^-]$ in DMSO-d_6 .

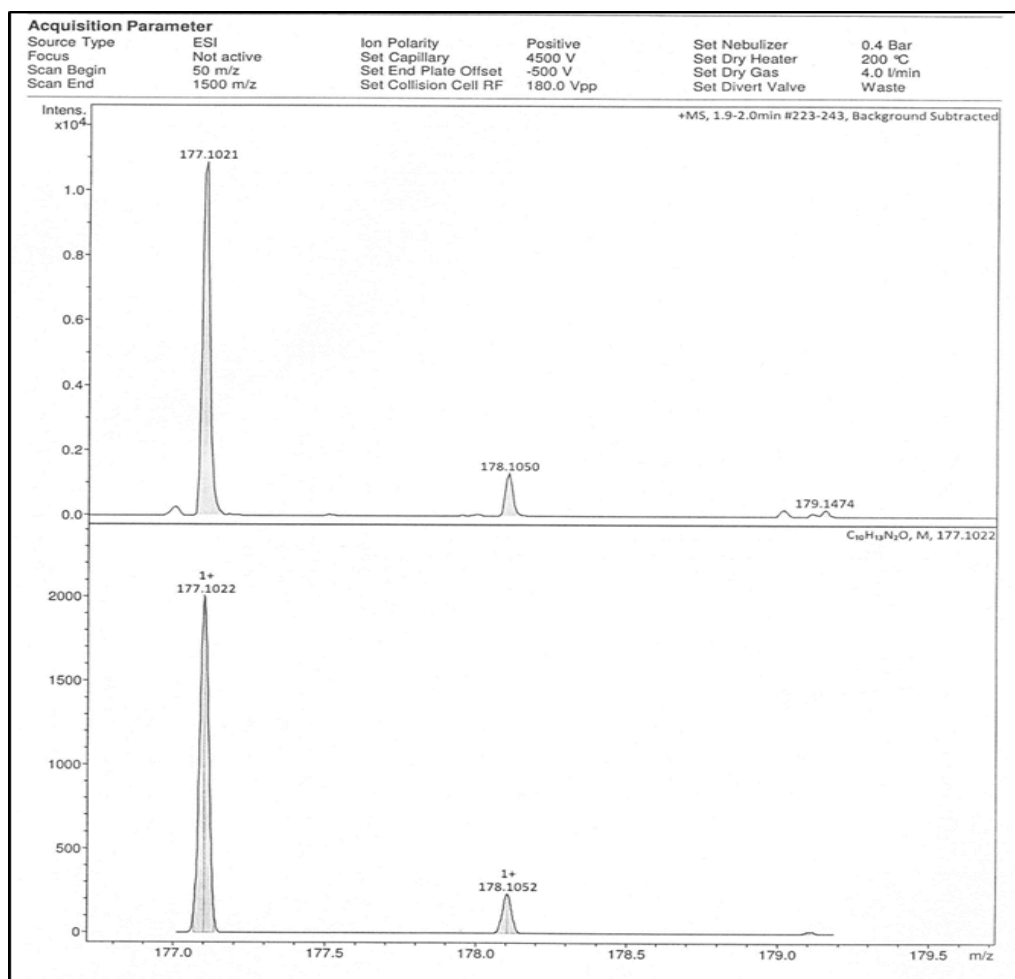


Figure S32: High-resolution mass spectrum of [NCO-C₆H₄-NMe₃⁺][BF₄⁻]. Found (top) and calculated (bottom) isotope distribution of the molecular ion peak.

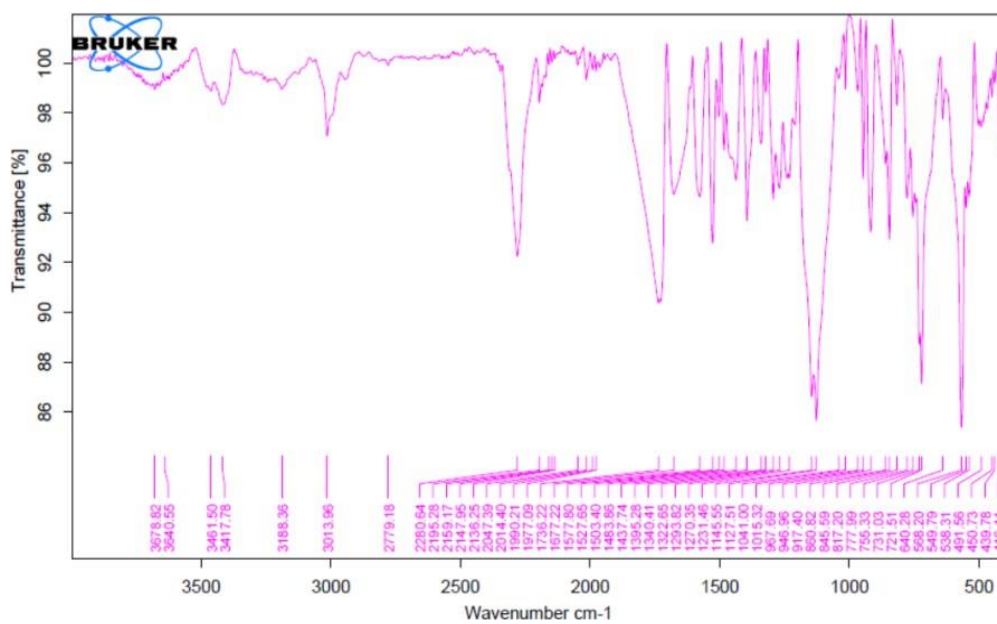


Figure S33: FT-IR spectrum of [NCO-C₆H₄-NMe₃][BF₄].

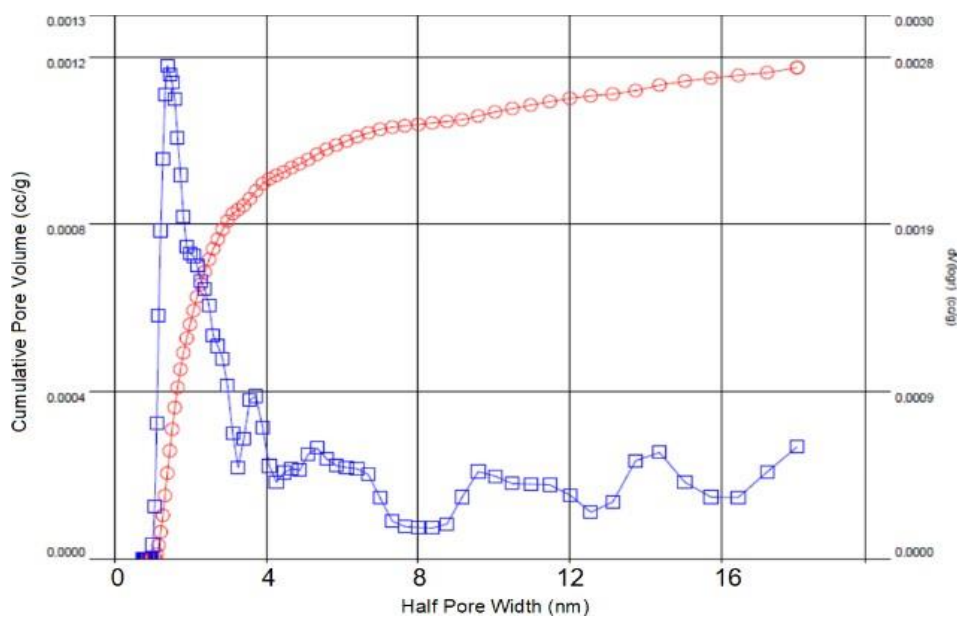


Figure S34: N₂-derived pore size distribution of the non-porous monolith (P1).

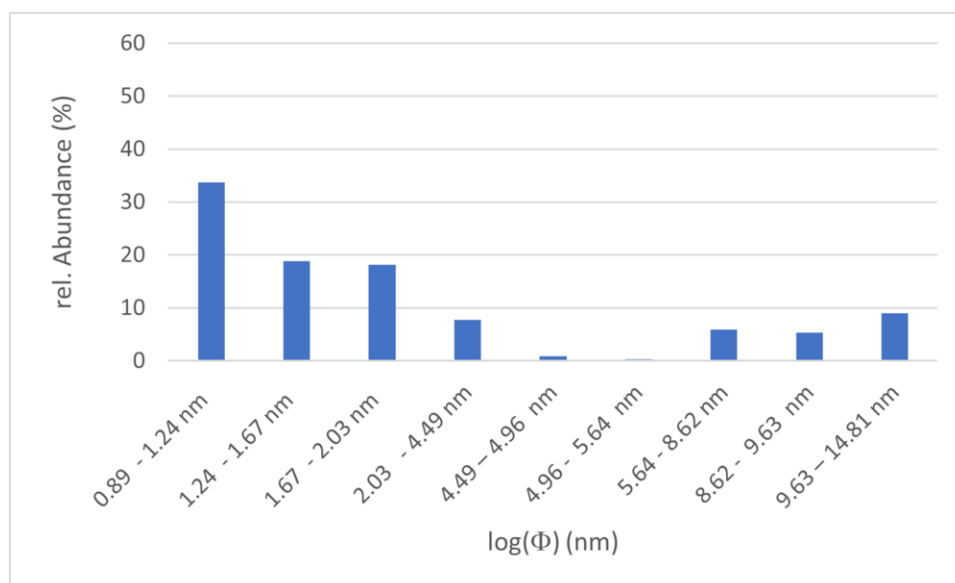


Figure S35: ISEC-derived distribution (relative abundance ΔR , %) of pore diameters (nm) of the non-porous monolith P1.

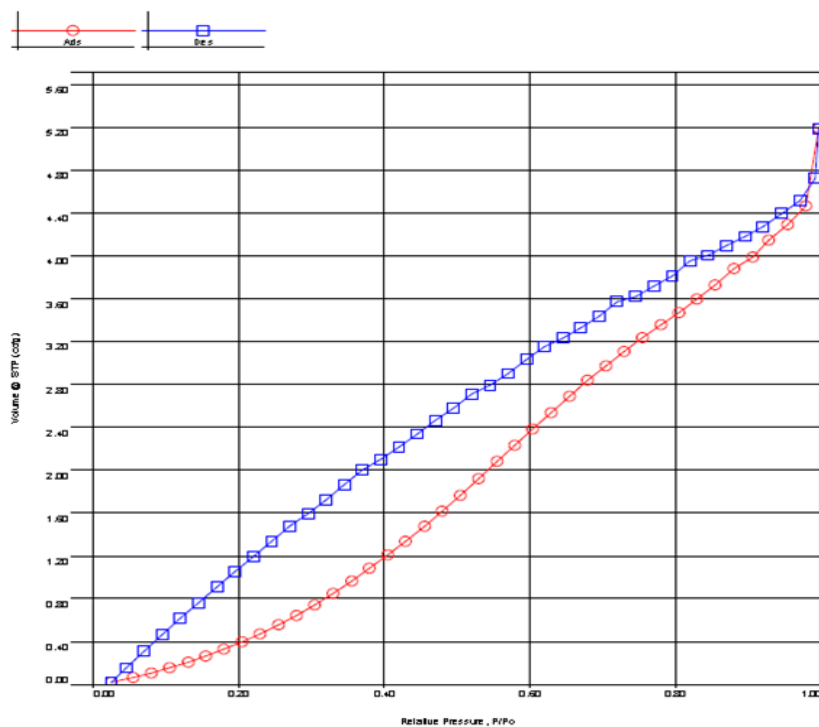


Figure S36: N₂-derived pore size distribution of monolith P2.

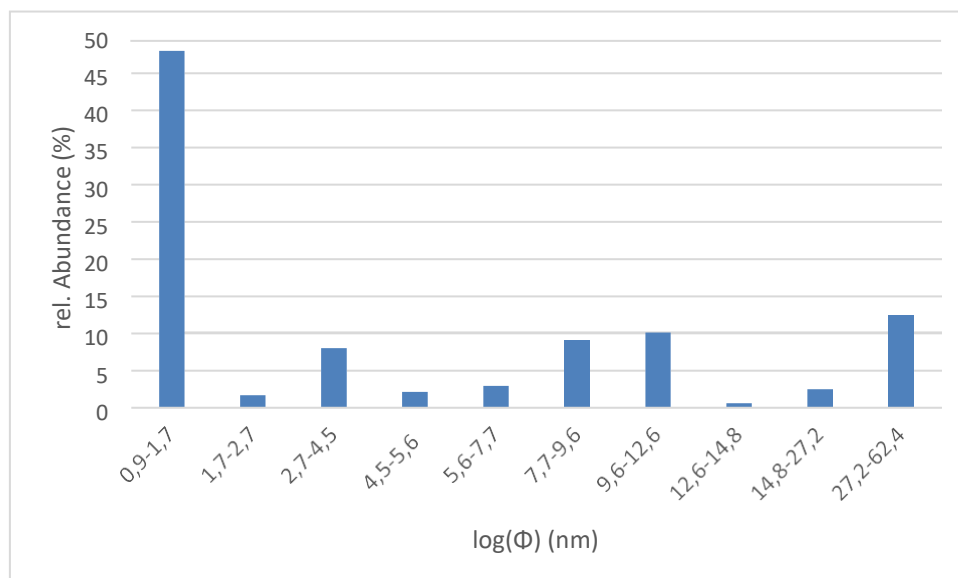


Figure S37: ISEC-derived distribution (relative abundance ΔR , %) of pore diameters (nm) of monolith P2.

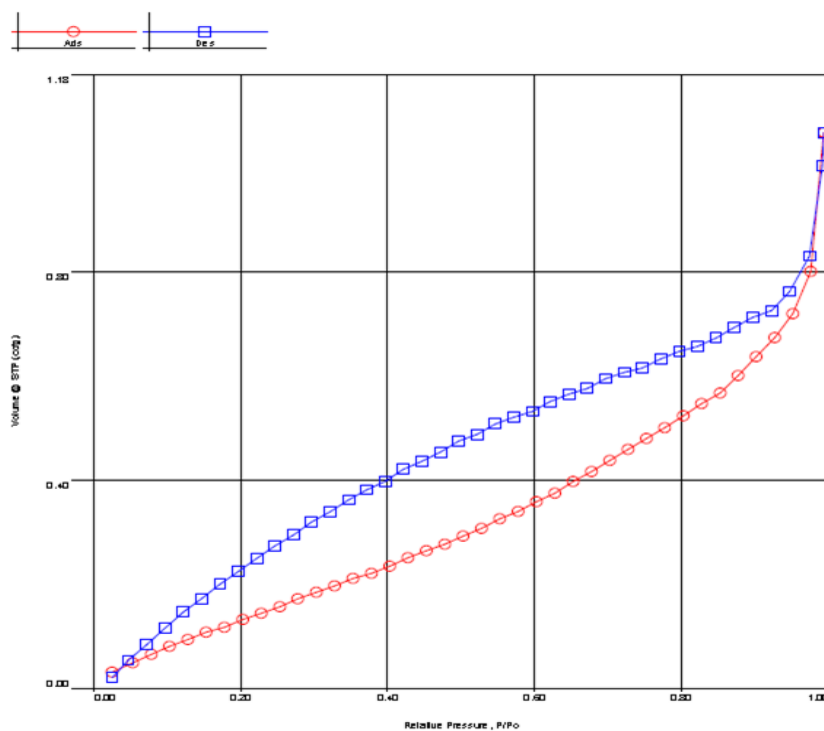


Figure S38: N_2 -derived-pore size distribution of monolith P3.

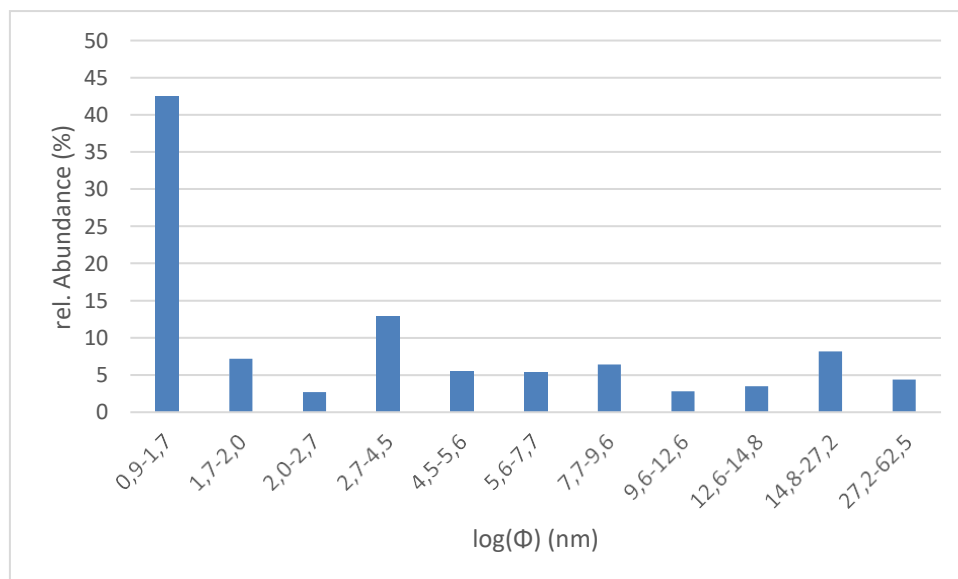


Figure S39: ISEC-derived distribution (relative abundance ΔR , %) of pore diameters (nm) of monolith P3.

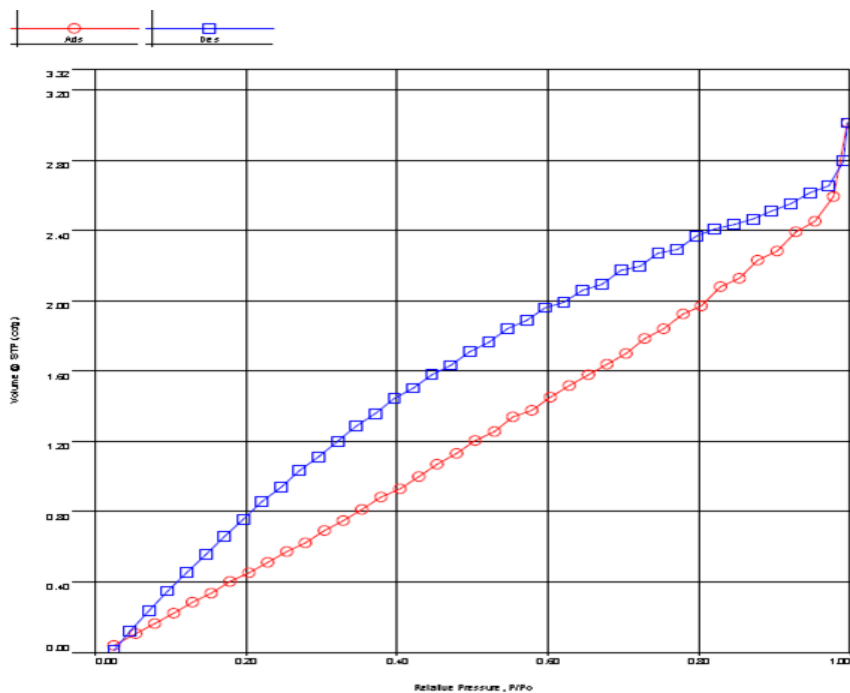


Figure S40: N₂-derived pore size distribution of monolith P4.

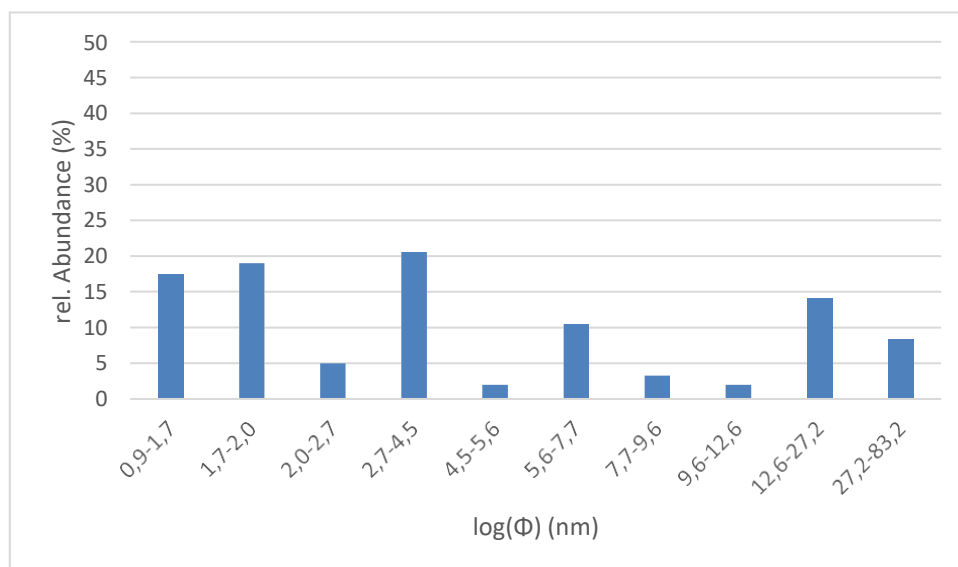


Figure S41: ISEC-derived distribution (relative abundance ΔR , %) of pore diameters (nm) of monolith P4.

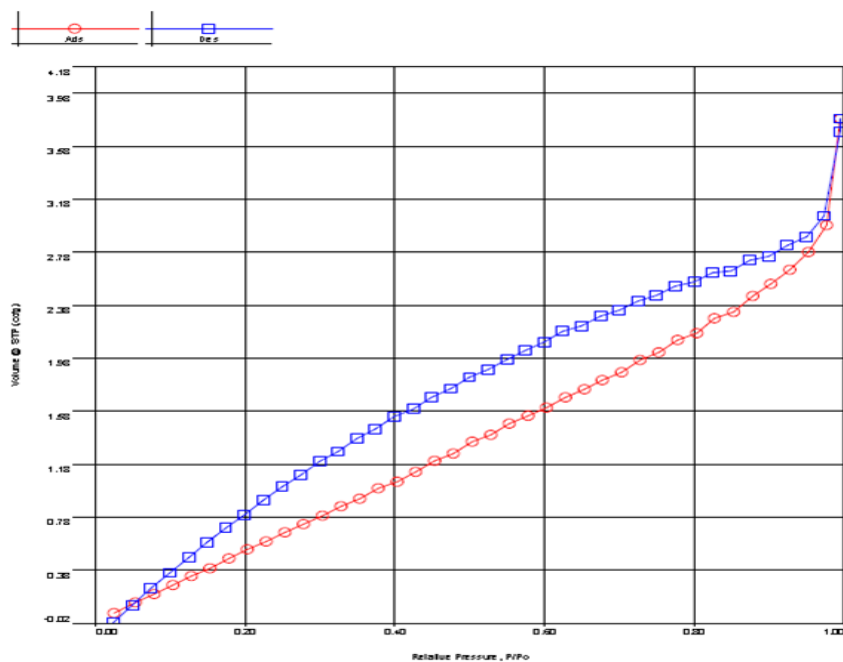


Figure S42: N₂-derived pore size distribution of monolith P5.

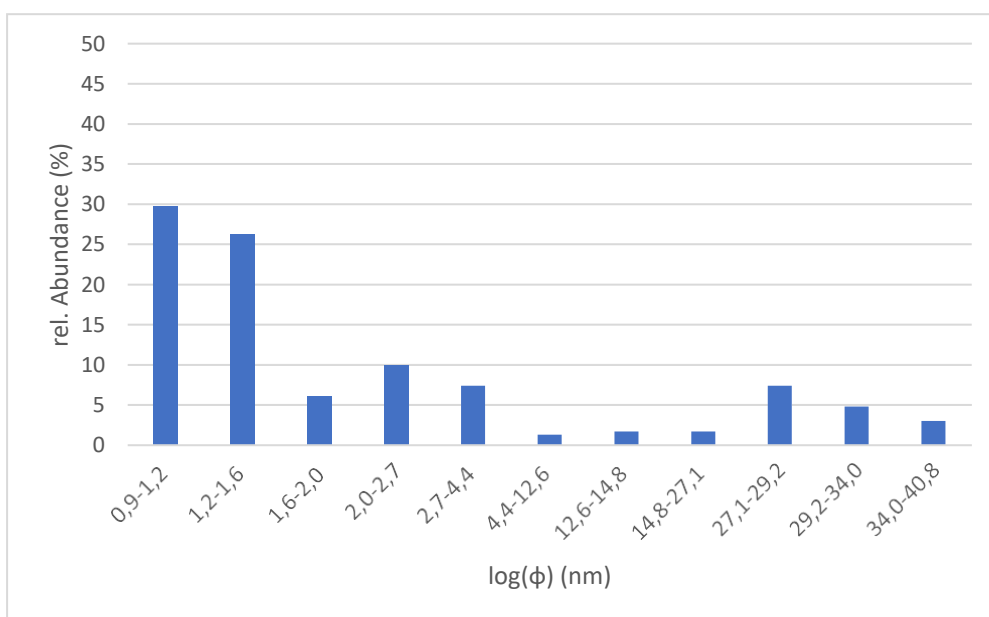


Figure S43: ISEC-derived distribution (relative abundance ΔR , %) of pore diameters (nm) of the surface-functionalized poly(urethane) monolith P5.

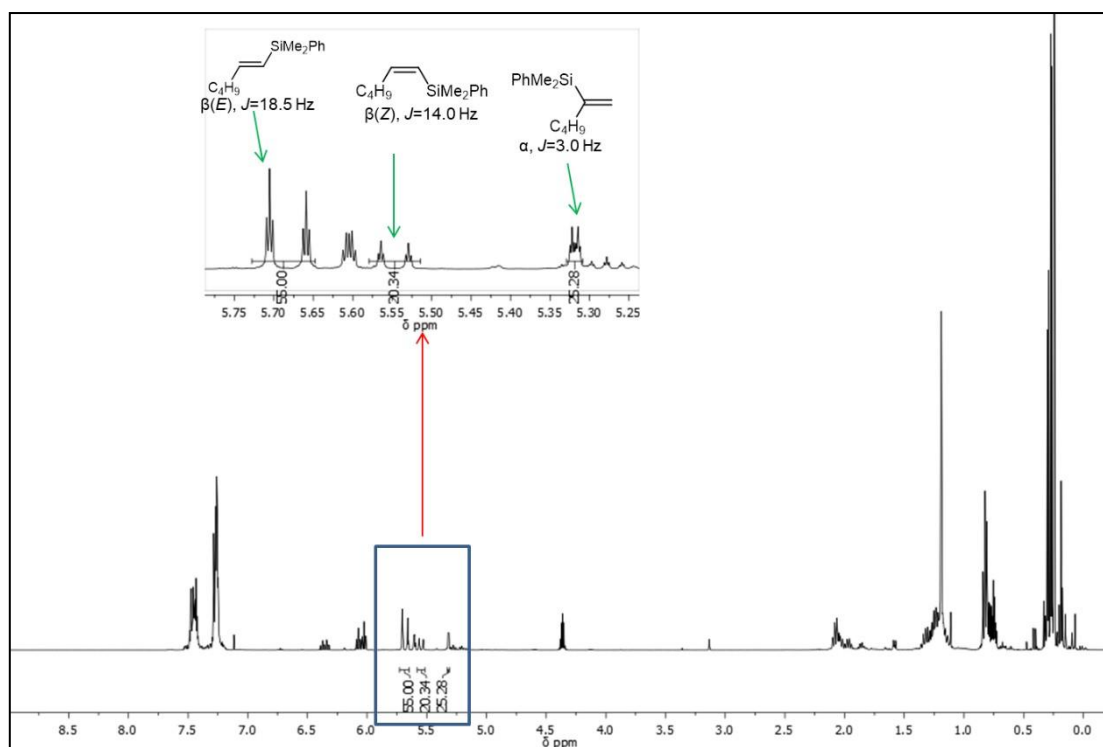


Figure S44: ^1H NMR (CDCl₃, 298K) of the hydrosilylation of 1-hexyne with dimethylphenylsilane under biphasic conditions.

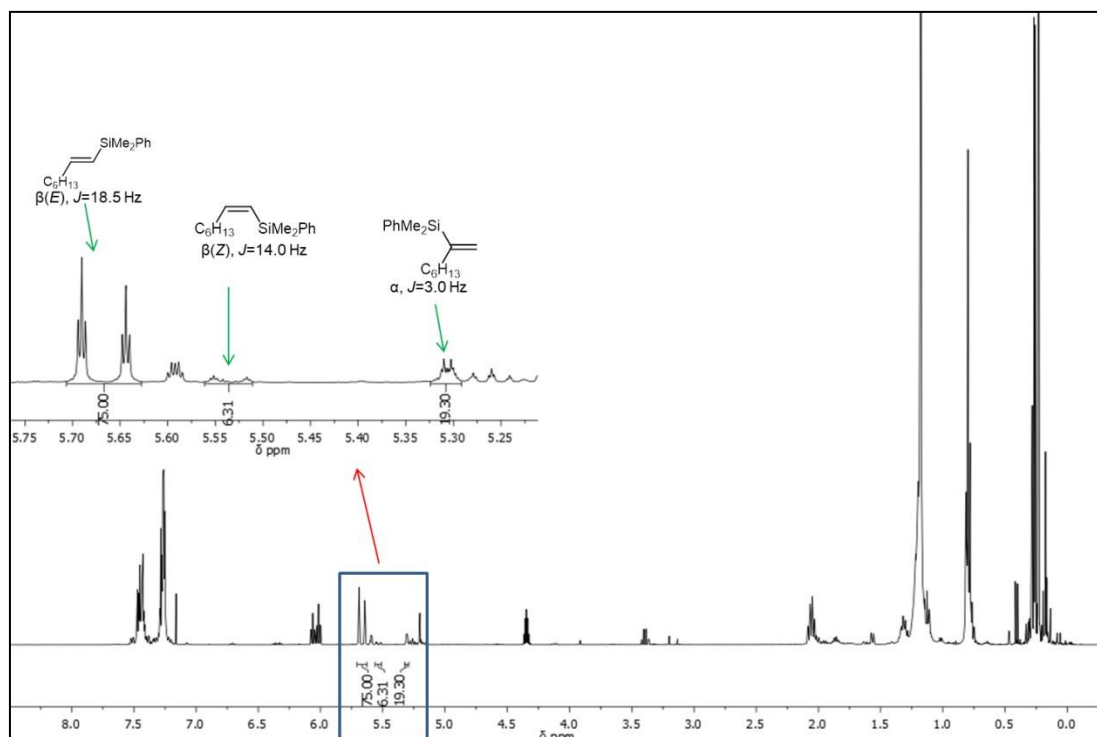


Figure S45: ^1H NMR (CDCl₃, 298K) of the hydrosilylation of 1-octyne with dimethylphenylsilane under biphasic conditions.

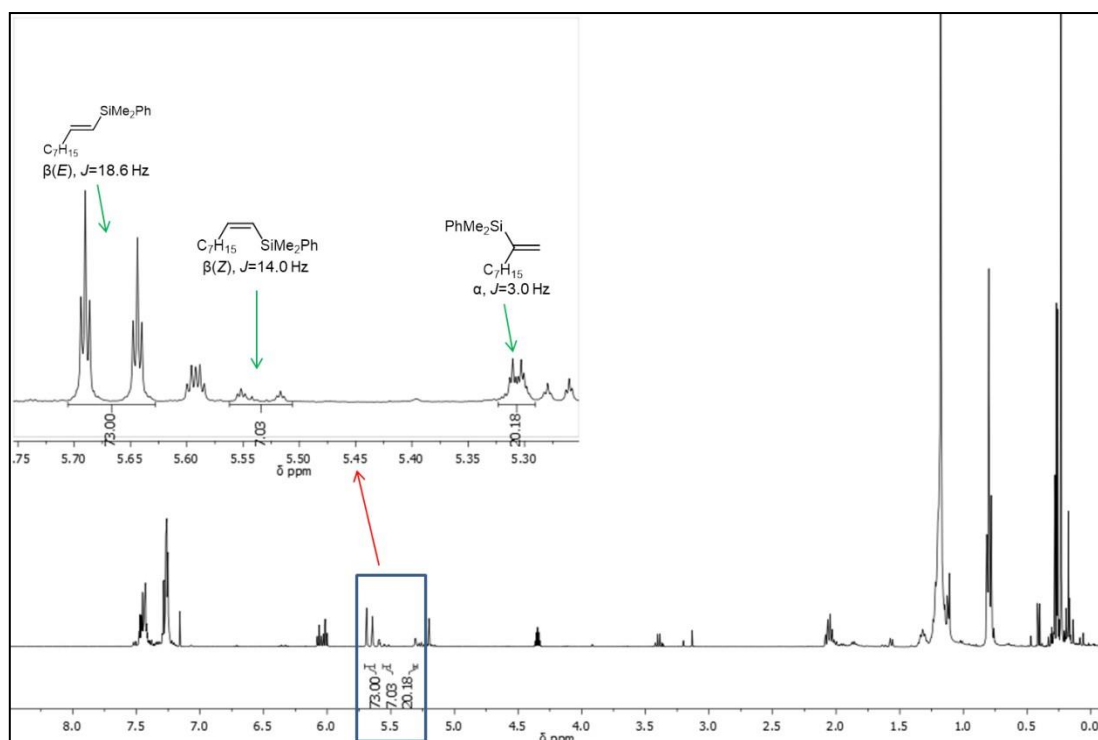


Figure S46: ^1H NMR (CDCl_3 , 298K) of the hydrosilylation of 1-nonyne with dimethylphenylsilane under biphasic conditions.

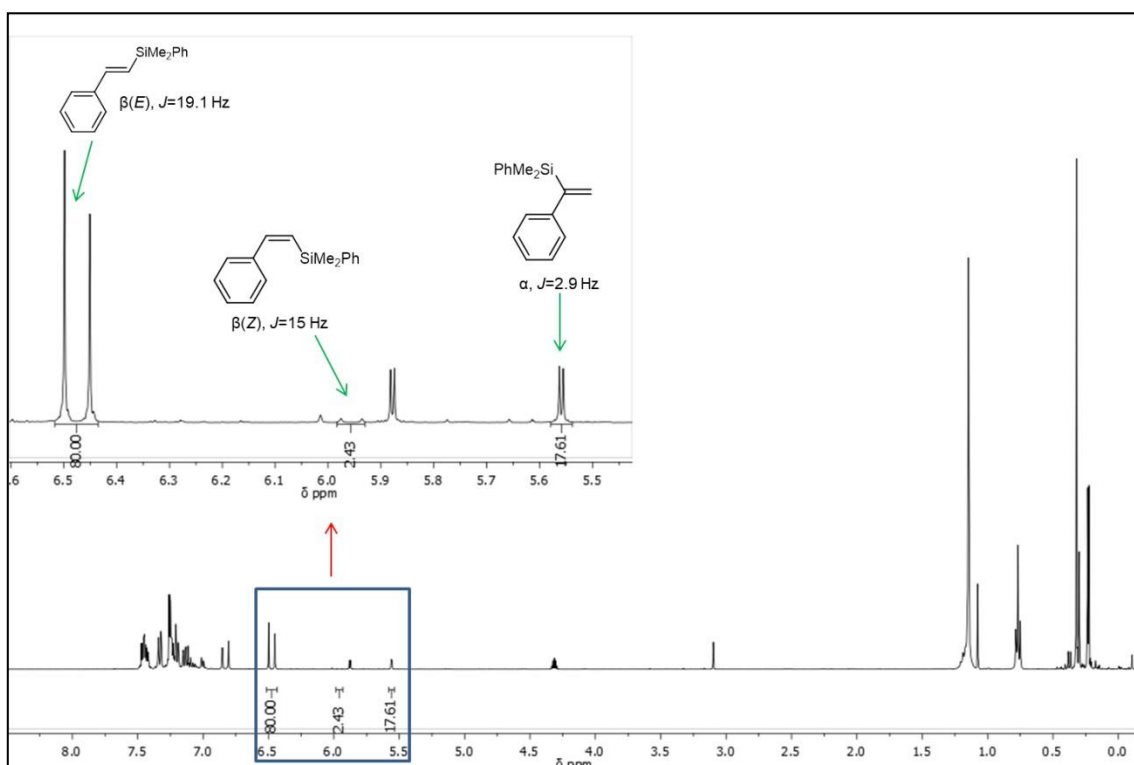


Figure S47: ^1H NMR (CDCl_3 , 298K) of the hydrosilylation of phenylacetylene with dimethylphenylsilane under biphasic conditions.

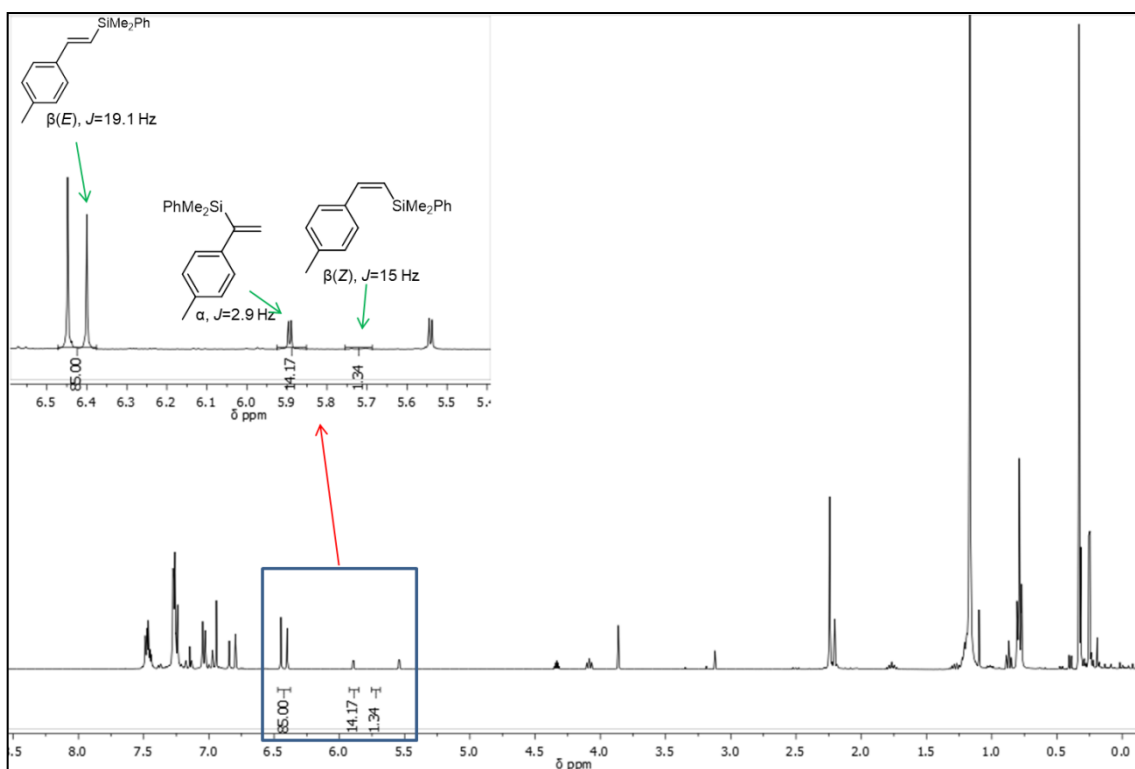


Figure S48: ^1H NMR (CDCl_3 , 298K) of the hydrosilylation of 4-ethynyltoluene with dimethylphenylsilane under biphasic conditions.

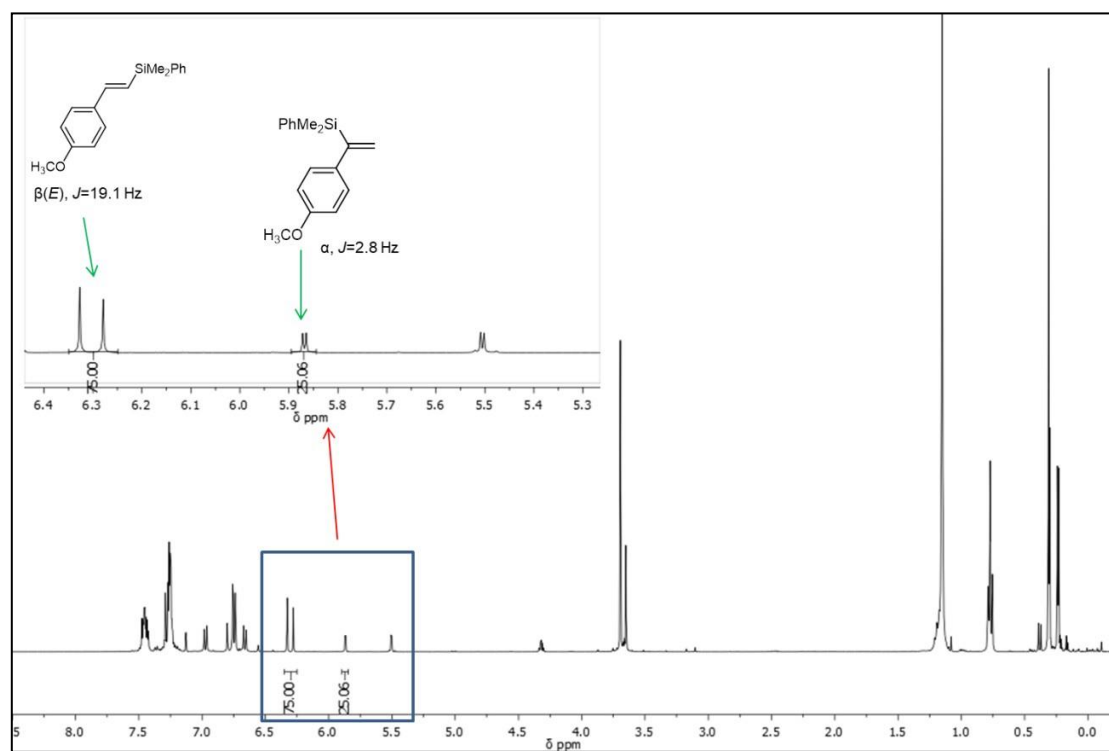


Figure S49: ^1H NMR (CDCl_3 , 298K) of the hydrosilylation of 4-ethynylanisole with dimethylphenylsilane under biphasic conditions.

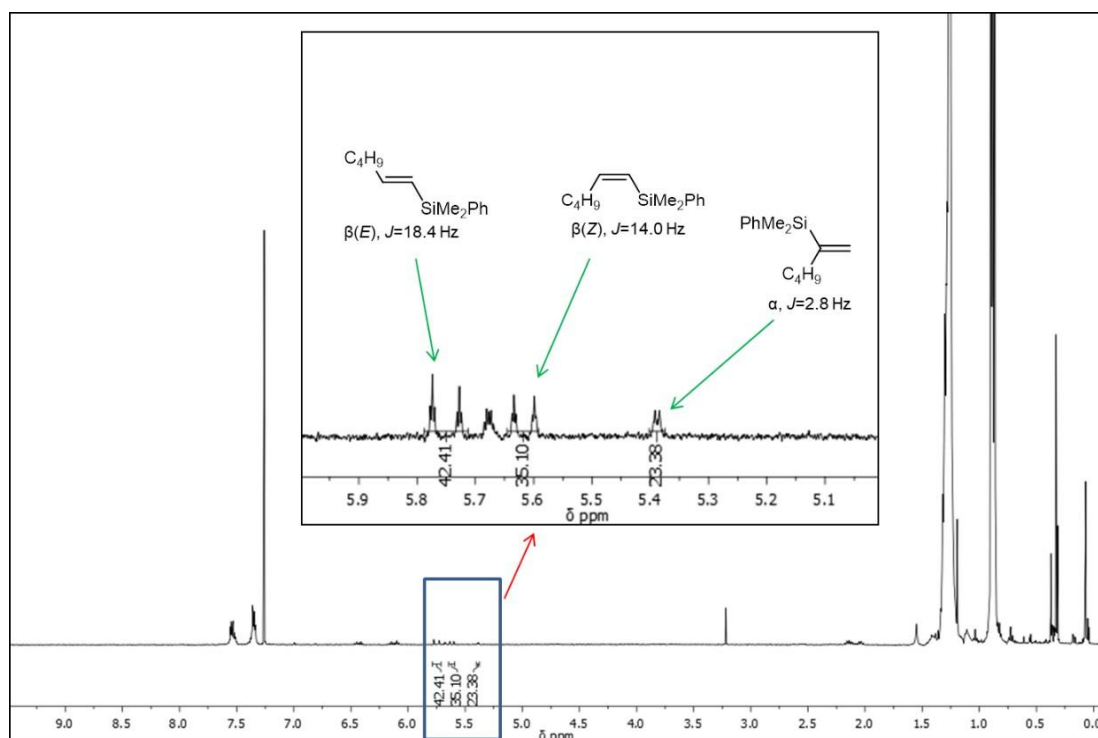


Figure S50: ^1H NMR (CDCl₃, 298K) of the hydrosilylation of 1-hexyne with dimethylphenylsilane under PUR-monolith supported continuous conditions.

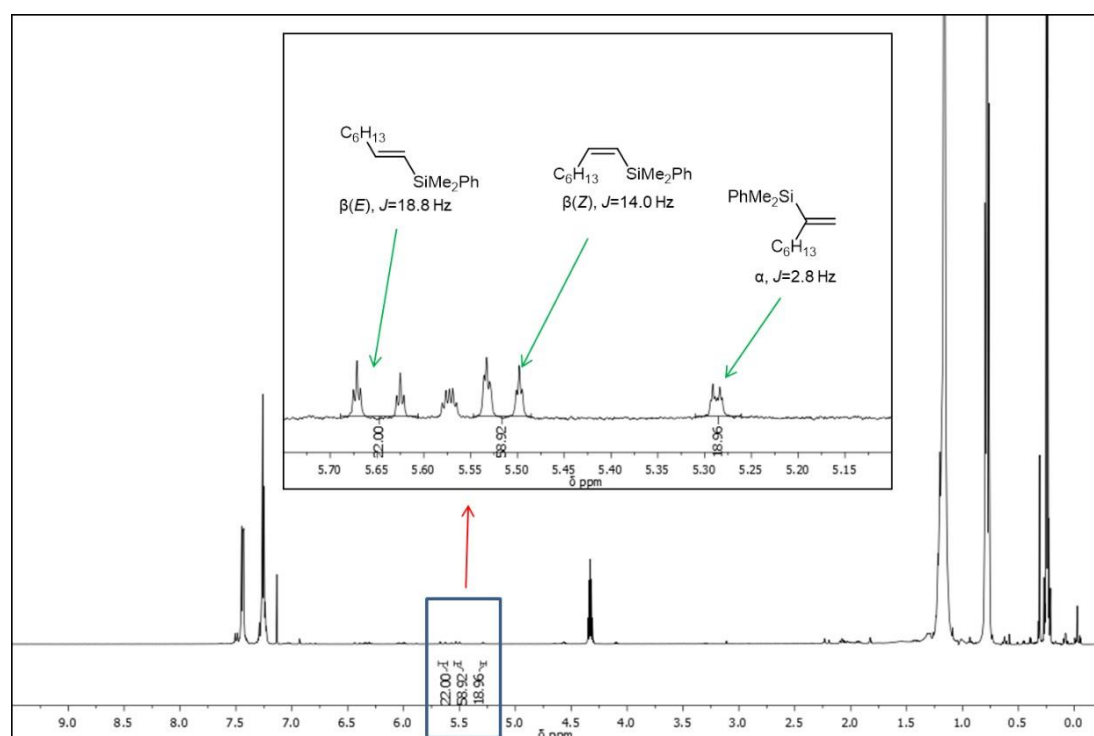


Figure S51: ^1H NMR (CDCl₃, 298K) of the hydrosilylation of 1-octyne with dimethylphenylsilane under PUR-monolith supported continuous conditions.

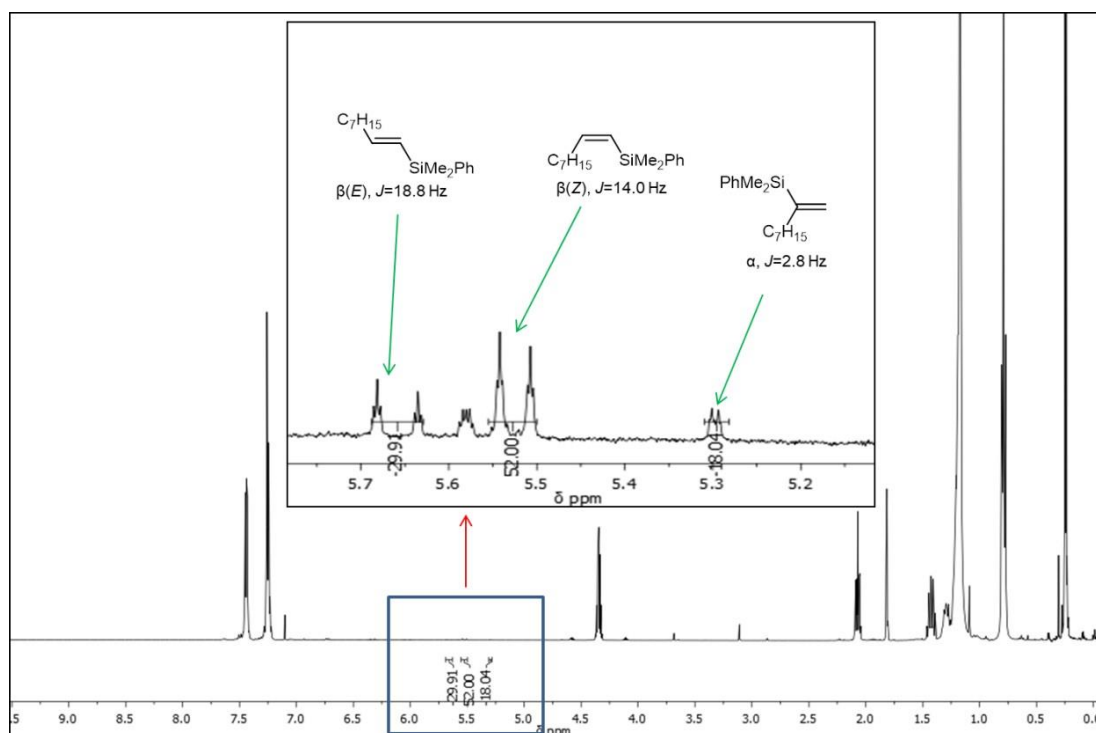


Figure S52: ^1H NMR (CDCl_3 , 298K) of the hydrosilylation of 1-nonyne with dimethylphenylsilane under PUR-monolith supported continuous conditions.

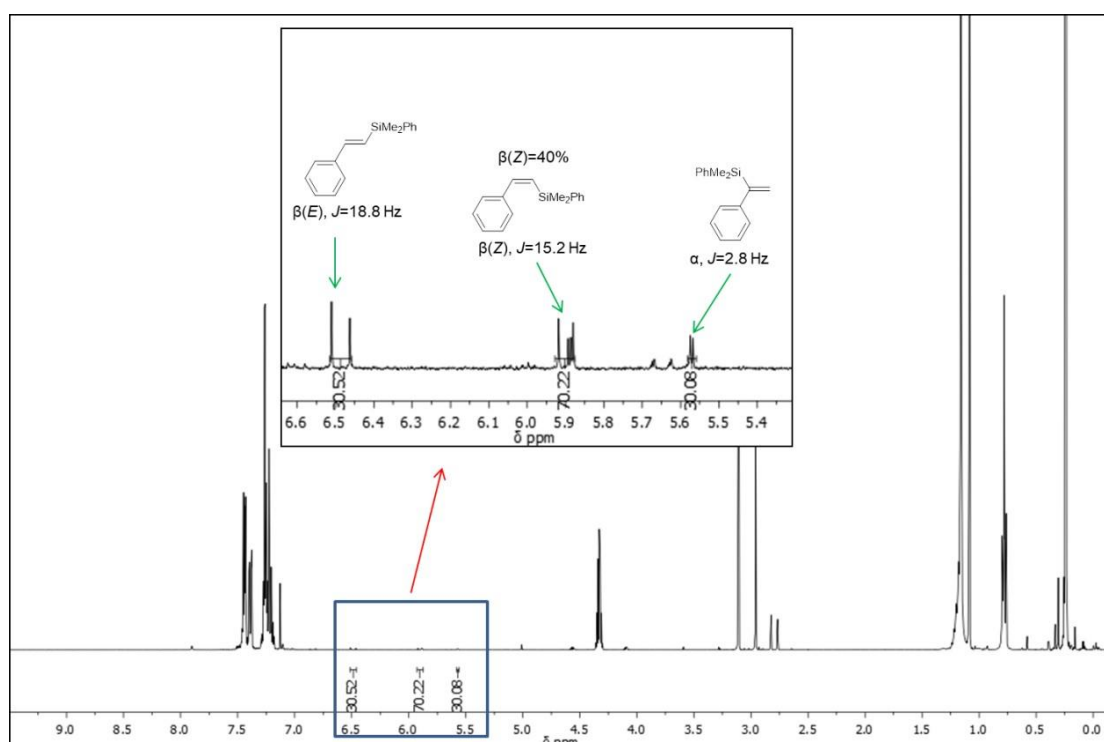


Figure S53: ^1H NMR (CDCl_3 , 298K) of the hydrosilylation of phenylacetylene with dimethylphenylsilane under PUR-monolith supported continuous conditions.

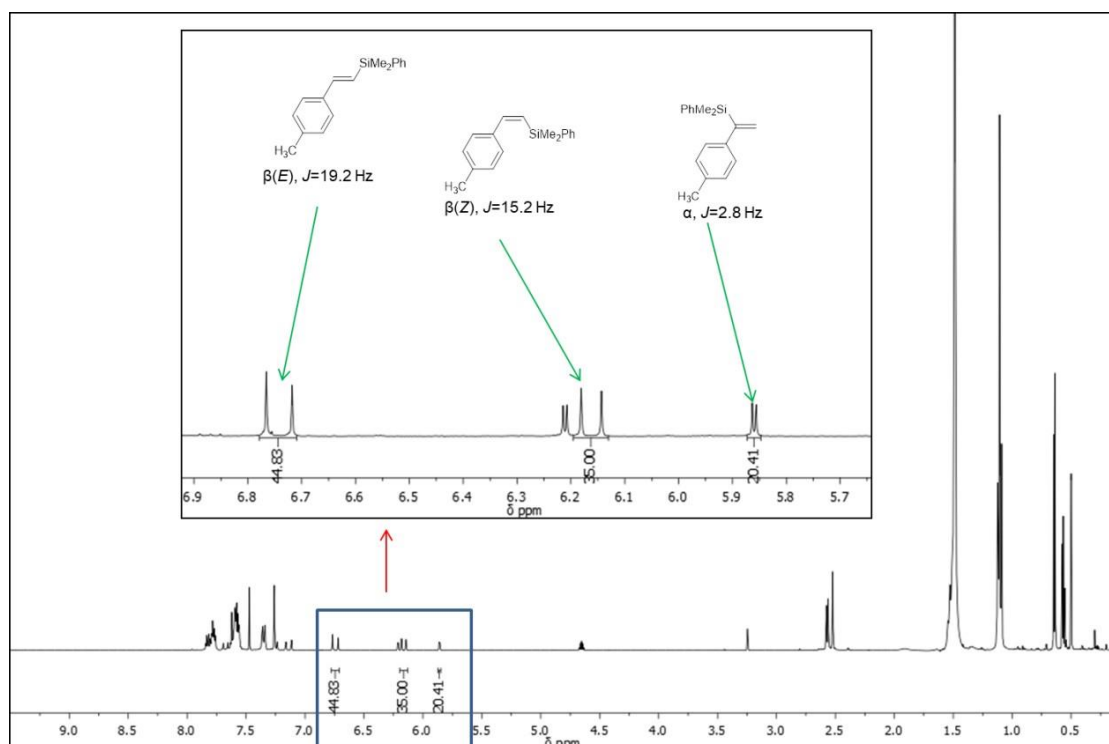


Figure S54: ^1H NMR (CDCl_3 , 298K) of the hydrosilylation of 4-ethynyltoluene with dimethylphenylsilane under PUR-monolith supported continuous conditions.

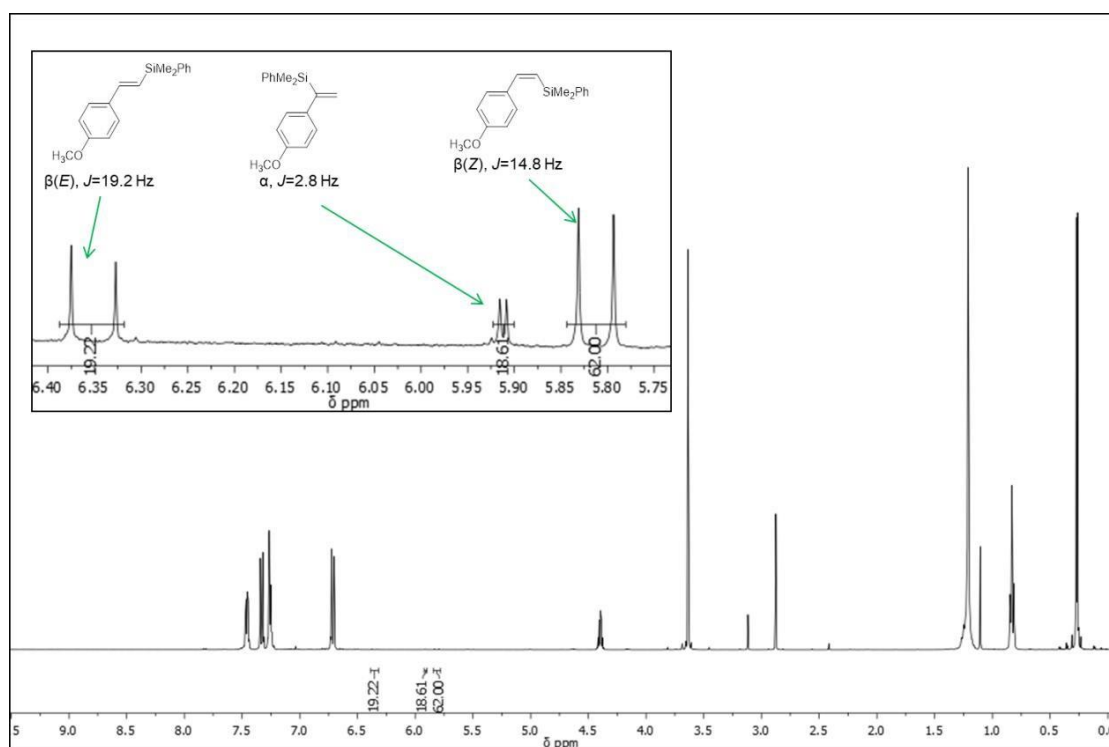
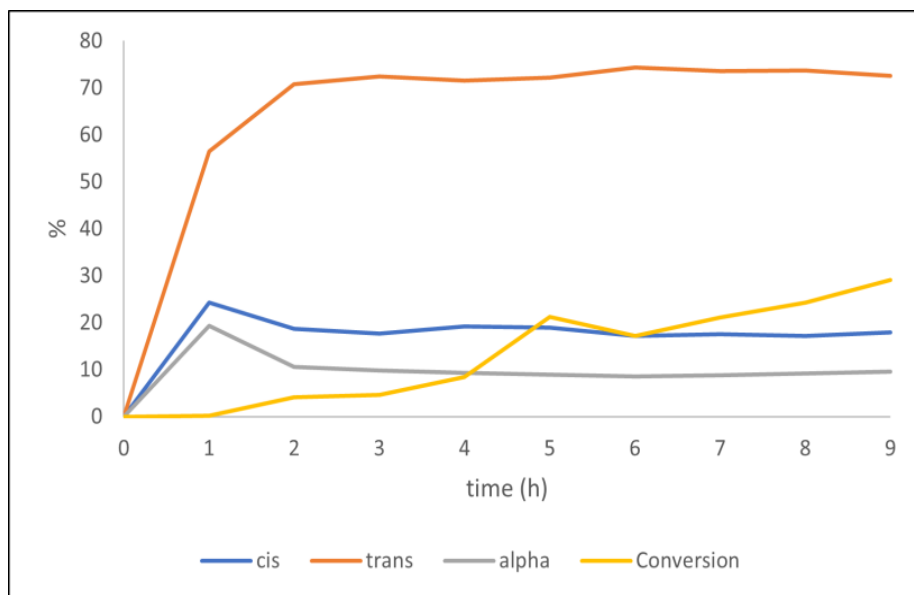


Figure S55: ^1H NMR (CDCl_3 , 298K) of the hydrosilylation of 4-ethynylanisole with dimethylphenylsilane under PUR-monolith supported continuous condition.

a)



b)

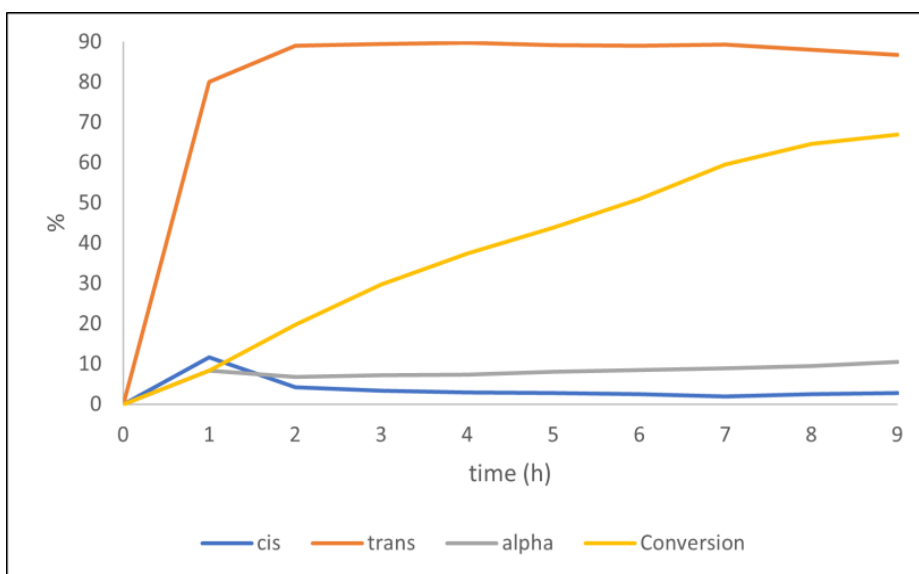


Figure S56: Time-dependent reaction profiles of the reaction of 1-octyne (a) and 4-ethynyltoluene (b) under biphasic conditions.

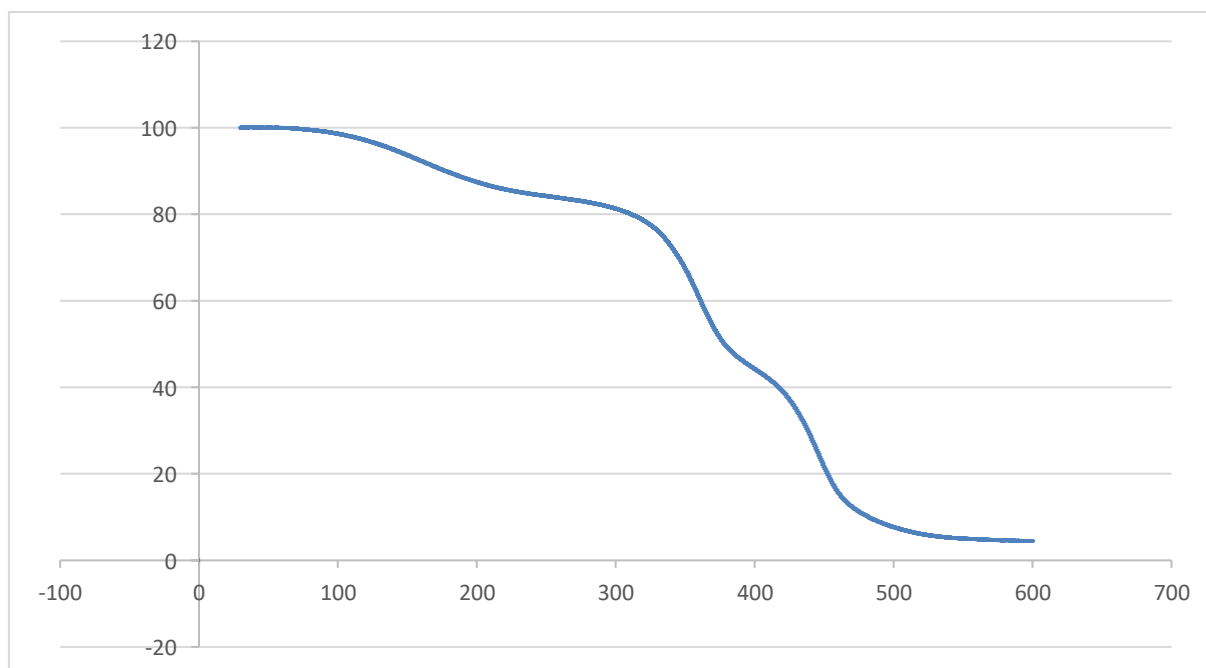


Figure S57: TGA curve of surface-functionalized PUR-monolith (P5).

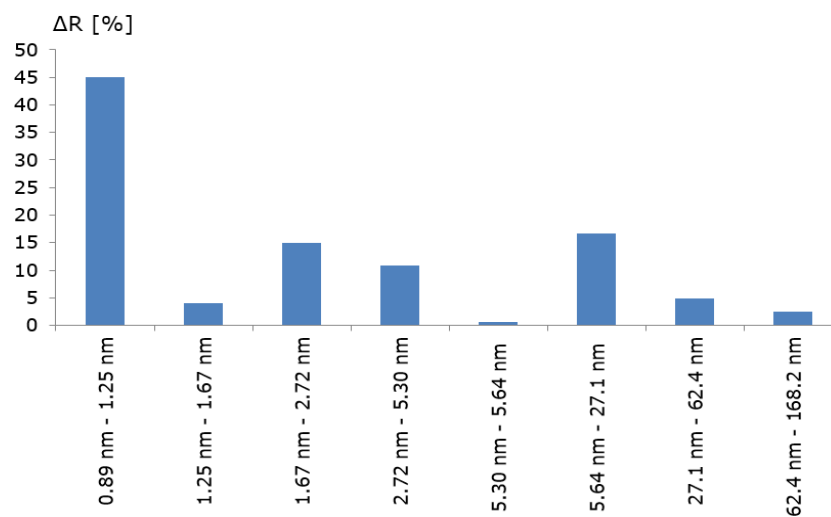


Figure S58: ISEC-derived distribution (relative abundance ΔR , %) of pore diameters (nm) of the ROMP monolith NbN1: 0.89 - 1.25 nm (ΔR : 45.1 %), 1.25 - 1.67 nm (ΔR : 4.1 %), 1.67 - 2.72 nm (ΔR : 15 %), 2.72 - 5.30 nm (ΔR : 10.8 %), 5.30 - 5.64 nm (ΔR : 0.6 %), 5.64 - 27.1 nm (ΔR : 16.7 %), 27.1 - 62.4 nm (ΔR : 4.8 %), 62.4 - 168.2 nm (ΔR : 2.5 %).

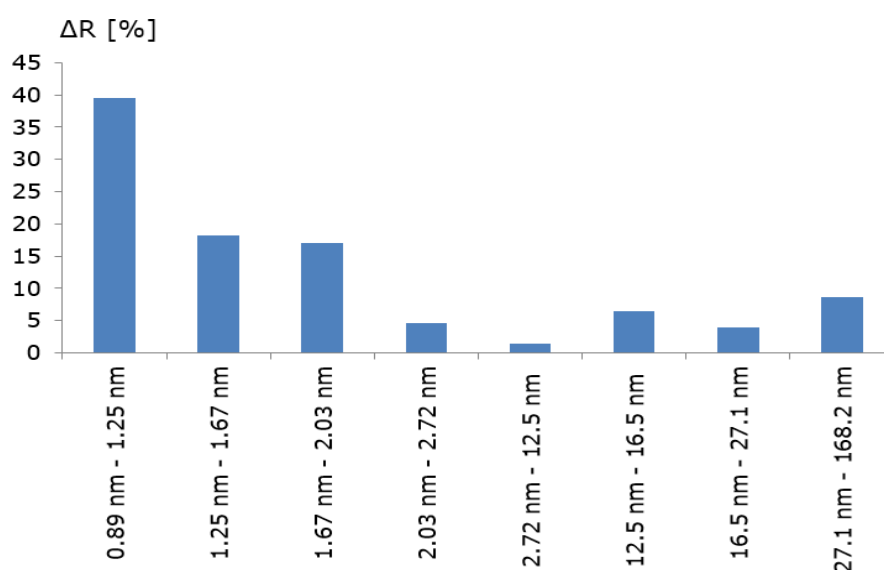


Figure S59: ISEC-derived distribution (relative abundance ΔR , %) of pore diameters (nm) of the ROMP monolith NbN2: 0.89 - 1.25 nm (ΔR : 39.5 %), 1.25 - 1.67 nm (ΔR : 18.2 %), 1.67 - 2.03 nm (ΔR : 17 %), 2.03 - 2.72 nm (ΔR : 4.7 %), 2.72 - 12.5 nm (ΔR : 1.4 %), 12.5 - 16.5 nm (ΔR : 6.4%), 16.5 - 27.1 nm (ΔR : 3.9 %), 27.1 - 168.2 nm (ΔR : 8.6 %).

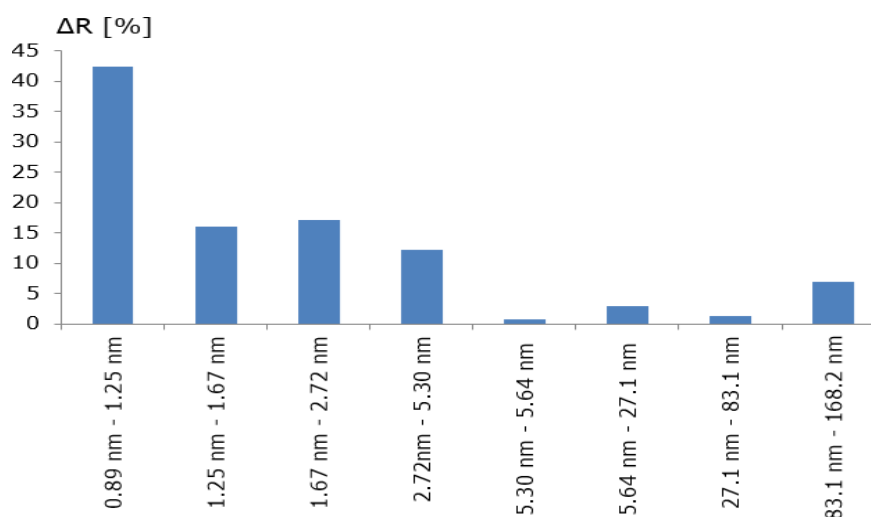


Figure S60: ISEC-derived distribution (relative abundance ΔR , %) of pore diameters (nm) of the ROMP monolith NbN3: 0.89 - 1.25 nm (ΔR : 42.5 %), 1.25 - 1.67 nm (ΔR : 16.1 %), 1.67 - 2.72 nm (ΔR : 17.2 %), 2.72 - 5.30 nm (ΔR : 12.2 %), 5.30 - 5.64 nm (ΔR : 0.7 %), 5.64 - 27.1 nm (ΔR : 2.9 %), 27.1 - 83.1 nm (ΔR : 1.2 %), 83.1 - 168.2 nm (ΔR : 6.9 %).

Table S18: Polystyrene Standards and Elution Volumes [NbN1].

Mw	Φ [Å]	Retention time [min]	V_e [μ l]	R [%]	ΔV_e [μ l]	ΔR [%]	Log Φ_{av} [Å]
Toluene	8.9	3.11	1405	100	135	45.15	1.023
162	12.5	2.84	1270	54.8	13	4.18	1.159
266	16.7	2.815	1258	50.6	45	15.05	1.328
607	27.2	2.725	1213	35.6	33	10.87	1.579
1880	53	2.66	1180	24.7	2	0.67	1.737
2090	56.4	2.656	1178	24.0	50	16.72	2.092
30000	271.6	2.556	1128	7.3	14	4.85	2.614
123000	624.4	2.527	1114	2.5	8	2.508	3.010
660000	1682.4	2.512	1106	0			

Table S19: Polystyrene Standards and Elution Volumes [NbN2].

Mw	Φ [Å]	Retention time [min]	V_e [μ l]	R [%]	ΔV_e [μ l]	ΔR [%]	Log Φ_{av} [Å]
Toluene	8.9	4.298	1999	100	126	39.53	1.023
162	12.5	4.047	1874	60	58	18.27	1.159
266	16.7	3.931	1816	42	54	17.01	1.265
370	20.3	3.823	1762	25.1	15	4.72	1.371
607	27.2	3.793	1747	20.4	5	1.42	1.767
8140	125.8	3.784	1742	19.0	21	6.46	2.159
13000	165.8	3.743	1722	12.5	13	3.94	2.326
30000	271.6	3.718	1709	8.6	28	8.661	2.829
660000	1682.4	3.663	1682	0			

Table S20: Polystyrene Standards and Elution Volumes [NbN3].

Mw	Φ [Å]	Retention time [min]	V_e [μ l]	R [%]	ΔV_e [μ l]	ΔR [%]	Log Φ_{av} [Å]
Toluene	8.9	3.413	1557	100	139	42.55	1.023
162	12.5	3.136	1418	57.45	53	16.13	1.159
266	16.7	3.031	1366	41.321	56	17.2	1.328
607	27.2	2.919	1310	24.117	40	12.29	1.579
1880	53	2.839	1270	11.828	2	0.77	1.737
2090	56.4	2.834	1267	11.06	10	2.92	2.092
30000	271.6	2.815	1258	8.141	4	1.23	2.676
200000	831.8	2.807	1254	6.912	23	6.912	3.072
660000	1682.4	2.762	1231	0			

6.CURRICULUM VITAE

Family name: Acikalin
First name: Hande
Date of birth / Nationality: 14.10.1993 / Turkish

Education

PhD-thesis: 2018 - 2022

“Porous monolithic polymeric supports porous with uniform diameter and tailored functional groups”

University of Stuttgart, Institute of Polymer Chemistry

Supervisor: Prof. Dr. Michael R. Buchmeiser

Diploma-thesis: 2016 - 2018

“Electrospun nanofibers from copolymers and terpolymers of acrylonitrile, vinyl acetate and vinylphosphonic acid “

Istanbul Technical University, Polymer Science and Technology Programme

Supervisor: Assoc. Prof. Dr. Nesrin Köken

Publications

A Hard Templating Approach to Functional Mesoporous Poly(norborn-2-ene)-Based Monolithic Supports

Hande Acikalin, Felix Ziegler, Dongren Wang, Michael R. Buchmeiser, *Macromol. Chem. Phys.* 2021,222, 2100247.

<https://doi.org/10.1002/macp.202100247>

Hydrosilylation of Alkynes Under Continuous Flow Using Polyurethane-Based Monolithic Supports With Tailored Mesoporosity

Hande Acikalin, Pradeep K. R. Panyam, Abdul Wasif Shaikh, Dongren Wang, Shravan R. Kousik, Petia Atanasova, Michael R. Buchmeiser, *Macromol. Chem. Phys.* 2023,224, 2200234.

<https://doi.org/10.1002/macp.202200234>

Posters

Monolithic Polymeric Supports with Uniform Diameter Pores for Continuous Catalytic Reactions

CRC 1333 Status Meeting, 01.04.2019 - 03.04.2019, Döttingen, Germany; CRC 1333 Status Meeting, 05.10.2020 - 07.10.2020, Vaihingen, Germany; CRC 1333 Status Meeting, 14.06.2021 - 16.06.2021, Bad Boll, Germany; CRC 1333 Summer School, 21.09.2020 - 23.09.2020, Vaihingen, Germany

Biennial Meeting of the GDCh Division of Macromolecular Chemistry 2020, September 28-29, 2020, online conference; Biennial Meeting of the GDCh Division of Macromolecular Chemistry 2021, 13.09.2021 - 14.09.2021, online Conference

Tailoring mesoporosity in poly(urethane) monolithic supports; Effect of steric confinement upon immobilization on regio- and stereoselectivity in the hydrosilylation of alkynes

CRC 1333 Catalysis Networking Conference, 03.05.2022 - 05.05.2022, Kassel, Germany

Oral Presentations

A Hard Templating Approach to Functional Mesoporous Poly(norborn-2-ene)-Based Monolithic Supports

CRC 1333 Young Researchers Colloquium, December 16-2021, Stuttgart, Germany

Porous Monolithic Polymeric Supports Based on Porous with Uniform Diameter and Tailored Functional Groups

CRC 1333 Summer School, 30.09. - 02.10.2019, Ellwangen, Germany; CRC 1333 Summer School, 30. 08.- 01. 09. 2021, Wetzlar, Germany

Workshops

Project Managements for PhD students, GRADUS, University of Stuttgart, January 12-19, 2021

Risk Technology and Risk Society, GRADUS, University of Stuttgart, October 4-18, 2021

Leadership for Female Scientists, CRC 1333, GRADUS, University of Stuttgart, 29.07.2020 - 19.11.2020